STRUCTURAL PROPERTIES OF ZnO BINARY ALLOY NANOSYSTEMS: MOLECULAR-DYNAMICS SIMULATIONS

A THESIS SUBMITTED TO
THE GRADUATE SCHOOL OF NATURAL AND APPLIED SCIENCES
OF
MIDDLE EAST TECHNICAL UNIVERSITY

BY
MEHMET EMİN KILIÇ

IN PARTIAL FULFILLMENT OF THE REQUIREMENTS
FOR
THE DEGREE OF DOCTOR OF PHILOSOPHY
IN
PHYSICS

MARCH 2015

Approval of the thesis:

STRUCTURAL PROPERTIES OF BINARY ZnO ALLOY NANOSYSTEMS: MOLECULAR-DYNAMICS SIMULATIONS

submitted by **MEHMET EMİN KILIÇ** in partial fulfillment of the requirements for the degree of **Doctor of Philosophy in Physics Department, Middle East Technical University** by,

Prof. Dr. Gülbin Dural Ünver _____
Dean, Graduate School of **Natural and Applied Sciences**

Prof. Dr. Mehmet T. Zeyrek _____
Head of Department, **Physics**

Prof. Dr. Şakir Erkoç _____
Supervisor, **Physics Dept., METU**

Examining Committee Members:

Prof. Dr. Kadri Aydınol _____
Metallurgical and Materials Engineering Dept., METU

Prof. Dr. Şakir Erkoç _____
Physics Dept., METU

Assoc. Prof. Dr. Hatice Kökten _____
Physics Dept., METU

Assoc. Prof. Dr. Engin Durgun _____
UNAM, Bilkent University

Assist. Prof. Dr. Emre Taşçı _____
Physics Eng., Hacettepe University

Date 16.03.2015

I hereby declare that all information in this document has been obtained and presented in accordance with academic rules and ethical conduct. I also declare that, as required by these rules and conduct, I have fully cited and referenced all material and results that are not original to this work.

Name, Last name: **MEHMET EMİN KILIÇ**

Signature :

ABSTRACT

STRUCTURAL PROPERTIES OF ZnO BINARY ALLOY NANOSYSTEMS: MOLECULAR-DYNAMICS SIMULATIONS

Kılıç, Mehmet Emin
Ph.D., Department of Physics
Supervisor: Prof. Dr. Şakir Erkoç

March 2015, 202 pages

ZnO nanostructures revealed novel implementations in optoelectronics, sensors, transducers and biomedical sciences. There are different shapes of ZnO nanostructures such as zero dimensional-0D (quantum dots, nanoparticles), one dimensional-1D (nanorods, nanowires, nanotubes) and two dimensional-2D (nanosheets) and their properties have been experimentally prepared and investigated. Thus, ZnO is one of the richest family of nanostructures among all materials, both in structures and in properties. In this thesis, structural properties of generated 0D (nanoparticles and nanorings), 1D (nanoribbons, nanorods and nanotubes) and 2D nanostructures (nanosheets) under different mechanical processes (tensile strain, compression strain, torsion) have been investigated. Additionally, the defects for nanoribbons and nanosheets have been studied both at 1 and 300 K under the applied tensile strain applications. The nanostructures have been studied both with and without periodic boundary conditions. Moreover, the thermal and structural properties of 0D nanoparticles have been investigated via the nonequilibrated molecular dynamics simulation process by increasing temperatures. Classical molecular dynamics simulations have been performed at 1 and 300 K using an atomistic potential energy function consisting of two body interactions among the atoms. Molecular Dynamics is one of the most promising methods commonly used for investigating the mechanical properties of nanostructures.

Keywords: ZnO Nanostructures, Binary Alloy Nanosystems, Mechanical Properties, Molecular Dynamics Simulations, Empirical Potential Energy Function.

ÖZ

İKİLİ ALAŞIMLI ZnO NANOYAPILARIN YAPI ÖZELLİKLERİ: MOLEKÜL DİNAMİĞİ BENZETİŞİMLERİ

Kılıç, Mehmet Emin
Doktora, Fizik Bölümü
Tez Yöneticisi: Prof. Dr. Şakir Erkoç

Mart 2015, 202 sayfa

ZnO nano yapıların optoelektronikler, algılayıcılar ve biomedikal alanlar gibi bir çok sahada uygulaması vardır. ZnO nano yapıların deneysel olarak sıfır boyutlu-0B (kuantum noktalar), bir boyutlu-1B (nano çubuk, nano tel, nano tüp) ve iki boyutlu-2B (nano tabaka) gibi birçok çeşiti çalışılmakta ve sentezlenmektedir. Bu yüzden ZnO tüm malzemeler içinde en zengin yapı ve özelliğe sahiptir denilebilir.

Bu tez çalışmasında 0B (nano parçacıklar ve nano yüzükler), 1B (nano şeritler, nano çubuklar ve nano tüpler) and 2B (nano tabaka) nano yapıların farklı mekanik işlemler (germe, sıkıştırma, burma) altında molekül dinamiği benzetişim yöntemi ile yapı özellikleri incelendi. Bunlara ek olarak; farklı tipte hasarlı nano şerit ve nano tabakalara germe işlemi uygulayarak onların yapı özellikleri incelendi. 1B ve 2B bu nano yapılar hem sonlu, hem de sonsuz yapılar olarak incelendi. 0B nano parçacıklar termal dengeye getirilmeden sıcaklıkları artırılarak yapı özellikleri incelendi. Söz konusu tüm nano yapılar klasik molekül dinamiği benzetişimi ile ikili etkileşim içeren potansiyel enerji fonksiyonu yardımı ile hem 1 hem de 300 K sıcaklıklarında incelendi. Nanoyapıların mekanik özelliklerinin araştırılmasında MD benzetişimleri yaygın olarak kullanılan yöntemlerin başında gelir.

Anahtar Kelimeler: Çinko Oksit Nanoyapılar, İkili Alaşım Nanoyapılar, Mekanik Özellikler, Molekül Dinamiği Benzetişimi, Ampirik Potensiyel Enerji Fonksiyonu

To My Loving Family

ACKNOWLEDGMENTS

Foremost, I would like to express my sincere gratitude to my supervisor Prof. Dr. Şakir Erkoç for the continuous support of my Ph.D study and research, for his patience, motivation, enthusiasm, and immense knowledge. His guidance helped me in all the time of research and writing of this thesis. I am much grateful to him for all he has done for me. I have learnt a lot from you.

Besides my advisor, I would like to thank the rest of my thesis committee: Prof. Dr. Kadri Aydınol, Assoc. Prof. Dr. Hatice Kokten, Assoc. Prof. Dr. Engin Durgun, and Assist. Prof. Dr. Emre Tasçi for their encouragement, insightful comments, and their valuable contributing comments and suggestions.

In addition, I express my appreciation to Prof. Dr. Osman Özcan for giving me the opportunities to research. I would like to thank everybody who was important to the successful realization of thesis, as well as expressing my apology that I could not mention personally one by one.

Finally and the most importantly I would like to thank my wife and my children. My wife was always there cheering me up and stood by me through the good times and bad. I admire my children for their sweet smiles and looks. I would also like to thank my parents and my sister.

TABLE OF CONTENTS

ABSTRACT v

ÖZ vii

ACKNOWLEDGMENTS ix

TABLE OF CONTENTS x

LIST OF TABLES xiii

LIST OF FIGURES xiv

CHAPTERS 1

1. INTRODUCTION 1

2. METHOD OF CALCULATIONS 7

2.1.1 The Molecular–Dynamics Method 9

2.1.2 Potential Energy Functions (PEF) 11

2.1.3 Details of Molecular Dynamics Method 17

2.1.4 Verlet Algorithm 21

2.1.5 Ensembles 22

2.1.5 Periodic Boundary Conditions: 23

2.3 ZnO Nanostructure Models 24

2.3.1 0D ZnO Nanostructure Models 24

2.3.1.1 ZnO Nanoparticles 24

2.3.1.2 ZnO Nanorings 24

2.3.2 1D ZnO Nanostructure Models 26

2.3.2.1 ZnO Nanoribbons 26

2.3.2.1.1 ZnO Pristine Nanoribbons 26

2.3.2.1.2 ZnO Defected Nanoribbons 26
2.3.2.2 ZnO Nanorods 30
2.3.2.3 ZnO Nanotubes 31
2.3.3. 2D ZnO Nanostructure Models 33
2.3.3.1 Pristine Nanosheets 33
2.3.3.2 Defected Nanosheets 33
2.4 Applied Mechanical Processes 36
2.4.1 Tensile Strain Process 36
2.4.2 Compression Strain Process 37
2.4.3 Torsion Process 37
3. RESULT AND DISCUSSION 39
3.1 0D ZnO Nanostructures 39
3.1.1. ZnO Nanoparticles 39
3.1.1.1 ZnO Spherical Nanoparticles 39
3.1.1.2 ZnO Cubic nanoparticles 55
3.1.2 ZnO Nanorings 59
3.2 1D ZnO Nanostructures 61
3.2.1 ZnO Nanoribbons 61
3.2.1.1 Pristen Nanoribbons 61
3.2.1.1.1 Zigzag Nanoribbons 61
3.2.1.1.2 Armchair Nanoribbons 69
3.2.1.2 Defected Nanoribbons 74
3.2.1.2.1 Zigzag Nanoribbons 74
3.2.1.2.1.1 Central Defect Zigzag Nanoribbons 74
3.2.1.2.1.2 Edge Defect Zigzag Nanoribbons 80
3.2.1.2.2 Armchair Nanoribbons 85
3.2.1.2.2.1 Central Defect Armchair Nanoribbons 85

3.2.1.2.2.2 Edge Defect Armchair Nanoribbons 93
3.2.2 ZnO Nanorods 99
3.2.3 ZnO Nanotubes 121
3.3 2D ZnO Nanostructures 142
3.3.1 ZnO Nanosheets 142
3.3.1.1 The Pristine Nanosheets 142
3.3.1.2 The Defected Nanosheets 144
4. CONCLUSION 165
REFERENCES 169
APPENDICES 179
A. NANOSTRUCTURE FIGURES 179
B. SAMPLE INPUT AND OUTPUT FILES 195
CURRICULUM VITAE 199

LIST OF TABLES

TABLES

Table 2.1 Mechanical properties of ZnO compared with experimental and calculated results using the interatomic potential function…….14

Table 2.2 Potential energy function parameters used in the calculations. Adapted from ref. [119]…….15

LIST OF FIGURES

FIGURES

Figure 1.1 The dimensional analysis of the nanostructures. Adapted from [107]. 4
Figure 2.1 Simulations as a bridge between theory and experiment. Adapted from ref. [118]. 7
Figure 2.2 The considered simulation methods a) QM methods b) Empirical methods. 8
Figure 2.3 The energetic, structural and dynamic behaviors through PEF. Adapted from ref. [118]. 9
Figure 2.4 Harmonic oscillator system (mass on a spring). 11
Figure 2.5 a) Represents two body interaction b) Three body interactions. 12
Figure 2.6 Lennard-Jones pair potential showing the repulsive and attractive contributions. Adapted from ref. [118]. 13
Figure 2.7 Potential energy functions for Zn-O atom pairs 15
Figure 2.8 Potential energy functions for O-O atom pairs. 16
Figure 2.9 Total potential energy function for both Zn-O and O-O atom pairs. 17
Figure 2.10 A draft MD algorithm. Adapted from ref. [123]. 20
Figure 2.11 Verlet algorithm for molecular dynamics. 22
Figure 2.12 Two–dimensional computational cell and image cells for the use of periodic boundary conditions. 23
Figure 2.13 The ideal ZnO spherical nanoparticle models. 25
Figure 2.14 The ideal ZnO cubic nanoparticle models. 25
Figure 2.15 The ideal ZnO nanoring models a) The R1 model b) The R2 model c) The R3 model d) The R4 model. 25
Figure 2.16 The ideal ZnO nanoribbon models a) The Z1L model b) The Z2L model c) The A1L model d) The A2L model. 27

Figure 2.17 The ideal ZnO vacancy type defect zigzag nanoribbon models a) The ZCDV-Zn model b) The ZEDV-Zn model c) The ZCDV-O model d) The ZEDV-O model e) The ZCDV-Zn-O model f) The ZEDV-Zn-O model. 28
Figure 2.18 The ideal ZnO exchange type defect zigzag nanoribbon models a) The ZCDE-Zn-O model b) The ZEDE-Zn-O model. 28
Figure 2.19 The ZnO ideal vacancy type defect armchair nanoribbon models a) The ACDV-Zn model b) The AEDV-Zn model c) The ACDV-O model d) The AEDV-O model e) The ideal ACDV-Zn-O model f) The ideal AEDV-Zn-O model. 29
Figure 2.20 The ideal ZnO exchange defect armchair nanoribbon models a) The ACDE-Zn-O model b) The AEDE-Zn-O model. 29
Figure 2.21 The ideal ZnO nanorod models a) The HR1, HR2, and HR3 models. b) The TR model c) The RR model. 30
Figure 2.22 The ideal ZnO zigzag nanotube models. 31
Figure 2.23 The ideal ZnO armchair nanotube models. 32
Figure 2.24 The ideal ZnO chiral nanotube models. 32
Figure 2.25 The ideal ZnO pristine nanosheet model. 33
Figure 2.26 The ideal ZnO vacancy type defect nanosheet models a) The SV-Zn model b) The SV-O model c) The SV-Zn-O model. 34
Figure 2.27 The ideal ZnO exchange type defect nanosheet models a) The SE-SB model b) The SE-SW model. 34
Figure 2.28 The ideal ZnO line type defect model. 35
Figure 2.29 The ideal ZnO circular hole defect type nanosheets. a) The CH1 model b) The CH2 model **c)** The CH3 model d) The CH4 model. 35
Figure 2.30 The 5% tensile strain application process. 38
Figure 2.31 The 5% compression strain application process. 38
Figure 2.32 The torsion application processes. 38
Figure 3.1 The SP1 model during the EMD process. 41
Figure 3.2 The structural properties of the SP1 model during the NEMD process.. 41
Figure 3.3 The structural properties of the model, which consisted of 2 more oxygen atoms than the SP1 model during the NEMD process. 42
Figure 3.4 The structural properties of the SP2 model during the NEMD process... 42
Figure 3.5 Radial atomic distribution of the SP2 model at 1 K. 43
Figure 3.6 The same as Figure 3.5, but at 200 K. 43

Figure 3.7 The same as Figure 3.5, but at 600 K. 44
Figure 3.8 The same as Figure 3.5, but at 900 K. 44
Figure 3.9 The structural and thermal properties of the SP3 model during the NEMD process. 45
Figure 3.10 Radial atomic distribution of the SP3 model at 1 K. 45
Figure 3.11 The same as Figure 3.10, but at 600 K. 46
Figure 3.12 The same as Figure 3.10, but at 900 K. 46
Figure 3.13 Radial atomic distribution of the ideal SP7 model. 48
Figure 3.14 The same as Figure 3.13, but at 100 K. 48
Figure 3.15 The same as Figure 3.13, but at 500 K. 49
Figure 3.16 The same as Figure 3.13, but at 700 K. 49
Figure 3.17 The same as Figure 3.13, but at 800 K. 50
Figure 3.18 The same as Figure 3.13, but at 1000 K. 50
Figure 3.19 The average potential energy of the SP7 model. 51
Figure 3.20 Radial atomic distribution of the ideal SP8 model. 52
Figure 3.21 The same as Figure 3.20, but at 100 K. 52
Figure 3.22 The same as Figure 3.20, but at 500 K. 53
Figure 3.23 The same as Figure 3.20, but at 900 K. 53
Figure 3.24 The same as Figure 3.20, but at 1000 K. 54
Figure 3.25 The average potential energy for per atom versus temperature of the SP8 model. 54
Figure 3.26 The CP1 model during the NEMD process. 55
Figure 3.27 The average potential energy for per particle of the CP1 model during the NEMD process. 56
Figure 3.28 a) The CP2A model during the NEMD b) The CP2B model during the NEMD. 56
Figure 3.29 The CP6A model during the NEMD process. 57
Figure 3.30 The CP6B model during the NEMD process. 57
Figure 3.31 The heat capacity of the CP6A model with NEMD. 58
Figure 3.32 The heat capacity of the CP6B model with NEMD. 58
Figure 3.33 The R1 model nanoring during the NEMD process. 59
Figure 3.34 The R2 nanoring model during the NEMD process. 60

Figure 3.35 The Z1L model nanoribbons with NoPBC, the top figure for at 1 K with top and side view and the bottom for at 300 K. 62
Figure 3.36 a) The Z1L model with PBC at 1 K. b) The same model under 5% tensile strain application at 1 K. Each row shows cross section view and side view. 62
Figure 3.37 a) The Z1L model with PBC at 300 K. b) The same model under 5% tensile strain application at 300 K. Each row shows cross section and side view. 63
Figure 3.38 The total potential energy versus MD steps for the Z1L model at 1 K with NoPBC. 64
Figure 3.39 The total potential energy versus MD steps for the Z1L model at 300 K with NoPBC. 64
Figure 3.40 The total potential energy versus MD steps for the Z1L model at 1 K with PBC. 65
Figure 3.41 The total potential energy versus MD steps for the Z1L model at 300 K with NoPBC. 65
Figure 3.42 The Z2L model with NoPBC, the top figure for at 1 K, the bottom at 300 K. 66
Figure 3.43 a) The Z2L model with PBC at 1 K b) The same model under 5% tensile strain application at 1 K. 67
Figure 3.44 a) The Z2L model with PBC at 300 K. b) The same model under 5% tensile strain application at 300 K. 68
Figure 3.45 The A1L model with NoPBC, the top figure for at 1 K with top and side view, the bottom at 300 K. 70
Figure 3.46 a) The A1L model with PBC at 1 K. b) The same model under 5% tensile strain at 1 K. 70
Figure 3.47 a) The A1L model with PBC at 300 K b) The same model under 5% tensile strain at 300 K. 71
Figure 3.48 The A2L model with NoPBC, the left figure for at 1 K, the right figure at 300 K. 71
Figure 3.49 a) The A2L model with PBC at 1 K b) The same model under 5% tensile strain application at 1 K. 72
Figure 3.50 a) The A2L model with PBC at 300 K. b) The same model under 5% tensile strain application at 300 K. 73

Figure 3.51 The ZCDVZn model, the top figure for ideal structure, the bottom figures for with NoPBC (the left bottom for at 1 K, the right bottom for at 300 K).....76
Figure 3.52 The ZCDVZn model under 5% tensile strain a) at 1 K b) at 300 K. 77
Figure 3.53 The ZCDVO model, the top figure for ideal and the bottom figures for with NoPBC, the left bottom figures for at 1 K at top and side views, the right bottom figures for at 300 K. 77
Figure 3.54 The ZCDVO model under 5% tensile strain a) at 1 K b) at 300 K.....78
Figure 3.55 The ZCDVZnO model at 1 K and 300 K a) with NoPBC b) with PBC. 79
Figure 3.56 The ZCDEXZnO model at 1 and 300 K a) with NoPBC b) with PBC. .79
Figure 3.57 The ZEDVZn model with NoPBC at 1 and 300 K. 81
Figure 3.58 The ZEDVZn model under 5% tensile strain applications a) at 1 K b) at 300 K. 82
Figure 3.59 The ZEDVO model with NoPBC at 1 and 300 K.....83
Figure 3.60 The ZEDVO model under 5% tensile strain applications a) at 1 K b) at 300 K. 83
Figure 3.61 The ZEDVZnO model at 1 and 300 K a) with NoPBC b) with PBC. 84
Figure 3.62 The ZEDEXZnO model with NoPBC at 1 and 300 K.....84
Figure 3.63 The ACDVZn model with NoPBC at 1 and 300 K. 87
Figure 3.64 The ACDVZn model under 5% tensile strain applications a) at 1 K b) at 300 K. 88
Figure 3.65 The ACDVO model with NoPBC at 1 and 300 K.....89
Figure 3.66 The ACDVO model under 5% tensile strain applications a) at 1 K b) at 300 K. 89
Figure 3.67 The ACDVZnO model, the top figure for ideal and the bottom figures for with NoPBC at 1 and 300 K.....90
Figure 3.68 The ACDVZnO model under 5% tensile strain applications a) at 1 K b) at 300 K. 90
Figure 3.69 The ACDEXZnO model, the top figure for ideal and the bottom figures for with NoPBC at 1 and 300 K. 91
Figure 3.70 The ACDEXZnO model with PBC at 300 K.....91
Figure 3.71 The ACDEXZnO model at 1 K under 5% tensile strain.....92
Figure 3.72 The AEDVZn model with NoPBC at 1 and 300 K.....95
Figure 3.73 The AEDVZn model under 5% tensile strain a) at 1 K b) at 300 K. 95

Figure 3.74 The AEDVO with NoPBC at 1 and 300 K. 96
Figure 3.75 The AEDVO model under %5 tensile strain applications a) at 1 K b) at 300 K. 96
Figure 3.76 The AEDVZnO model with NoPBC at both 1 and 300 K. 97
Figure 3.77 The AEDVZnO model under 5% tensile strain a) at 1 K b) at 300 K. .. 97
Figure 3.78 The AEDEXZnO model at 1 and 300 K. a) without NoPBC b) with PBC. 98
Figure 3.79 The HR1 model with NoPBC at both 1 and 300 K. 100
Figure 3.80 The HR1 model at 1 K under strain applications a) compression b) tensile strain. 101
Figure 3.81 Tensile strain energy with respect to elongation for the H1 model at 1 K. 101
Figure 3.82 The HR1 model at 1 K under torsion applications. 102
Figure 3.83 The HR1 model at 300 K under 5% strain applications a) compression b) tensile strain. 103
Figure 3.84 The HR1 model at 300 K under torsion applications. 103
Figure 3.85 The HR2 model with NoPBC at 1 and 300 K. 105
Figure 3.86 The HR2 model at 1 K under 5% strain applications a) compression b) tensile strain. 105
Figure 3.87 The HR2 model at 1 K under torsion applications. 106
Figure 3.88 The HR2 model at 300 K under 5% strain applications a) compression b) tensile strain. 107
Figure 3.89 The HR2 model under torsion applications at 300 K. 108
Figure 3.90 The HR3 model at 1 K under 5% strain applications a) compression b) tensile strain. 110
Figure 3.91 The HR3 model at 1 K under torsion applications. 111
Figure 3.92 The HR3 model at 300 K under 5% strain applications a) compression b) tensile strain. 112
Figure 3.93 The HR3 model at 300 K under torsion applications. 113
Figure 3.94 The average bond length of HR1, HR2, HR3 models at both 1 and 300 K under compression and tensile strain applications. 114
Figure 3.95 The average potential energy for per atom of HR2, HR3 models at both 1 and 300 K under torsion applications. 114

Figure 3.96 The TR model with NoPBC at 1 and 300 K. 116
Figure 3.97 The TR model at 1 K under 5% strain applications a) compression b) tensile strain.....116
Figure 3.98 The TR model at 300 K under 5% strain applications a) compression b) tensile strain applications. 117
Figure 3.99 The RR model with NoPBC at 1 and 300 K. 118
Figure 3.100 The RR model at 1 K under 5% strain applications a) compression b) tensile strain.....119
Figure 3.101 The RR model at 300 K under 5% strain applications a) compression b) tensile strain.....120
Figure 3.102 The ZT1 model with NoPBC at 1 and 300 K. 123
Figure 3.103 The ZT1 model structure at 1 K under strain applications a) 5% compression b) 5% tensile strain. 124
Figure 3.104 The ZT1 model structure at 300 K under strain applications a) 5% compression b) 5% tensile strain. 125
Figure 3.105 The ZT2 model structure with NoPBC at both 1 and 300 K. 125
Figure 3.106 The ZT2 model structure at 1 K under strain applications a) 5% compression b) 5% tensile strain. 126
Figure 3.107 The ZT2 model structure at 300 K under strain applications a) 5% compression b) 5% tensile strain. 127
Figure 3.108 The average bond length between atoms versus tube length of the ZT1and ZT2 models at both 1 and 300 K under compression and tensile strain applications.....128
Figure 3.109 The average tube radius versus tube length of the ZT1 and the ZT2 models at both 1 and 300 K under compression and tensile strain. 128
Figure 3.110 The average potential energy for per particle versus tube length for the ZT1 and ZT2 models at both 1 and 300 K under compression and tensile strain....129
Figure 3.111 The AT1 model structure at both 1 and 300 K with NoPBC. The left picture views from the top, the right picture view from the side in each figures.....131
Figure 3.112 The AT1 model structure at 1 K under strain applications a) 5% compression b) 5% tensile strain. 132
Figure 3.113 The AT1 model at 300 K under strain applications a) 5% compression b) 5% tensile strain. 133

Figure 3.114 The AT2 model structure at both 1 and 300 K with NoPBC. 134
Figure 3.115 The AT2 model at 1 K under 5% strain application a) compression b) tensile strain. 135
Figure 3.116 The AT2 model at 300 K under 5% strain applications a) compression b) tensile strain. 136
Figure 3.117 The average bond length between atoms versus tube length at both 1 and 300 K under compression and tensile strain applications. 137
Figure 3.118 The average potential energy for per atom versus tube length of AT1 and AT2 models at both 1 and 300 K under compression and tensile strain applications. 137
Figure 3.119 The CT1 model at 1 and 300 K a) with NoPBC b) with PBC. 139
Figure 3.120 The CT1 model at 1 K under 5% tensile strain applications. 139
Figure 3.121 The CT1 model at 300 K under 5% tensile strain applications. 140
Figure 3.122 The CT2 model at 1 and 300 K a) with NoPBC b) with PBC. 140
Figure 3.123 The CT2 model at 1 K under 5% tensile strain applications. 141
Figure 3.124 The CT2 model at 300 K under 5% tensile strain applications. 141
Figure 3.125 The PS model nanosheet structure at 1 and 300 K a) with NoPBC b) with PBC. 143
Figure 3.126 The PS model nanosheet under tensile strain applications at 1 K a) 5% strain b) 10% strain c) 15% strain 143
Figure 3.127 The PS model nanosheet at 300 K under tensile strain applications a) 5% strain b) 10% strain c) 15% strain. 144
Figure 3.128 The ideal SV-Zn defect model nanosheet at 1 and 300 K b) with NoPBC c) with PBC. 147
Figure 3.129 The SV-Zn defect model nanosheet at 1 K under tensile strain applications a) 5% strain b) 10% strain c) 15% strain. 147
Figure 3.130 The SV-Zn defect model nanosheet at 300 K under tensile strain applications a) 5% strain b) 10% strain. 148
Figure 3.131 The SV-O defect model nanosheets a) ideal b) with NoPBC at 1 and 300 K c) with PBC at 1 and 300 K. 148
Figure 3.132 The SV-O defect model nanosheet at 1 K under tensile strain applications a) 5% strain b) 10% strain c) 15% strain. 149

Figure 3.133 The SV-O defect model nanosheets at 300 K under tensile strain applications a) 5% strain b) 10% strain. 149
Figure 3.134 The SV-Zn-O defect model nanosheets a) ideal b) with NoPBC at 1 and 300 K c) with PBC at 1 and 300 K. 150
Figure 3.135 The SV-Zn-O defect model nanosheet at 1 K under tensile strain applications a) 5% strain b) 10% strain c) 15% strain. 151
Figure 3.136 The SV-Zn-O defect model nanosheets at 300 K under tensile strain applications a) 5% strain b) 10% strain. 152
Figure 3.137 The SE-SB defect model nanosheets a) ideal b) with NoPBC at 1 and 300 K c) with PBC at 1 and 300 K. 155
Figure 3.138 The SE-SW defect model nanosheets a) ideal b) with NoPBC at 1 and 300 K c) with PBC at 1 and 300 K. 156
Figure 3.139 The LD defect model nanosheets a) ideal b) with NoPBC at 1 and 300 K c) with PBC at 1 and 300 K. 157
Figure 3.140 The LD defect model nanosheets under tensile strain applications a) 5% strain at 1 K b) 10% strain at 1 K c) 5% at 300 K. 158
Figure 3.141 The CHD1 defect model nanosheets at 1 and 300 K b) with NoPBC c) with PBC. 159
Figure 3.142 The CHD1 defect model nanosheets at 1 K under tensile strain applications a) 5% strain b) 10% strain. 160
Figure 3.143 The CHD1 defect model nanosheets at 300 K under tensile strain applications a) 5% strain b) under 10% strain. 161
Figure 3.144 The CHD2 defect model nanosheets at 1 and 300 K b) with NoPBC c) with PBC. 162
Figure 3.145 The CHD2 defect model nanosheets at 1 K under tensile strain applications a) 5% strain b) 10% strain. 163
Figure 3.146 The CHD2 defect model nanosheets at 300 K under tensile strain applications a) 5% strain b) 10% strain. 164
Figure A.1 The structural properties of the SP4 model under the increasing temperatures during the NEMD process. 179
Figure A.2 Radial atomic distribution of the SP4 model at 1 K. 180
Figure A.3 The same as Figure A.2, but at 300 K. 180
Figure A.4 The same as Figure A.2, but at 600 K. 180

Figure A.5 The same as Figure A.2, but at 800 K. 181
Figure A.6 The structural properties of the SP5 model under the increasing temperatures during the NEMD process. 181
Figure A.7 Radial atomic distribution of the SP5 model at 1 K..... 182
Figure A.8 The same as Figure A.2, but at 300 K. 182
Figure A.9 The same as Figure A.2, but at 600 K. 182
Figure A.10 The same as Figure A.2, but at 1100 K. 183
Figure A.11 The structural properties of the SP6 model under the increasing temperatures during the NEMD process. 183
Figure A.12 Radial atomic distribution of the SP6 model at 1 K..... 184
Figure A.13 The same as Figure A.12, but at 300 K. 184
Figure A.14 The same as Figure A.12, but at 600 K. 185
Figure A.15 The same as Figure A.12, but at 1000 K. 185
Figure A.16 The R3 model nanoring at the increasing temperatures in the case of NEMD. 186
Figure A.17 The R4 model nanoring at the increasing temperatures in the case of NEMD. 186
Figure A.18 The ZT3 model with NoPBC and PBC at both 1 and 300 K. 187
Figure A.19 The ZT3 model structure under tensile strain applications at 1 K. 187
Figure A.20 The ZT3 model structure under tensile strain applications at 300 K. . 187
Figure A.21 The ZT4 model with NoPBC and PBC at both 1 and 300 K. 188
Figure A.22 The ZT4 model structure under tensile strain applications at 1 K. 188
Figure A.23 The ZT4 model structure under tensile strain applications at 300 K. . 188
Figure A.24 The AT3 model with NoPBC and PBC at both 1 and 300 K. 189
Figure A.25 The AT3 model structure under tensile strain applications at 1 K. 189
Figure A.26 The AT3 model structure under tensile strain applications at 300 K. . 190
Figure A.27 The AT4 model with NoPBC and PBC at both 1 and 300 K. 190
Figure A.28 The AT4 model structure under tensile strain applications at 1 K. 191
Figure A.29 The AT4 model structure under tensile strain applications at 300 K. . 192
Figure A.30 The CT3 model with NoPBC and PBC at both 1 and 300 K. 193
Figure A.31 The CT3 model structure under tensile strain applications at 1 K. 193
Figure A.32 The CT3 model structure under tensile strain applications at 300 K. . 193
Figure A.33 The CT4 model with NoPBC and PBC at both 1 and 300 K. 194

Figure A.34 The CT4 model structure under tensile strain applications at 1 K.....194
Figure A.35 The CT4 model structure under tensile strain applications at 300 K...194

CHAPTER 1

INTRODUCTION

Nanoscience enables the understanding of fundamental phenomena and materials at the nanoscale or atomic and molecular levels (the length scale being approximately 1-100 nanometer range). Nanotechnology, on a similar path, is the application of nanoscience and engineering methods to produce novel materials and devices. The terms nanostructure, nanoscience, and nanotechnology have rapidly become popular in scientific and general press. The novel and intrinsic properties are actually developed at a critical length scale of matter typically under 100 nm. Many properties of systems such as physical and chemical, are size dependent in nanometer region, resulting in an interest for the nanoscale structures.

In contemporary condensed matter sciences, semiconducting oxides, such as zinc oxide (ZnO), indium oxide (In_2O_3), tin oxide (SnO_2) and gallium oxide (Ga_2O_3) are among the most widely studied and topical materials[1,2]. Among these oxides, ZnO as an important functional oxide has become the second most widely studied material after Si as seen from a surge of a relevant number of publications. ZnO is not a newly learned material. Actually, it has been studied dating back to 1935. For instance, in 1935, Bunn studied its lattice parameters[3]. In 1954, Mollwo studied its optical properties[4]. In 1966, its vibration properties have been studied by Damen and co-workers[5]. In 1975, ZnO/ZnSe n-p junctions have been studied by Tsurkan et al[6].

It is known that many properties of ZnO such as crystal[7], lattice[7], mechanical[8,9–13], electronic, magnetic[14–18] and optical[19–24] have been studied[25]. ZnO as being an II-VI compound semiconductor has three possible crystal phases namely, wurtzite, zinc-blend and rock salt. Under most circumstances, the natural structure of ZnO is wurtzite, which having a hexagonal unit cell with two independent lattice

parameters, a and c. The lattice parameters of ZnO have been studied in both experimental measurements[26–28] and theoretical calculations[29–31]. The lattice constants are in a very good agreement for the wurtzite crystal structure at room temperature with experimental and theoretical parameters. Experimentally, the "a" parameters are ranged from 3.2475 to 3.2501 Å, the "c" parameters are ranged from 5.2042 to 5.2075 Å and the the c/a ratios are ranged from 1.593 to 1.6035 Å[26–28]. However, the c/a ratios were experimentally observed smaller than ideal ratios, for which the c/a ratio is 1.633 in ideal wurtzite structure. The wurtzite and zinc blend structures differ only in the bond angle of the second-nearest neighbors. The wurtzite structure of ZnO can transform into the rock salt phases at high pressure (10-15 GPa)[29,32]. In other words, the rock salt structure is stable only under high pressure. In addition, the mechanical properties of ZnO are widely studied as well[33]. The elastic, bulk, Young moduli, hardness, stiffness and piezoelectric constants are pivotal in determining the mechanical properties of ZnO. Especially, the elastic constants namely, C_{11}, C_{33}, C_{12}, C_{13} and C_{44} have been studied in hexagonal crystal structure of ZnO[34–36]. And it is reported that the Young's modulus values are ranging from low values of 20-58 GPa to around the bulk value(140 GPa) of 100-220 GPa[37–39] and hardness values of 2.5-4.3 GPa[40]. Moreover, the tetrahedral coordination in ZnO result in non-central symmetric structure and consequently supports piezoelectricity and pyroelectricity[41]. ZnO has the highest piezoelectric tensor among the tetrahedral bonded semiconductors[42]. The other property of ZnO is having polar surfaces. The most common polar surface of ZnO is the basal plane (0001)[33,43]. Furthermore, the electronic band structure of ZnO, playing an important key for understanding electronic properties of the material[25,33], has been widely studied for wurtzite, zinc blend and rocksalt phases[14,33,43]. Additionally, in theoretical[44] and experimental[45] studies it was shown that materials with high transition temperatures, such as ZnO doped with transition metal showed ferromagnetism at room temperature[46]. For example, Mn:ZnO nanoparticles and thin films only exhibit ferromagnetism at room temperature[47]. Recently, carbon-doped ZnO films have been found ferromagnetic at room temperature, whereas carbon-doped ZnO powder has been found nonferromagnetic[48].

ZnO is a chemically stable and enviromentally friendly material, resulting in considerable interest in studying ZnO, in different forms such as powders[19,21,49–53],

single crystals[25,41,54–58], thin films[59,60] and nanostructures[25,43,61]. Among these forms, the nanostructured ZnO is a multifunctional material with a great potential for a variety of practical applications, such as piezoelectric[62], optical waveguides[63], surface acoustic wave devices[64], varistors, phosphors, transparent conducting oxides[65], functional spin-electronic devices[7], field emitters[66], UV-light emitters/detectors[67], biomedicals[68], etc. It is also a promising material for photonic applications[69] in the UV or blue spectral range because of having a wide direct band gap (3.37 eV at room temperature), and it has high exciton-binding energy (60 meV), which makes it a suitable material for efficient excitonic lasing at room temperature. Additionally, it is one of the earliest discovered and well-established gas sensing oxides[7]. Since Seiyama et al. reported the gas sensor based on ZnO thin film in 1962, many ZnO gas sensors have been developed[70]. Furthermore, there also are many studies investigating for the vibrational[5,25,43,71], optical[19,25,49,72] and thermal properties[7] of ZnO material.

Up to now, many methods[73] such as thermal chemical vapor deposition (CVD)[74], thermal evaporation[75], metal organic CVD[21], solution based synthesis[19,76–78] etc. have been shown to synthesize ZnO nanostructures[33]. There are different experimentally synthesized shapes of ZnO nanostructures such as nanoribbons[52,79–81], nanobelt[51,82–84,85], nanorods[20,57,78,86–90], nanowires[74,75,61,84,87,91,92], nanocombs[93], nanorings[55,94,95], nanotubes[24,50,53,77,96–98,99,100], nanoparticles[18,101,102,103], nanosheets[22,104–106], nanoplates[103]. Therefore, ZnO probably has the richest family of nanostructures among all materials.

These nanostructures would be better to classify with respect to dimensionality as zero-dimensional (0D), one-dimensional (1D), two-dimensional (2D) and three-dimensional (3D) nanostructures (see Figure 1.1). At the nanoscale 0D, 1D and 2D are commonly used, but 3D is usually considered as macroscopic systems.

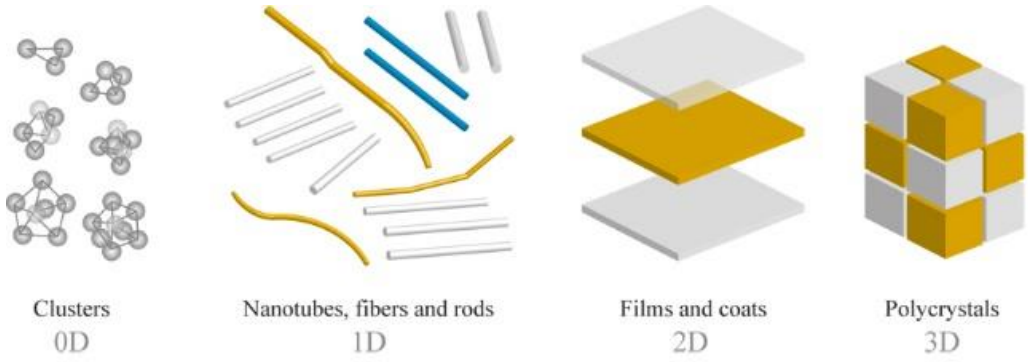

Figure 1.1 The dimensional analysis of the nanostructures. Adapted from [107].

First of all, for the 0D ZnO nanostructures, such as clusters, nanoparticles have extensively been studied. ZnO nanoparticles are prepared with the sol-gel route methods, which were commonly used by Spanhel and Anderson in 1991[107]. Zhang et al. reported flower-like ZnO nanoparticles using hydrothermal method at high temperature of 180 C [108]. The flower-like ZnO nanostructures, used for photocatalytic and heterogeneous catalytic applications, have been studied[108]. ZnO nanoparticles find a widespread potential for applications such as varistors, cathode-ray phosphor, transparent electrodes, chemical sensors and UV-protection films. ZnO nanoparticles are utilized from photocatalytic, heterogenous catalytic (for methanol synthesis) and mostly magnetic applications[18,61,86]. Secondly, 1D nanostructures with various morphologies such as ribbon, wires, rods, tubes, have stimulated wide interest due to their great potential for fundamental studies of the effects of morphology, dimensionality, and size on their physical and chemical properties as well as for their application in optoelectronic devices and as building blocks[109]. 1D ZnO nanostructures have also been synthesized via various kinds of techniques[33]. For instance, Yan et al. synthesized ZnO nanoribbons via carbon thermal reduction process at 900 K[110]. ZnO nanorods and nanowires, have been synthesized via chemical and physical vapor deposition[111]. ZnO nanotubes have been synthesized via thermal evaporation[7]. At present all the synthesized ZnO nanotubes are of thick walls. Thirdly, two dimensional (2D) nanostructures such as nanosheets have been studied both experimentally[112] and theoretically[113,71]. The 2D ZnO nanostructure have mostly been used for optoelectronic devices. However, a few reports have been made for the synthesis of 2D ZnO nanostructures grown by different fabrication techniques up to now. For instance, Chen et al. have prepared ZnO nanosheets by vapor-transport

process[22]. Hu et al. indirectly prepared the 2D micrometer-sized single-cristalline ZnO thin nanosheets via reduction of ZnS powders[56]. Deng et al synthesized ZnO nanosheets with a simple solid vapor deposition[106].

We have investigated the structural properties of 0D (nanorings[13], nanoparticles[13]), 1D (nanoribbons[10,11], nanorods[12], nanotubes[9]) and 2D (nanosheets) nanostructures via molecular dynamics simulation techniques.

CHAPTER 2

METHOD OF CALCULATIONS

Simulations establish a bridge between theory and experiment. In this aspect, we may test a theory by conducting a simulation using the same model. We may test the model by comparing with experimental results. We may also carry out simulations on the computer that are difficult in the laboratory (e.g. working at high temperatures and pressures). Fundamentally, we may want to make direct comparisons with experimental measurements made on specific materials, in which case a good model of molecular interactions is essential.

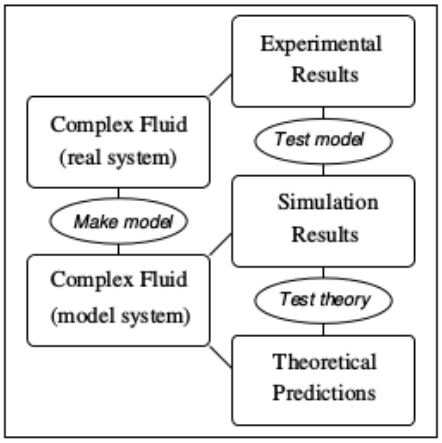

Figure 2.1 Simulations as a bridge between theory and experiment. Adapted from ref. [118].

It is utilized from the computer simulation techniques to calculate the properties of a collection of atoms which interact with one another through a potential energy function (PEF).

The atomistic methods, which explicitly consider every individual atom, can be categorized Quantum-mechanical (QM), or ab initio methods and Atomistic methods using empirical inter-atomic potential. The main idea of the quantum mechanical methods is to solve electronic Schrodinger equation for atoms and molecules, as well as various approximation of that solution. Electronic structure of each atom is accounted for. QM methods are very accurate, but extremely expensive. The QM methods are currently applicable for systems involving a few 100 s of atoms. The major QM methods are Density Functional Theory (DFT), Hartree-Fock (HF), and Tight Binding (TB). According to the empirical methods, on the other hand, the whole atom is defined just as a ball (soft sphere). In which case, it is not required to account for the complex electronic structure of each atom. The methods are less accurate, but relatively inexpensive. The empirical interatomic potentials can handle much larger systems. In atomistic level simulations atoms are considered as point like particles, that means no electronic information no nuclear information, no spin, no angular momentum, no wave function, etc. The major methods of the empirical methods are Molecular Mechanics (MM), Molecular Dynamics (MD) and Monte Carlo (MC).

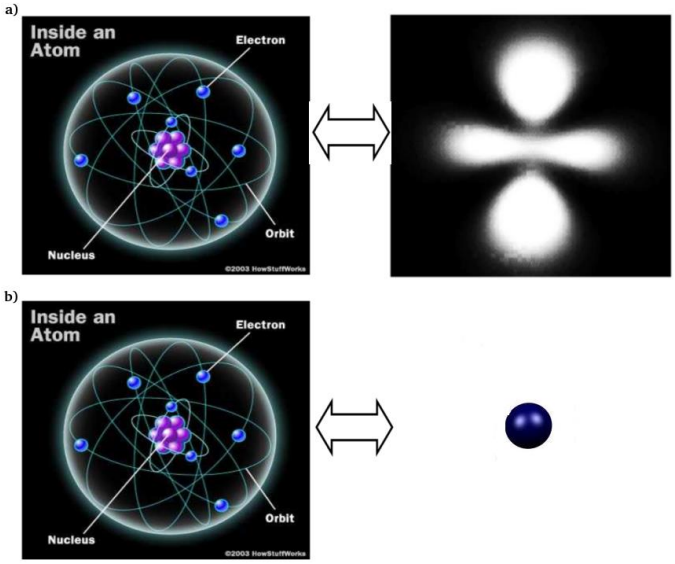

Figure 2.2 The considered simulation methods a) QM methods b) Empirical methods.

In practice, the PEF parameters are determined by using experimental data. If enough experimental data are not exist them accurate quantum results may also be used to determine PEF parameters. Once the basic physical behavior of the system is embodied in the PEF, large–scale numerical calculations, referred to as Atomistic Computer Simulations (ACS), provide an iterative solution to the basic structural, energetic and dynamical behavior of the interacting atoms.

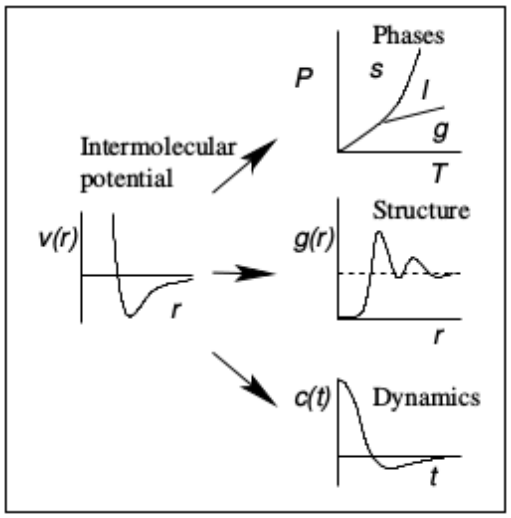

Figure 2.3 The energetic, structural and dynamic behaviors through PEF. Adapted from ref. [118].

2.1.1 The Molecular–Dynamics Method

Molecular dynamics methods were originally devised in the 1957 by Alder and Wainwright, for investigating a solid-fluid transition in a system composed of hard spheres interacting by instantaneous collisions. For a system of 500 particles, simulation of inter-particle collisions took about an hour on an IBM 704 computer[114]. Moreover, in 1960 Born-Mayer interaction potential was used for the first time in MD simulation of radiation damage in a Cu target performed at Brookhaven Lab by Gibson and workers [115], applying a constant inward force to each atom on the boundary of crystallite to account for the attractive part for the interatomic interaction (computational cell composed of 446 to 998 copper atoms was simulated. One integration step took about one minute on an IBM 704 computer). Furthermore, Aneesur Rahman in 1964 used Lennard-Jones potential to describe both attractive and

repulsive interaction in a system of 864 argon atoms[116]. Therefore, MD have been received widespread attention in the mid-1970s by incorporating more powerful and affordable digital computers. 1980's, on the other hand, was an important decade for the Molecular Dynamics Method. Such that many new algorithms were presented: Non equilibrium molecular dynamics method, ab initio molecular dynamics method known as the Car-Perinello method, and most importantly, simulations in ensembles different from the traditional microcanonical ensemble.

Molecular dynamics simulation technique has been used to investigate a wide range applications in different fields such as Chemistry and Biochemistry (drug design, structure of membrane, dynamics of large biomolecules, etc.), Statistical Mechanics and Physics (correlated many-body motion, properties of statistical ensembles, structure and properties of small clusters, phase transitions, etc.), Material Science (point, linear defects in crystals and their interactions, melting and faceting, film growth, etc.)[117].

The content of Molecular dynamics simulations is that it consists of the numerical (step by step) solution of the classical equations of motion.

Fundamentally, a simple atomic system may be written as

$$m_i \ \frac{\partial^2 \vec{r}_i}{\partial t^2} = \vec{f}_i = -\vec{\nabla}_i \phi; \quad i = 1,2,\dots,N \tag{2.1}$$

Each time step of the simulation commences with the calculation of the force for each particle. To calculate the forces, e.g. acting on the atom i, are usually derived from the potential energy function. If their separation r_{ij} between i and j atoms is greater than some cut-off radius (R_C), the interaction between i and j atoms is ignored.

2.1.2 Potential Energy Functions (PEF)

The most important and remarkable data for MD is to use the suitable interatomic potential (PEF) because of calculating forces acting each particle. The potential energy function ϕ representing both bonded and non-bonded interactions between atoms is traditionally split into 1-body, 2-body, 3-body… terms:

$$\phi(r_1, r_2, r_3, .., r_N) = \phi_1(r_i) + \phi_2(r_i, r_j) + \phi_3(r_i, r_j, r_k,) + \cdots \quad (2.2)$$

where the ϕ_1 term represents (one body potentials) an externally applied potential field or the effects of the container walls; it is usually dropped for fully periodic simulations for bulk systems. So the term depends on the distance between the atom and the external source, e.g. harmonic oscillator (mass on a spring) (see Figure 2.4).

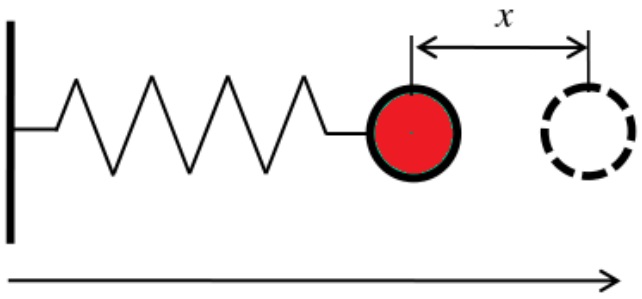

Figure 2.4 Harmonic oscillator system (mass on a spring).

$$\phi_1(x) = \frac{1}{2}kx^2 \quad (2.3)$$

In Eq. (2.2), the second term ϕ_2 represents two body interactions (see Figure 2.5 a) whereas the last term ϕ_3 represents three body interactions[118](see Figure 2.5 b).

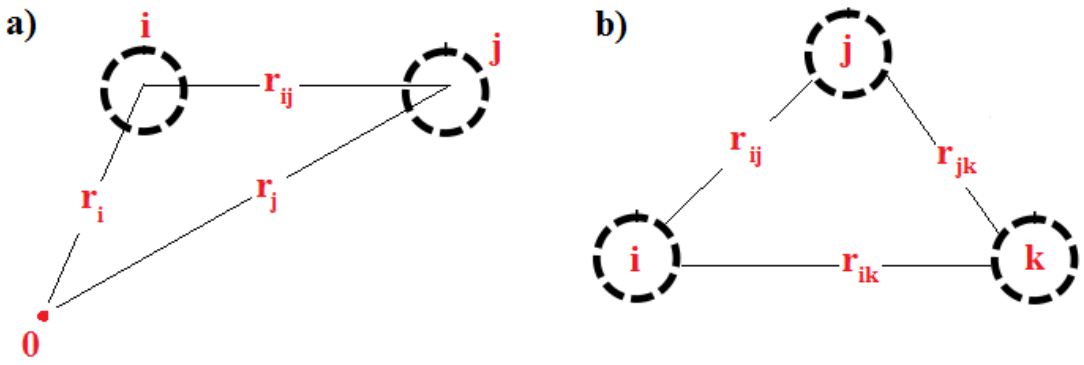

Figure 2.5 a) Represents two body interaction b) Three body interactions.

The PEF used in this study contains only pair interactions.

$$\phi_2(r) = \sum_{i<j}^{N} U_{ij} \tag{2.4}$$

In literature, the Lennard-Jones potential is the most commonly used for the two body interaction potentials (pair-wise). This potential form:

$$U_{ij}(r) = 4\epsilon\left[\left(\frac{\sigma}{r}\right)^{12} - \left(\frac{\sigma}{r}\right)^{6}\right] \tag{2.5}$$

where σ parameter represents the diameter (the separations for which the energy is zero), and ϵ parameter represent the well depth (which is the difference between zero energy and the minimum energy). The $\left(\frac{\sigma}{r}\right)^{6}$ term represents the attractive van der Waals interactions, whereas the $\left(\frac{\sigma}{r}\right)^{12}$ term represents the repulsive force (see Figure 2.6).

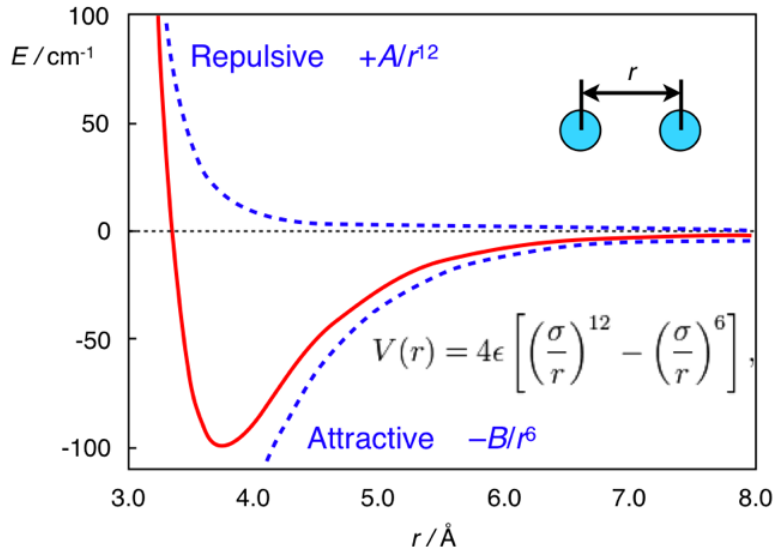

Figure 2.6 Lennard-Jones pair potential showing the repulsive and attractive contributions. Adapted from ref. [118].

In this study, the potential energy function given in Eq. (2.6), which was developed for ionic and semi-ionic oxides[119], has been used. Actually, the parameters of this PEF represents the bulk form of ZnO reasonably well. Its transferability property was tested by the developers of the PEF. Both structural and mechanical properties, such as bulk moduli, elastic constants and latice parameters for ZnO bulk materials, were found in very good agreement compared with experimental data. For example, the lattice parameters of ZnO have been produced with errors less than 2% (see Table 2.1). As a result of this, we used this potential for ZnO nanostructures and found very good results[9–13,120,121].

Table 2.1 Mechanical properties of ZnO compared with experimental and MD calculated results using the interatomic potential function. Adapted from ref. [119].

	Lattice Parameters				**Elastic Constants**				
	a (Å)	b(Å)	c (Å)		C_{11}	C_{33}	C_{44}	C_{12}	C_{13}
Expt.	3.2494	3.2494	5.2038		20.90	21.80	4.41	12.00	10.4
Calc.	3.2463	3.2463	5.0974		21.29	17.77	4.31	13.99	12.1
%Err.	-0.1	-0.1	-2.0		1.87	-18.5	-2.2	16.6	16.3

$$U_{ij} = \frac{Z_i Z_j e^2}{r_{ij}} + D_{ij}\left[\left\{1 - e^{-a_{ij}(r_{ij}-r_0)}\right\}^2 - 1\right] + \frac{C_{ij}}{r_{ij}^{12}} \qquad (2.6)$$

In Eq. (2.6), three terms contributed to the PEF used in this work: The first term is a long-range Coulomb potential, the second term is a short-range Morse function, and the last term is a repulsive contribution C/r^{12}, necessary to model the interaction at high temperature and pressure. The PEF used in this study has been expressed in two different notations for both Zn-O and O-O pairs, respectively in Eq. (2.10) and Eq. (2.14). The Zn-Zn interactions were not considered in this potential[119]. The potential parameters used in the calculations are shown in Table 2.2. In which, Z_i is the charges of ion i, D_{ij} is the bond dissociation energy of pair ij, a_{ij} is a function of the slope of the potential energy well, and r_0 is the equilibrium bond distance. C_{ij} is another parameter, r_{ij} represents the distance between atoms i and j. The charges of ions are Z (Zn) = +1.2e, Z (O) = -1.2e. The equations of motion were solved by Verlet algorithm (see section 2.1.4).

Table 2.2 Potential energy function parameters used in the calculations. Adapted from ref. [119].

Parameters	Zn-O	O-O
D (eV)	0.001221	0.042395
a ($Å^{-1}$)	3.150679	1.379316
r_0 (Å)	2.851850	3.618701
C (eV $Å^{12}$)	1.0	22.0

The potential energy function for Zn-O atom pair;

$$U^{(1)}{}_{12} = \frac{Z_1 Z_2 e^2}{r_{12}} \tag{2.7}$$

$$U^{(2)}{}_{12} = D_{12}\left[\left\{1 - e^{-a_{12}(r_{12}-r_0)}\right\}^2 - 1\right] \tag{2.8}$$

$$U^{(3)}{}_{12} = \frac{C_{12}}{r_{12}^{12}} \tag{2.9}$$

$$U_{12} = U^{(1)}{}_{12} + U^{(2)}{}_{12} + U^{(3)}{}_{12} \tag{2.10}$$

where the subscript i=1 represents for Zn atom, j=2 for O atom.

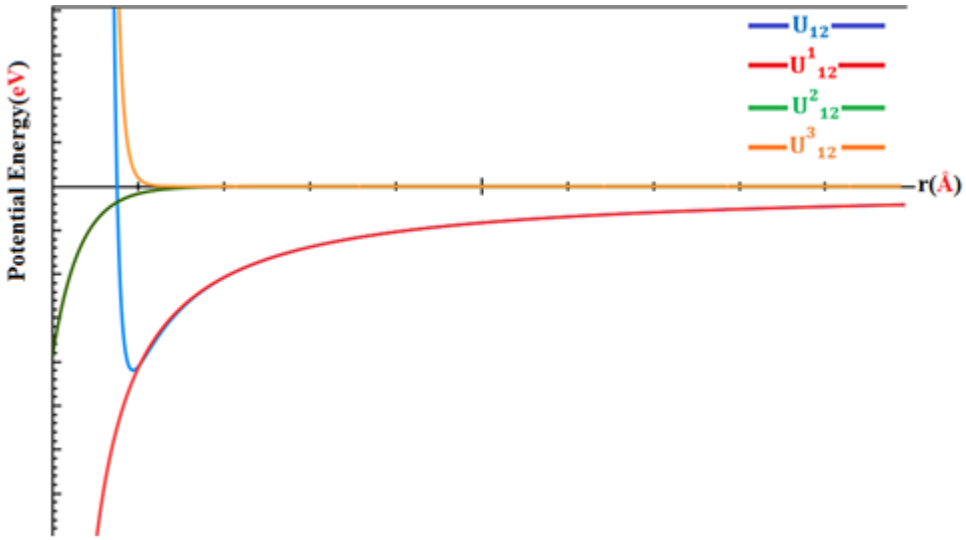

Figure 2.7 Potential energy functions for Zn-O atom pairs

Moreover, the potential energy function for O-O atom pair;

$$U^{(1)}{}_{22} = \frac{Z_2 Z_2 e^2}{r_{22}} \tag{2.11}$$

$$U^{(2)}{}_{22} = D_{22}\left[\left\{1 - e^{-a_{22}(r_{22}-r_0)}\right\}^2 - 1\right] \tag{2.12}$$

$$U^{(3)}{}_{22} = \frac{C_{22}}{r_{22}^{12}} \tag{2.13}$$

$$U_{22} = U^{(1)}{}_{22} + U^{(2)}{}_{22} + U^{(3)}{}_{22} \tag{2.14}$$

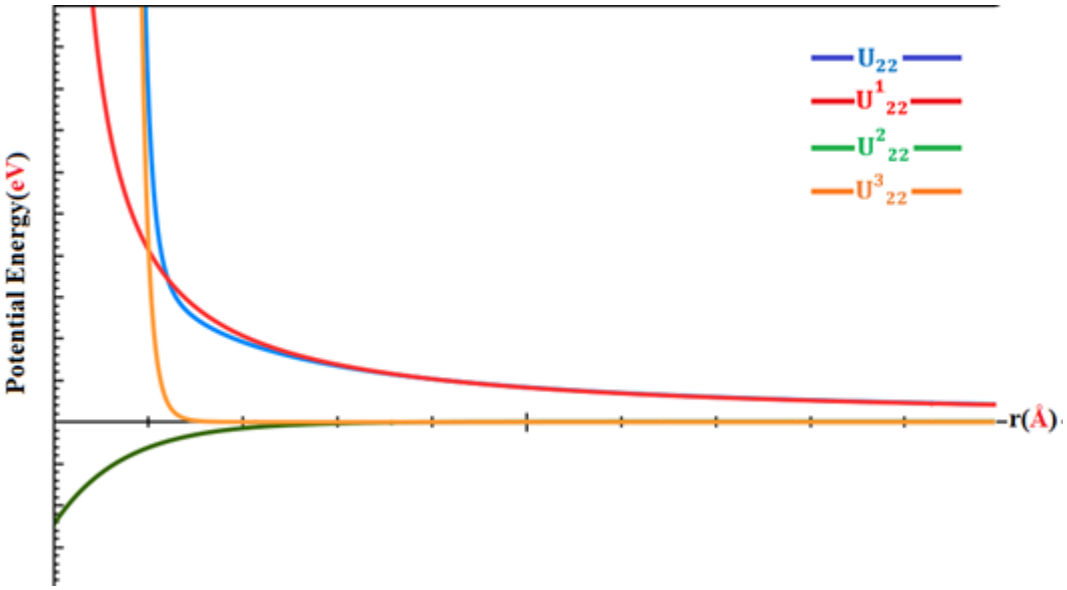

Figure 2.8 Potential energy functions for O-O atom pairs.

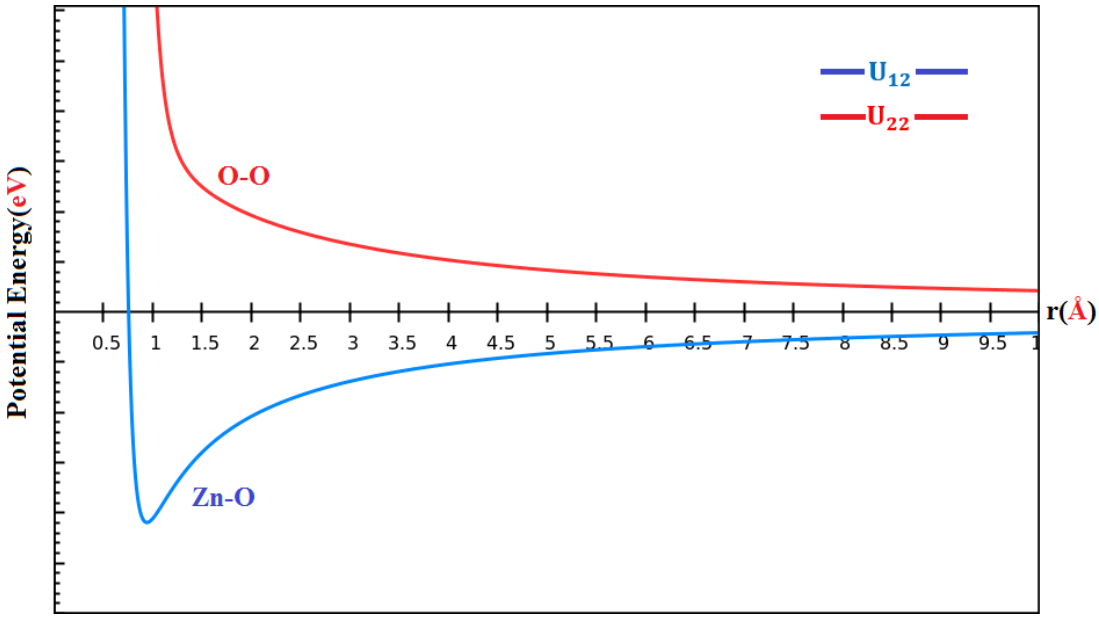

Figure 2.9 Total potential energy function for both Zn-O and O-O atom pairs.

2.1.3 Details of Molecular Dynamics Method

A typical Molecular Dynamics Simulation (MD) on the basis of microcanonical ensemble (N, V, T) (see section 2.1.2) consisted of the following steps (see Figure 2.10): At the start of the simulation, we must specify a set of initial conditions such as initial positions and velocities for each atoms in addition to setting cut-off distance, potential function parameters (see Table 2.2), time step value and the number of time steps, namely the number of MD steps. After the forces are calculated by PEF, then solving molecular dynamics equation of motions, the time evolution of coordinates, velocities and kinetic energies. All procedures of calculation are repeated until the number of MD steps defined in the input is reached.

Initial Positions: For bulk phases, we can start the simulation by placing all the atoms on a crystalline lattice positions. The other option for determining the initial positions, atoms should be placed in idealized or approximate geometries that satisfy the known bond length and angles. The details of model generations are given in section 2.3.

Initial Velocities: The initial velocity components of each particle have been determined considering the Maxwell-Boltzmann distribution at a given temperature[122].

Distribution for velocity vector

$$f_v(\vec{v}) = \left(\frac{m}{2\pi k_B T}\right)^{\frac{3}{2}} exp\left[-\frac{m(v^2)}{2kT}\right] \tag{2.15}$$

For a single velocity component

$$f_v(\alpha) = \left(\frac{m}{2\pi k_B T}\right)^{\frac{1}{2}} exp\left[-\frac{m(\alpha^2)}{2kT}\right]; \qquad \alpha = v_x, v_y, v_z \tag{2.16}$$

The form of this distribution is Gaussian with zero mean;

$$f_v(\alpha) = (2\pi\sigma_v^2)^{-\frac{1}{2}} exp\left[-\frac{\alpha^2}{2\sigma_v^2}\right]; \qquad \sigma_v^2 = \frac{k_B T}{m} \tag{2.17}$$

However, randomly picking each velocity component this way can lead to a nonzero net momentum of the system, which would create a systematic translational drift of our system.

Molecular Dynamics Time Step: A typical time step in MD simulation is on the order of a femtosecond. Using modern computers it is possible to calculate 10^6-10^8 time steps.

Using the total energy conservation of a dimer

$$E = \frac{1}{2}mv^2 \tag{2.18}$$

$$E = \frac{1}{2}m\left(\frac{\Delta r}{\Delta t}\right)^2 \tag{2.19}$$

where Δr can be taken as r_0, and E as ϵ_0, then Δt becomes

$$\Delta t = \sqrt{\frac{m r_0^2}{2\epsilon_0}} \tag{2.20}$$

In practice molecular dynamics time step usually taken as $\frac{\Delta t}{100}$ .Molecular dynamics time step can be calculated for ZnO atom pair as the following[123]:

$$\Delta t_{Zn-o} = \sqrt{\frac{mr_0^2}{2\epsilon_0}} \times 10^{-2}$$

In this study time step are taken as

$$\Delta t_{Zn-O} \cong 1.0 \times 10^{-15} \text{ second.}$$

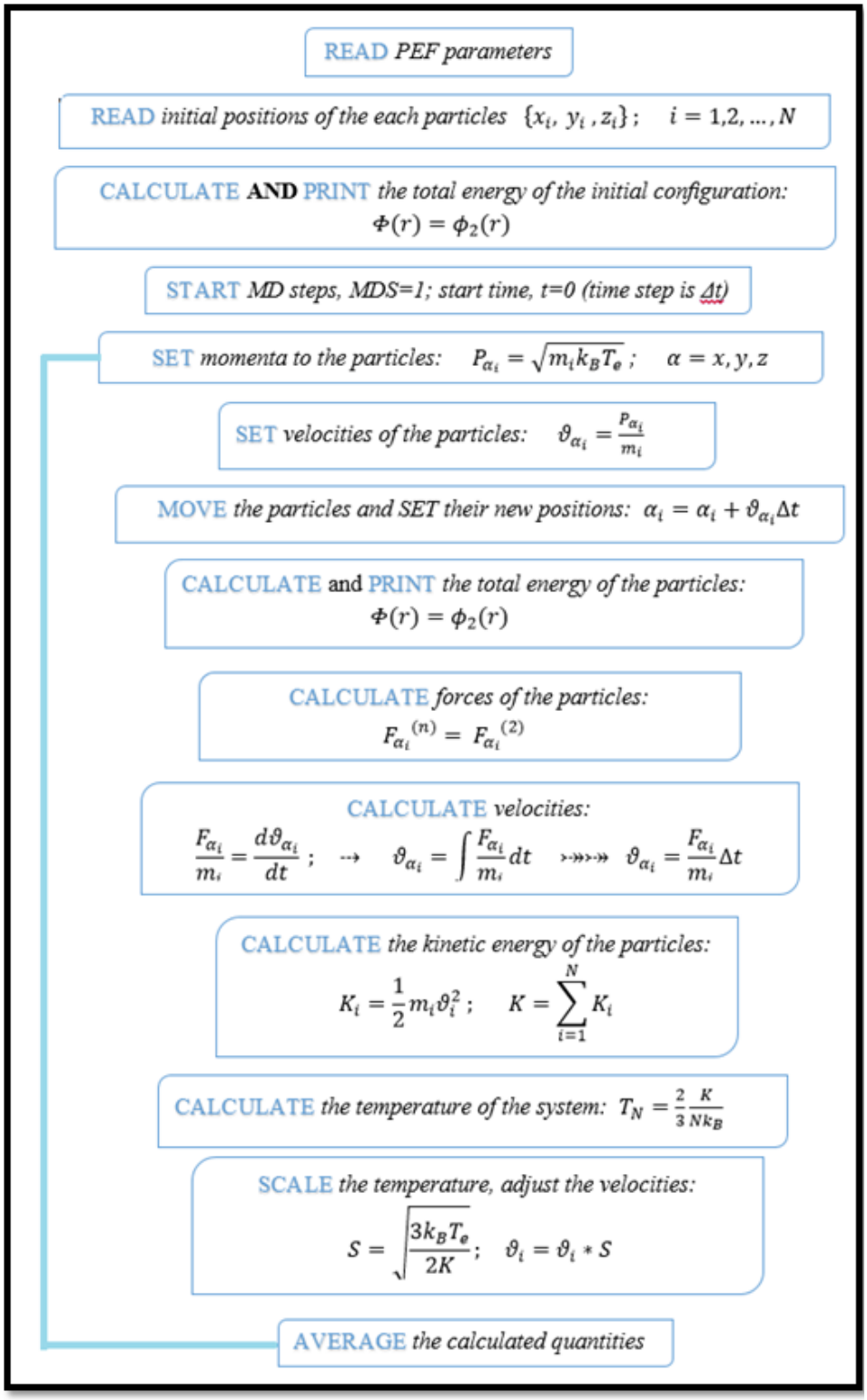

Figure 2.10 A draft MD algorithm. Adapted from ref. [123].

The MD code used in this work has been prepared in FORTRAN language by Şakir Erkoç. The code uses single processor and runs with double precision.

2.1.4 Verlet Algorithm

Considering a Taylor expansion of the position vector $r(t)$ in time:

$$r(t+\delta t) = r(t) + \frac{dr(t)}{dt}\delta t + \frac{d^2r}{dt^2}\frac{\delta t^2}{2} + \frac{d^3r}{dt^3}\frac{\delta t^3}{6} + \xi(\delta t^4)$$

$$r(t+\delta t) = r(t) + \vartheta(t)\delta t + \frac{f(t)}{m}\frac{\delta t^2}{2} + \frac{d^3r}{dt^3}\frac{\delta t^3}{6} + \xi(\delta t^4) \quad (2.21)$$

Similarly

$$r(t-\delta t) = r(t) - \vartheta(t)\delta t + \frac{f(t)}{m}\frac{\delta t^2}{2} - \frac{d^3r}{dt^3}\frac{\delta t^3}{6} + \xi(\delta t^4) \quad (2.22)$$

From the (2.21) and (2.22) equations:

$$r(t+\delta t) = 2r(t) - r(t-\delta t) + \frac{f(t)}{m}\delta t^2 + \acute{\xi}(\delta t^4) \quad (2.23)$$

The (2.23) equation forms the basis of Verlet algorithm for MD [124,125]. Here, we propagate a system forward in time by a time step (δt). To do so, we use the positions at previous two time steps ($r(t-\delta t)$ and $r(t)$) as well as the forces at current time step. To get the forces, we use the force field and the current position set at time t:

$$f(t) = \frac{dU(r(t))}{dt} \quad (2.24)$$

The accuracy of this equation is of order $\xi(\delta t^4)$. That is, the smaller time steps increase the accuracy of this discrete time approximation. In this aspect, one disadvantage of Verlet algorithm is to require to store in memory two sets of positions, namely $r(t-\delta t)$ and $r(t)$.

The Verlet algorithm does not use the velocity to determine a solution to the atomic positions at the next time step. We can approximate the velocities using;

$$\vartheta(t) = \frac{r(t+\delta t) - r(t-\delta t)}{2\delta t} + \xi(\delta t^3) \quad (2.25)$$

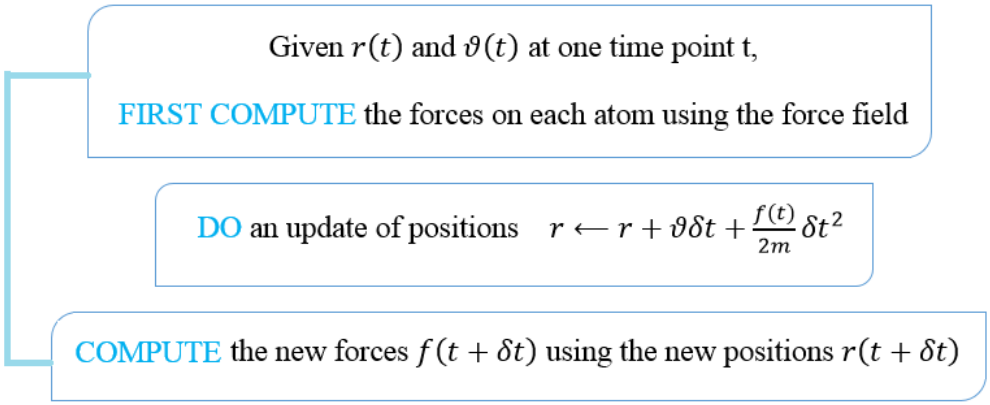

Figure 2.11 Verlet algorithm for molecular dynamics.

2.1.5 Ensembles

Assume that, a gas is contained in a box of volume $1cm^3$ is consistent with an infinite number of ways to distribute the molecules in space. In macroscopic measurements, it is not possible to distinguish two gases existing in different microscopic states, but they are the same under macroscopic conditions. A collection of systems identical in composition and macroscopic condition but in different microscopic states is called an "ensemble"[126].

Considering a simulated system which includes a large number (10^2 - 10^8) of atoms, whose macrostates consists of many microstates. However, for predicting macroscopic quantities and observables and also noticing the degree of freedom of each single atom, we need to solve many equations of motion (($3x10^8$) equations should be solved for both positions and momentum vs.). We do not need such an extensive information, so we only need information about average values which is provide by the ensemble theory. Using ensembles, we can reduce the information which is needed to describe the system and finding an observable by applying some restrictions on the observables of the system under study.

- In microcanonical ensemble (NVE): In which the ensemble contains a constant number of particle (N), constant volume (V), and constant internal energy (E).
- Canonical ensemble (NVT): Where N, V and temperature (T) are constants.

- The isothermal–isobaric ensemble (NPT): Where pressure (P) is constant, in addition to N, T.
- The grand canonical ensemble (μ, V, T): In which the number of particle is not constant but may vary in order to achieve constant chemical potential (μ).

2.1.6 Periodic Boundary Conditions:

Simulations necessarily concern finite number of particles which are contained in the simulation box. However, an infinite system may be simulated by application of periodic boundary conditions (PBC), achieved by generating an infinite number of images of the basic simulation working cell. So as a particle moves out the simulation box, an image particle moves in to replace it. In calculating particle interactions within the cut off range, both real and image neighbors are included. In which it is necessary to ensure that when a particle leaves the box on one side, its image from a neighboring box re-enters on the opposite side. Care must also be taken with simulations which will extend into the neighboring boxes.

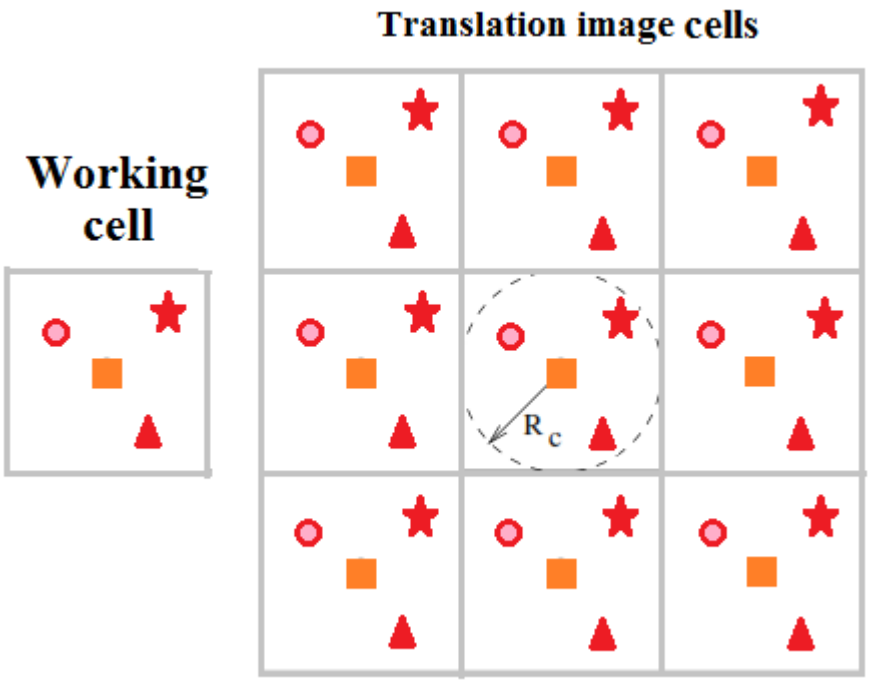

Figure 2.12 Two–dimensional computational cell and image cells for the use of periodic boundary conditions.

2.3 ZnO Nanostructure Models

2.3.1 0D ZnO Nanostructures

2.3.1.1 ZnO Nanoparticles

Spherical Nanoparticles: ZnO nanoparticles are constructed from the hexagonal crystal structure (wurtzite structure). The nanoparticles generated from the part of crystalline structure are formed as in almost spherical shapes. The numbers of Zn and O atoms are almost taken equally in all spherical shapes models. The eight spherical model for nanoparticles are considered with different sizes (radius). The smallest nanoparticle will be referred to as SP1 and similar notations are used for the other models such as SP2, SP3, etc. (see Figure 2.13).

Cubic Nanoparticles: ZnO cubic nanostructures are constructed from the rock salt crystal structure. The generated cubic models are considered different sizes and different stoichiometry. The cubic particle models will be referred to as CP, the smallest size cubic model will be referred to as the CP1 and similar notations are used for the other models such as the CP2, CP3, etc. (see Figure 2.14). The CP2A and the CP2B model are to having the same total number of atoms, but the number of Zn and O atoms for the two model are different. The CP2A model contained with 13 O and 14 Zn atoms whereas the CP2B model contained with 14 O and 13 Zn atoms.

2.3.1.2 ZnO Nanorings

ZnO nanorings are constructed from zigzag nanotubes. Nanorings are generated by removing one layer in the nanotubes. Layers with different sizes are considered for the nanorings. The R1 , R2 , R3, and R4 nanorings are generated from the (5,0), (6,0), (7,0) and (8,0) nanotubes respectively (see Figure 2.15).

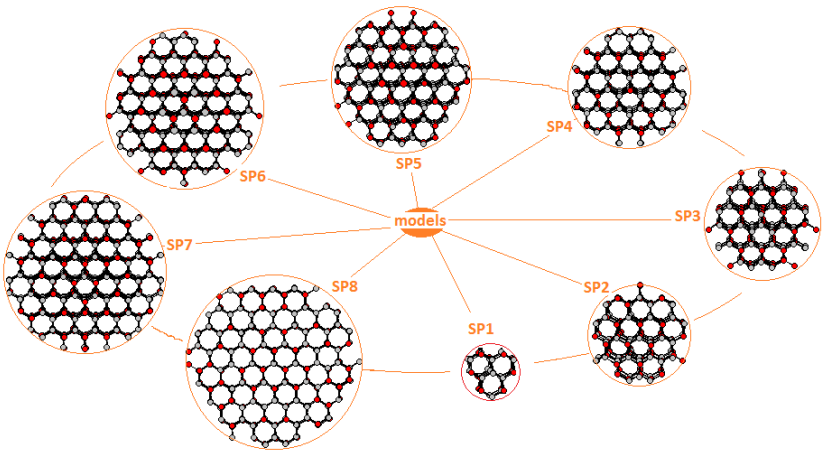

Figure 2.13 The ideal ZnO spherical nanoparticle models.

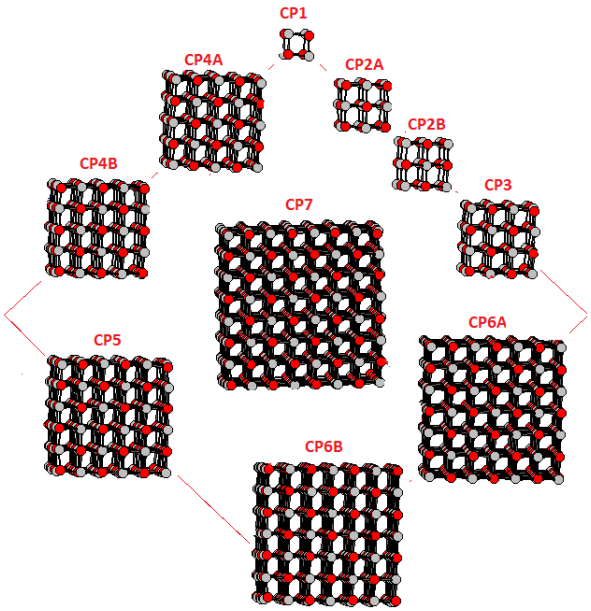

Figure 2.14 The ideal ZnO cubic nanoparticle models.

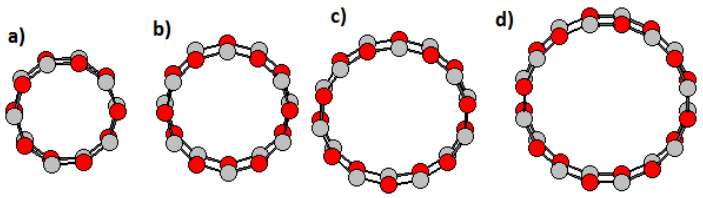

Figure 2.15 The ideal ZnO nanoring models a) The R1 model b) The R2 model c) The R3 model d) The R4 model.

2.3.2 1D ZnO Nanostructures

2.3.2.1 ZnO Nanoribbons

2.3.2.1.1 ZnO Pristine Nanoribbons

ZnO nanoribbons are modeled in honeycomb structure with zigzag and armchair edges. Two different widths (1L and 2L) are considered for nanoribbons. The ideal structures of nanoribbons are shown in Figure 2.16. We represent the zigzag one and two layer nanoribbons referred to as Z1L and Z2L, the armchair one and two layer nanoribbons referred to as A1L and A2L, respectively.

2.3.2.1.2 ZnO Defected Nanoribbons

Generating defects formation process: The defected nanoribbons are modeled using honeycomb structures with zigzag and armchair edges. All the defects are applied in both the central and edge regions. Firstly, the defects are applied in central region: The different type of defects, namely vacancy and exchange, are considered for the nanoribbons. The vacancy type defects are modeled in two forms as monovacancy and divacancy. A Zn-monovacancy defect is generated by removing a single Zn atom from the central and edge region of the zigzag nanoribbons (will be referred to as ZCDV-Zn and ZEDV-Zn) (see Figure 2.17 a,b). Similarly, an O-monovacancy defect is generated by removing a single O atom from the central and edge region of the zigzag nanoribbons (will be referred to as ZCDV-O and ZEDV-O) (see Figure 2.17 c and d). And, a Zn-O-divacancy defect is generated by removing a two neighboring atoms from the central and edge region of the zigzag nanoribbons (will be referred to as ZCDV-Zn-O and ZEDV-Zn-O) (see Figure 2.17 e and f).

The other type of defect is generated by exchanging two neighboring Zn and O atom pairs (or rotated 180 degree) from the central and edge region of the zigzag nanoribbons (will be referred to as ZCDE-Zn-O and ZEDE-Zn-O) (see Figure 2.18 a,b). Moreover, similar procedures are also considered for the armchair nanoribbons. For example, a Zn-monovacancy defect is generated by removing a single Zn atom

from central and edge region of the armchair nanoribbons, which we represent them as ACDV-Zn and AEDV-Zn, respectively) (see Figure 2.19 and Figure 2.20).

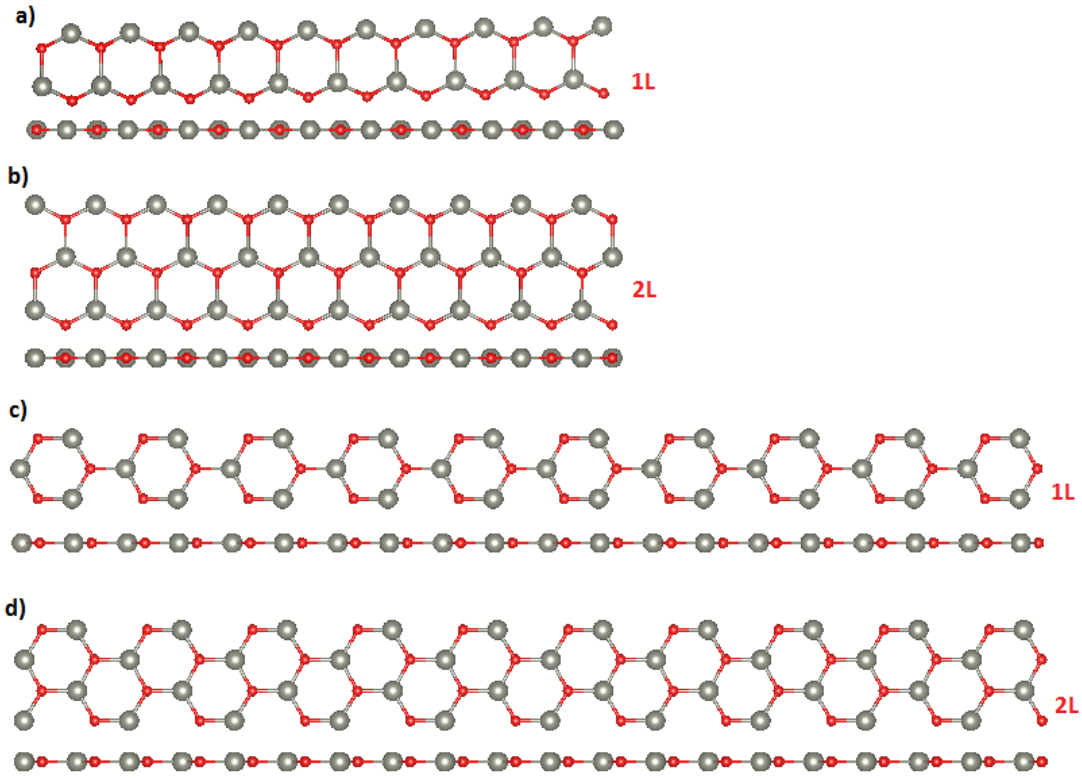

Figure 2.16 The ideal ZnO nanoribbon models a) The Z1L model b) The Z2L model c) The A1L model d) The A2L model.

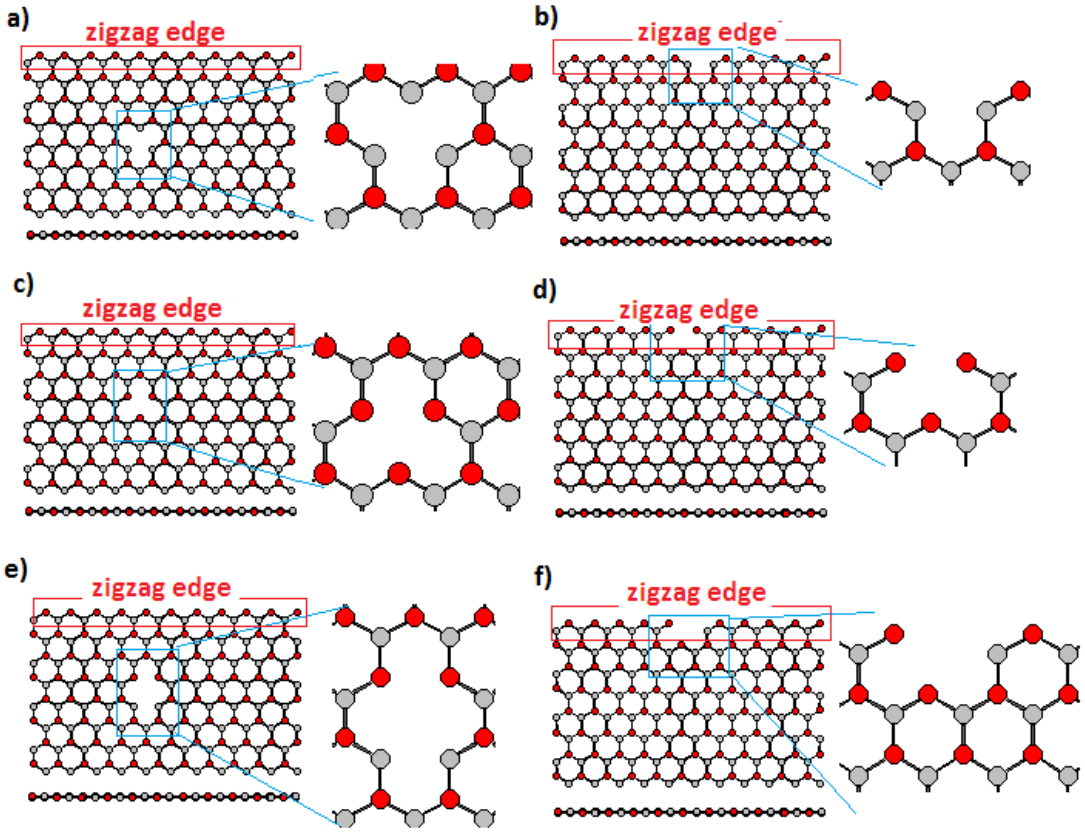

Figure 2.17 The ideal ZnO vacancy type defect zigzag nanoribbon models a) The ZCDV-Zn model b) The ZEDV-Zn model c) The ZCDV-O model d) The ZEDV-O model e) The ZCDV-Zn-O model f) The ZEDV-Zn-O model.

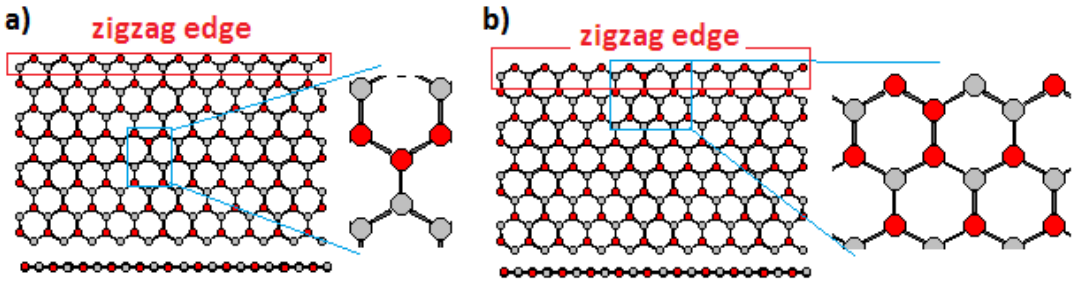

Figure 2.18 The ideal ZnO exchange type defect zigzag nanoribbon models a) The ZCDE-Zn-O model b) The ZEDE-Zn-O model.

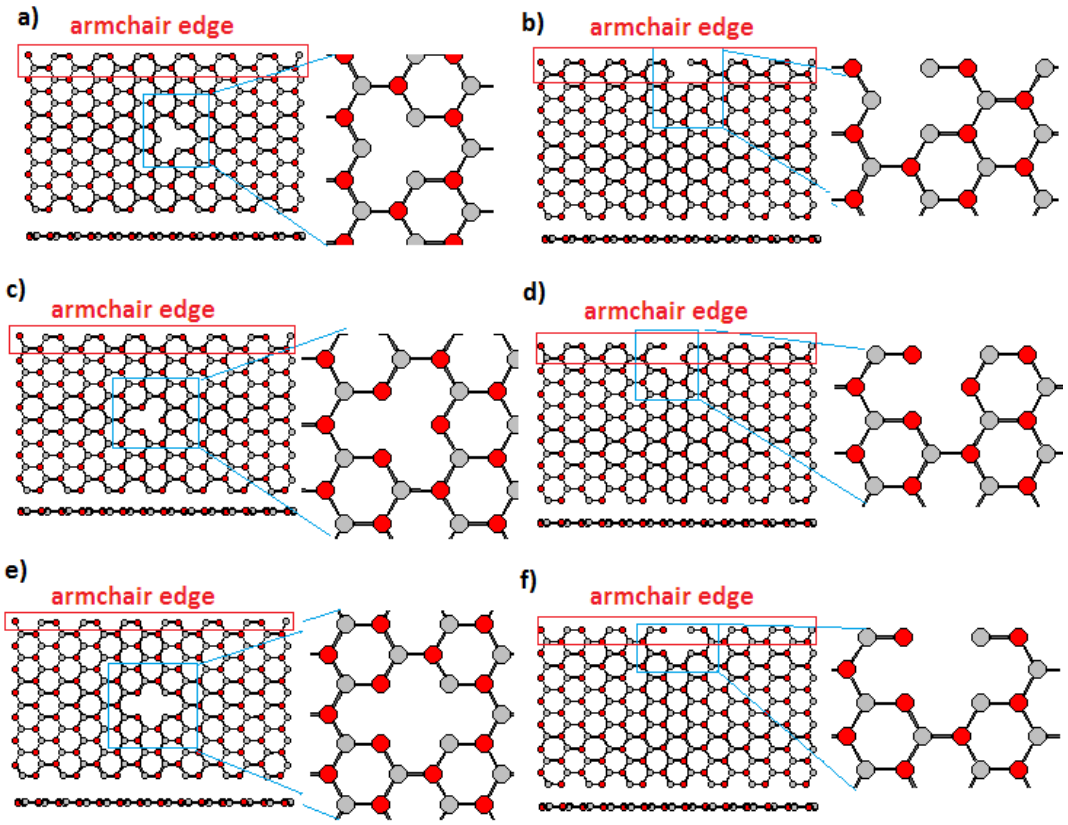

Figure 2.19 The ideal ZnO vacancy type defect armchair nanoribbon models a) The ACDV-Zn model b) The AEDV-Zn model c) The ACDV-O model d) The AEDV-O model e) The ideal ACDV-Zn-O model f) The ideal AEDV-Zn-O model.

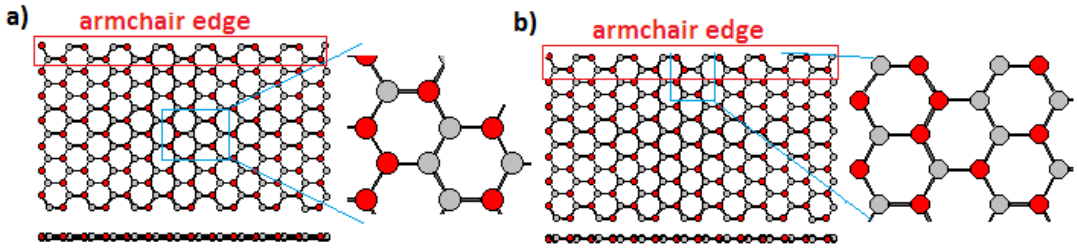

Figure 2.20 The ideal exchange defect armchair nanoribbon models a) The ACDE-Zn-O model b) The AEDE-Zn-O model.

2.3.2.2 ZnO Nanorods

The nanorods are modeled from wurtzite crystal structure with cross section view on (1000) surface. Three different cross sectional type models, namely hexagonal (HR), trigon (TR) and rhombus (RR) are considered for the nanorods. In addition, three type models of the hexagonal cross sectional nanorods with different sizes (HR1, HR2 and HR3) are taken (see Figure 2.21).

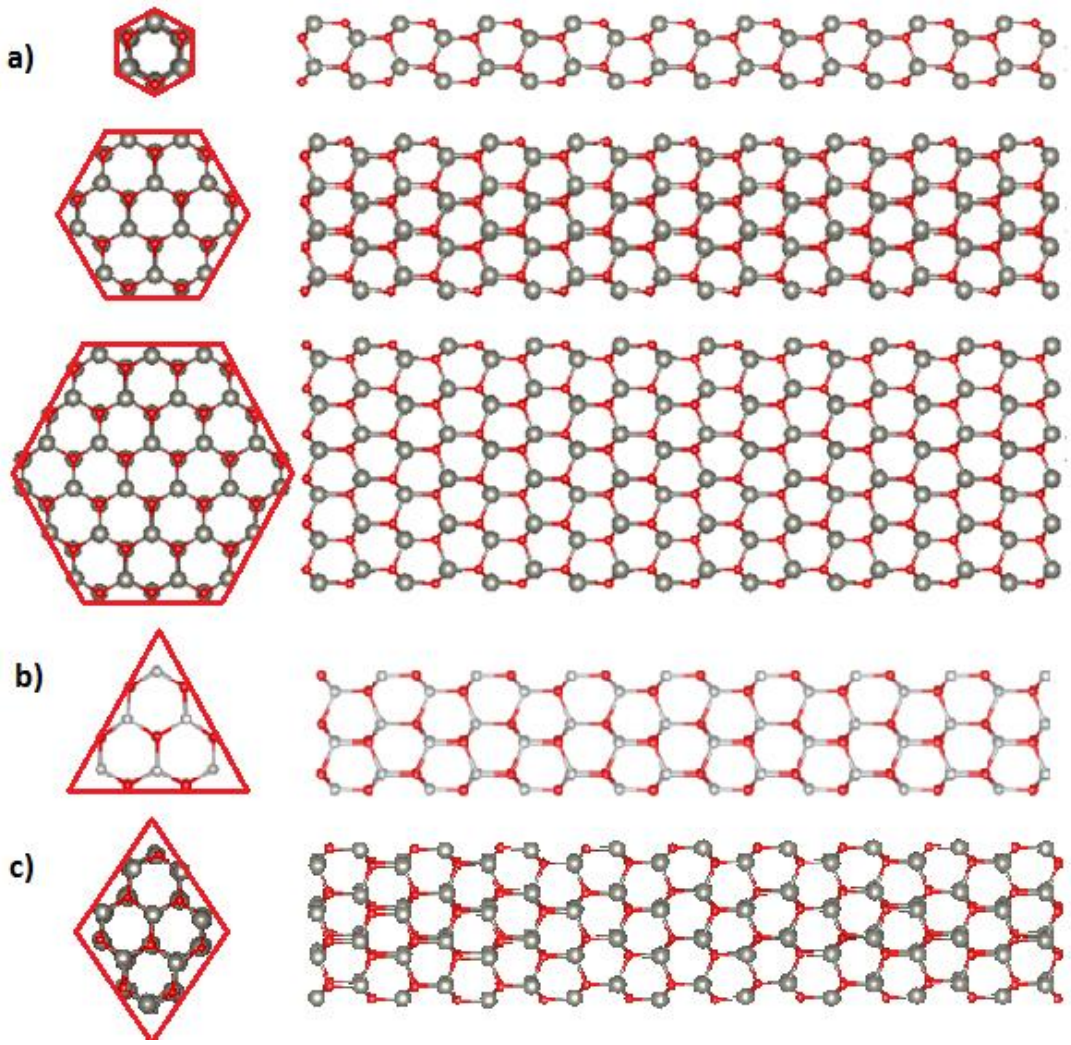

Figure 2.21 The ideal ZnO nanorod models a) The HR1, HR2, and HR3 models. b) The TR model c) The RR model.

2.3.2.3 ZnO Nanotubes

ZnO nanotubes are constructed from the hexagonal ribbon structure. Nanotubes are classified into three types, namely armchair (*n*, *n*) nanotubes, zigzag (*n*, 0) nanotubes and chiral (*n*,*m*) nanotubes with n≠m. In this study, four different sizes, namely (5,0), (6,0), (7,0) and (8,0) for the zigzag nanotubes (will be referred to as ZT1, ZT2, ZT3 and ZT4, respectively)(see Figure 2.22) and four different sizes, namely (3,3), (4,4), (5,5) and (6,6) for the armchair nanotubes (will be referred to as AT1, AT2, AT3 and AT4, respectively) (see Figure 2.23) are considered. On the other hand, four different chiralities of (5,0) nanotubes model, namely (5,1), (5,2), (5,3) and (5,4), which represented CT1, CT2, CT3 and CT4, respectively (see Figure 2.24), are considered. The tube radius in the first models of all the considered nanotube models are taken as almost closest.

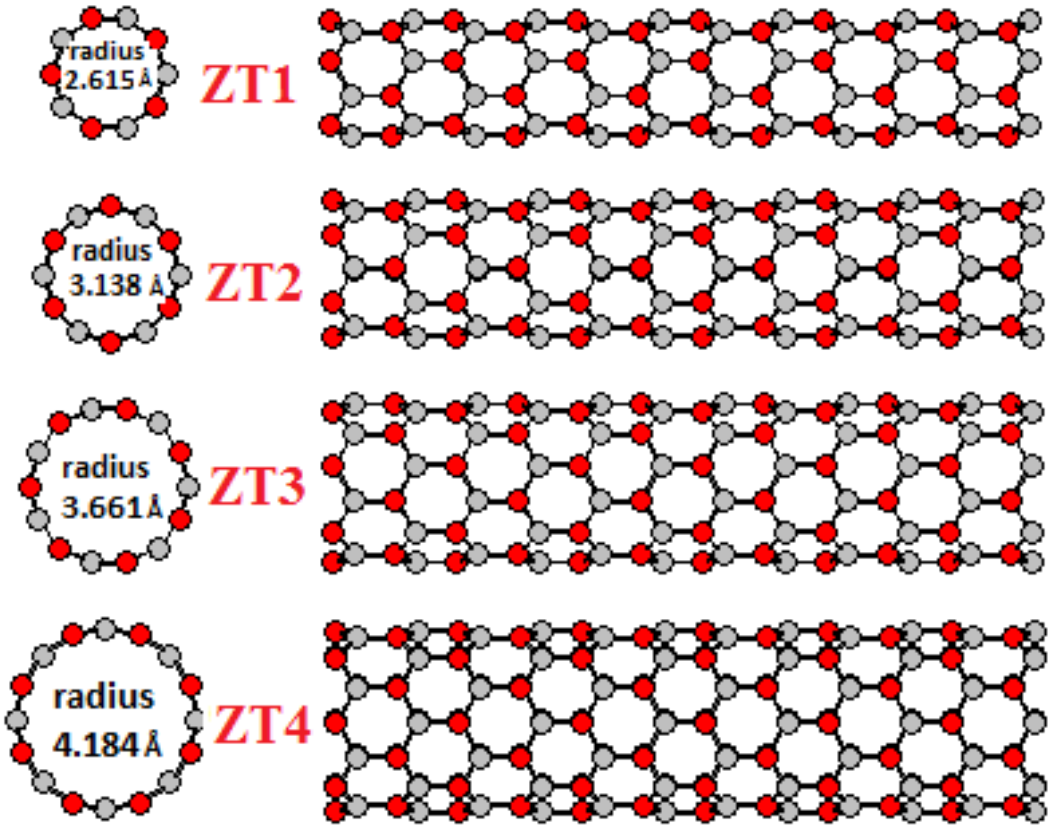

Figure 2.22 The ideal ZnO zigzag nanotube models.

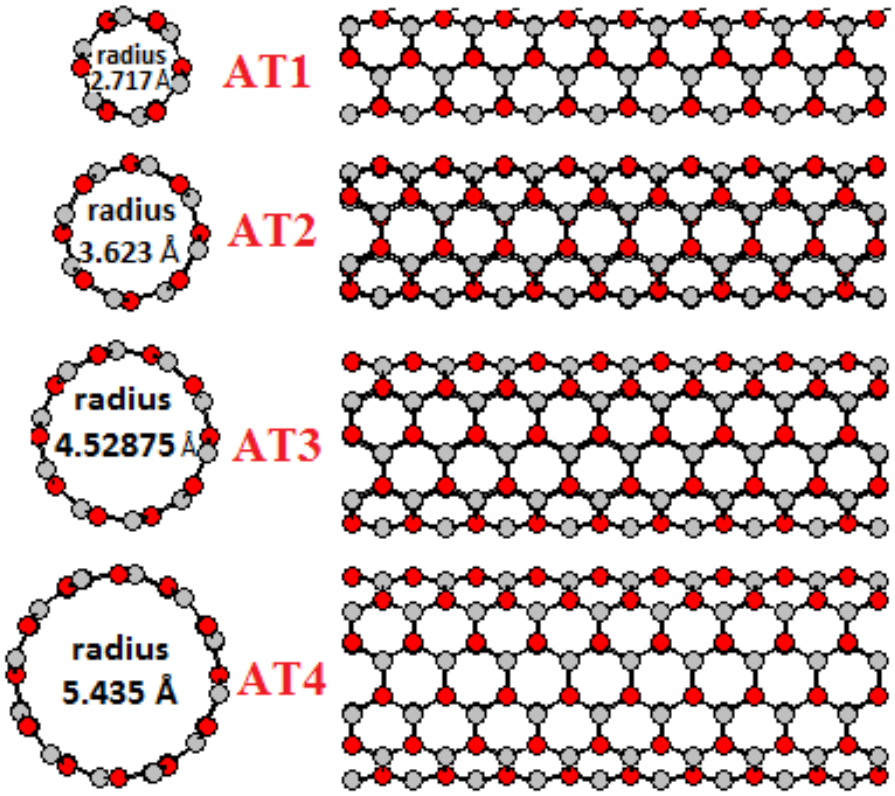

Figure 2.23 The ideal ZnO armchair nanotube models.

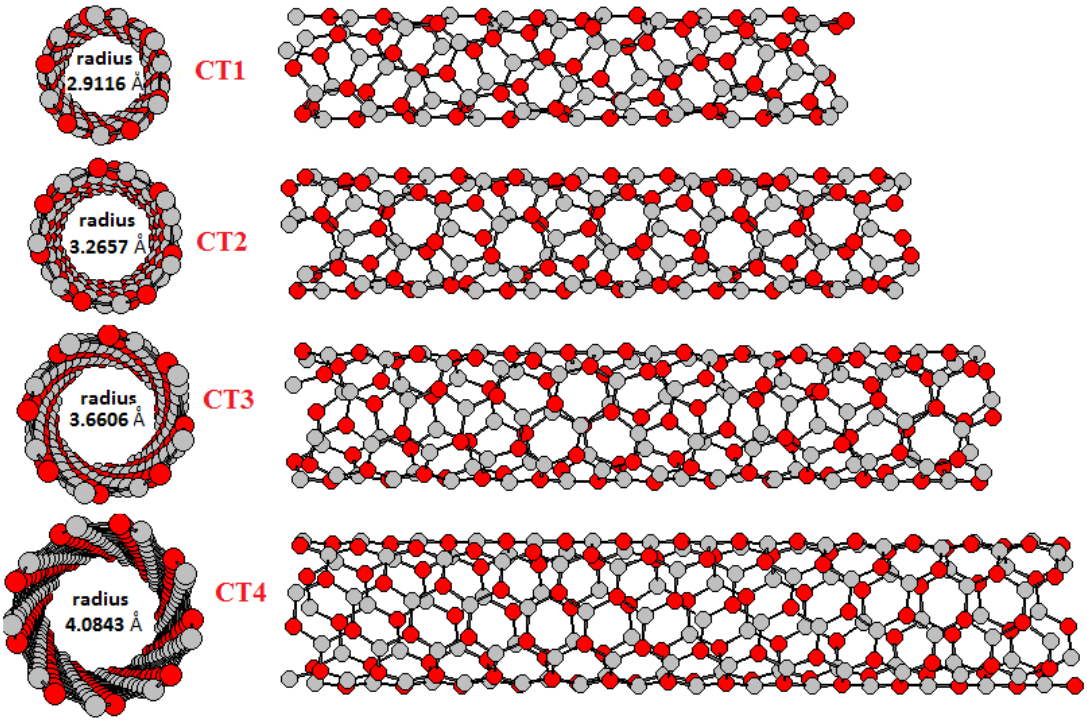

Figure 2.24 The ideal ZnO chiral nanotube models.

2.3.3. 2D ZnO Nanostructure

2.3.3.1 Pristine Nanosheets

The nanostructure are modeled from the honeycomb structure, without any defects (defect free) in the structure and we will refer to as PS model. One edge of the nanosheets consisted of zigzag edges whereas the other edge of the nanosheets consisted of armchair edges (see Figure 2.25).

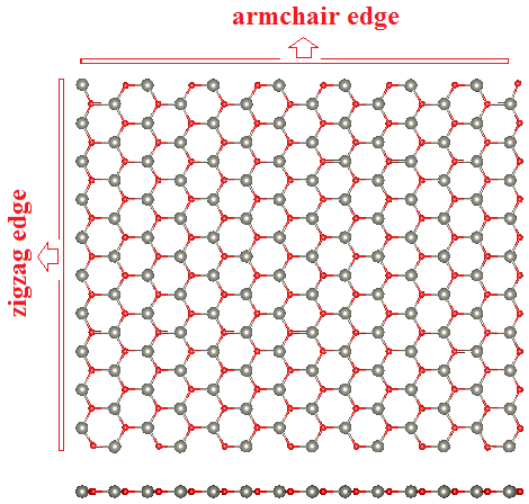

Figure 2.25 The ideal ZnO pristine nanosheet model.

2.3.3.2 Defected Nanosheets

The defected nanosheets are also modeled using honeycomb structures. The vacancy defects (monovacancy, divacancy), exchange (substitute and Stone-Wales like) defects, line defects, and hole (circular hole) defects are considered for the nanosheets. All the defect models are generated at the central region of the nanosheets. The first type of defect is vacancy defect namely, monovacancy and divacancy. A Zn-monovacancy defect is generated by removing a single Zn atom from the central region of the nanosheets (will be referred to as SV-Zn). Similarly, an O-monovacancy defect is generated by removing a single O atom from the central region of the nanosheets (will be referred to as SV-O). And, a ZnO-divacancy defect is generated by removing a two neighboring atoms from the central region of the nanosheets (will be referred to as SV-Zn-O) (see Figure 2.26). The second type of defect is exchange. The substitution type defect is generated by exchanging two neighboring Zn and O

atoms from the central region of the nanosheets whereas Stone-Wales like type defect formed by rotating a Zn-O atom pair bond by 90°, which are represented as SE-SB and SE-SW, respectively (see Figure 2.27). The third type of defect is the line defect, generated by changing the hexagonal geometry in a certain array into square and octagon formations (see Figure 2.28). Finally, the circular hole defect types are generated by removing the atoms in the central region by forming ring like holes. The hole defects are considered as four different models: The first type of the circular hole defect is generated by removing three neighboring Zn-O pairs atoms in the central region (Figure 2.29 a). The second type of the circular defect is generated by removing six neighboring Zn-O pairs atoms in the central region (see Figure 2.29 b).

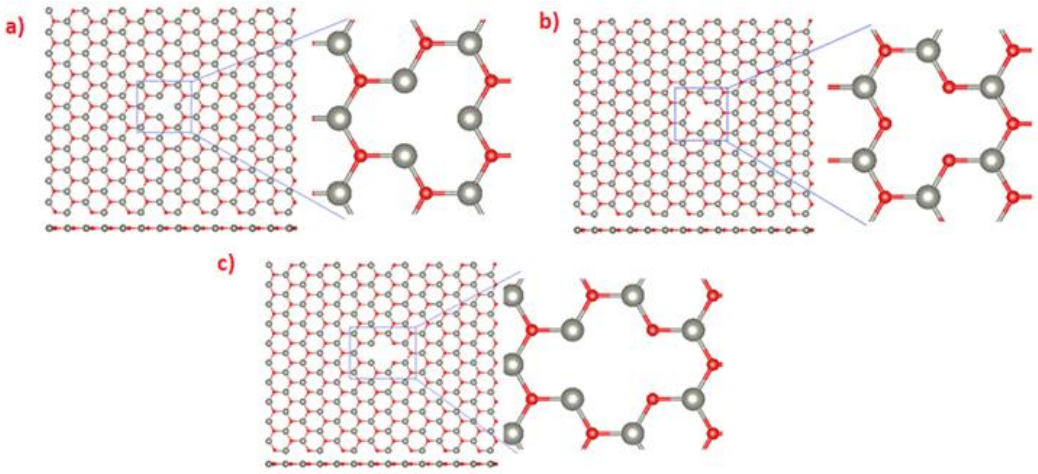

Figure 2.26 The ideal vacancy type defect nanosheet models a) The SV-Zn model b) The SV-O model c) The SV-Zn-O model.

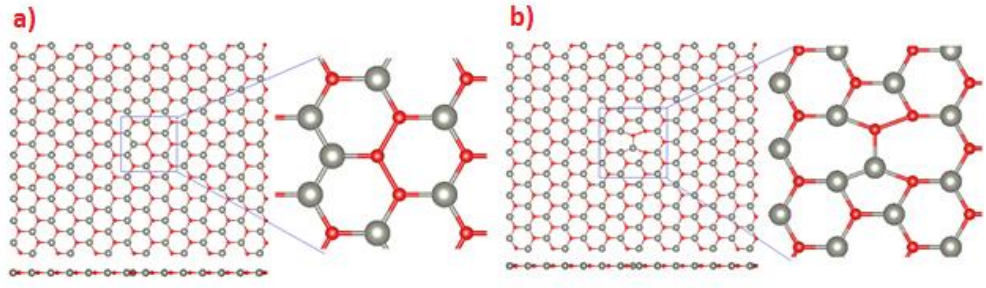

Figure 2.27 The ideal ZnO exchange type defect nanosheet models a) The SE-SB model b) The SE-SW model.

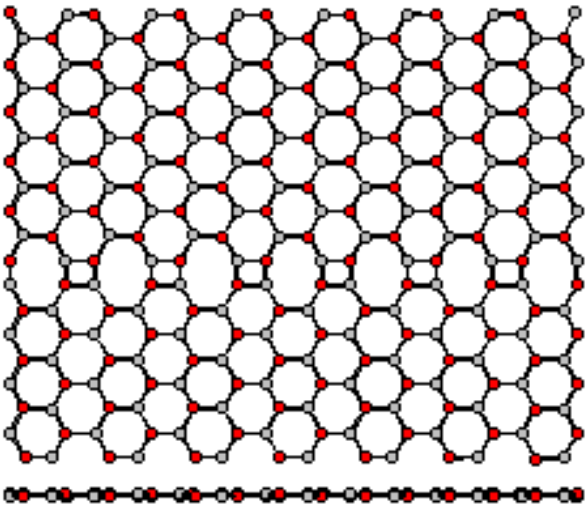

Figure 2.28 The ideal ZnO line type defect model.

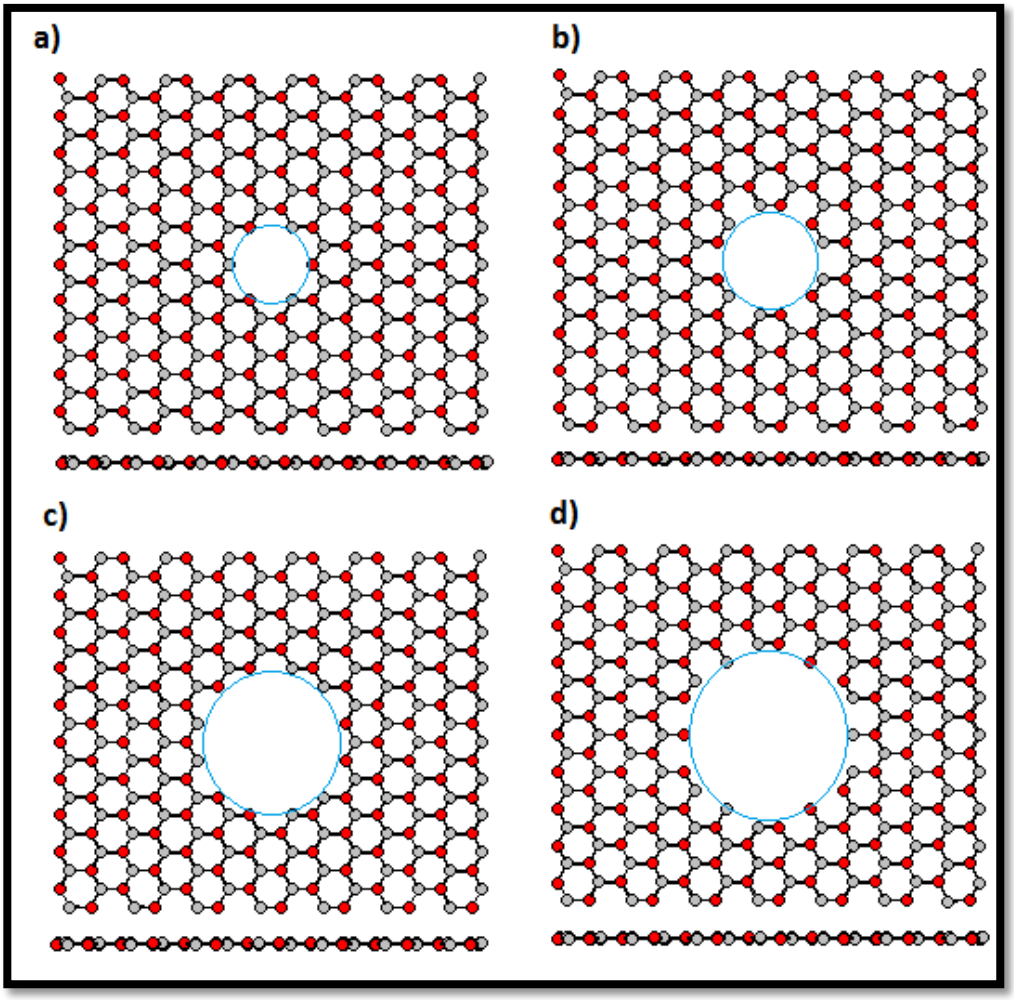

Figure 2.29 The ideal ZnO circular hole defect type nanosheets. a) The CH1 model b) The CH2 model **c)** The CH3 model d) The CH4 model.

2.4 Applied Mechanical Processes

Mechanical processes, namely tensile strain, compression strain and torsion were applied to the models generated to investigate their effects on the ZnO nanostructures.

2.4.1 Tensile Strain Process

The uniaxial tensile strain applications were applied to the 1D nanostructures (nanoribbons, nanorods, and nanotubes) while the biaxial tensile strain applications were applied to the 2D nanostructures (nanosheets). Both uniaxial and biaxial strain applications were applied along the periodic boundary lengths. The stretching processes, namely the applications of tensile strain, were realized in different rates by multiplying the corresponding component (along the periodic boundary length) of the coordinates of the atoms by a factor 1.05 (corresponding to a %5 tensile strain) (see Figure 2.30), 1.10 (corresponding to a %10 tensile strain) and 1.15 (corresponding to a %15 tensile strain). Following the strain applications, the nanostructure was relaxed and the relaxation procedure has been realized at every tensile strain step and the periodic boundary length was also changed accordingly. It was called every strain application process as the "strain step". The nanostructures were stretched gradually until they broke (or deformed). The energetics of tensile strain process can be presented by drawing a strain energy (ΔE_i) versus strain (ΔL_i) graph.

$$\Delta E_i = E_i - E_0 \quad \text{and} \quad \Delta L_i = \frac{L_i - L_0}{L_0} \times 100 \tag{2.26}$$

In Eq. (2.26), E_0 is the initial relaxed total potential energy and E_i is the corresponding energy at strain step i. Similarly L_0 is the initial length of the system along the PBC and L_i is the corresponding length at strain step i.

2.4.2 Compression Strain Process

The uniaxial compression strain applications were applied to both the nanorods and nanotubes for 1D nanostructures. The compression strain application process was similar to the tensile strain applications: the compression processes, namely the application of compression, were realized in the different rates by multiplying the corresponding component (along the periodic boundary length) of the coordinates of the atoms by a factor 0.95 (corresponding to a %5 compression) (see Figure 2.31), 0.90 (corresponding to a %10 compression) and 0.85 (corresponding to a %15 compression). Following the compression application, the nanostructure was relaxed, and the relaxation procedure was realized at every compression steps and the periodic boundary length has been also changed accordingly. It was called every compression application process as the "compression step". The nanostructures were compressed gradually until they broke (or deformed).

2.4.3 Torsion Process

The torsion process was applied to only the hexagonal cross sectional nanorod models (HN1, HN2 and HN3) gradually until deformation took place in the structure. The atoms in the first two and the last two layers, perpendicular to the nanorod axis, were kept fixed and the remaining atoms were left moving, and periodic boundary condition is not necessary for this processes. The measure of torsion was defined as the following: the torsional angle in the first layer (1^{st} layer) of the nanorods was taken as zero degree while the torsional angle in the last layer (N^{th} layer) of the nanorods was taken as 20 degree (θ_t represents a maximum torsional angle in layers). The intermediate layers (range between 2^{nd} and $(N-1)^{th}$ layers) rotated proportional to the layer height. Following each torsion process referred to as "torsion step" (see Figure 2.32).

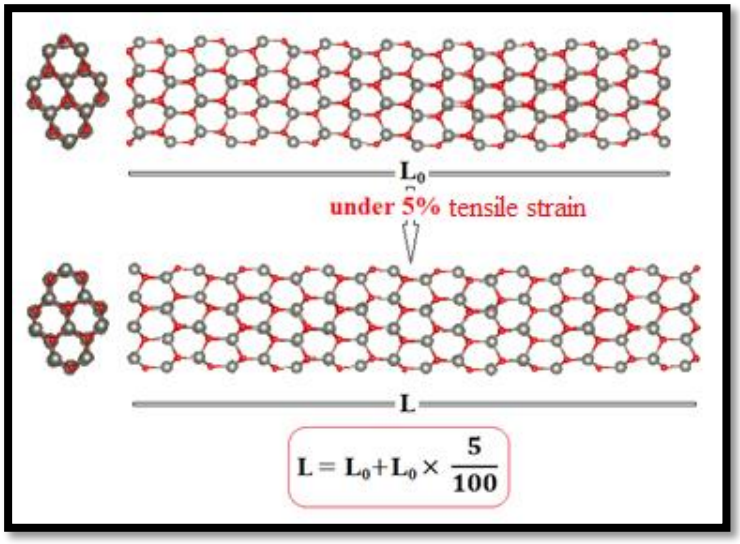

Figure 2.30 The 5% tensile strain application process.

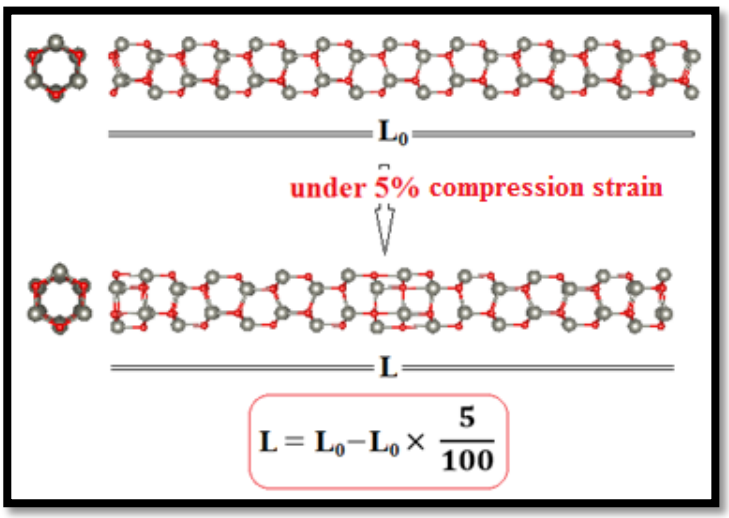

Figure 2.31 The 5% compression strain application process.

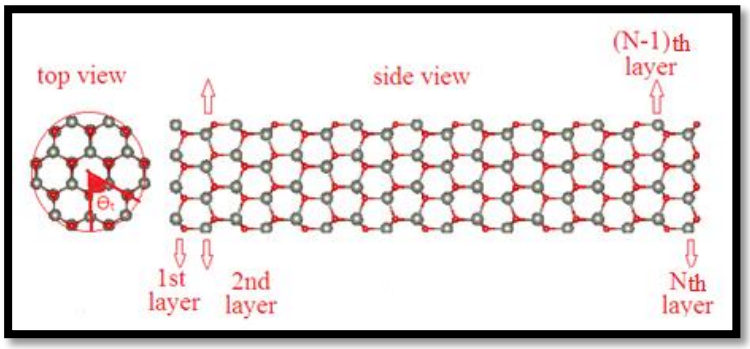

Figure 2.32 The torsion application processes.

CHAPTER 3

RESULT AND DISCUSSION

3.1 0D ZnO Nanostructures

All the 0D nanostructures simulated at various temperatures ranging 1 K to 3000 K. In nonequilibrated molecular dynamics simulation case (NEMD), the temperature of the nanostructures without full relaxation was increased by 100 K. On the other hand, temperature of the fully relaxed nanostructures was also increased by 100 K in the case of equilibrated molecular dynamics simulations (EMD).

3.1.1. ZnO Nanoparticles

3.1.1.1 ZnO Spherical Nanoparticles

In the first stage of the NEMD study we have investigated the structural and thermal properties of the spherical nanoparticle models[13].

The SP1 model maintained its initial form despite the increasing temperature range between 1 and 600 K with NEMD whereas it abruptly transformed into cubic structure in the case of EMD (see Figure 3.1). At high temperatures, the SP1 model was abruptly deformed, so some hexagons turned into squares (see Figure 3.2). The number of total atoms of the SP1 model was 27, including 13 Zn and 14 O atoms. Therefore, the numbers of Zn and O atoms of that model were taken as nearly equal, resulting in a more stable form in the structure during the NEMD process despite the increasing temperature.

Both the structural stability and the thermal equilibrium under increasing temperature were difficultly maintained, when changing of the ratios of O atoms (or Zn atoms) in the SP1 model, taken as relatively different. The spherical model was deformed during the NEMD. Some atoms in the structure were branched at 1 and 100 K (see Figure 3.3). As a consequence, it was realized that the mechanical and thermal stability of the structures were related to the atomic stoichiometry ratios.

The number of total atoms in the SP2 model was 168, including 84 Zn and 84 O atoms, and the initial radius of the model was 7.87 Å. During the NEMD process, the SP2 model was not deformed much more despite temperatures ranged between 1 and 800 K (see Figure 3.4). However, at 800 K the radius of the model became 8.52 Å, so the volume increased. Furthermore, the average bond distance between atoms increased, such that the distance was initially 1.897 Å, 1.975 Å at 1 K, and 1.995 Å at 300 K. Additionally, the radial atomic distributions of the SP2 model were shown in the Figure 3.5-3.8. The radial atomic distribution was determined by counting number of atoms in a shell with thickness dr at a distance r from the center of the spherical nanoparticle. In the Figures 3.5-3.8 the Gaussian broadening was applied to the radial atomic distributions. When the structural deformation was not much (are shown the radial atomic distributions), a small energy fluctuation evolved, resulting in the smooth increase of the average potential energy. At high temperature, the rock salt phase of the structure revealed (see Figure 3.4). Recalling in the chapter 1 had been determined that the wurtzite crystal structure changed into rock salt phase under at high pressure.

The number of total atoms in the SP3 model was 204, including 102 Zn and 102 O atoms, and the initial radius of the model was 8.47 Å. During the NEMD process, the SP3 model almost preserved its spherical appearance under the increasing temperatures ranged between 1 and 300 K. However, the average bond distance between atoms increased, such that the distance was 1.895 Å initially, 1.911 Å at 1 K, and 2.022 Å at 600 K. In addition, at 600 K temperature the structure deformed relatively and the radius of the structure became $r = 8.68$ Å. At 900 K temperature, the rock salt phase also took place in the structure, and the radius of the structure became $r = 9.15$ Å (see Figure 3.9). The radial atomic distributions for this model

were shown in the Figure 3.10-3.12. As a result, the volume of the structure increased during the NEMD process, and the energy fluctuations also became vanishingly small.

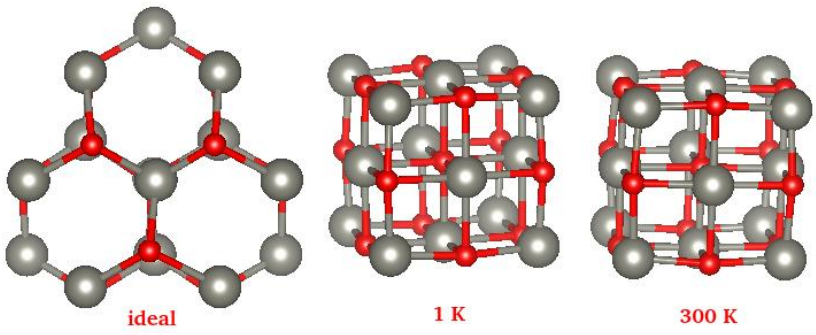

Figure 3.1 The SP1 model during the EMD process.

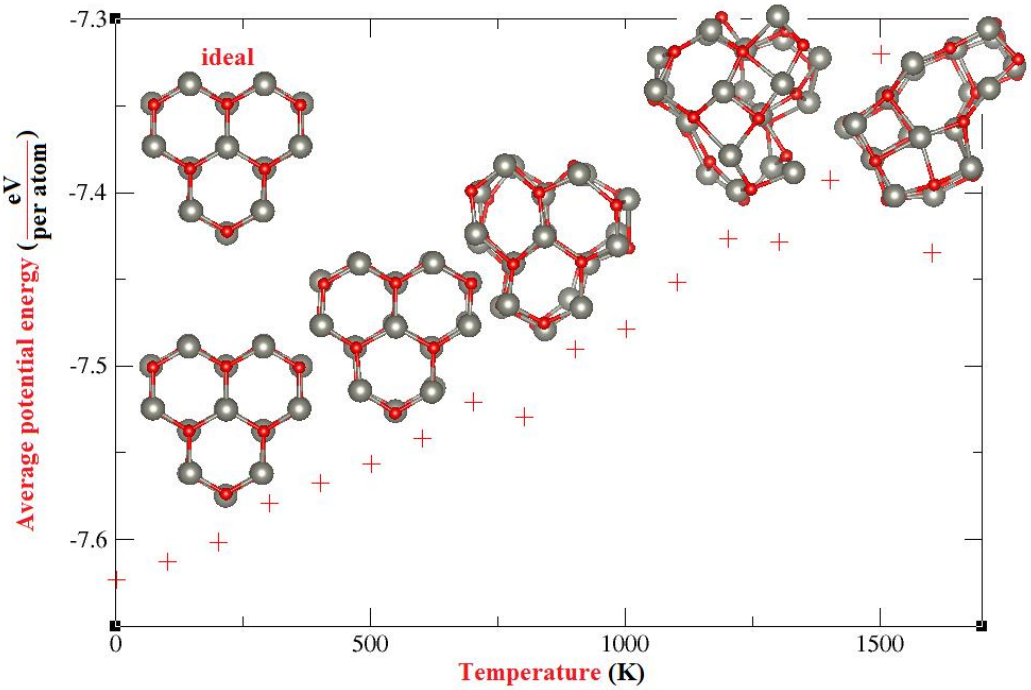

Figure 3.2 The structural properties of the SP1 model during the NEMD process.

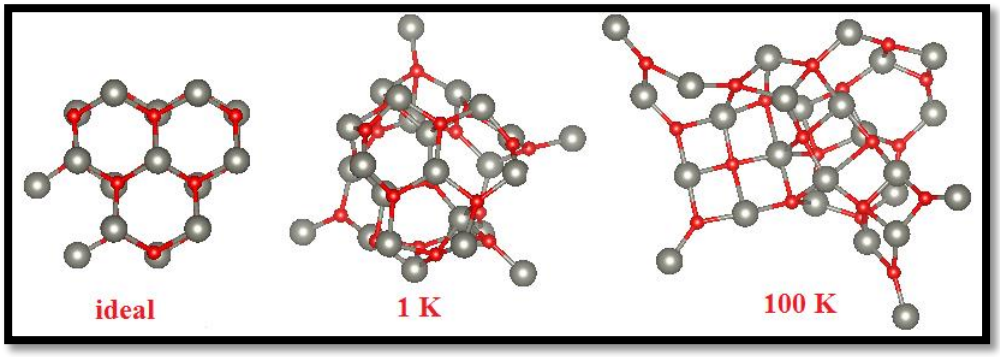

Figure 3.3 The structural properties of the model, which consisted of 2 more oxygen atoms than the SP1 model during the NEMD process.

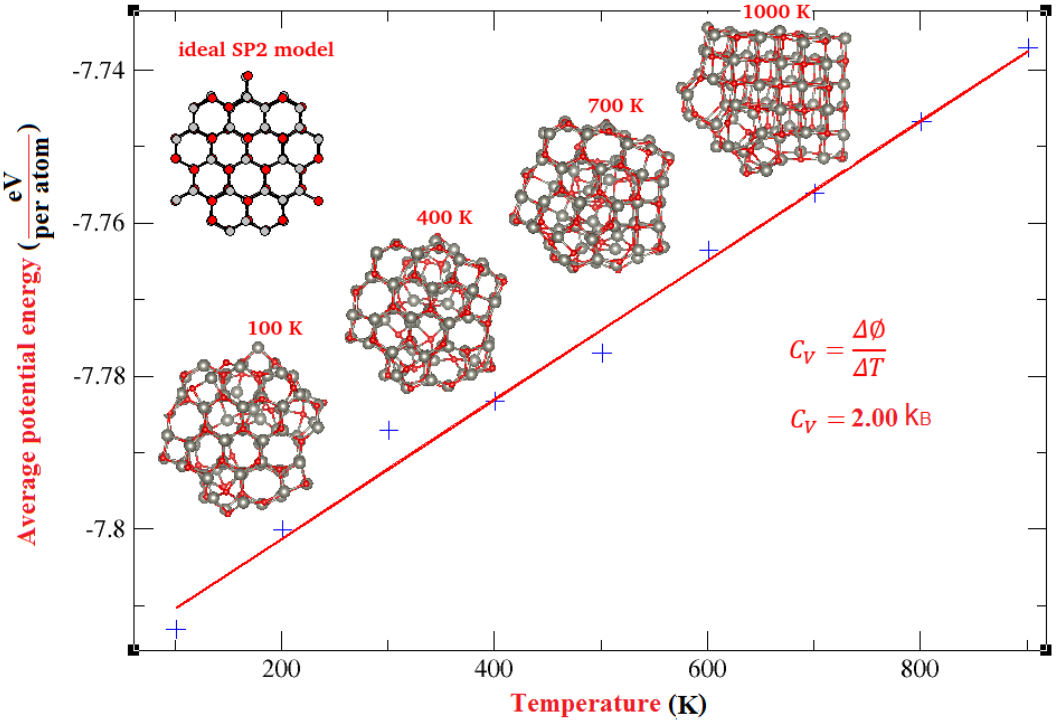

Figure 3.4 The structural properties of the SP2 model during the NEMD process.

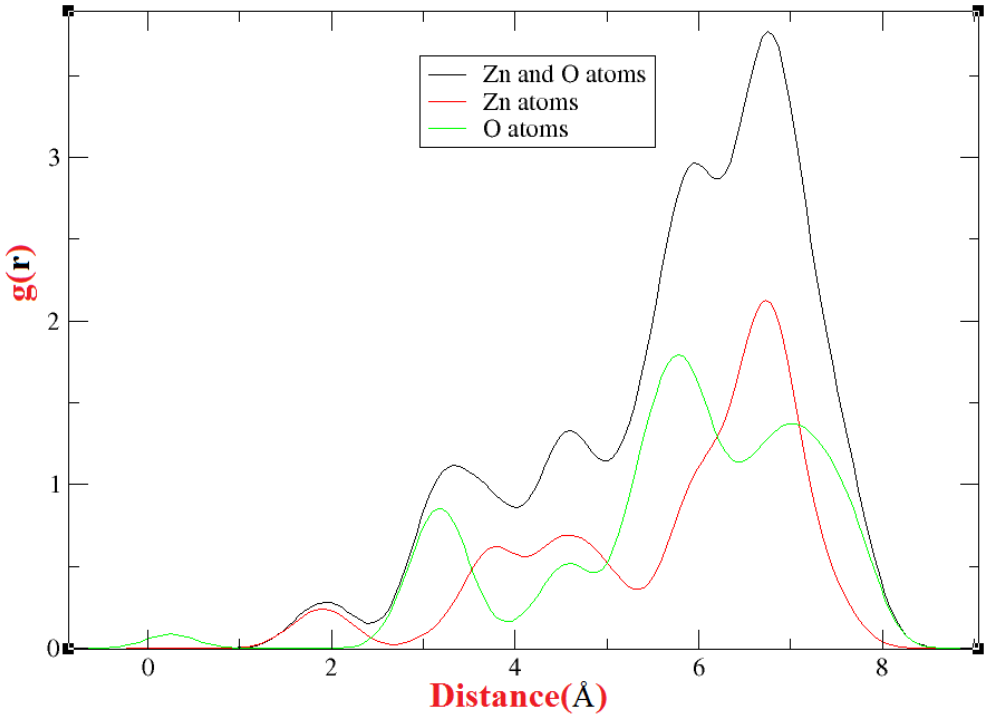

Figure 3.5 Radial atomic distribution of the SP2 model at 1 K.

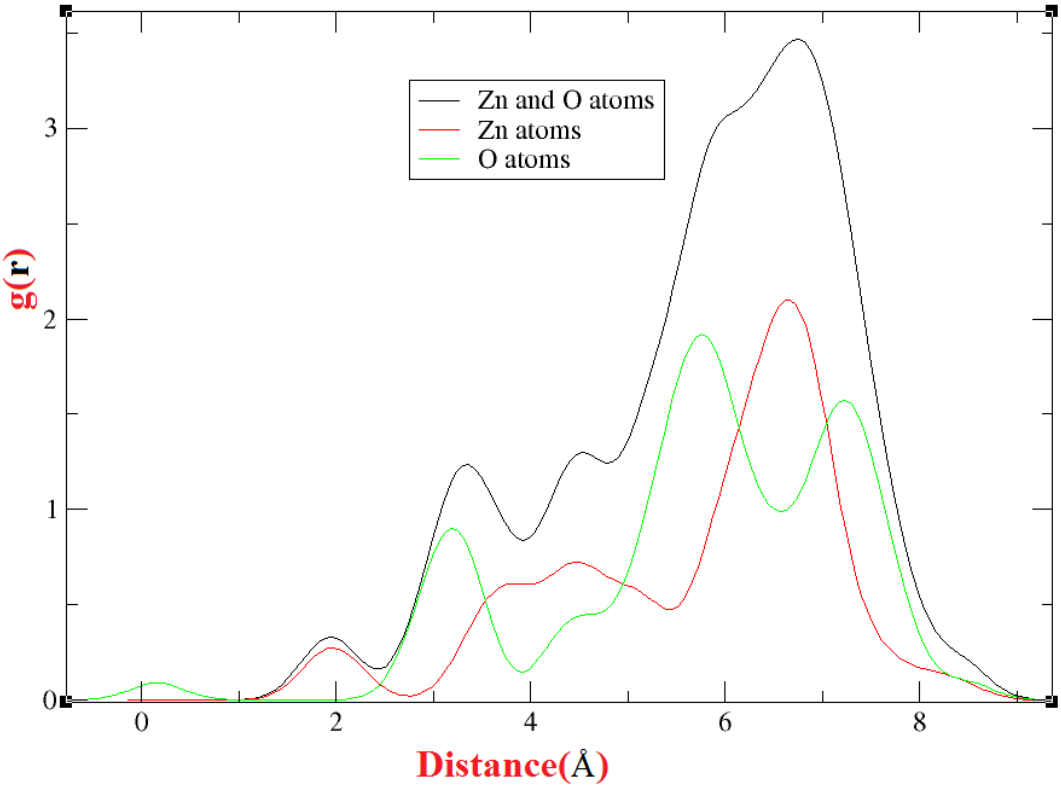

Figure 3.6 The same as Figure 3.5, but at 200 K.

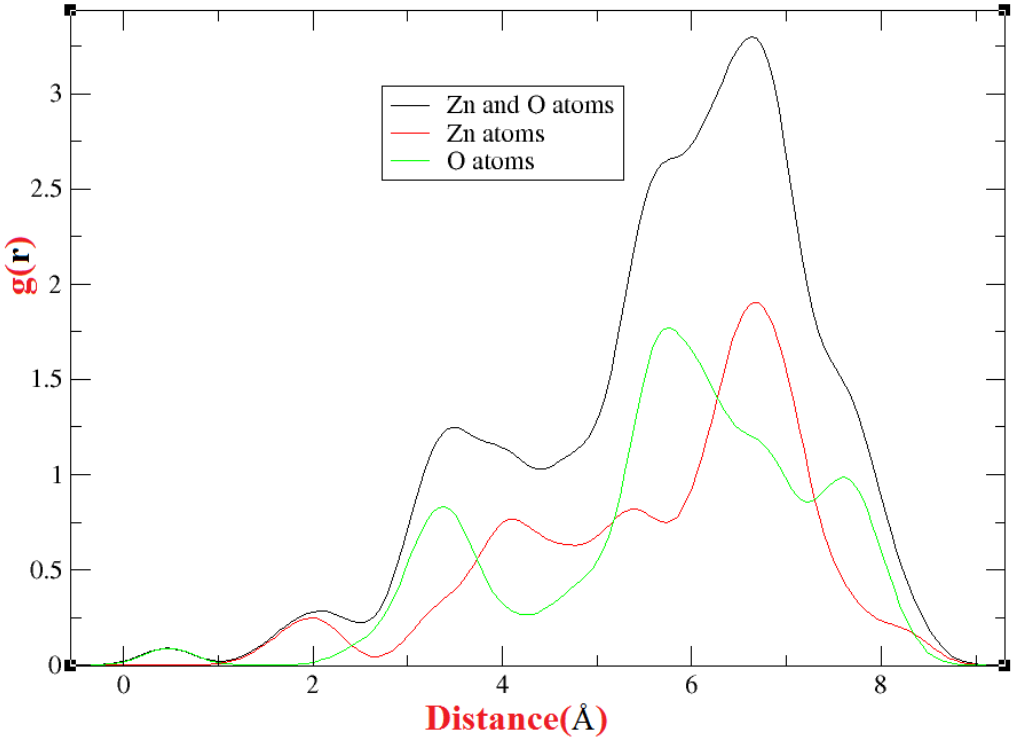

Figure 3.7 The same as Figure 3.5, but at 600 K.

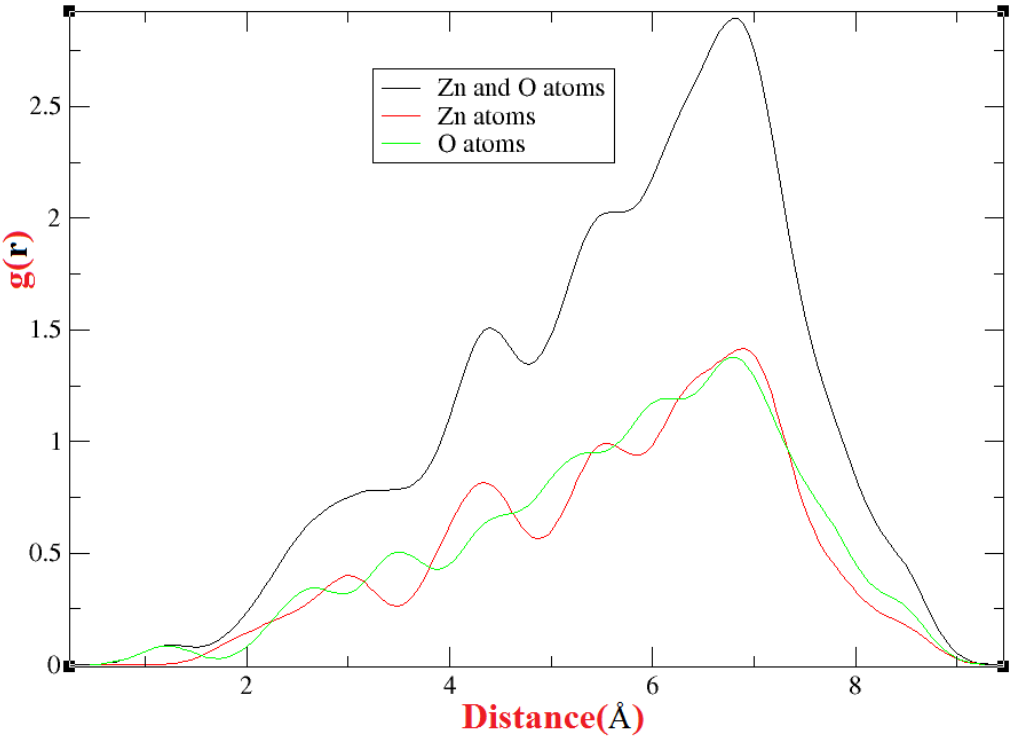

Figure 3.8 The same as Figure 3.5, but at 900 K.

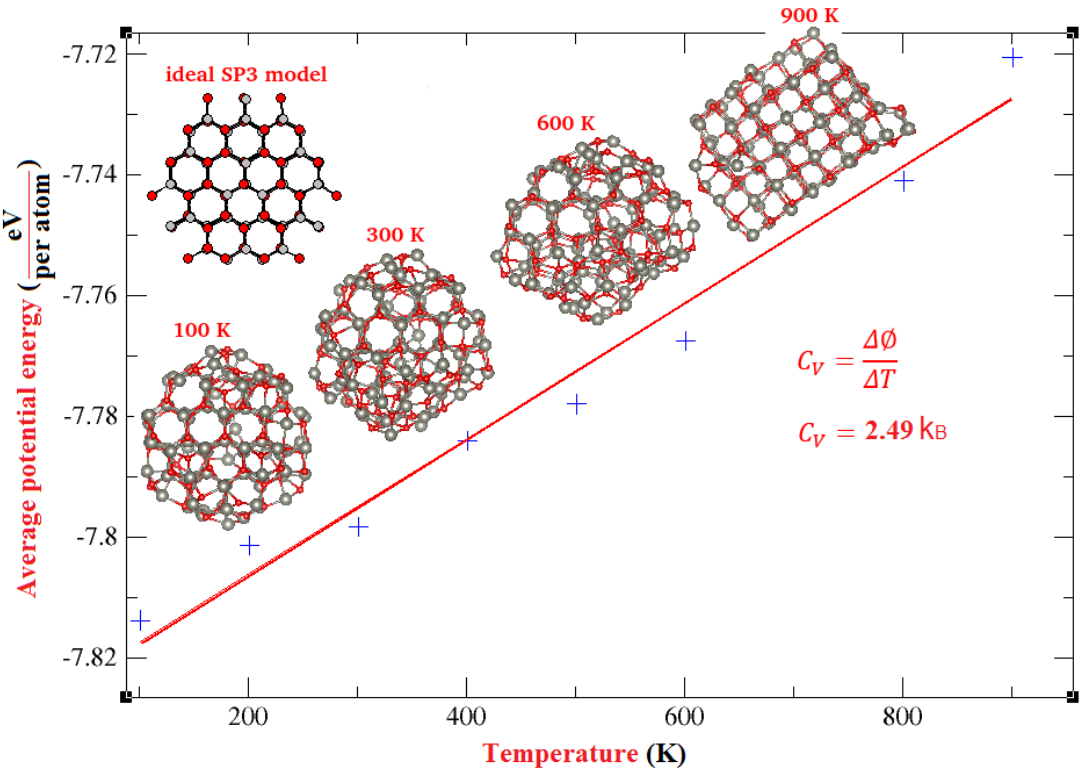

Figure 3.9 The structural and thermal properties of the SP3 model during the NEMD process.

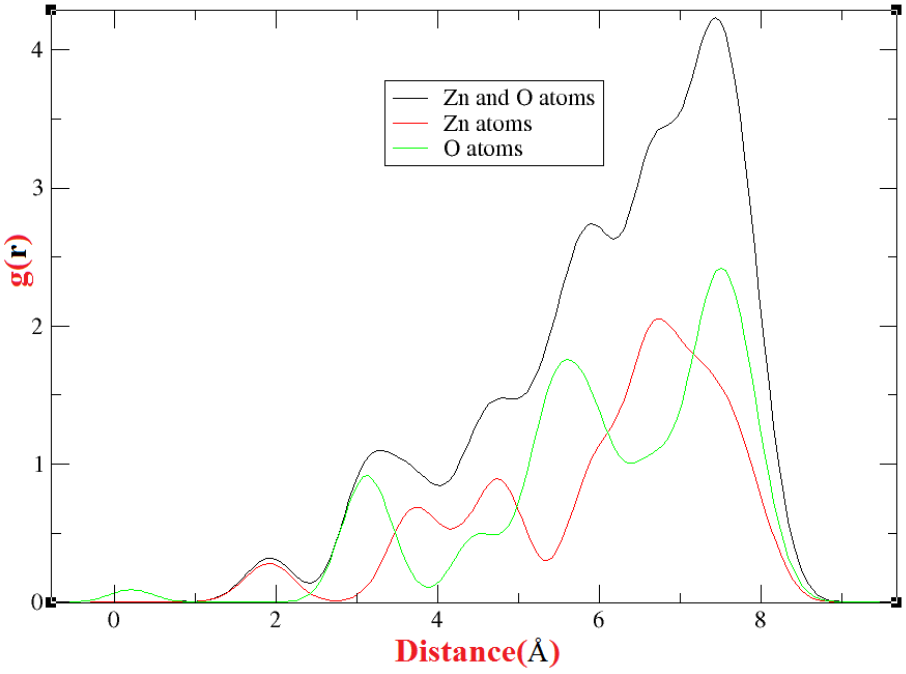

Figure 3.10 Radial atomic distribution of the SP3 model at 1 K.

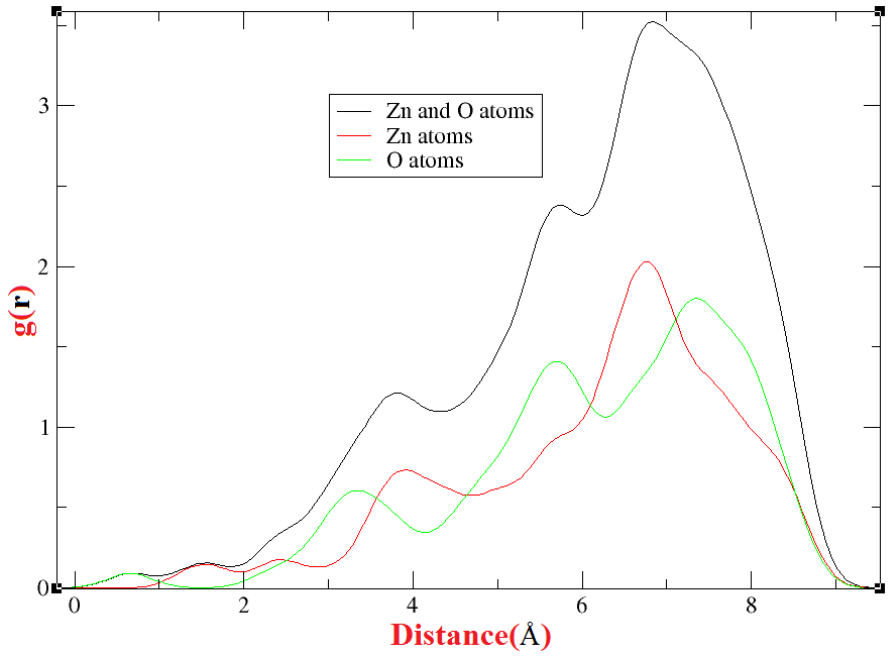

Figure 3.11 The same as Figure 3.10, but at 600 K.

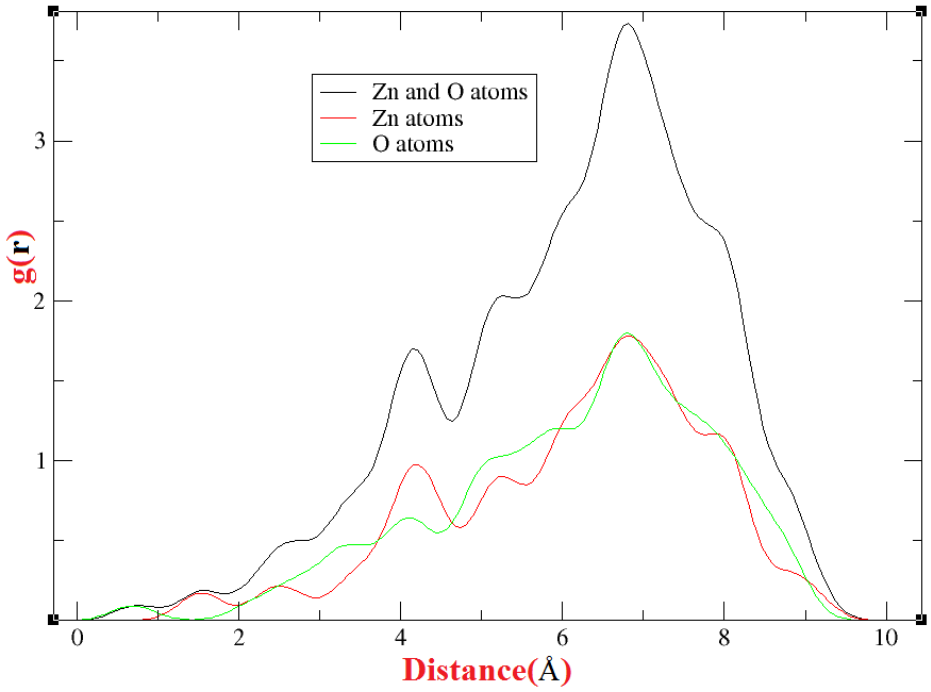

Figure 3.12 The same as Figure 3.10, but at 900 K.

The SP4, SP5, SP6 models exhibited similar structural properties to the SP3 (see Appendix A).

In the second stage of the study we have investigated the thermodynamics (thermal) properties of the SP2, SP3, SP4 and SP7 models. Because the thermal energetic fluctuation for the SP5, SP6, and SP8 models became larger, their heat capacity was not calculated. Thus, the heat capacity calculates were investigated for only the SP2, SP3, SP4 and SP7 models. The structural, thermal (heat capacity) and radial atomic distribution of the SP7 model were shown in Figure 3.13Figure 3.19. Even if the SP8 model almost looked like keeping its spherical appearance, the radial atomic distribution changed much more under the increasing temperature range between 1 and 500 K during the NEMD process (see Figure 3.20-3.24). It was observed that the average potential energy of the SP8 model did not regularly increase during the NEMD process (see Figure 3.25).

The heat capacity was found as 2.0 k_B for the SP2 model, 2.49 k_B for the SP3 model, 2.68 k_B for the SP4 model, and 3.1 k_B for the SP7 model. In addition, the heat capacity for bulk form of ZnO was found as 5 k_B. As a result, the heat capacity of the spherical nanoparticle models became proportional to their radius (or volume). In other words, when the radius (ranged from 7.87 Å to bulk) of the spherical nanoparticles increased, their heat capacity for per atom increased ranged from 2.0 k_B to 5.0 k_B. Similarly, the heat capacities of these models increased in relation to their numbers of atoms.

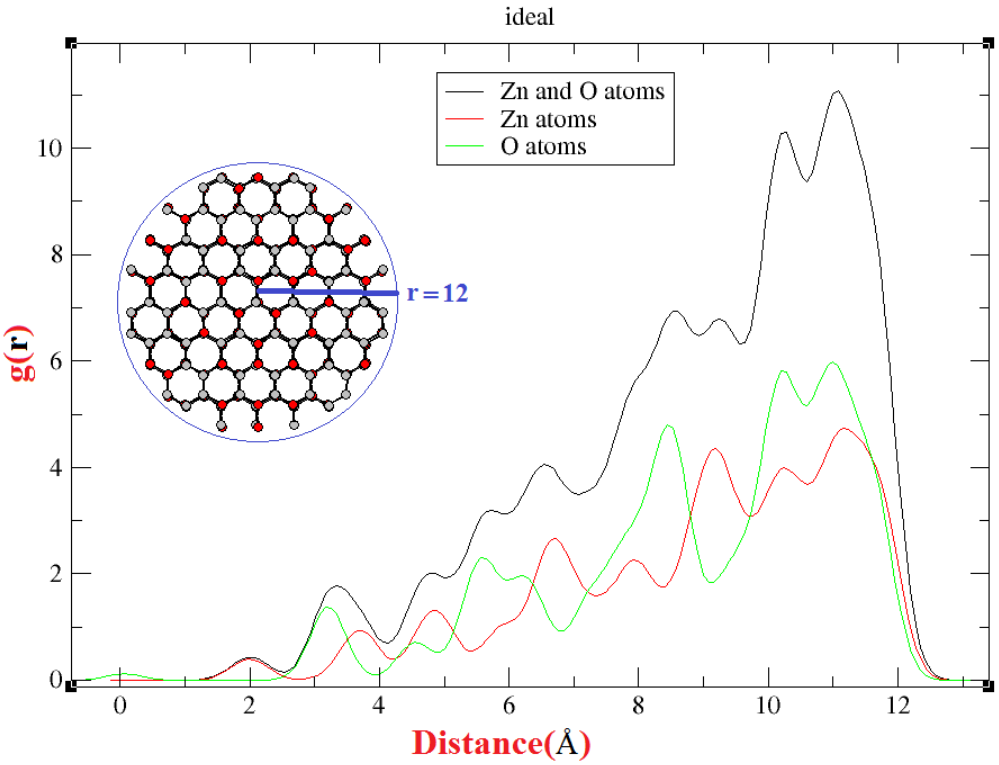

Figure 3.13 Radial atomic distribution of the ideal SP7 model.

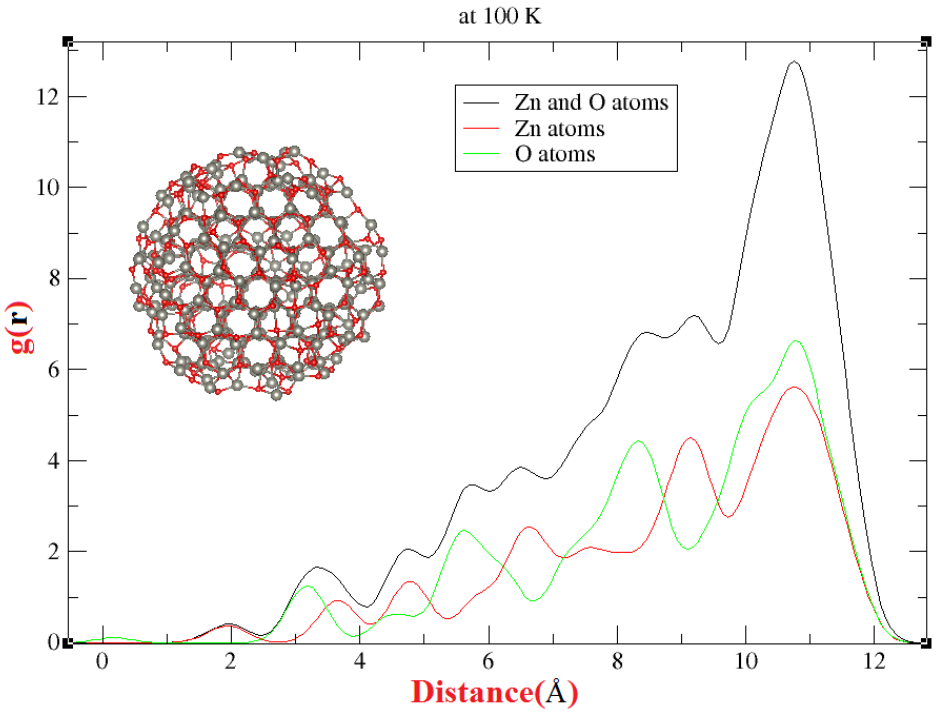

Figure 3.14 The same as Figure 3.13, but at 100 K.

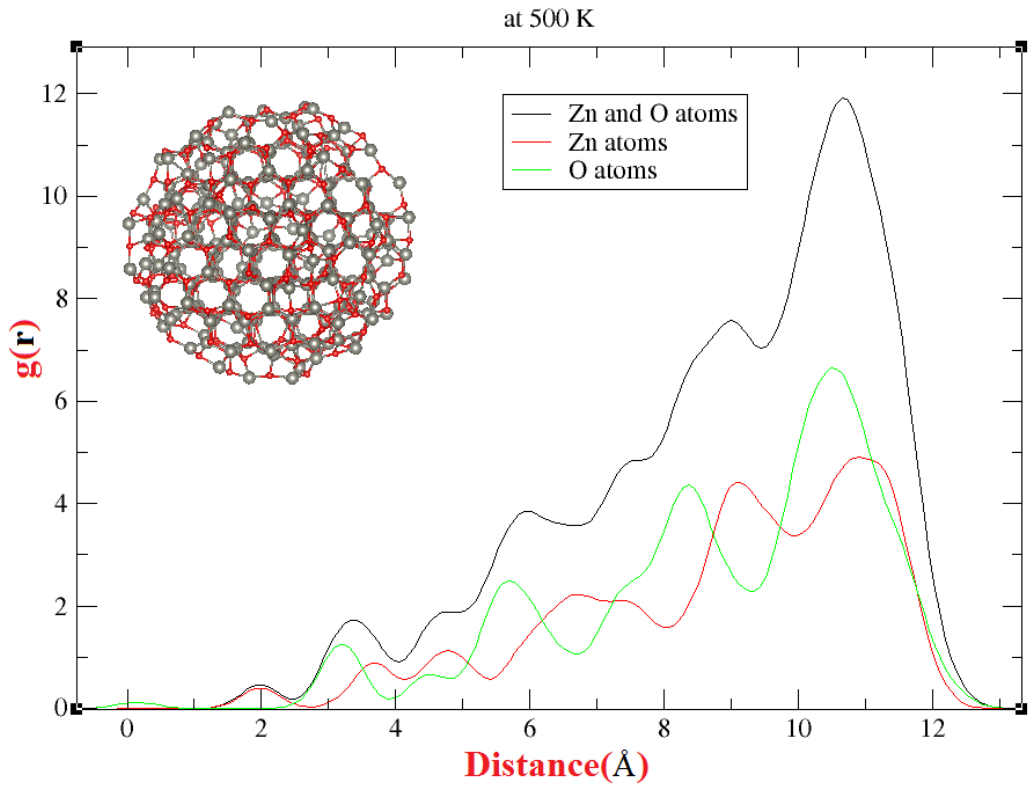

Figure 3.15 The same as Figure 3.13, but at 500 K.

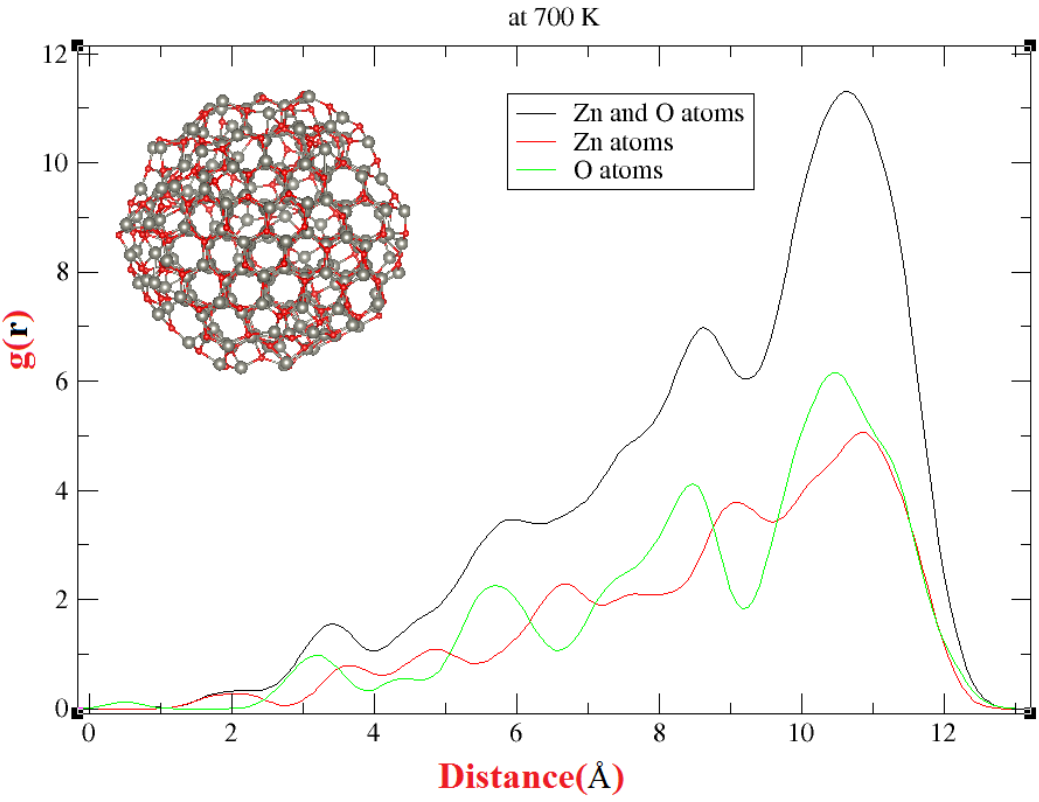

Figure 3.16 The same as Figure 3.13, but at 700 K.

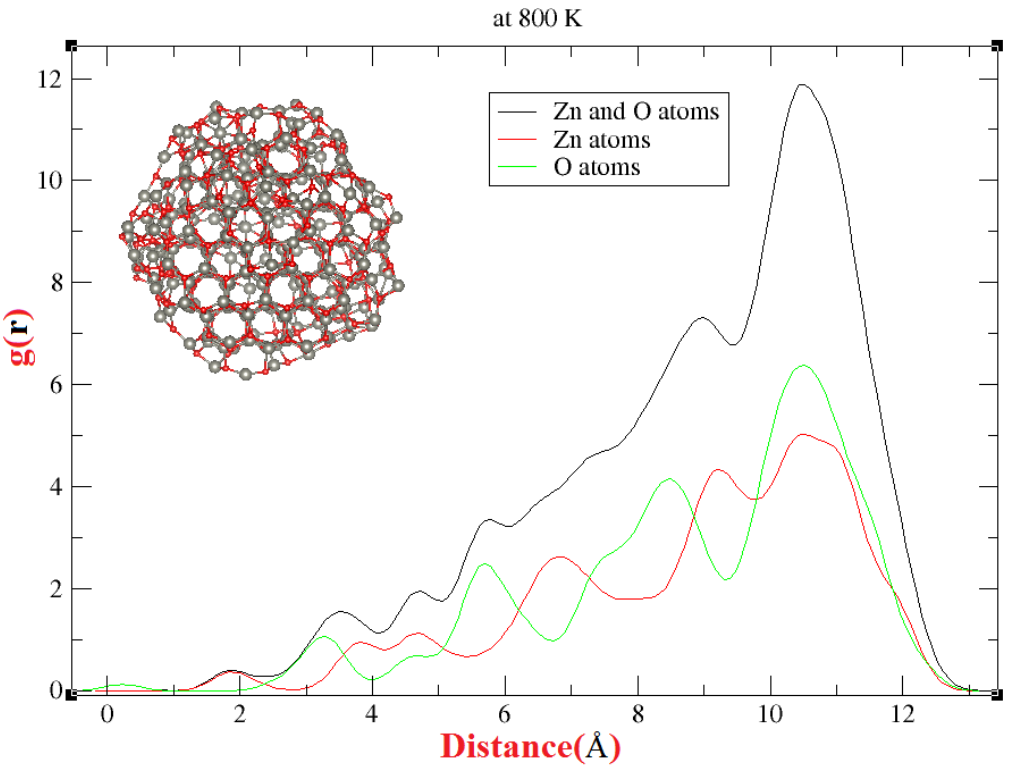

Figure 3.17 The same as Figure 3.13, but at 800 K.

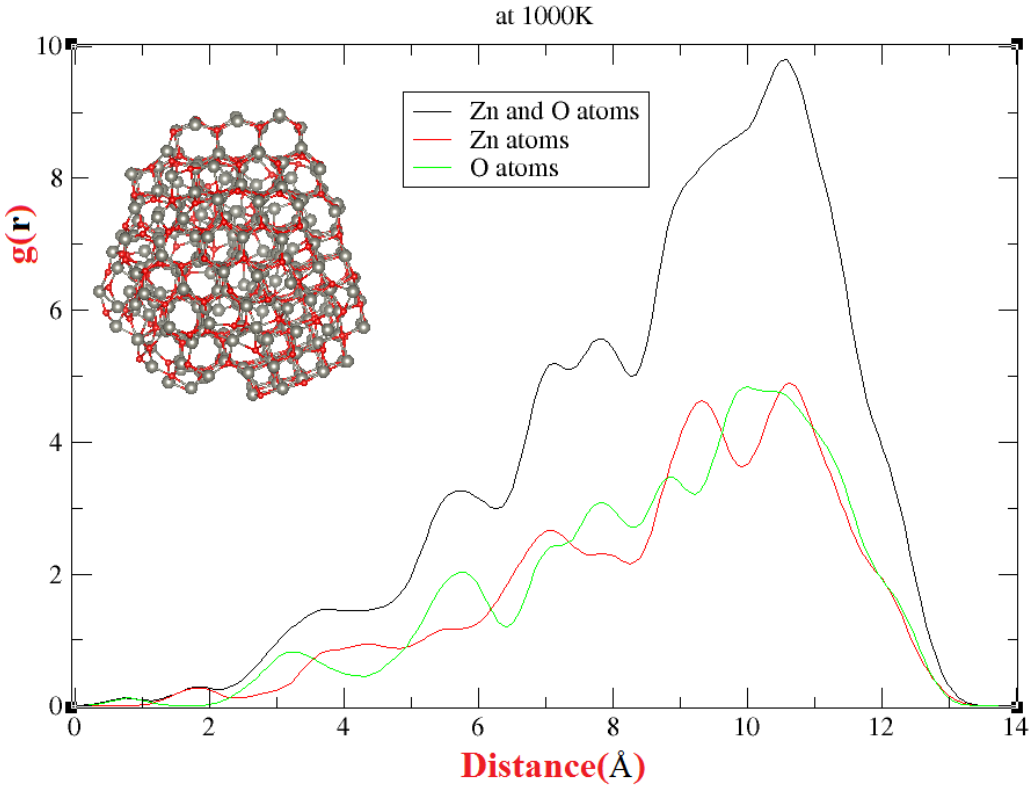

Figure 3.18 The same as Figure 3.13, but at 1000 K.

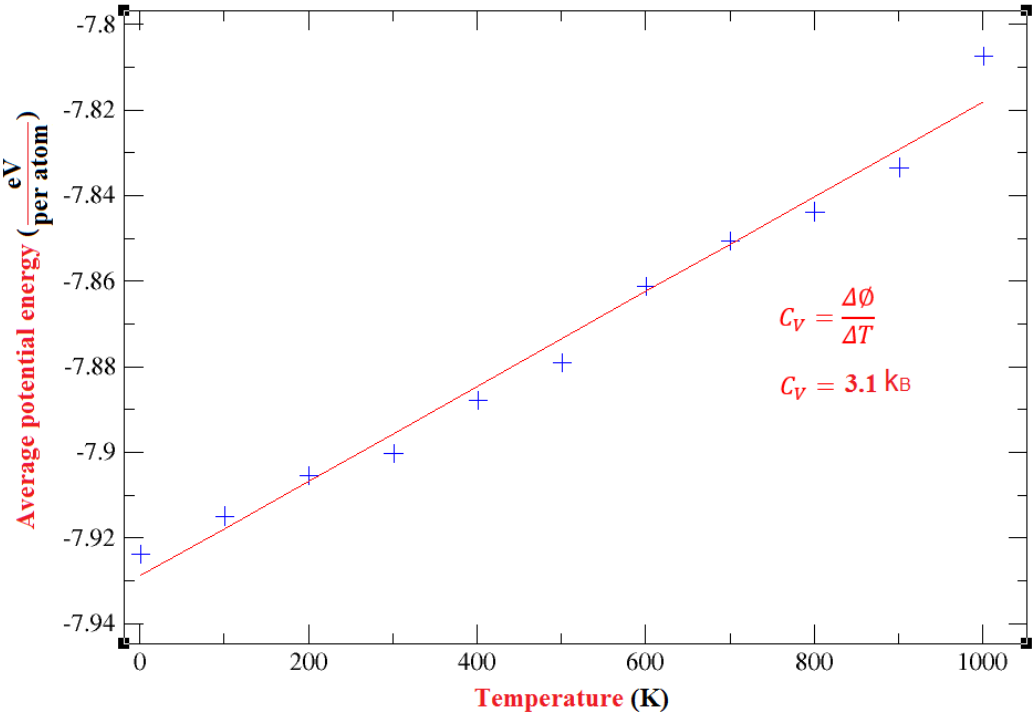

Figure 3.19 The average potential energy of the SP7 model.

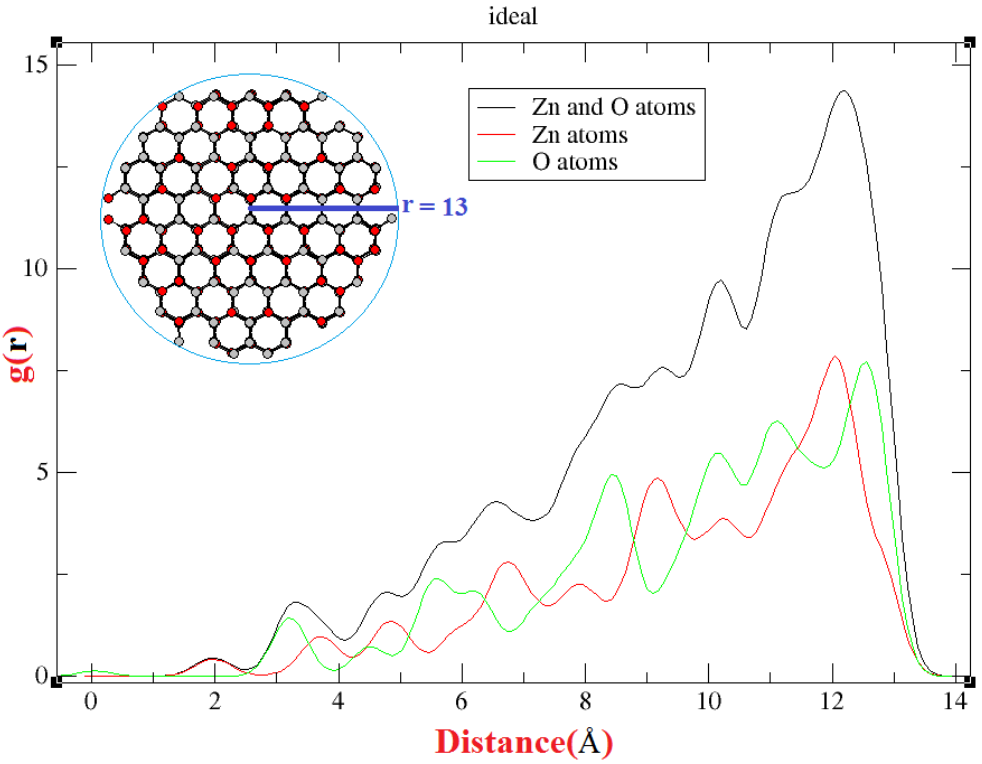

Figure 3.20 Radial atomic distribution of the ideal SP8 model.

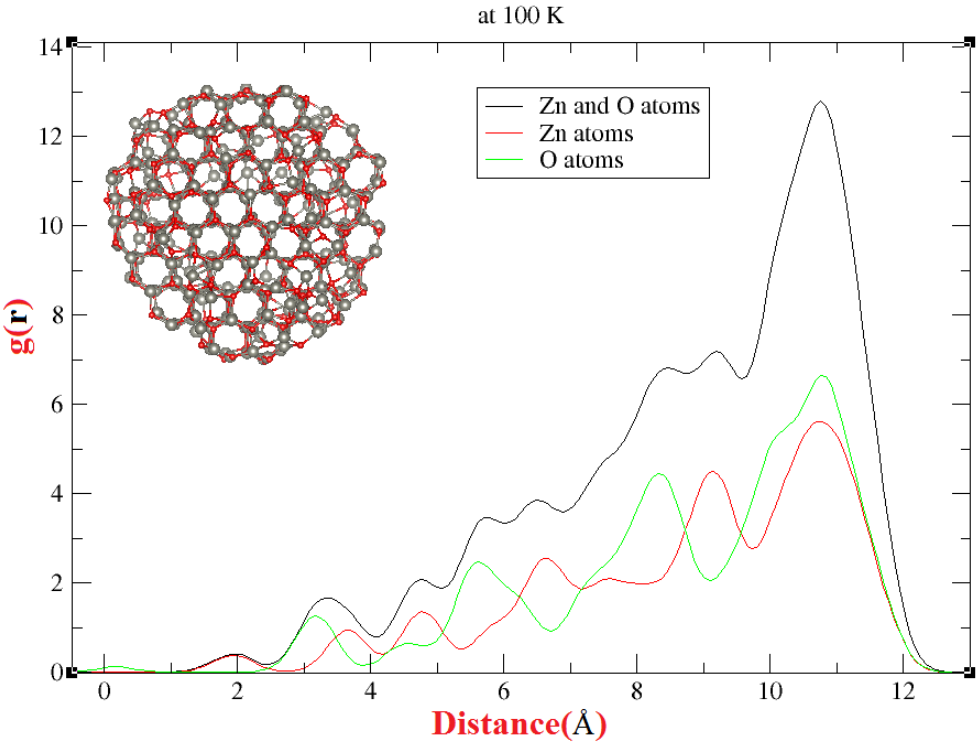

Figure 3.21 The same as Figure 3.20, but at 100 K.

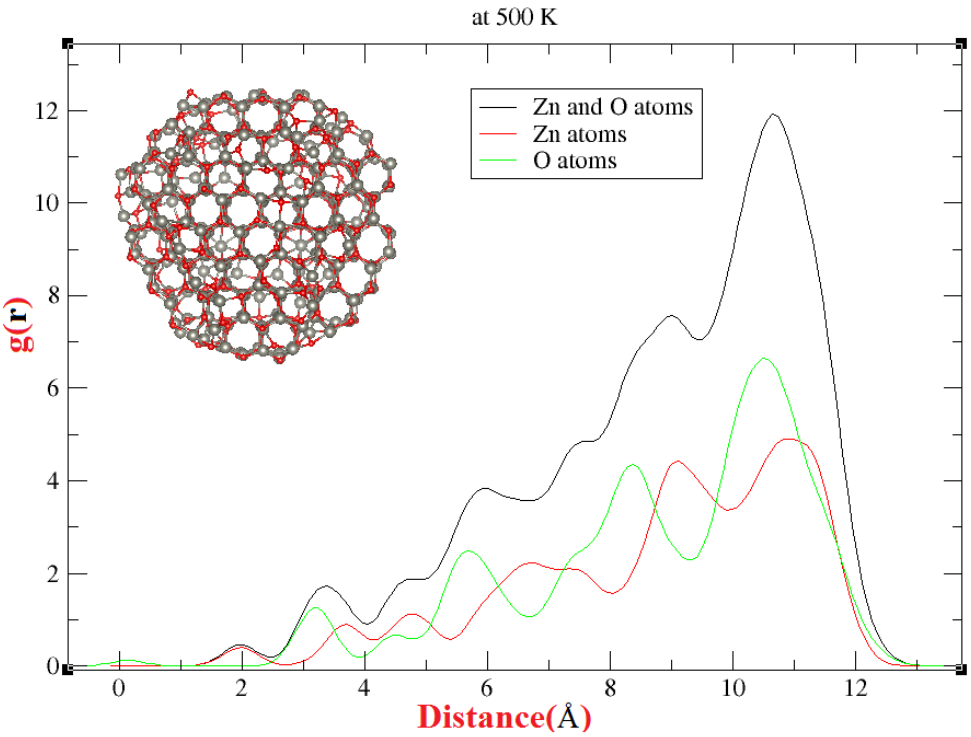

Figure 3.22 The same as Figure 3.20, but at 500 K.

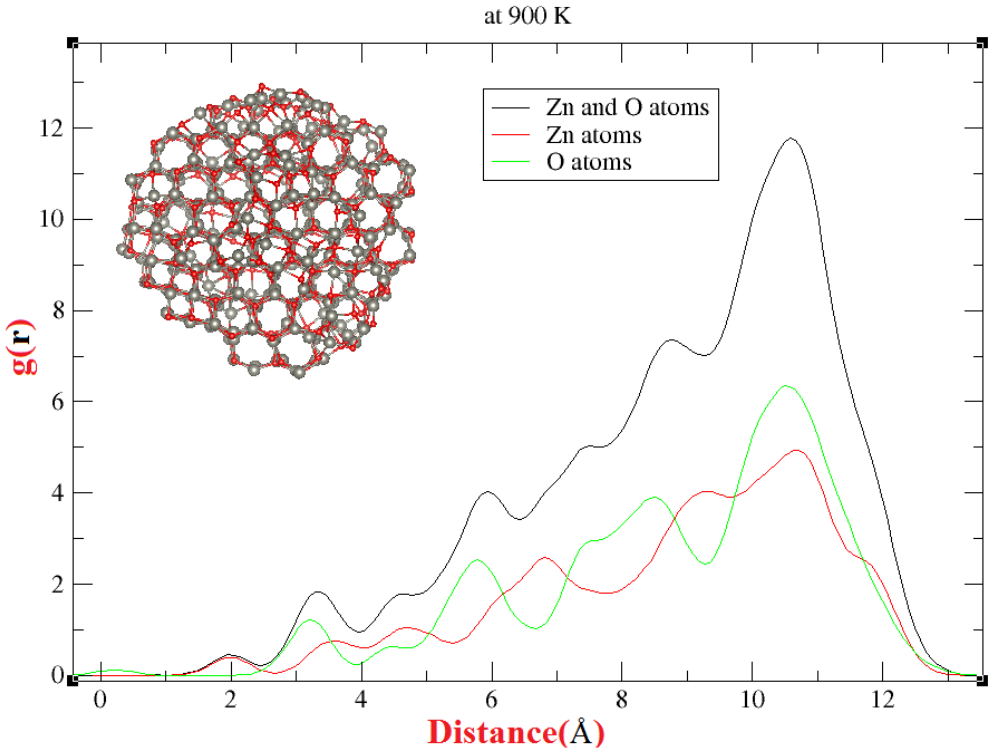

Figure 3.23 The same as Figure 3.20, but at 900 K.

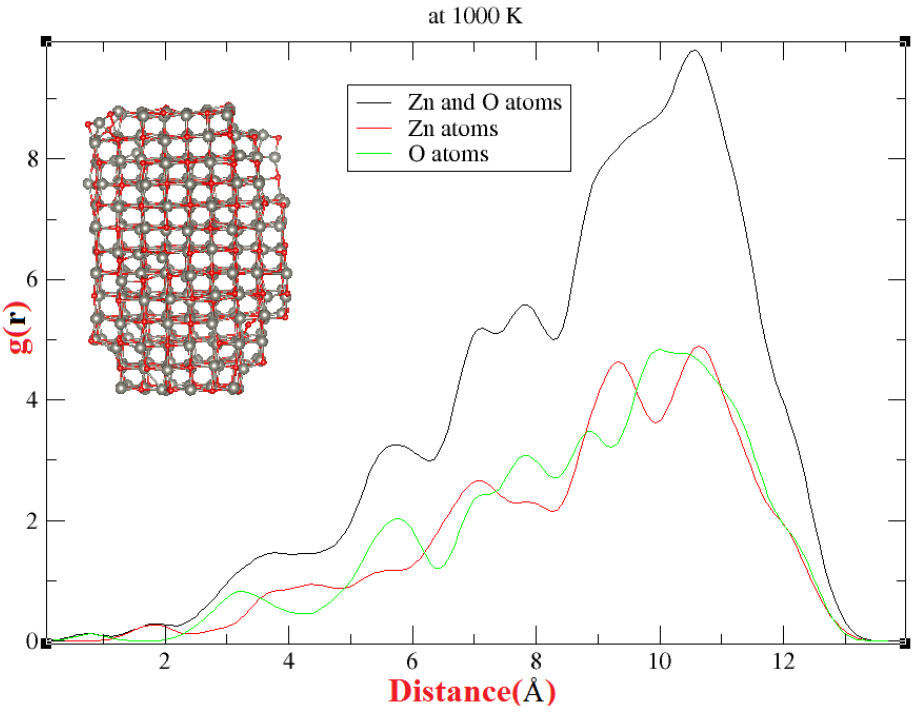

Figure 3.24 The same as Figure 3.20, but at 1000 K.

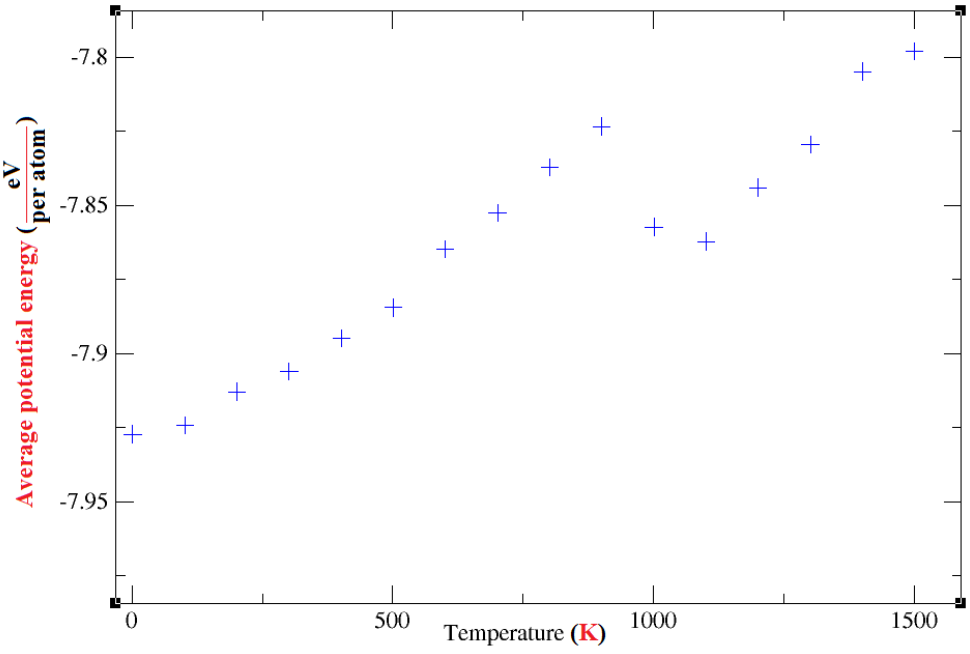

Figure 3.25 The average potential energy for per atom versus temperature of the SP8 model.

3.1.1.2 ZnO Cubic nanoparticles

The cubic nanoparticles exhibited more durable structural properties during the NEMD process by increasing 100 K-interval temperatures. Thus, the rock salt crystal structure was more stable than the wurtzite crystal structure.

The CP1 model preserved its initial structure during the NEMD process (see Figure 3.26). The average bond distance between atoms did not almost change under increasing temperatures. However, the energy fluctuation occurred with effect of the increasing temperatures (see Figure 3.27). The other models showed similar structural properties with CP1 model. The CP2 model also maintained its initial rock salt structure by increasing temperatures during the NEMD (see Figure 3.28). Moreover, the ratio of Zn to O in the CP6A model was a 172 to 171, whereas the ratio of Zn to O in the CP6B model was 171 to 172. Both the CP6A and the CP6B models also retained their initial structure during the NEMD process (Figure 3.29,Figure 3.30). The heat capacity of CP6A model was calculated as 1.64 K_B whereas the heat capacity of the CP6B model was calculated as 1.58 k_B (see Figure 3.31Figure 3.32). As a consequence, in this study it was realized that the heat capacity of the nanostructures depended on the ratio of the Zn and O atoms.

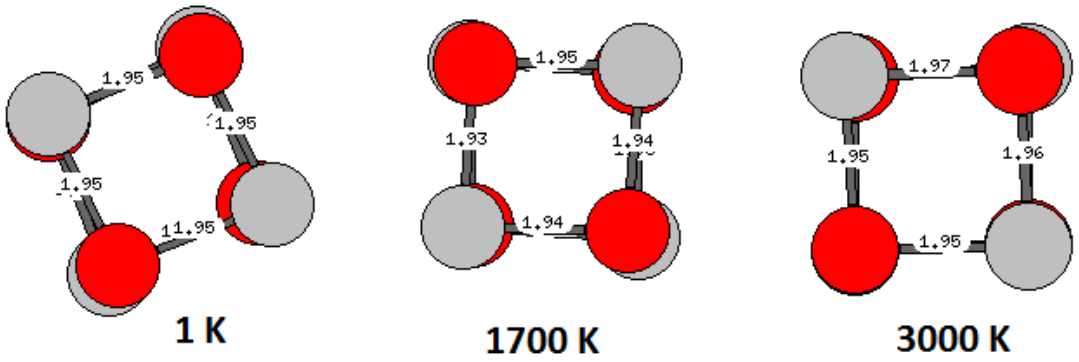

Figure 3.26 The CP1 model during the NEMD process.

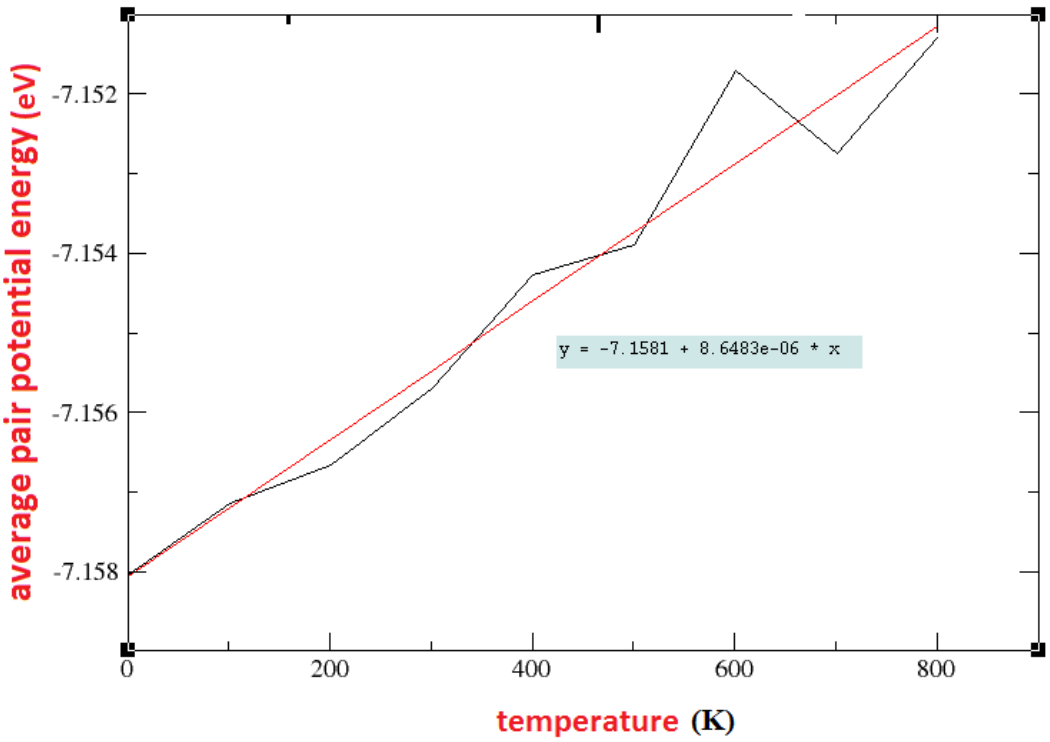

Figure 3.27 The average potential energy for per particle of the CP1 model during the NEMD process.

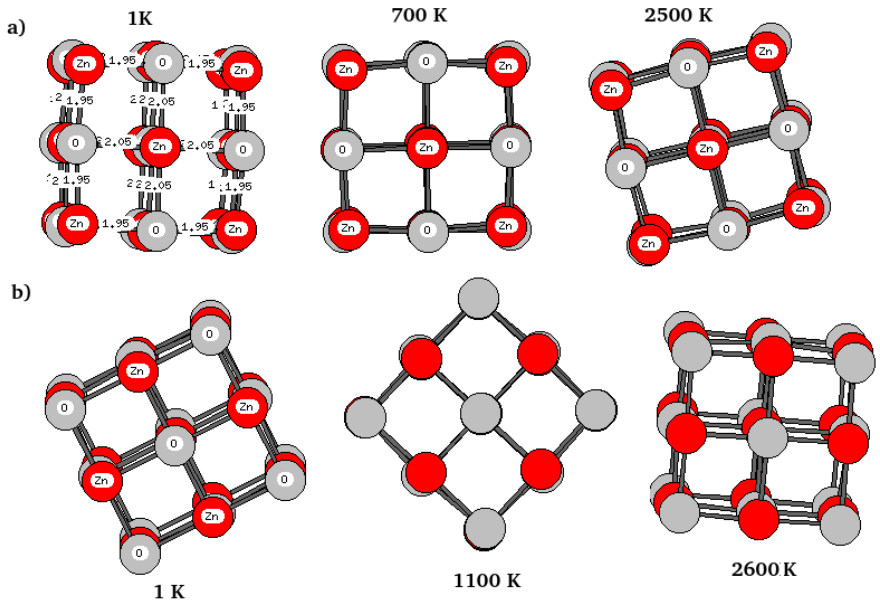

Figure 3.28 a) The CP2A model during the NEMD b) The CP2B model during the NEMD.

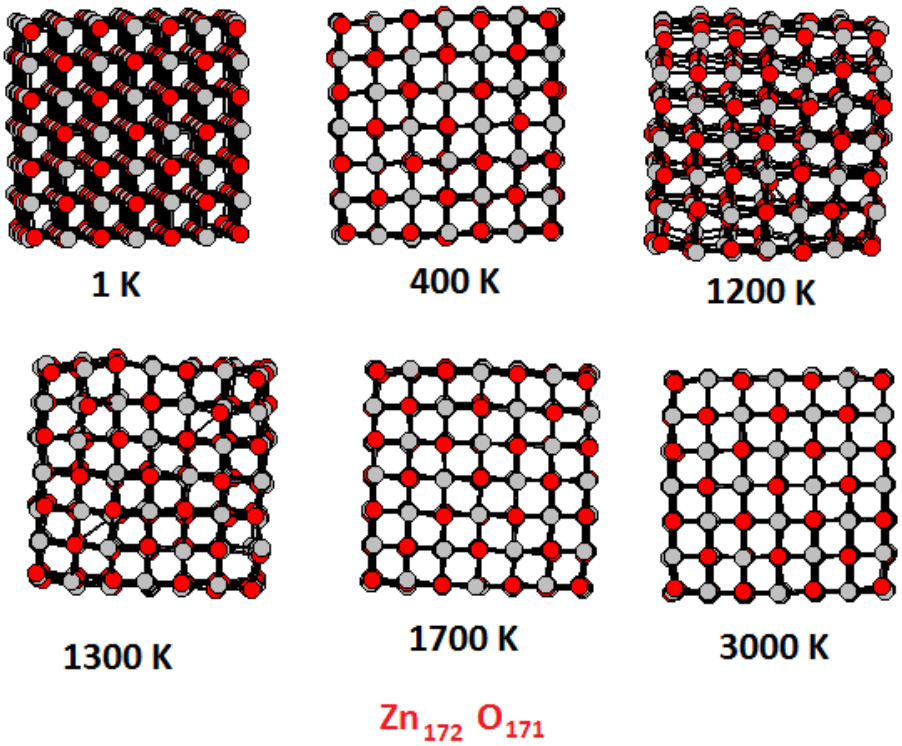

Figure 3.29 The CP6A model during the NEMD process.

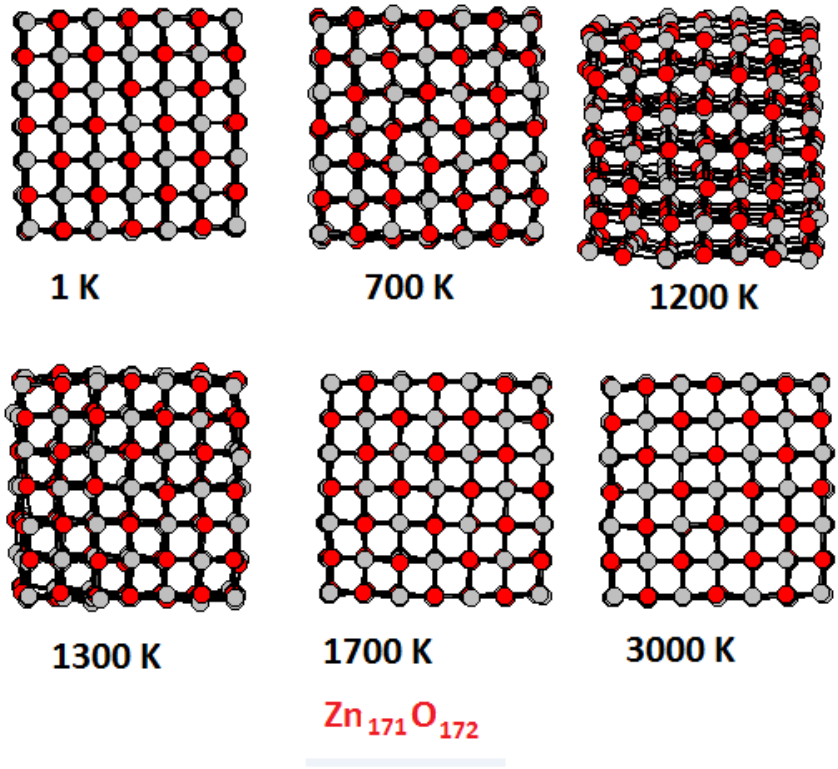

Figure 3.30 The CP6B model during the NEMD process.

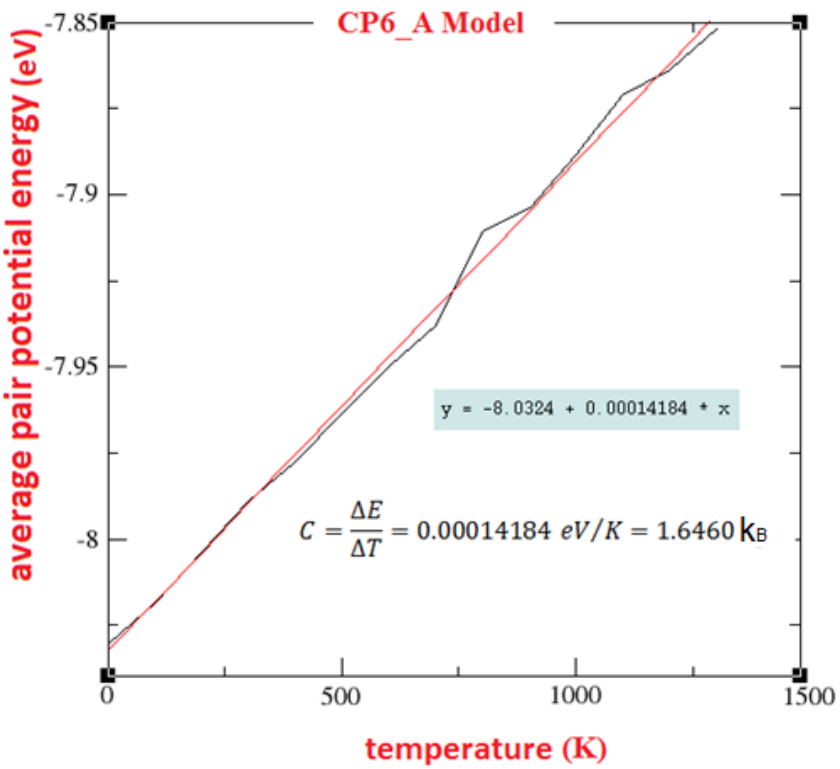

Figure 3.31 The heat capacity of the CP6A model with NEMD.

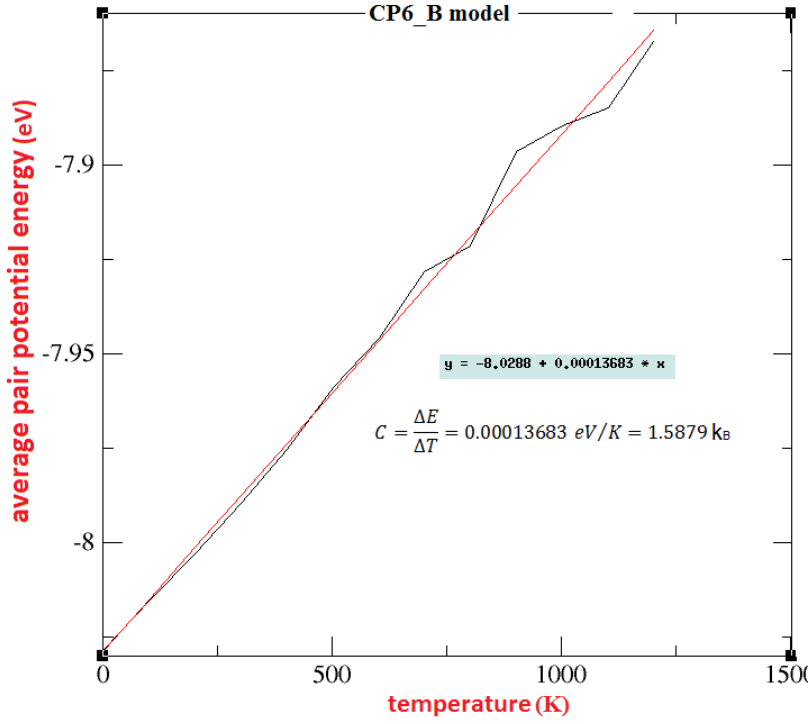

Figure 3.32 The heat capacity of the CP6B model with NEMD.

From the structural and energetic point of view the present calculated results show a good agreement with the literature data. For example, the nanoclusters constructed from wurtzite crystal contained with squares after the energetic relaxation and rock salt structure are found to produce low energy clusters[127,128]. Furthermore, the calculated heat capacity values also show a good agreement with literature values[129].

3.1.2 ZnO Nanorings

The R1 model abruptly changed into rod structure during the NEMD process. The rod structure consisted of one hexagon and two squares when viewed from the side[13]. The rod structure did not change despite the increasing temperature ranging from 300 and 1700 K. Then, the rod structure configured with completely squares at 1800 K (see Figure 3.33). Moreover, the R2 model also changed from ring into rod. Similarly, the rod structure consisted of two hexagons and two squares during the temperatures ranging between 100 and 2800 K (see Figure 3.34).

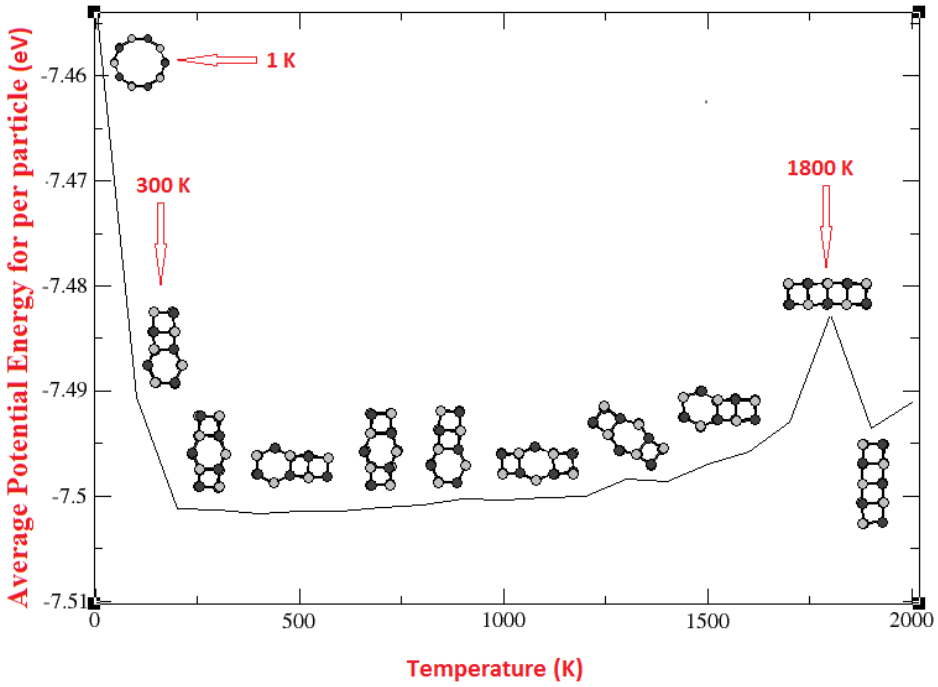

Figure 3.33 The R1 model nanoring during the NEMD process.

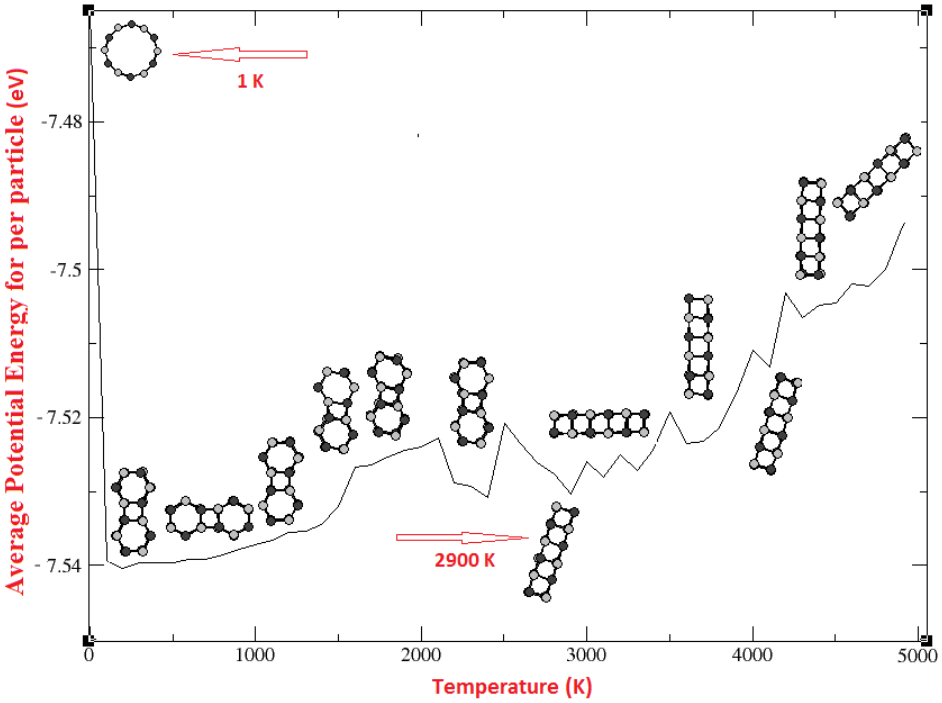

Figure 3.34 The R2 model nanoring during the NEMD process.

3.2 1D ZnO Nanostructures

One dimensional systems mean that the cross sectional dimension is much smaller than their length. In this stage, we have investigated the structural properties of the nanoribbons (pristine and defects), nanorods and nanotubes under uniaxial compression strain and tensile strain applications. Moreover, only the hexagonal cross sectional nanorod models were subject to torsion applications.

3.2.1 ZnO Nanoribbons

3.2.1.1 Pristen Nanoribbons

ZnO nanoribbons are modeled in the honeycomb structure with zigzag and armchair edges[10]. Two different widths (1L and 2L) have been considered for zigzag nanoribbons. We used the notation Z1L to represent zigzag nanoribbon with one layer (1L) width. Similar notations were used for the other models, namely Z2L, A1L and A2L. Ideal structures of ZnO nanoribbons are shown in Figure 2.16. Ciraci and co-workers studied the ZnO honeycomb structures by using the first-principle method. In their study, the armchair nanoribbons maintained the honeycomb geometry under uniaxial tensile strain, but the atom chains was revealed in the high strain applications[71].

3.2.1.1.1 Zigzag Nanoribbons

After the energetic relaxation, when the periodic boundary was not applied, the Z1L model at 1 K appeared as a ribbon structure again, but arranged with square grid geometry except for two ends of the structure, which retained hexagons as they were free. However, the same model at 300 K disappeared a ribbon structure, changed into rod with NoPBC (see Figure 3.35). In the case of PBC, the structure at 1 K appeared as a wavy like ribbon when viewed from the side, but arranged with square grid geometry (see Figure 3.36 a). In addition, when subjected to 5% tensile strain, the structure at 1 K still maintained its wavy like ribbon in the first two tensile strain steps. The wavy view disappeared at 3rd tensile strain step. After a few strain applications,

the neck points were observed in the structure. In the 16th tensile strain step, the ribbon structure completely changed into atom chain formation (see Figure 3.36 b). On the other hand, the same model at 300 K also appeared as a wavy ribbon structure and arranged with square grid geometry with PBC (see Figure 3.37 a). In addition, when subjected to 5% tensile strain, the structure retained its wavy like ribbon structure in the first two tensile strain steps. In the 3rd tensile strain step, the perfect ribbon structure was observed with square grid geometry. Then, the structure was broken into two parts as a ribbon (see Figure 3.37 b).

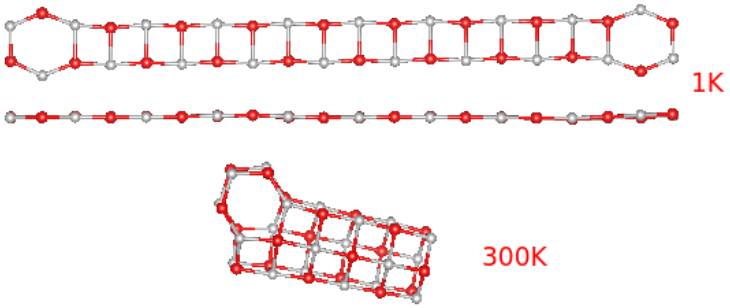

Figure 3.35 The Z1L model nanoribbons with NoPBC, the top figure for at 1 K with top and side view and the bottom for at 300 K.

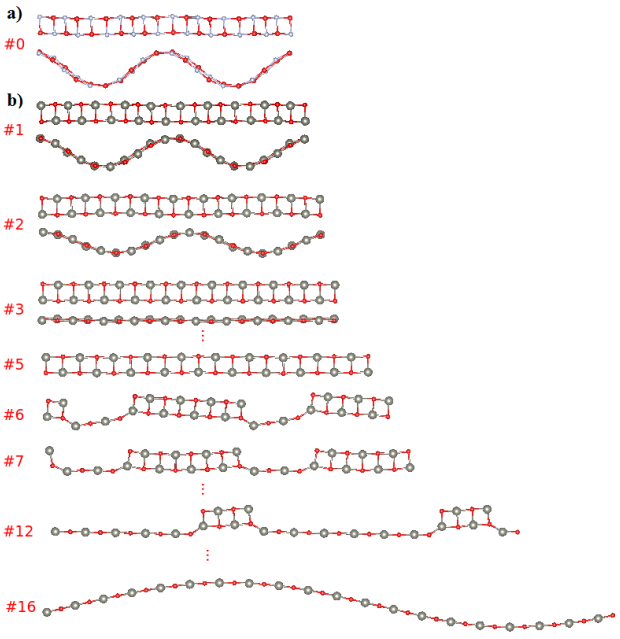

Figure 3.36 a) The Z1L model with PBC at 1 K. b) The same model under 5% tensile strain application at 1 K. Each row shows cross section view and side view.

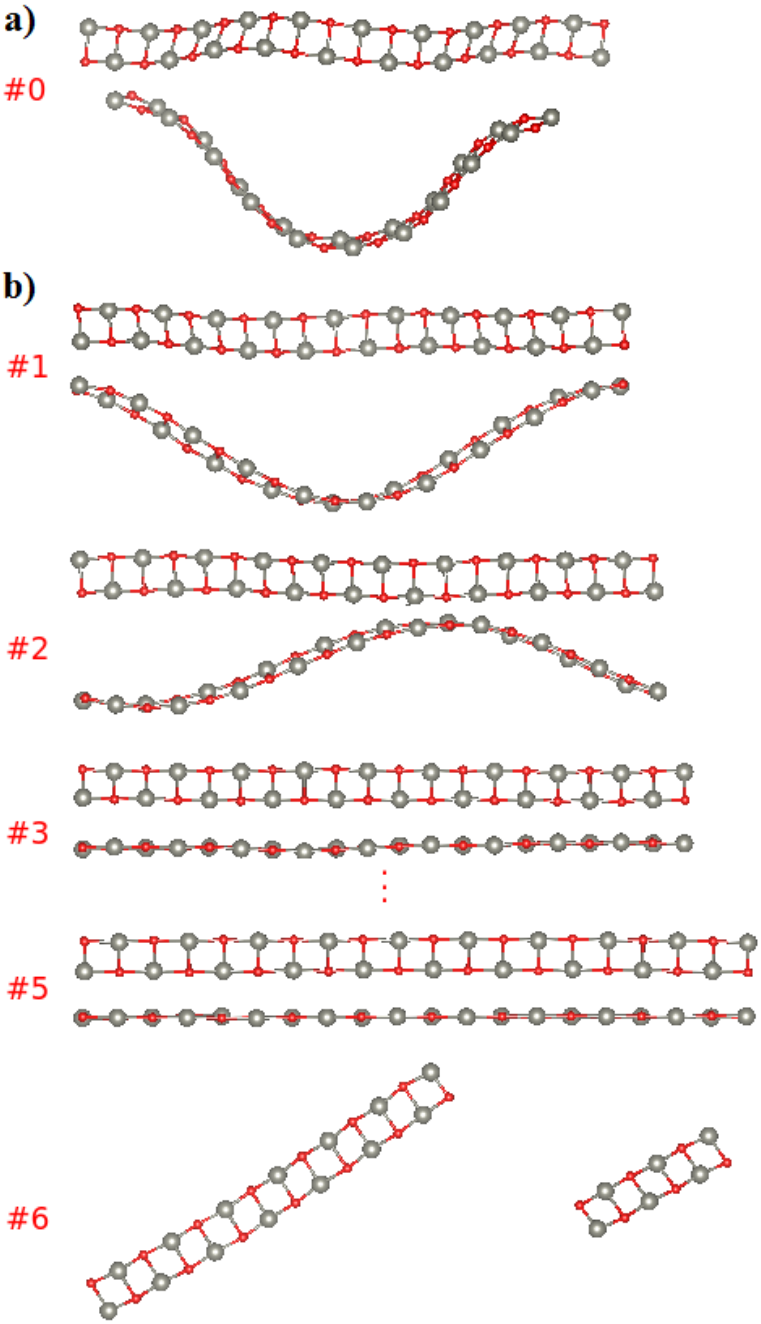

Figure 3.37 a) The Z1L model with PBC at 300 K. b) The same model under 5% tensile strain application at 300 K. Each row shows cross section and side view.

In the simulation procedures all the systems studied relaxed until thermal equilibrium has been reached. Sample graphs for Z1L model both with NoPBC and PBC cases are displayed in FiguresFigure 3.38-Figure 3.41.

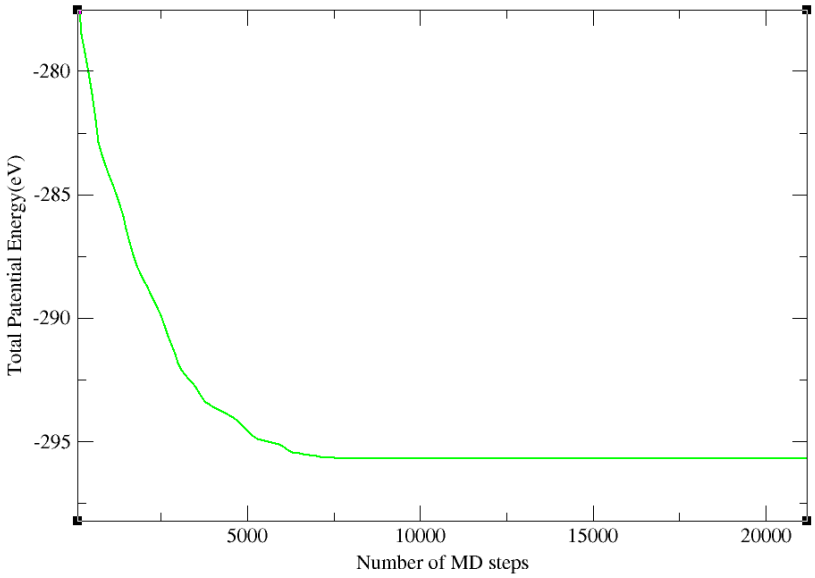

Figure 3.38 The total potential energy versus MD steps for the Z1L model at 1 K with NoPBC.

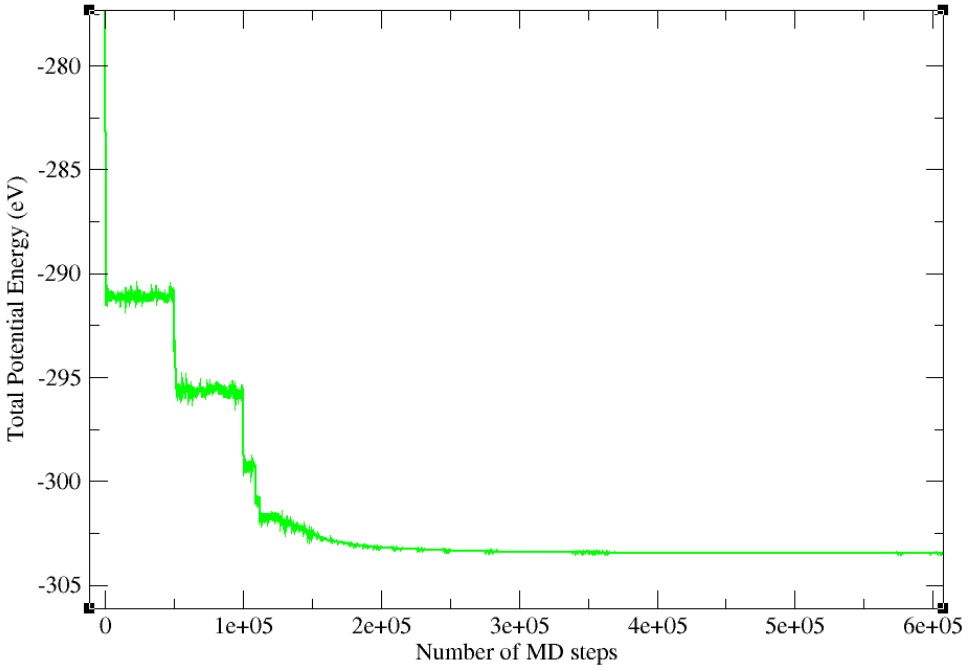

Figure 3.39 The total potential energy versus MD steps for the Z1L model at 300 K with NoPBC.

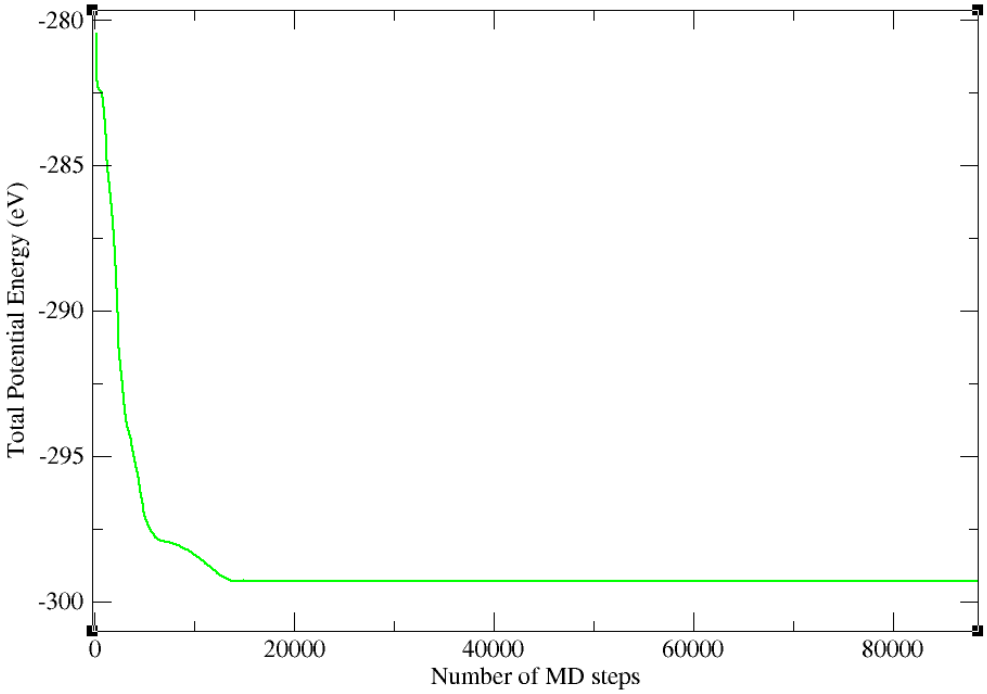

Figure 3.40 The total potential energy versus MD steps for the Z1L model at 1 K with PBC.

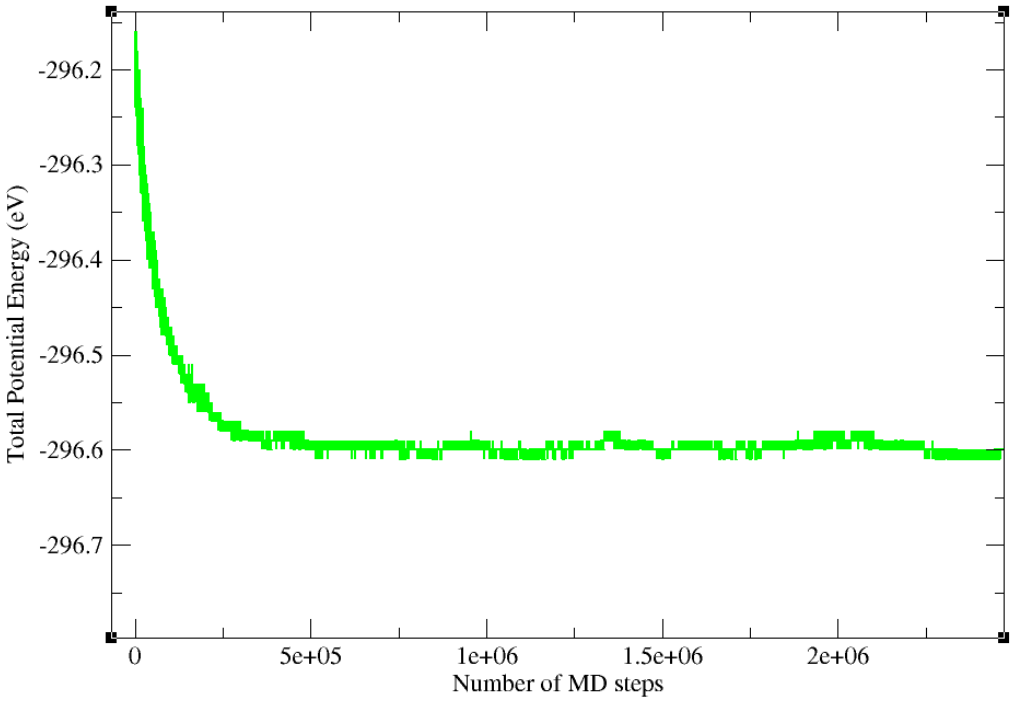

Figure 3.41 The total potential energy versus MD steps for the Z1L model at 300 K with NoPBC.

After the relaxation process, the Z2L model at 1 K transformed from ribbon into ring structure when PBC was not applied. However, the same model at 300 K transformed into rod like structure without PBC. The rod structure was arranged with square grid geometry except for two ends (see Figure 3.42). In the case of PBC, the Z2L model at 1 K arranged with square grid geometry. It also appeared as a wavy like ribbon when viewed from the side (see Figure 3.43 a). Furthermore, when subject to 5% tensile strain, the structure, configured with square grid geometry, at 1 K maintained its a wavy like ribbon structure in the first three tensile strain steps. Then, the perfect ribbon structure emerged at the 4^{th} and 5^{th} tensile strain steps, so a wavy view disappeared. Then, the structure was broken into two parts at the 6^{th} tensile strain step (see Figure 3.43 b). On the other hand, the same model at 300 K also arranged with square grid geometry, and appeared wavy like structure when viewed from the side (see Figure 3.44 a). Moreover, when 5% subject to strain at 300 K, it maintained a wavy like structure in the first four tensile strain steps. Then, the neck points were detected at 6^{th} tensile strain step. Then, following the further strain applications, the 2L ribbon structure changed into 1L ribbon. A perfect 1L square-net planar structure appeared at 13^{th} tensile strain step (see Figure 3.44 b).

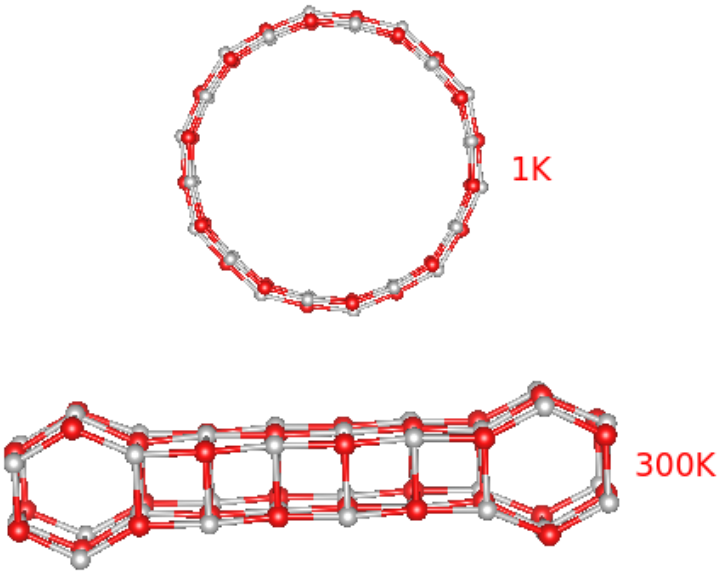

Figure 3.42 The Z2L model with NoPBC, the top figure for at 1 K, the bottom at 300 K.

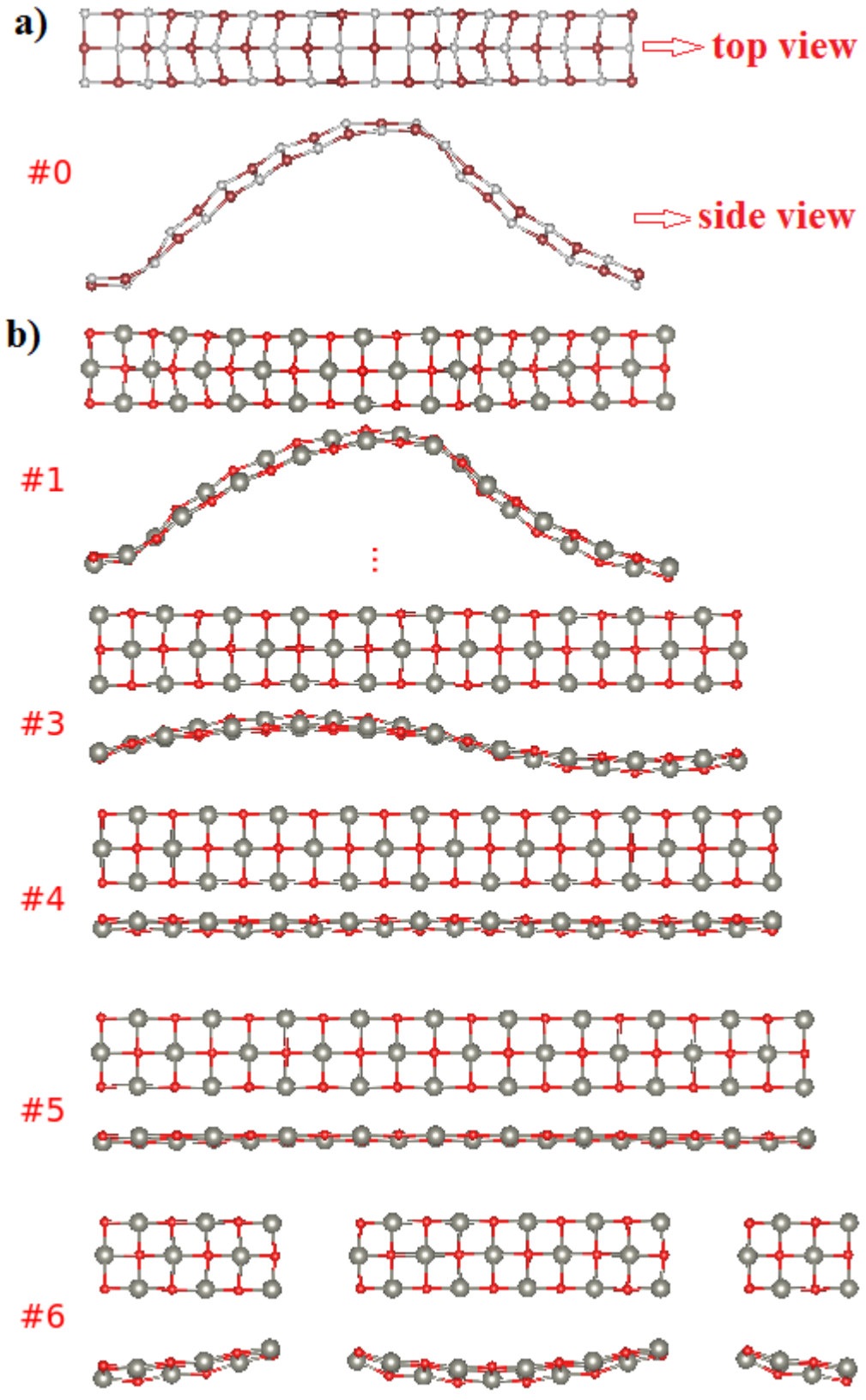

Figure 3.43 a) The Z2L model with PBC at 1 K b) The same model under 5% tensile strain application at 1 K.

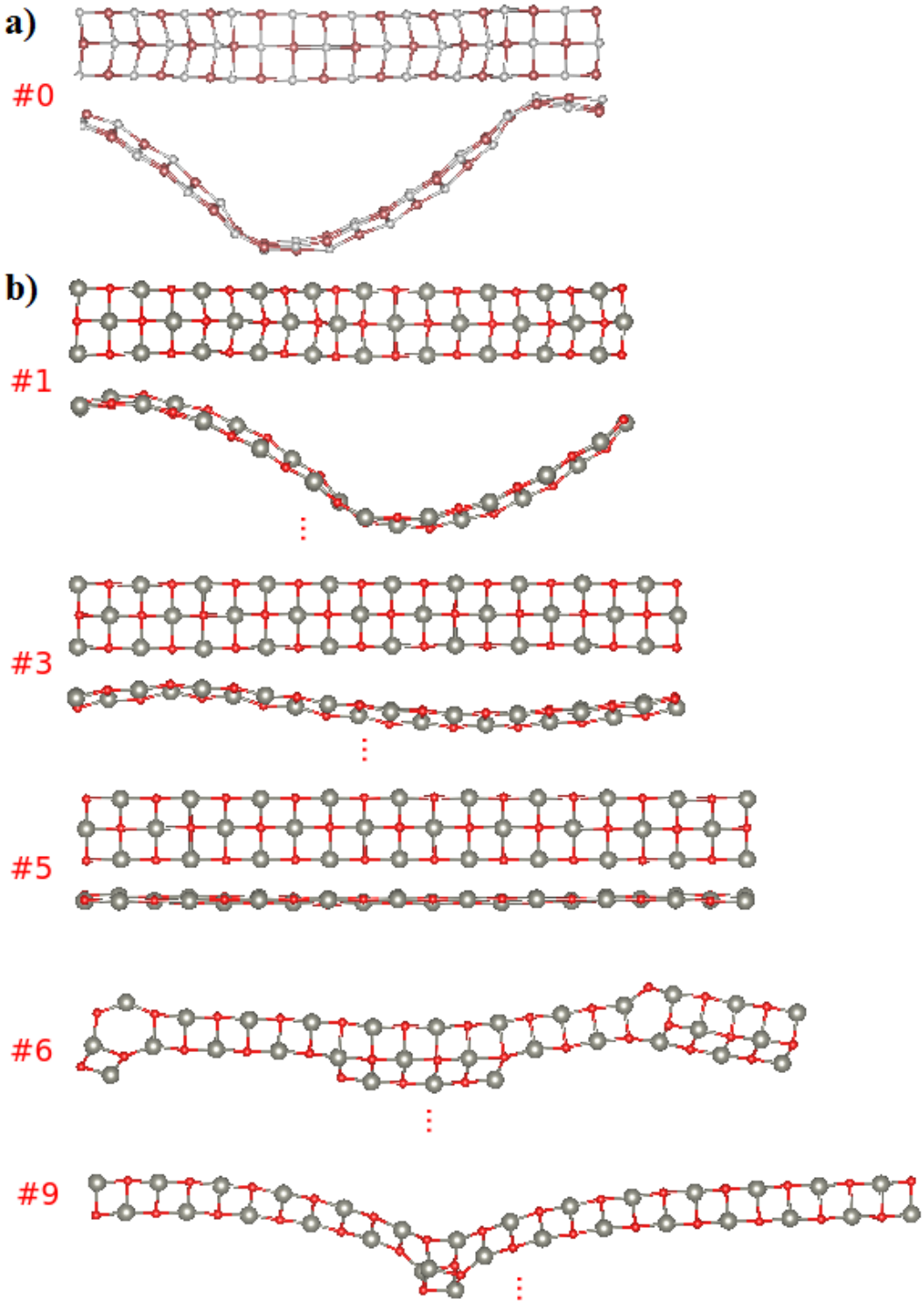

Figure 3.44 a) The Z2L model with PBC at 300 K. b) The same model under 5% tensile strain application at 300 K.

3.2.1.1.2 Armchair Nanoribbons

After the relaxation, the ends of the A1L model structure at 1 K kept its hexagons while the other part completely configured with square grid geometry with NoPBC. However, the same model at 300 K did not maintain its ribbon structure with NoPBC. So one end of the structure appeared amorphous like whereas the other end appeared ribbon like structure (see Figure 3.45). In the case of PBC, the same model at 1 K retained its honeycomb ribbon structure, but appeared as a slightly wavy structure when viewed from the side (Figure 3.46 a). In addition, when subject to 5% tensile strain, the structure preserved its initial structure in the first three tensile strain steps. Then, the structure was also broken into two parts at 4^{th} tensile strain step (see Figure 3.46 b). On the other hand, the same model at 300 K maintained its ribbon structure with PBC, but completely arranged with square grid geometry (Figure 3.47 a). Additionally, when subject to 5% tensile strain, the square net structure did not change in the first two tensile strain steps. Then, the neck points appeared in the structure at 3^{rd} tensile strain step. After the following strain applications, the ribbon transformed into atom chain formation (see Figure 3.47 b).

After the relaxation, the A2L model structure at 1 K changed from ribbon into ring like structure when PBC was not applied, and configured with square grid geometry. However, the same model at 300 K turned into a weapon like structure without PBC, which dominantly configured with square grid geometry (see Figure 3.48). In the case of PBC, the A2L model at 1 K preserved its initial honeycomb ribbon structure with PBC, but appeared as a slightly wavy ribbon when viewed from the side (see Figure 3.49 a). Furthermore, when subject to 5% tensile strain, the perfect honeycomb ribbon structure was observed at 1^{st} tensile strain step, so a wavy view disappeared. After a few strain applications, the structure changed from 2L into 1L ribbon with square geometry. Then, both neck points and atom chain formation were observed in the structure (see Figure 3.49 b). Similarly, the same model at 300 K exhibited similar properties to that of 1 K (see Figure 3.50).

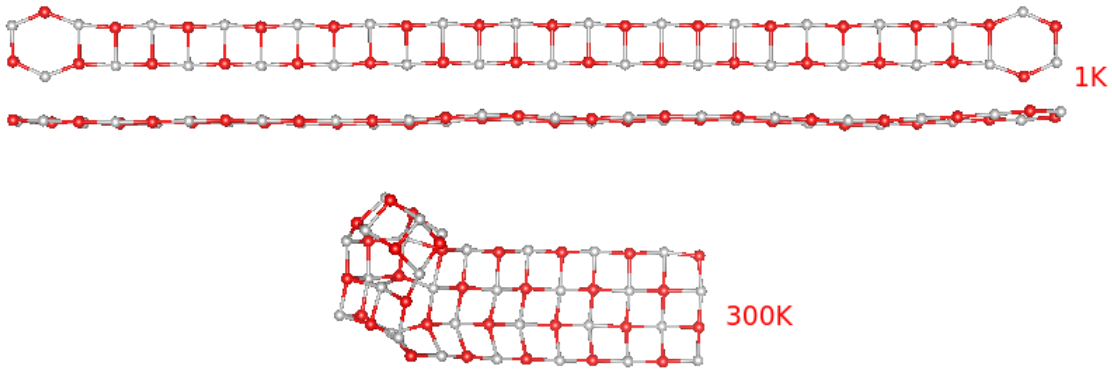

Figure 3.45 The A1L model with NoPBC, the top figure for at 1 K with top and side view, the bottom at 300 K.

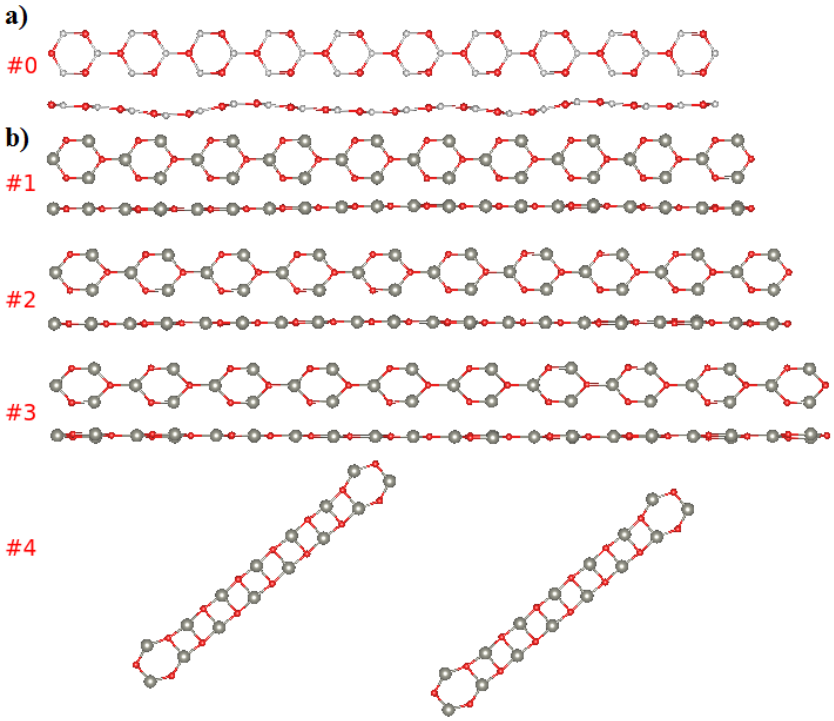

Figure 3.46 a) The A1L model with PBC at 1 K. b) The same model under 5% tensile strain at 1 K.

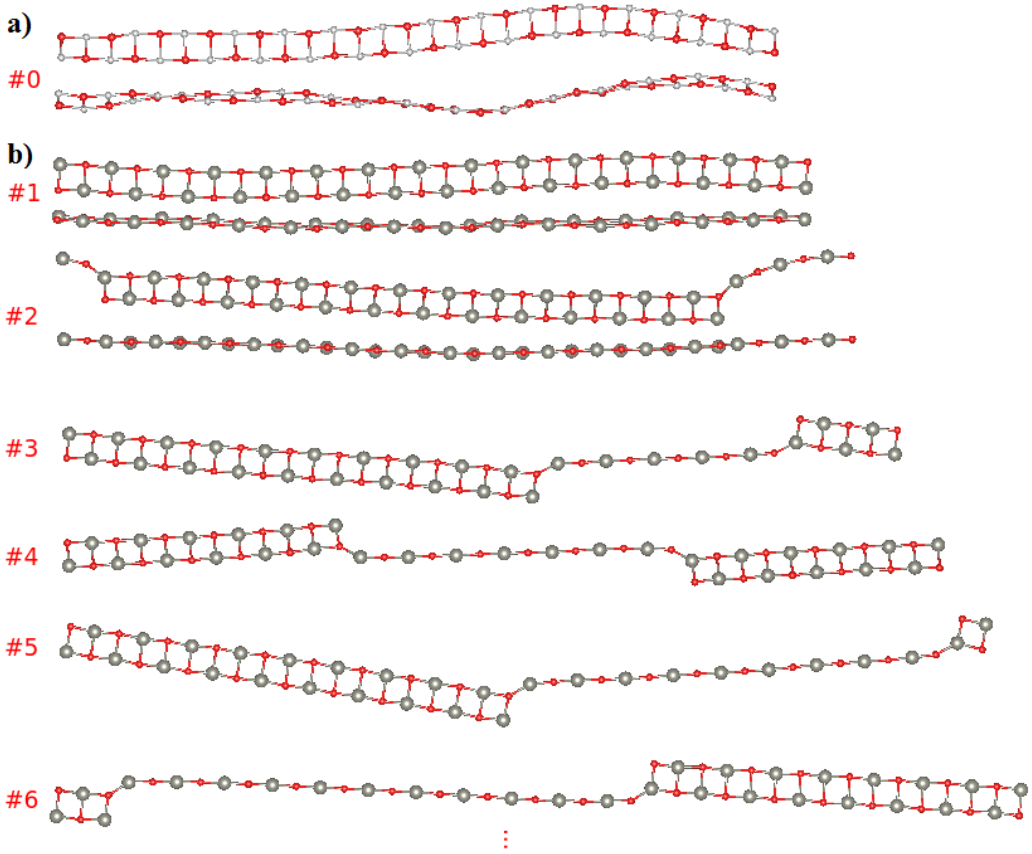

Figure 3.47 a) The A1L model with PBC at 300 K b) The same model under 5% tensile strain at 300 K.

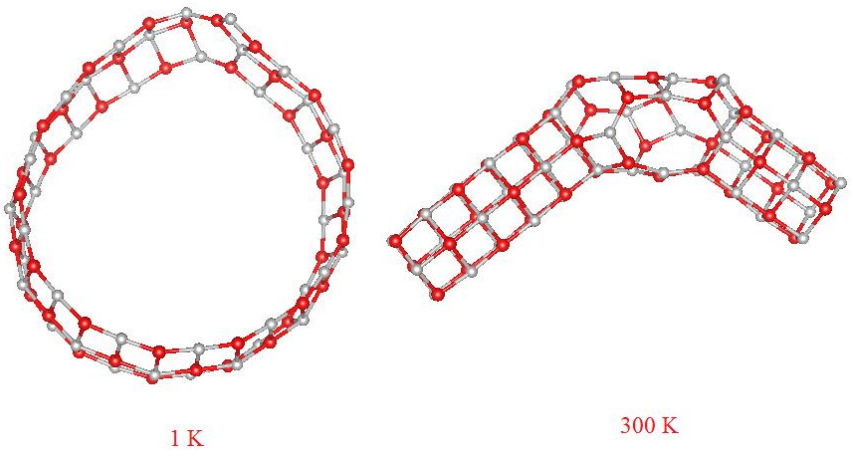

Figure 3.48 The A2L model with NoPBC, the left figure for at 1 K, the right figure at 300 K.

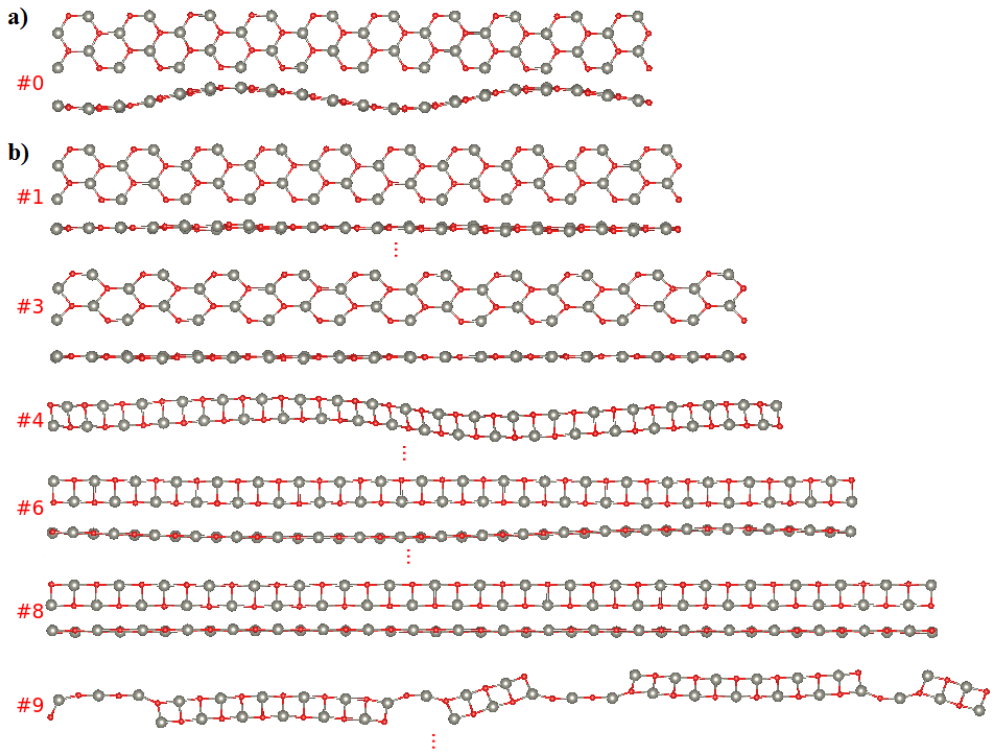

Figure 3.49 a) The A2L model with PBC at 1 K b) The same model under 5% tensile strain application at 1 K.

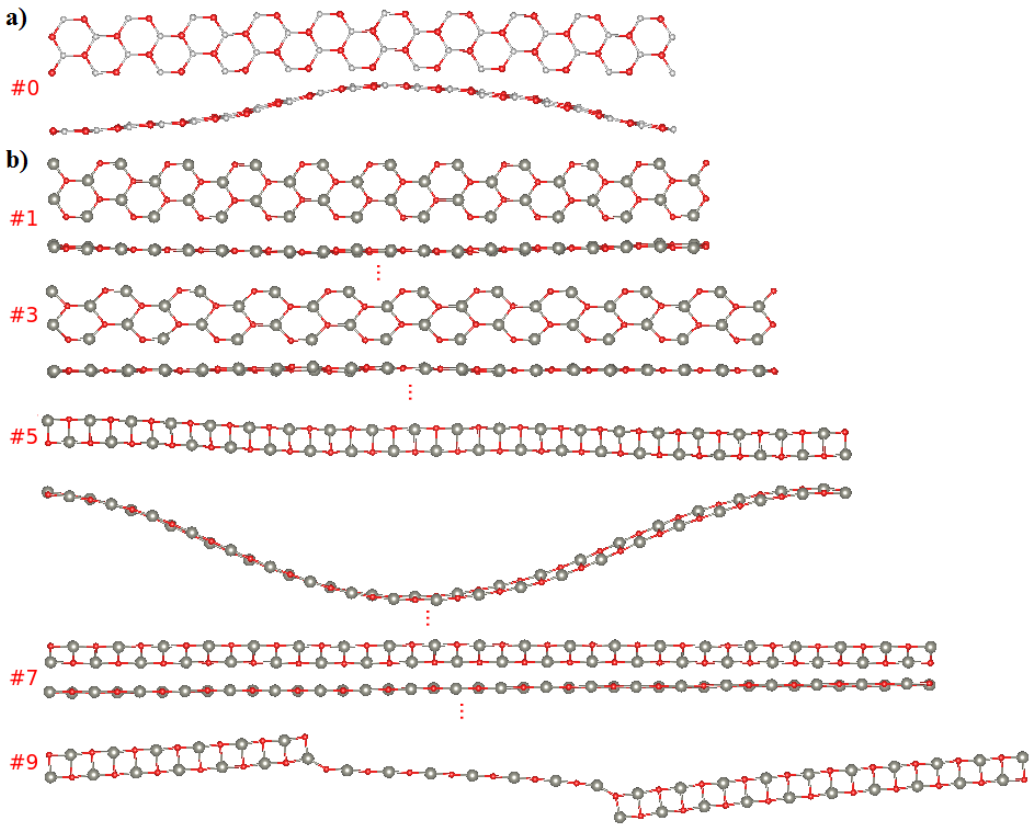

Figure 3.50 a) The A2L model with PBC at 300 K. b) The same model under 5% tensile strain application at 300 K.

3.2.1.2 Defected Nanoribbons

3.2.1.2.1 Zigzag Nanoribbons

3.2.1.2.1.1 Central Defect Zigzag Nanoribbons

After the energetic relaxation process, the ZCDVZn defect model at 1 K was completely arranged with square grid geometry when the PBC was not applied[11]. Moreover, three holes consisted of around the defect site relatively squares. In addition, the ribbon was stretched along x-axis, appeared as a wavy like when viewed from the side. However, the same model at 300 K was also arranged with square grid geometry, including a rectangular hole in the central region of the structure. In addition, the structure bended toward out of plane (see Figure 3.51). In the presences of the PBC, the ZCDVZn model at 1 K did not maintain its ideal defect ribbon, and the whole structure configured with a square grid geometry, and the structure appeared as wavy view from the side. Additionally, some atoms of the structure took place out of plane. Moreover, when subject to 5% tensile strain, it still maintained both mostly monolayer and the atoms replacing out of plane the first three tensile strain steps, not including the ideal vacancy in the central region. Then, the whole structure evolved into completely a monolayer sheet structure, and including a rectangular hole in central region at 4^{th} tensile strain step. Then, the edge defects were detected, and the rectangular hole disappeared in the structure at 5^{th} tensile strain step. Moreover, the width of the ribbon was decreased during the tensile strain steps (see Figure 3.52 a). However, the same model at 300 K looked like similarly in that of 1 K with PBC. Moreover, the structure did not maintaine its monolayer sheet structure under tensile strain. That is, the ribbon was appeared as a scissor-like structure. However, when subject to 5% tensile strain at 300 K, the structure mostly changed into 3D, so the ribbon shape disappeared (see Figure 3.52 b).

After the relaxation process, the ZDCVO model at 1 K mostly kept its monolayer, but including both one rod and edge defects when PBC was not applied. However, the same model at 300 K changed into 3D with NoPBC (see Figure 3.53). In the presences of PBC, the ZCDVO model consisted of holes in the defect site, and

the whole structure configured with square grid geometry at 1 K. In addition, the structure was appeared as bending from the side view. Moreover, when subject to 5% tensile strain, the same model consisted of a bended monolayer structure with completely square geometry, and including three holes in the defect site in the first three tensile strain steps. Then, the out of plane shape of the structure disappeared at 4^{th} tensile strain step, and detected a hole in the central region. Then, the holes disappeared in the central region, and the width of the structure was decreased (see Figure 3.54 a). On the other hand, the same model at 300 K in the presences of PBC disappeared vacancy in the central of the structure, consisted of some defects in the edge of the structure. When subject to 5% tensile strain, the structure maintained the defects in the first two tensile strain steps, and including a hole appeared in the central region of the structure at 3^{nd} and 4^{th} tensile strain steps. Then, the hole disappeared at 5^{th} tensile strain step, but appeared some defects in the edges of the structure (see Figure 3.54 b).

After the relaxation process, the ZCDVZnO model at 1 K changed from 2D into 3D when PBC was not applied. The ends of 3D structure configured with hexagons while the others configured squares when viewed from the side. However, the same model at 300 K retained a wavy like monolayer ribbon structure with completely square geometry, and consisted of a rectangular hole in central region with NoPBC (see Figure 3.55 a). The width length of the structure was decreased whereas the length of the structure was increased. On the other hand, the ZCDVZnO model, in the presences of PBC, mostly retained its monolayer ribbon with completely squares at 1 K, but forming bending like. However, the bilayers took place in the middle of the structure at 300 K with PBC (Figure 3.55 b). We did not need to apply the strain applications for that model.

After the relaxation process the ZCDEXZnO defect model at both 1 and 300 K changed into defect free ribbon with completely square grid geometry when PBC was not applied, but appeared as a wavy like from the side view at both 1 and 300 K. That is, the exchange defect disappeared in this conditions (Figure 3.56 a). On the other hand, the same model consisted of two rod-like (facet-like) structures at both temperature runs, whereas at 300 K each rod of the structure moved along the PBC (Figure 3.56 b).

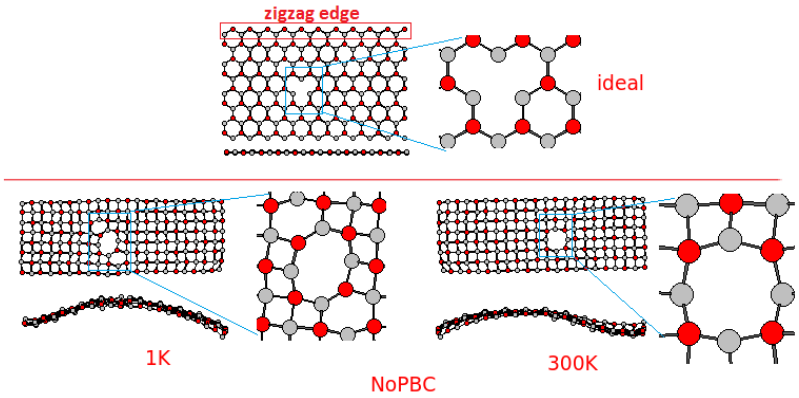

Figure 3.51 The ZCDVZn model, the top figure for ideal structure, the bottom figures for with NoPBC (the left bottom for at 1 K, the right bottom for at 300 K).

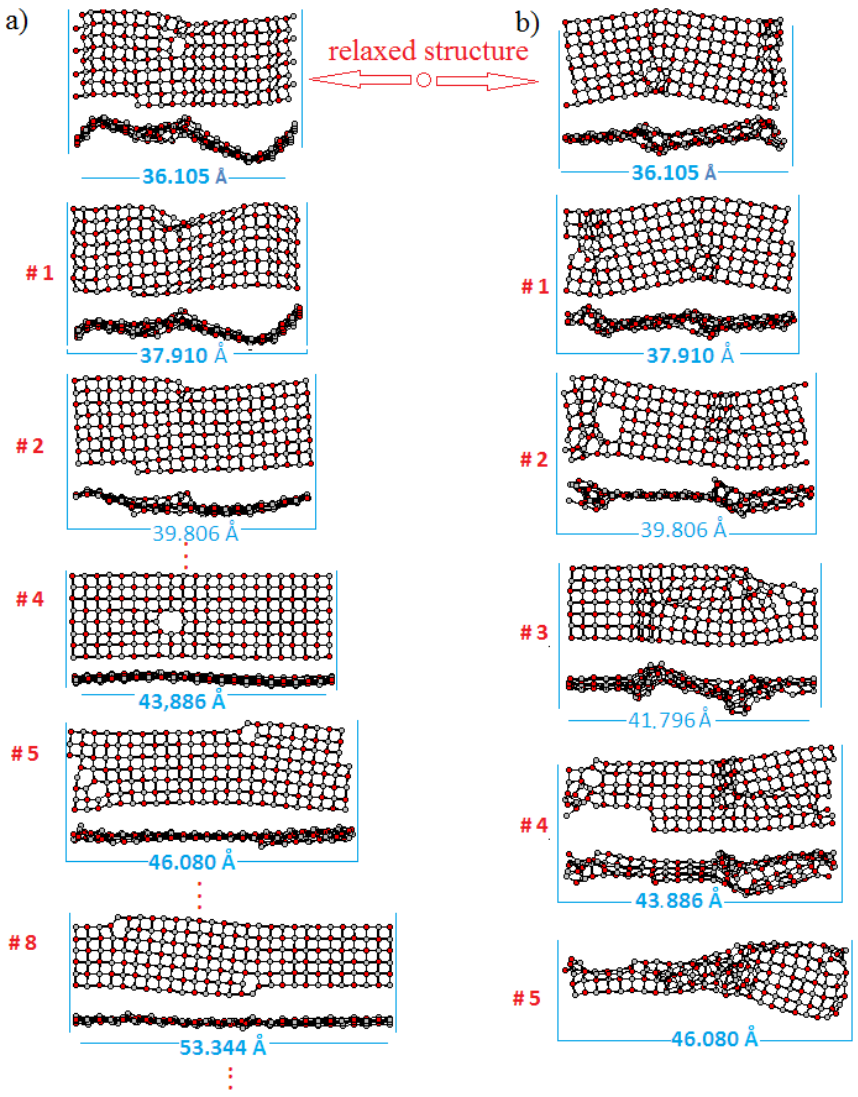

Figure 3.52 The ZCDVZn model under 5% tensile strain a) at 1 K b) at 300 K.

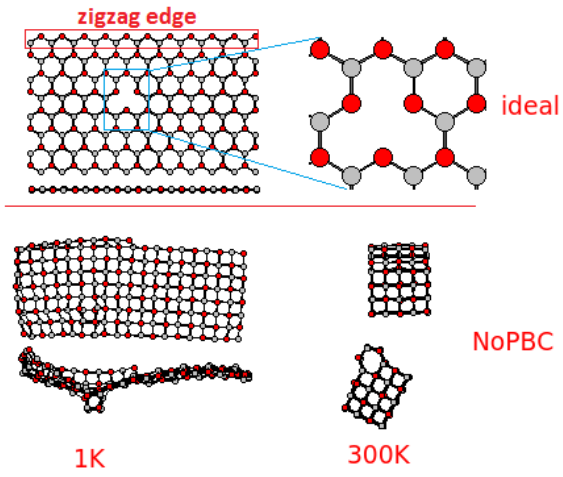

Figure 3.53 The ZCDVO model, the top figure for ideal and the bottom figures for with NoPBC, the left bottom figures for at 1 K at top and side views, the right bottom figures for at 300 K.

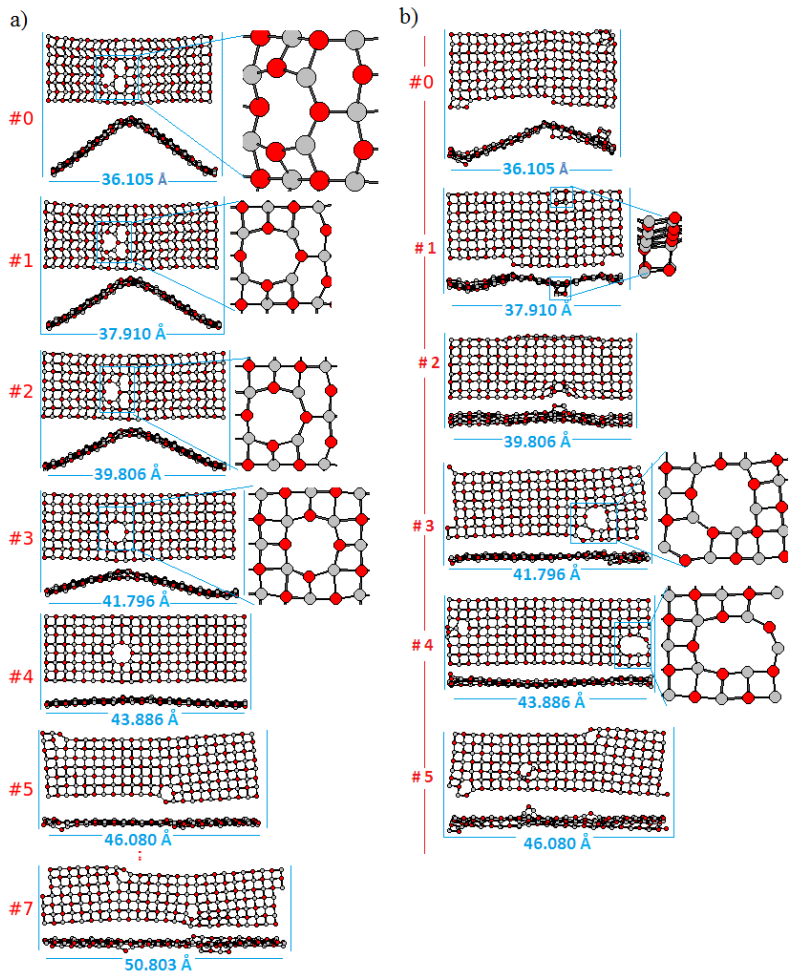

Figure 3.54 The ZCDVO model under 5% tensile strain a) at 1 K b) at 300 K.

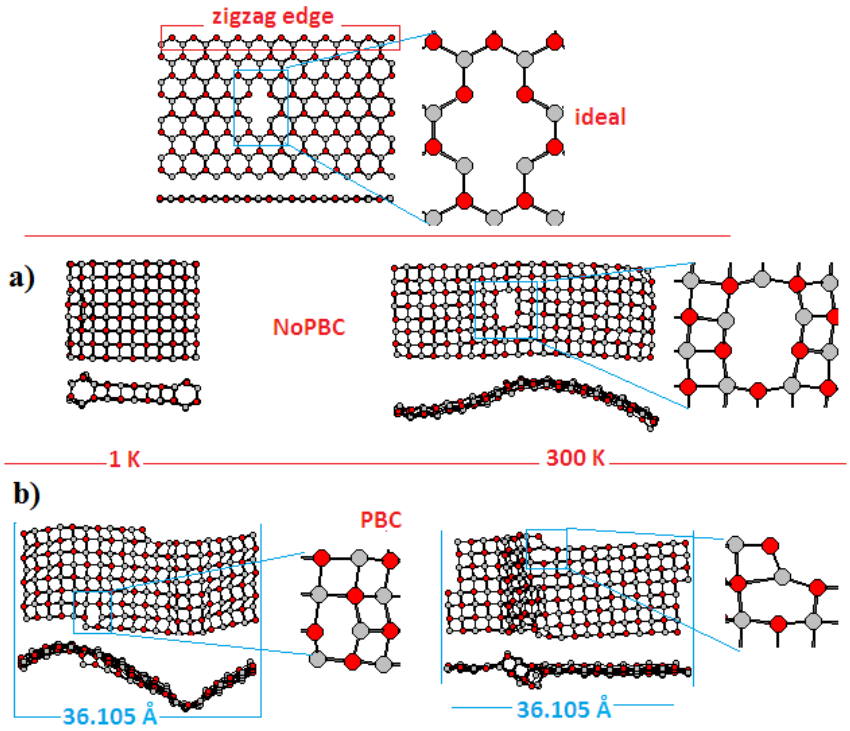

Figure 3.55 The ZCDVZnO model at 1 K and 300 K a) with NoPBC b) with PBC.

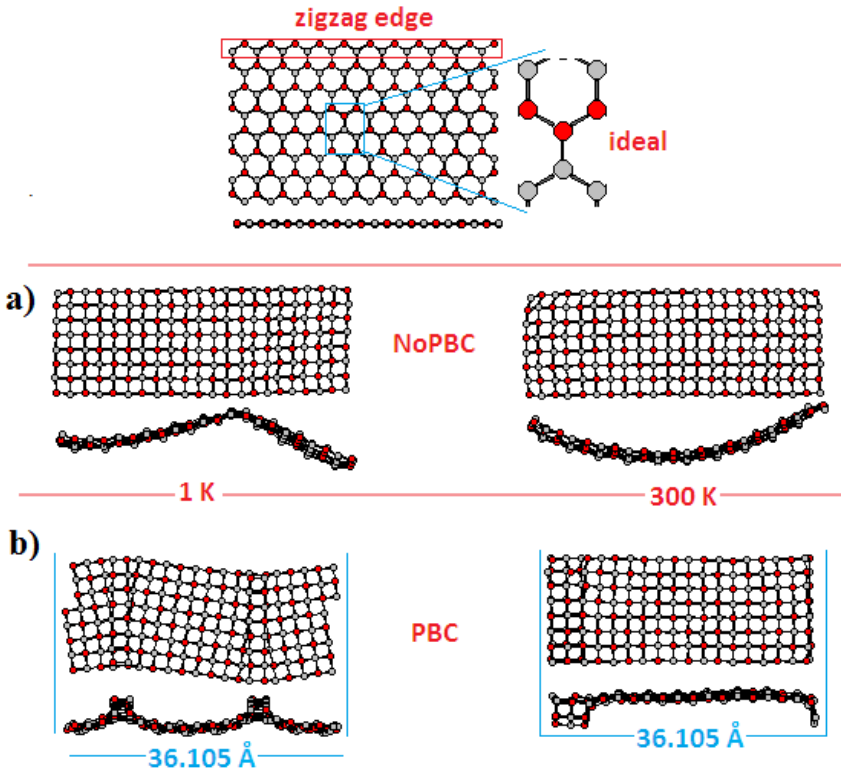

Figure 3.56 The ZCDEXZnO model at 1 and 300 K a) with NoPBC b) with PBC.

3.2.1.2.1.2 Edge Defect Zigzag Nanoribbons

The ZEDVZn model structure, after the relaxation process, kept its monolayer ribbon structure but viewed out of plane form from the side at both 1 and 300 K when PBC was not applied. Moreover, the length of the structure was extended along the PBC direction and the structure completely configured with square grid geometry. Additionally, the vacancy was also appeared in the defect site at 1 K, whereas the hole appeared in the same place at 300 K (see Figure 3.57). In the case of presences of PBC, the ZEDVZn model consisted of a hole in the defect site, and forming completely square grid geometry. Interestingly, the structure was bended in two places when viewed from the side with PBC at 1 K. In the case of 5% tensile strain applications, the hole in the defect site and the square grid geometry in the structure did not change in the first three tensile strain steps. Then, the bending appearance in the structure changed into a flat structure and one hexagon in addition to the vacancy took place in the defect site when viewed from the side at 4^{th} tensile strain step. Then, the defects in the edges of the ribbon were detected at 5^{th} tensile strain step. During the strain applications, the length of the structure increased whereas the width of the structure decreased. In other words, the layer of the ribbon was decreased during the tensile strain steps (see Figure 3.58 a). However, the same model at 300 K with PBC did not retain its monolayer ribbon structure. The middle part of the structure was amorphed, and completely forming with square grid geometry. In the case of 5% the strain at 300 K, the face like shape on the structure was detected and configured with completely square grid geometry at 1^{st} tensile strain step. Then, the facet like shape was disappeared but the edge defects were formed in the structure at 4^{th} tensile strain step (see Figure 3.58 b).

The ZEDVO model, after the energetic relaxation, mostly maintained its monolayer ribbon, but the structure bended and the grid geometry changed into completely squares and when PBC was not applied at 1 K. In addition to the vacancy, some atoms in which the edge part of defect site took place out of plane. However, the same model at 300 K changed into 3D structure with NoPBC (see Figure 3.59). In the case of the present PBC, the model consisted of two rod like structures (facet-like) with square grid geometry when PBC was applied at 1 K. In the case of 5% tensile

strain applications, the facet like structure in the model maintained and consisted of hexagons and holes in the structure at 1st tensile strain step. At 2nd tensile strain step, the two rods disappeared in the structure and the atoms around the defect site slightly was tilted. Additionally, the structure was appeared as a bended structure when viewed from the side. Then, after a few strain applications the width of the structure was decreased and formed defects in the edges (see Figure 3.60 a). In the case of PBC at 300 K, the same model also maintained its monolayer structure, but consisted of square grid geometry and including two rod like (facet like). Furthermore, the width of the structure was decreased during the following applications of strain (Figure 3.60 b).

The divacancy of the ZEDVZnO model in the absence of PBC at 1 K disappeared, and the grid geometry changed into squares in addition to consisted of two rod (facet like). However, the same model completely changed into 3D structure with NoPBC at 300 K (see Figure 3.61 a). In the case of PBC, the divacancy of the structure also disappeared and configured with square grid geometry and facet like structure took place at both 1 and 300 K (see Figure 3.61 b)

The ZEDEXZnO defect model changed into defect free structure, but configured with square grid geometry with NoPBC at both 1 and 300 K. Moreover, the structures at 1 and 300 K were appeared as a slightly bended structure when viewed from the side (see Figure 3.62).

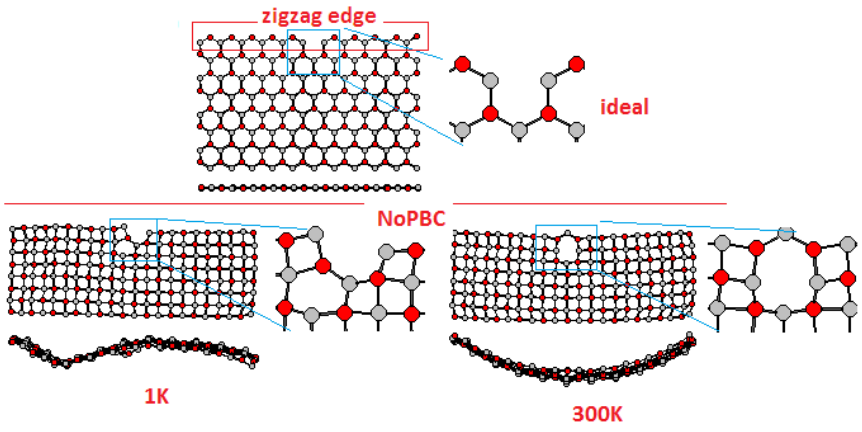

Figure 3.57 The ZEDVZn model with NoPBC at 1 and 300 K.

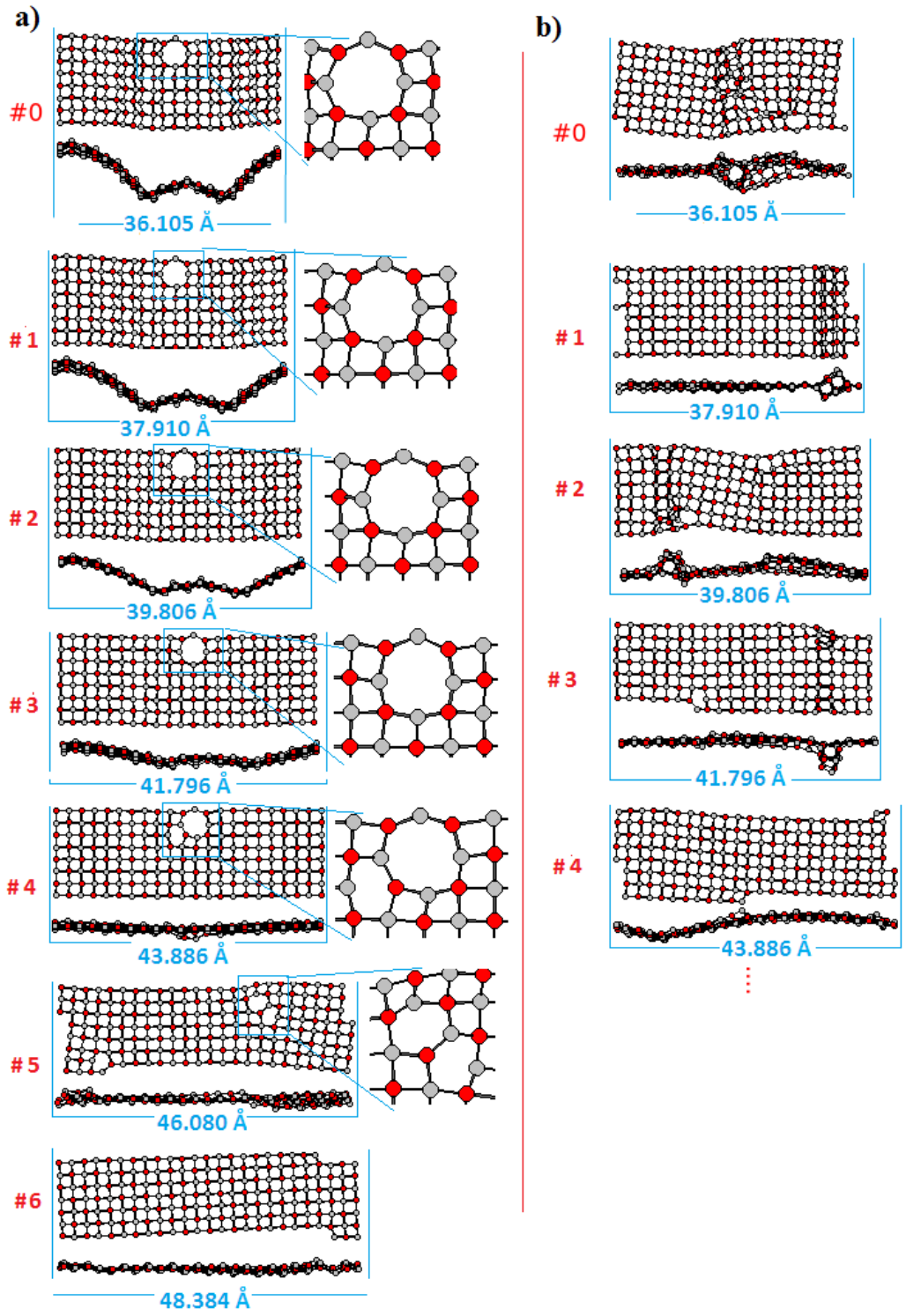

Figure 3.58 The ZEDVZn model under 5% tensile strain applications a) at 1 K b) at 300 K.

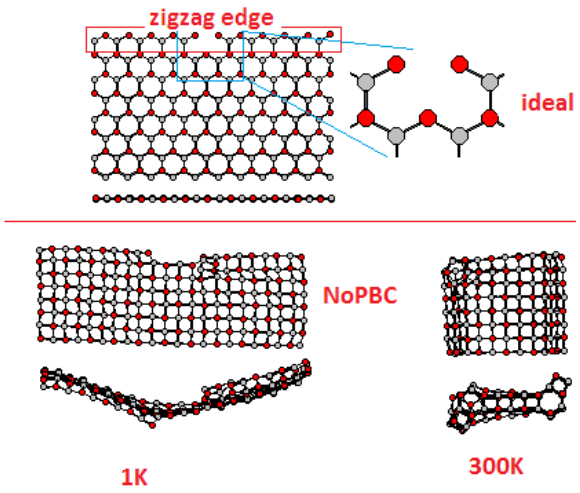

Figure 3.59 The ZEDVO model with NoPBC at 1 and 300 K.

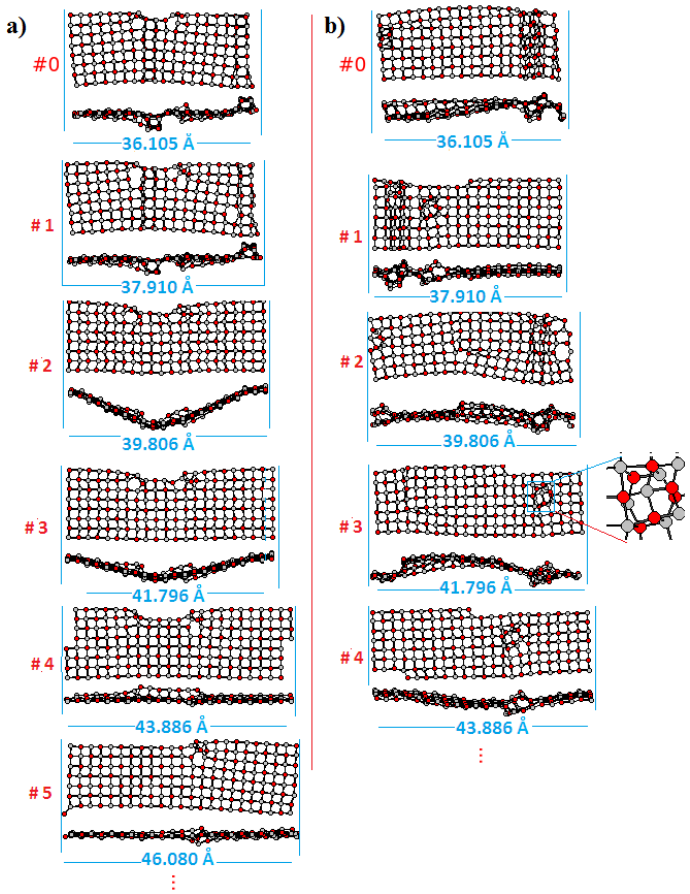

Figure 3.60 The ZEDVO model under 5% tensile strain applications a) at 1 K b) at 300 K.

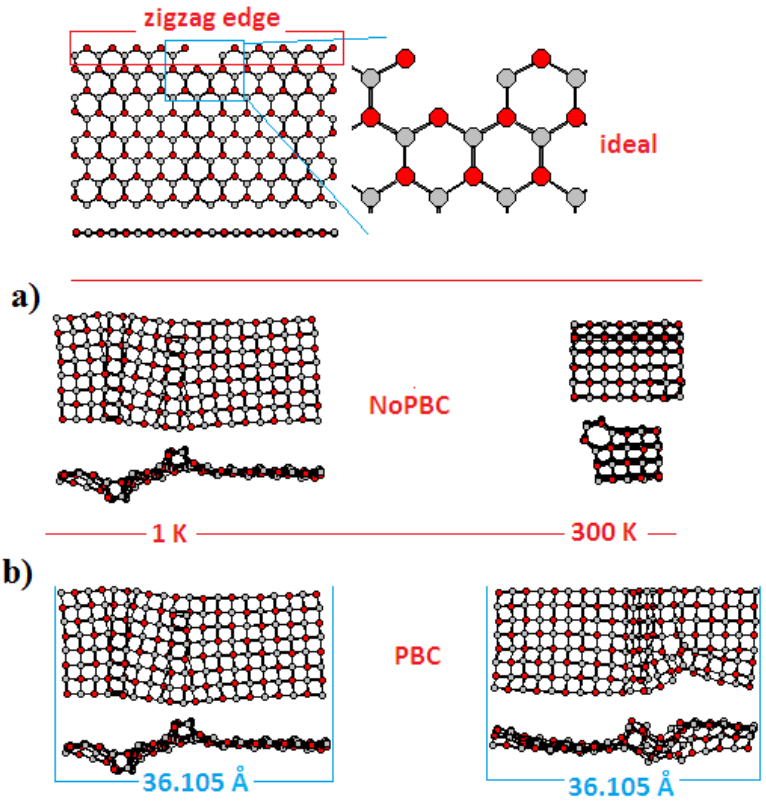

Figure 3.61 The ZEDVZnO model at 1 and 300 K a) with NoPBC b) with PBC.

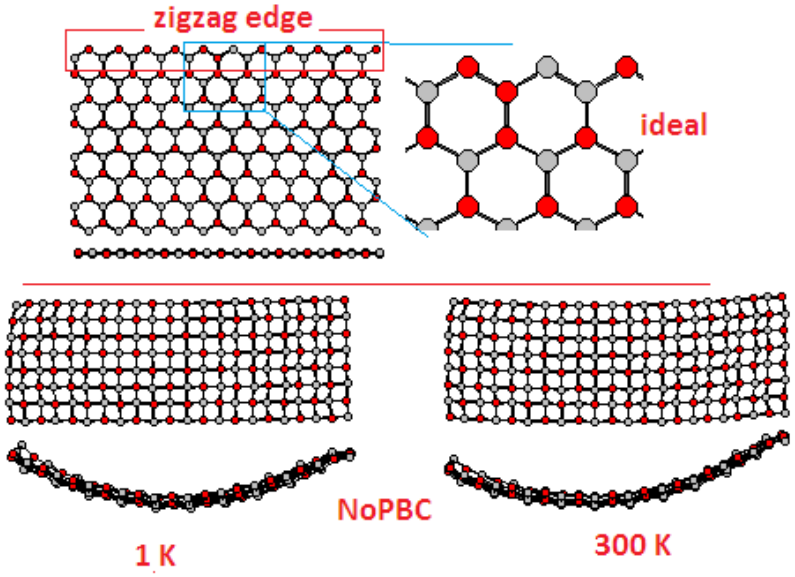

Figure 3.62 The ZEDEXZnO model with NoPBC at 1 and 300 K.

3.2.1.2.2 Armchair Nanoribbons

3.2.1.2.2.1 Central Defect Armchair Nanoribbons

After the relaxation process, the ACDVZn model at 1 K did not retain its ideal defect structure, and arranged with completely square grid geometry when PBC was not applied. The vacancy was disappeared whereas the edge defects were detected, and the some atoms migrated toward to the vacancy site. However, the same model at 300 K retained its monolayer ribbon, but the model both changed into square structure and configured with square grid geometry and consisted of a hole in the defect site (see Figure 3.63). In the case of PBC, the ACDVZn model at 1 K preserved its ideal vacancy type honeycomb structure, but appeared as a wavy like when viewed from the side. In addition, when subject to 5% tensile strain, the structure at 1 K maintained its ideal relaxed structure, but a wavy view disappeared in the first three tensile strain steps. Then, the structure broken into two part, which configured hexagonal grid geometry at 5^{th} tensile strain step (see Figure 3.64 a). On the other hand, the ACDVZn model at 300 K, when PBC was applied, also maintained its ideal vacancy type structure, but the vacancy site moved along the PBC direction. Furthermore, when subject to 5% tensile strain, the structure at 300 K retained its initial structure, but the defect site also moved along the PBC direction because of the effect of the temperature. At the 2^{nd} and 3^{rd} tensile strain step, the squares were detected around the vacancy site. At 4^{th} tensile strain step, the structure fragmented (see Figure 3.64 b).

After the relaxation process, the ACDVO model at 1 K was tilted backwards from the defected site when PBC was not applied. So the structure looked like a bird like from the side view. However, the same structure at 300 K changed into 3D in the absences of PBC (see Figure 3.65). In the presences of PBC, the same model retained its ideal defect structure, but some hexagons around the vacancy transformed into squares at both 1 and 300 K. In addition, the temperature lead to move the defect site along the PBC direction at 300 K. When subjected to a 5% tensile strain, the structure maintained its initial structure, but the squares still appeared around the vacancy site in the first three tensile strain step. Then, the structure was broken into two parts through the vacancy at the 5^{th} tensile strain step (see Figure 3.66 a). However, the

structure at 300 K looked like similarity in that of strained 1 K when the strain was applied (see Figure 3.66 b).

After the relaxation process, the ACDVZnO model did not preserve its ideal defect ribbon structure, but configured with completely square grid geometry both at 1 and 300 K in the absences of PBC. Furthermore, the structure bent downward and upward with respect to the vacancy site at 300 K (see Figure 3.67). In the presence of PBC, the same model retained its ideal defect type structure at 1 K, but revealed as a wavy structure when viewed from the side. In addition, one side of the vacancy bent upward while the other side bent downward. When the strain was applied, the structure at 1 K maintained its relaxed structure in the first three consecutive applications of the tensile strain steps. The neck points were detected in the vacancy site at the 4^{th} tensile strain step. Then, the structure was separated into two parts through the vacancy site. Following the excessive tensile strain steps, the vacancy appearance changed into as an elliptical shape (see Figure 3.68 a). In the presences of PBC, on the other hand, the same model at 300 K also retained its ideal defect structure, but the defect site moved due to the effect of temperature. When subjected to 5% tensile strain, the structure exhibited similar features to that of the 1 K run, but the vacancy site moved along the PBC direction during the further tensile strain step applications. Moreover, under excessive tensile strain step applications, the vacancy changed into an elliptical shape at 300 K (Figure 3.68 b).

The ACDEXZnO model structure at 1 K, after the relaxation process, did not maintain its ideal defect ribbon structure and hexagonal grid geometry changed into squares when PBC was not applied. In addition, the atoms around the defect site migrated towards into defect site. However, the same model at 300 K changed into 3D with completely square grid geometry when PBC was not applied. In the presences of PBC, the ACDEXZnO model structure mostly retained its ideal defect ribbon, but the defected pair atoms moved into left site. Additionally, when subject to 5% tensile strain, the structure retained its relaxed ribbon structure, but the defected atom pairs still kept left site at first two tensile strain step. Then, the structure changed into defect free ribbon structure, so the exchange defect disappeared at 2^{nd} tensile strain step. On the other hand, the ACDEXZnO defect model at 300 K changed into defect free structure when PBC was applied. The defect disappeared at that temperature. The

reason for the reexchange mechanism could be due to the differences in the strength of the interatomic interactions. The PEF used in the present study does not consider the Zn-Zn interactions. On the other hand, the O-O interaction is relatively stronger than the Zn-O interaction, but the equilibrium distance of Zn-O is much shorter than that of O-O. Because the defect model at 300 K with PBC turned into defect free, we did not apply the strain application on the model.

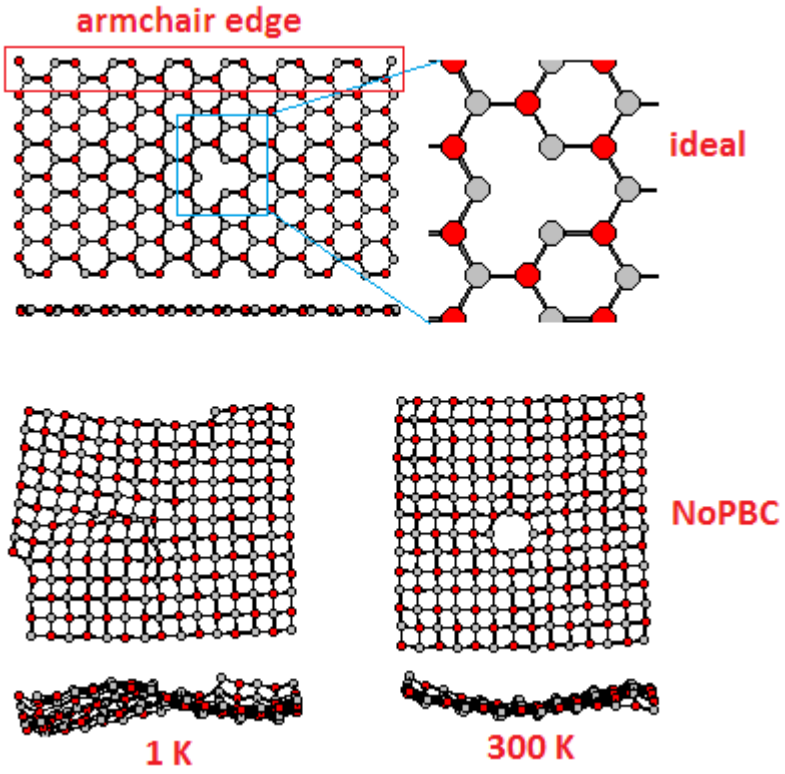

Figure 3.63 The ACDVZn model with NoPBC at 1 and 300 K.

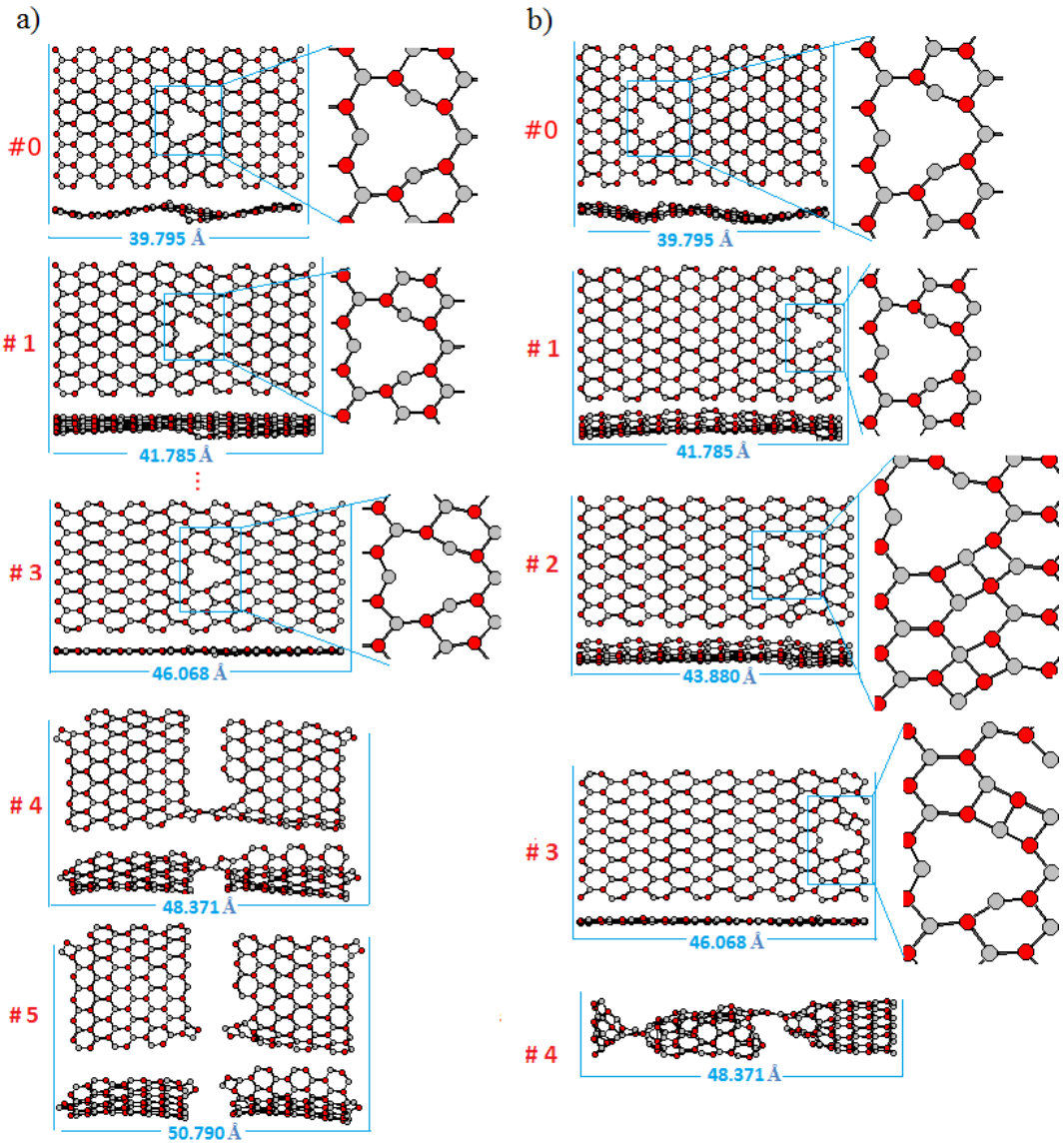

Figure 3.64 The ACDVZn model under 5% tensile strain applications a) at 1 K b) at 300 K.

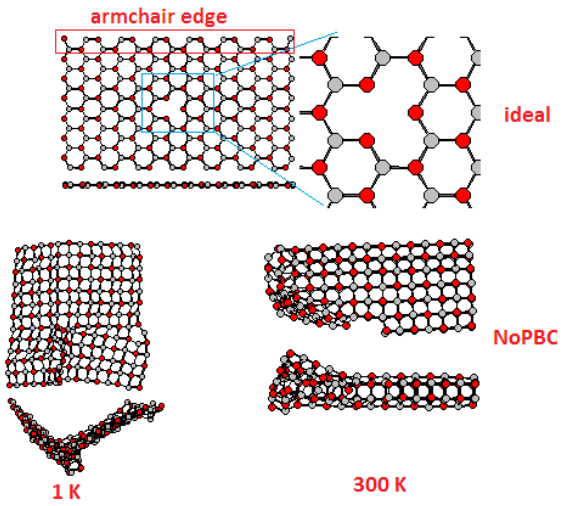

Figure 3.65 The ACDVO model with NoPBC at 1 and 300 K.

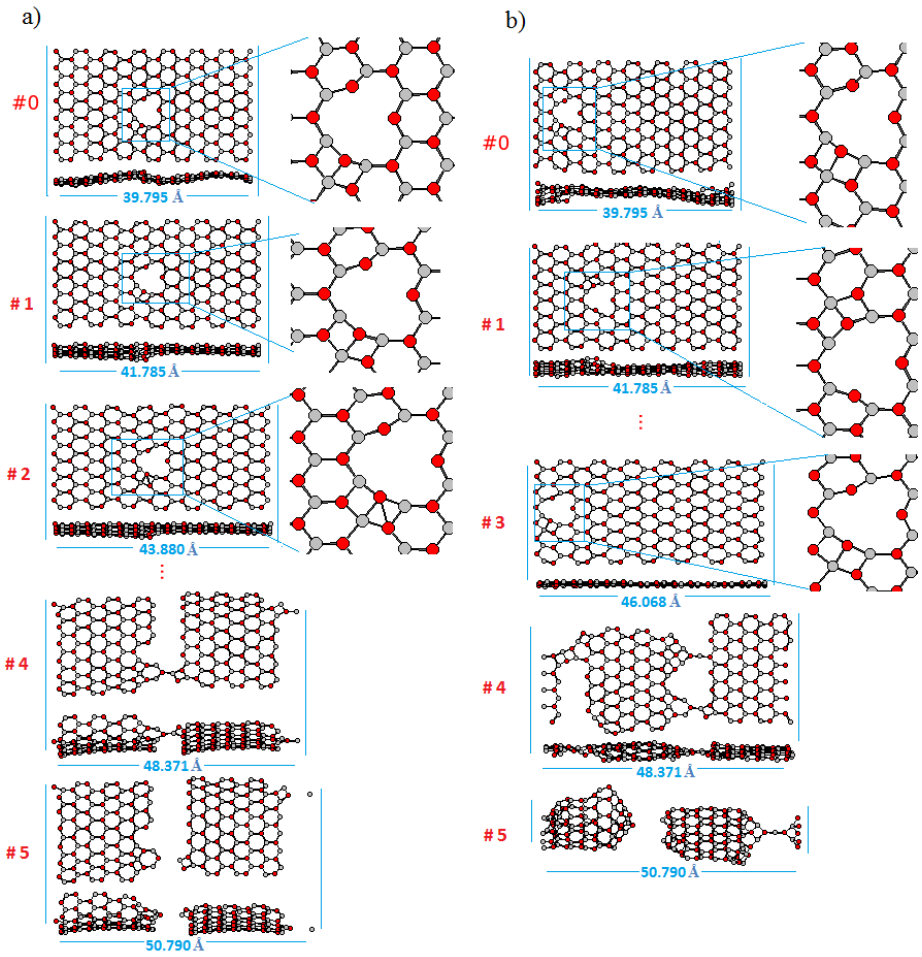

Figure 3.66 The ACDVO model under 5% tensile strain applications a) at 1 K b) at 300 K.

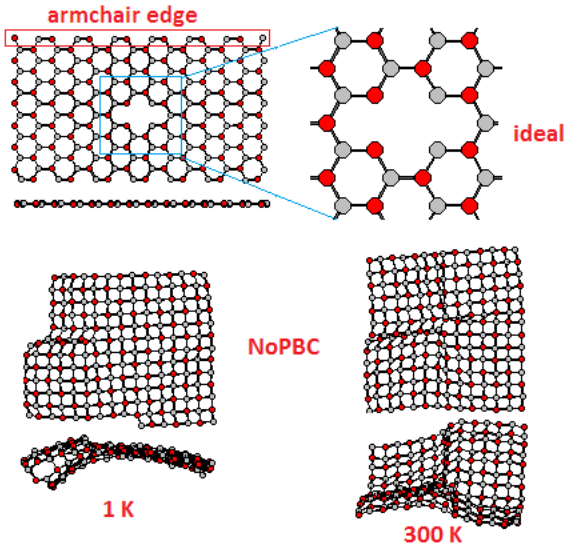

Figure 3.67 The ACDVZnO model, the top figure for ideal and the bottom figures for with NoPBC at 1 and 300 K.

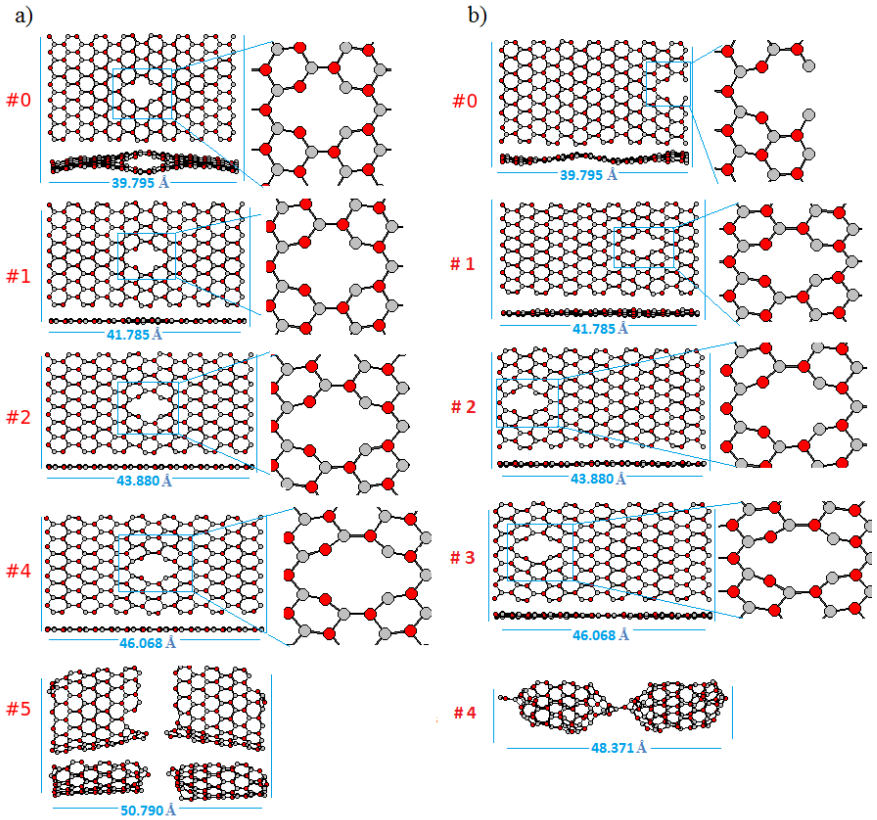

Figure 3.68 The ACDVZnO model under 5% tensile strain applications a) at 1 K b) at 300 K.

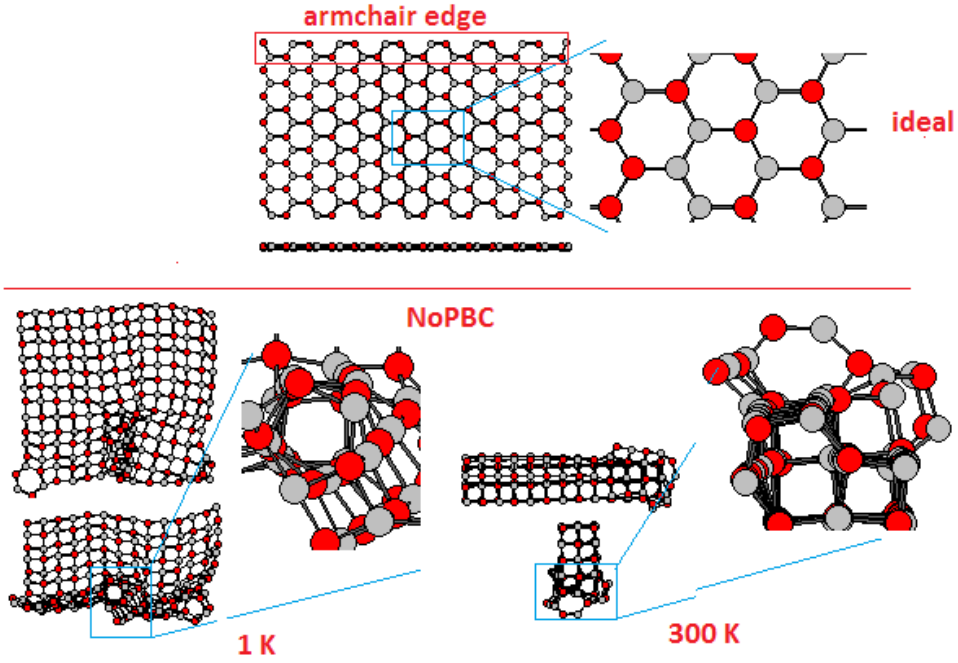

Figure 3.69 The ACDEXZnO model, the top figure for ideal and the bottom figures for with NoPBC at 1 and 300 K.

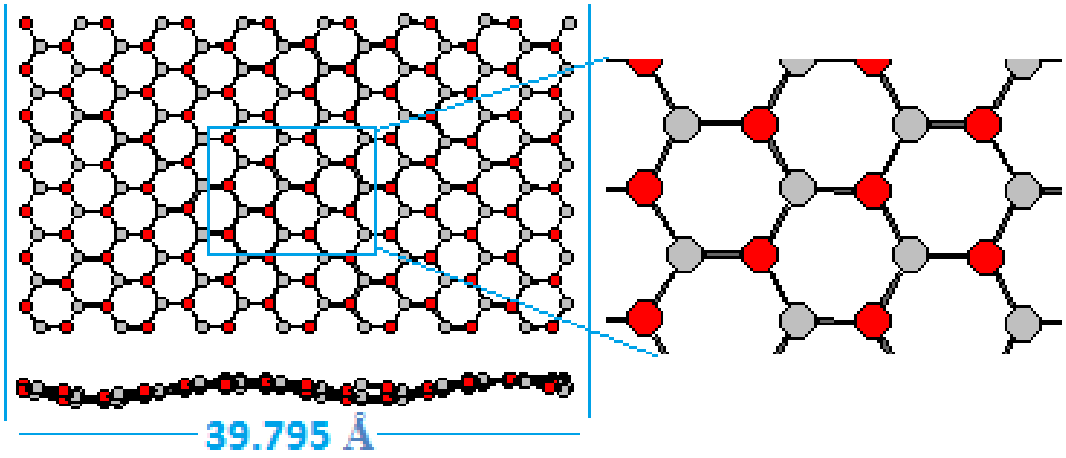

Figure 3.70 The ACDEXZnO model with PBC at 300 K.

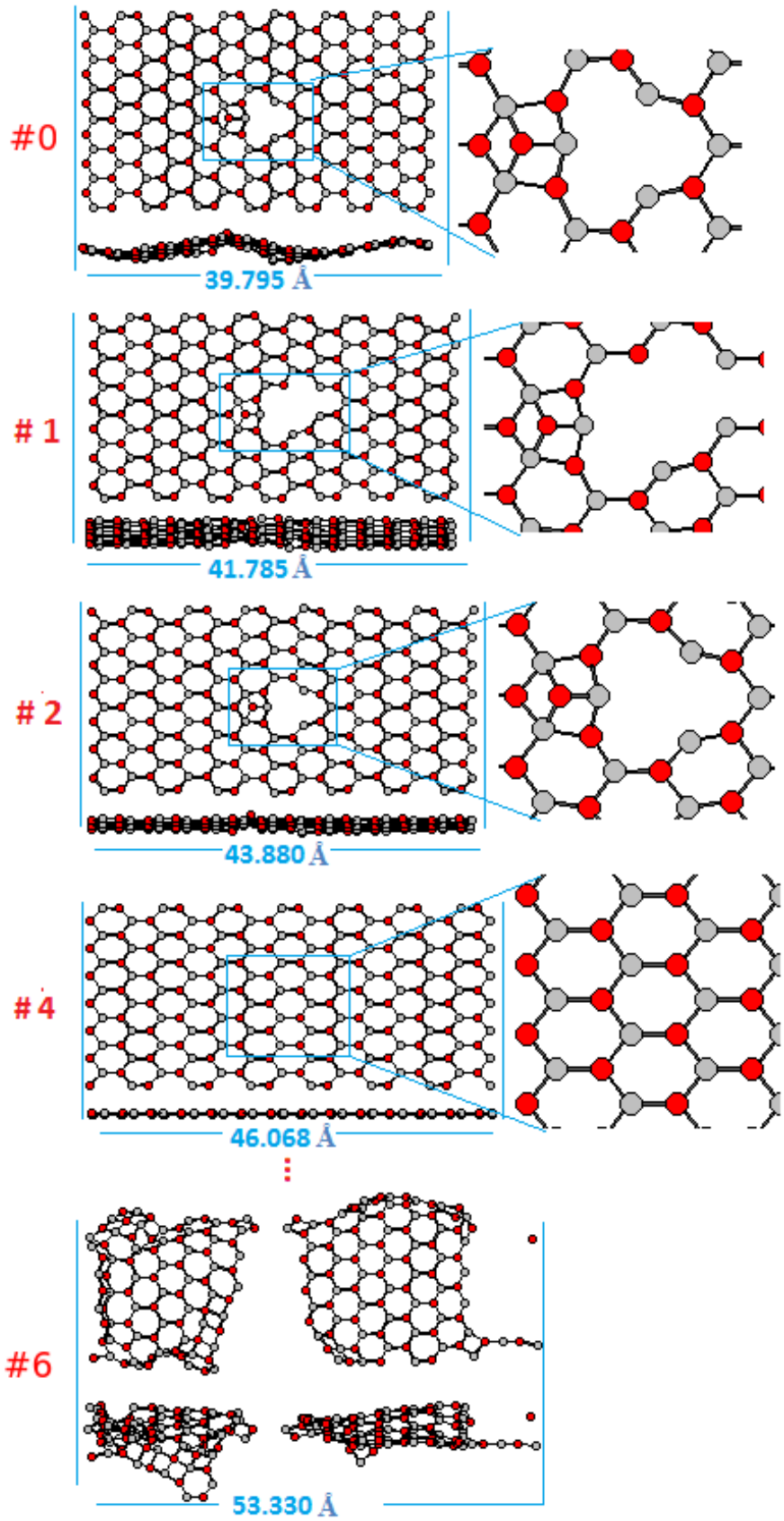

Figure 3.71 The ACDEXZnO model at 1 K under 5% tensile strain.

3.2.1.2.2.2 Edge Defect Armchair Nanoribbons

After energetic relaxation, the AEDVZn model, when PBC was not applied, configured with completely square net geometries except for one at both 1 and 300 K. In addition, the model consisted of the defects in the edges of the structure and the vacancy defected part in the edge was slightly tilted into out of plane (see Figure 3.72). However, the same model mostly maintained its initial defect structure, but viewing a slightly wavy like from the side in addition to including one square around the vacancy site when PBC was applied at 1 K. In the case of 5% tensile strain, the structure preserved its relaxed structure, but the square part, in which one part of the vacancy, moved toward to out of plane at 1 K in the first three tensile strain steps. Then, the structure was separated into two parts through the defect at the 5^{th} tensile strain step (see Figure 3.73 a). The same model at 300 K in both the presences of PBC and 5% tensile strain applications exhibited similarity to that of 1 K. However, the vacancy moved along the PBC direction due to the effect of the temperature (see Figure 3.73 b).

After the relaxation process the AEDVO defect model did not retain its initial structure at 1K when PBC was not applied. The structure consisted of both monolayer and bilayer, and configured with completely squares except for one hexagon in the corner of the structure. However, the same model at 300 K preserved its ribbon structure, viewed slightly bended structure from the side, but configured with completely squares in addition to the edge defects (see Figure 3.74). On the other hand, the model mostly kept its initial structure, but one atom pair nearby to the vacancy site was branched due to being at the edge with PBC at 1 K. In the case of 5% tensile strain applications, the structure maintained its relaxed structure at first three tensile strain steps. Then, the structure separated into two parts through the defect site at 5^{th} tensile strain step (see Figure 3.75 a). In the presences of PBC at 300 K, the same model mostly preserved its initial structure. In addition, some hexagons around the vacancy also transformed into two square geometries and the vacancy site moved along the PBC direction at 300 K. When subjected to strain, the structure kept its relaxed structure during the first three applications of tensile strain steps. One side of the vacancy consisted of the branched atom pair and two square geometries, whereas

the other side included a perfect hexagons during these applications of tensile strain steps. Then, the structure was fragmented into three pieces at the 4th tensile strain step (see Figure 3.75 b).

After the relaxation process, the AEDVZnO model in the absences of PBC at 1 K did not maintain its initial structure, such that the structure was bended upwards from the middle part. Additionally, the structure configured with square grid geometry and the defects took place in the edges of the structure. However, the same model at 300 K appeared as a slightly bended from the vacancy site and the structure configured with square grid geometries without PBC (see Figure 3.76). On the other hand, the model in the case of PBC appeared as perfect ribbon like structure at 1 K, but viewed slightly wavy like. Additionally, the ideal defect site appeared as a V shape. When subject to strain, the structure also preserved its relaxed structure at the first three strain applications. The vacancy depth decreased along each application of tensile strain steps, tending to change into a defect free structure. Then, the structure broke into two parts through the vacancy at the 4th tensile strain step. The model at 300 K also exhibited similar features to that of at1 K run. It is interesting to note that the defect position translate during a long MD run, whether PBC is applied or not. This is a typical characteristic appearing in MD simulations (see Figure 3.77).

After the relaxation process, the AEDEXZnO model changed into a bilayer structure and the structure arranged with square grid geometries at 1 K when PBC was not applied. However, the same model at 300 K changed into defect free structure, but configured with completely squares without PBC at 300 K (see Figure 3.78 a). In the case of PBC, on the other hand, the same model appeared as a perfect ribbon at both 1 and 300 K. In that, the exchange defect type of the structure was disappeared, and viewed a wavy like from the side (see Figure 3.78 b).

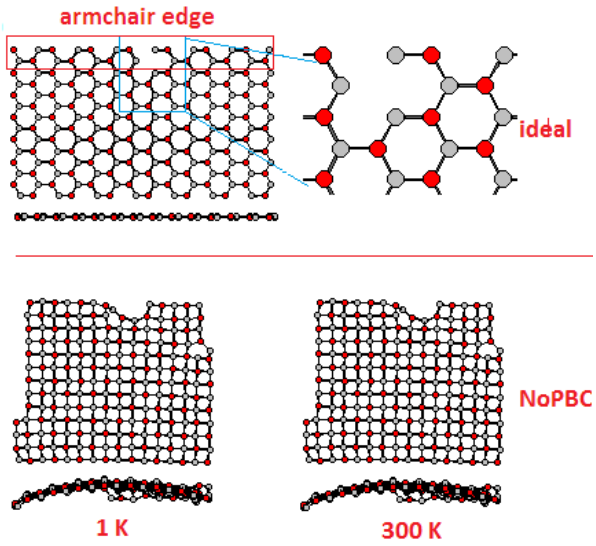

Figure 3.72 The AEDVZn model with NoPBC at 1 and 300 K.

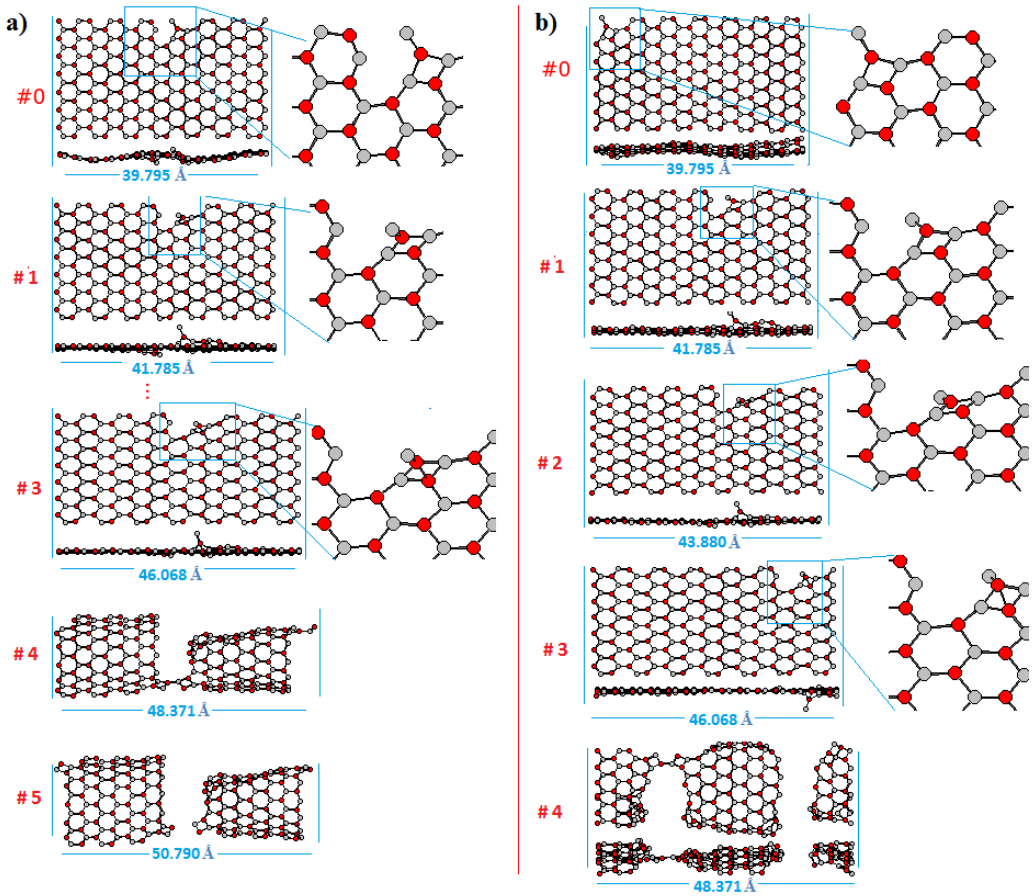

Figure 3.73 The AEDVZn model under 5% tensile strain a) at 1 K b) at 300 K.

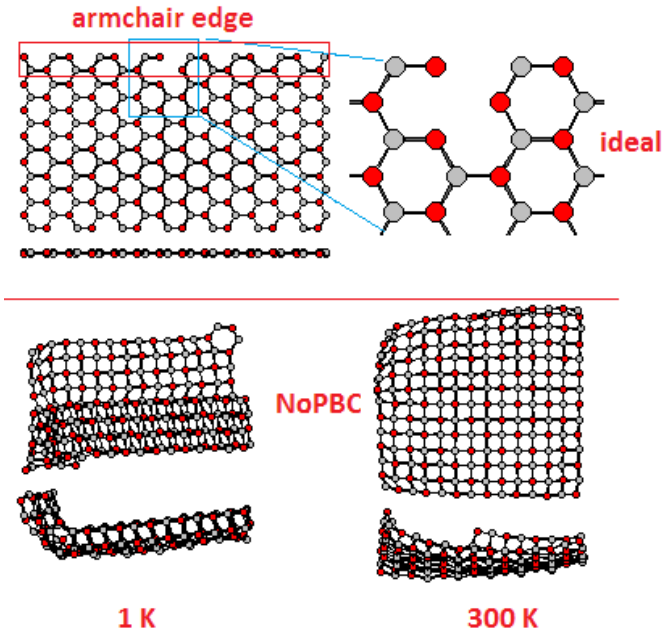

Figure 3.74 The AEDVO with NoPBC at 1 and 300 K.

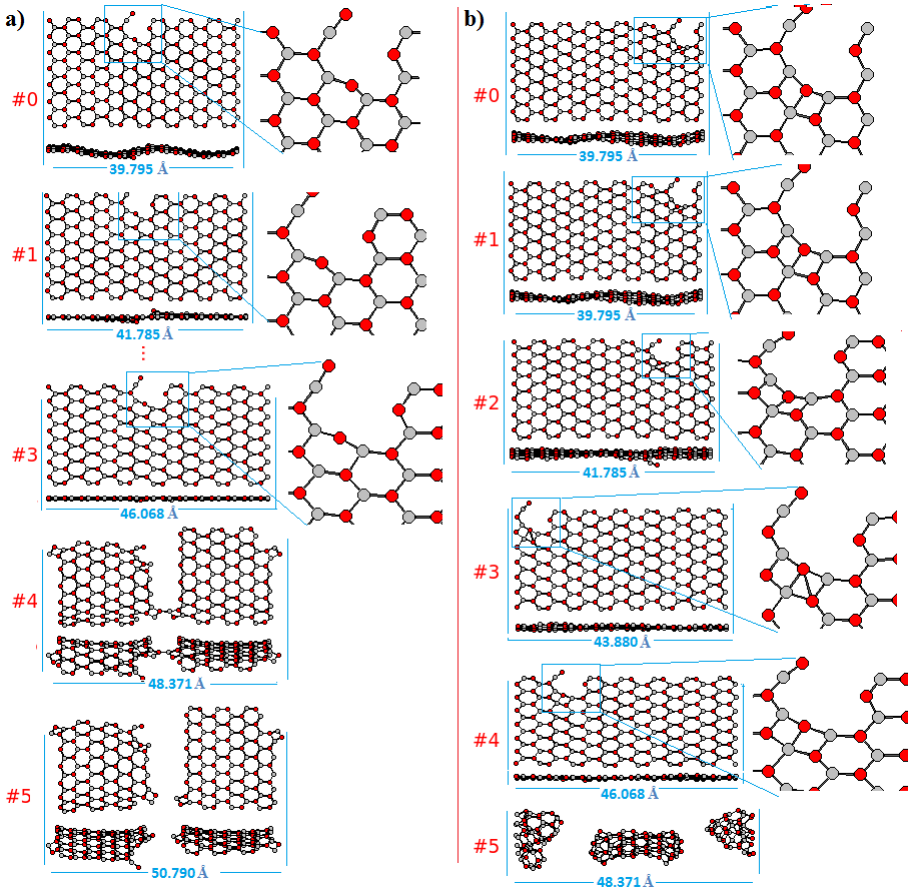

Figure 3.75 The AEDVO model under %5 tensile strain applications a) at 1 K b) at 300 K.

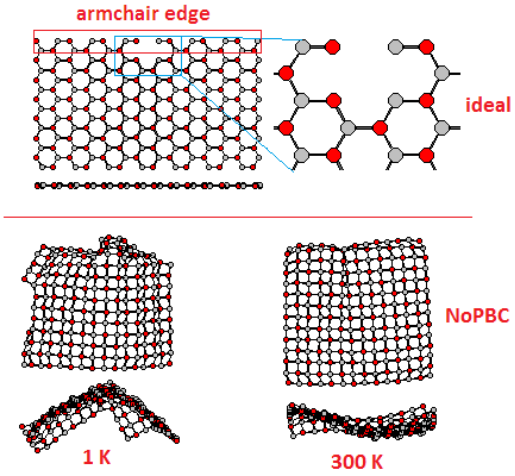

Figure 3.76 The AEDVZnO model with NoPBC at both 1 and 300 K.

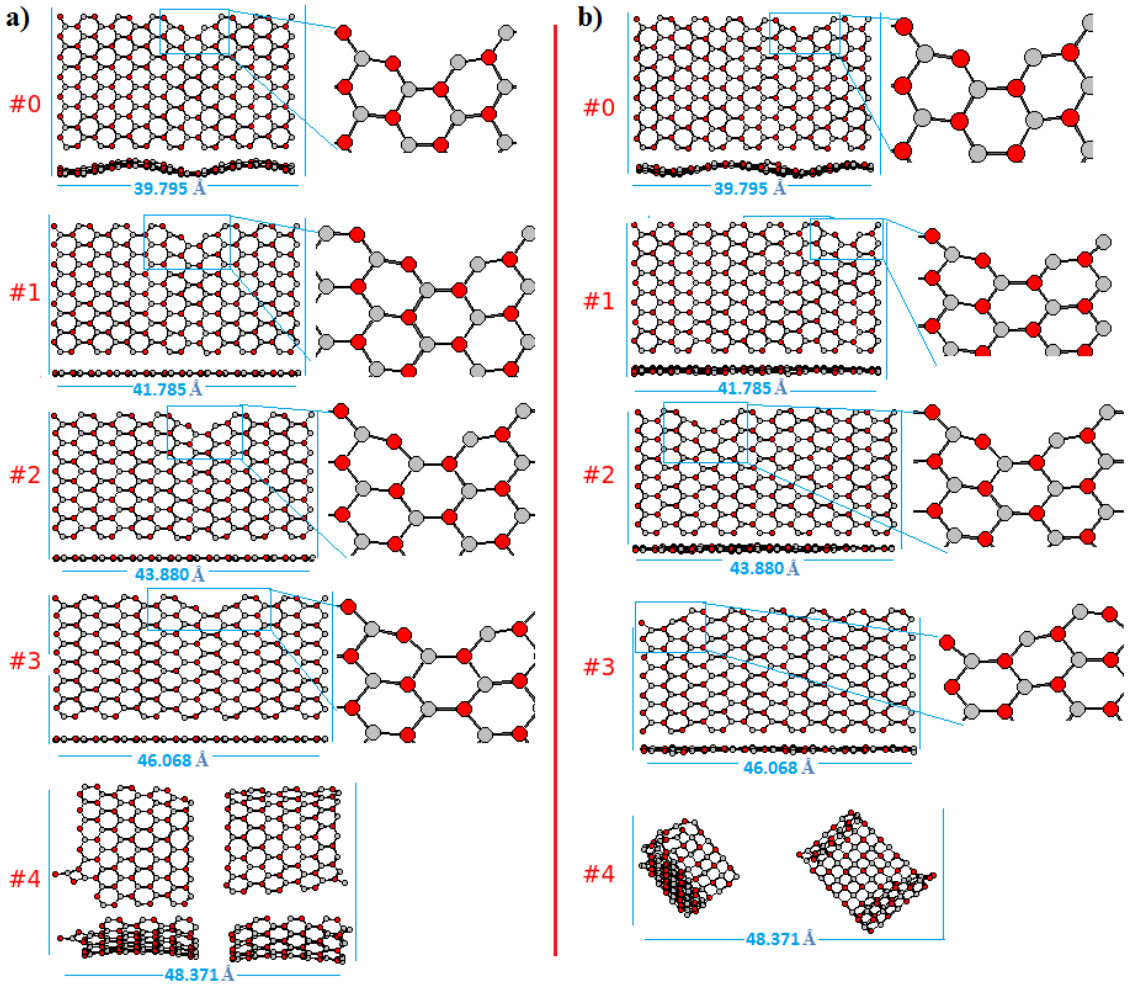

Figure 3.77 The AEDVZnO model under 5% tensile strain a) at 1 K b) at 300 K.

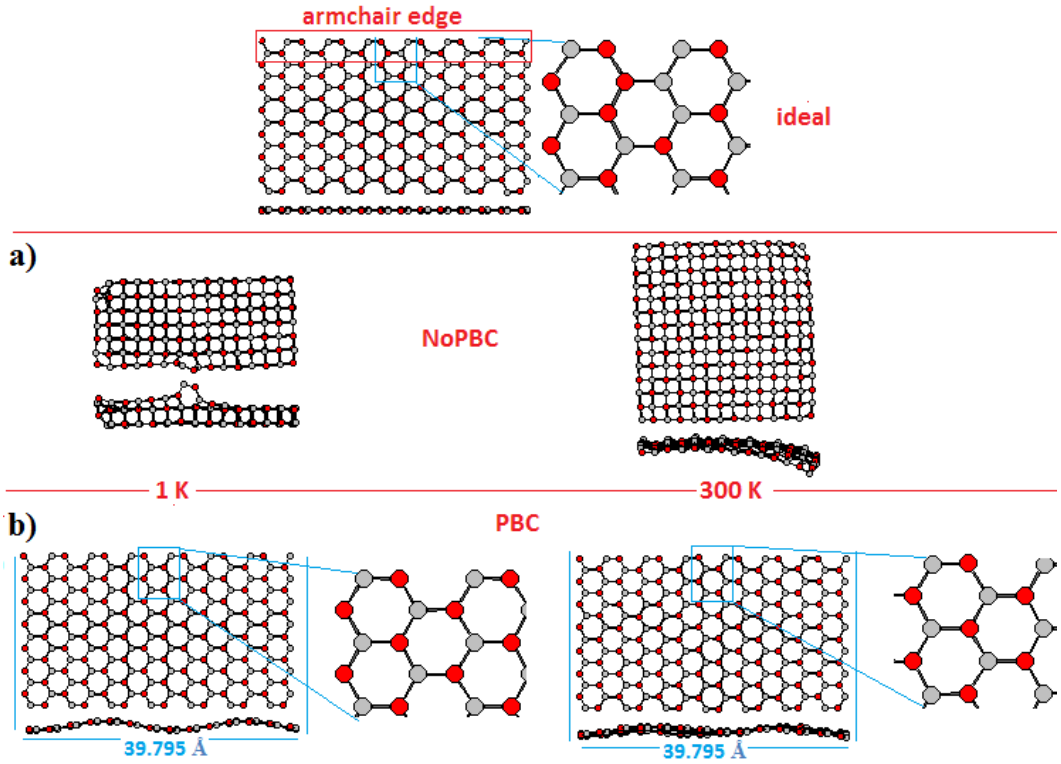

Figure 3.78 The AEDEXZnO model at 1 and 300 K. a) without NoPBC b) with PBC.

3.2.2 ZnO Nanorods

We have mentioned in previous section that three different cross sectional type models, namely hexagonal (HR), trigonal (TR) and rhombus (RR) have been considered for the nanorods[12]. In addition, three type models of the hexagonal cross sectional nanorods with different sizes (HR1, HR2 and HR3) are taken (see Figure 2.21)[121].

The HR1 model, after the energetic relaxation, almost maintained its ideal structure when PBC was not applied at 1 K, but the ends of the structure have widened since they are free. However, the same model at 300 K, has been clustered with NoPBC (see Figure 3.79). The HR1 model preserved its ideal structure when PBC was applied at 1 K. Then, in the case of 5% compression strain applications at 1 K, the same model, also preserved its ideal rod structure with hexagonal grid geometry at 1st compression step. In the second and third applications of compression step, some hexagons in the structure changed into squares. In the fifth application of compression steps, the hexagonal cross sectional appearance was preserved when viewed from the cross section whereas configured with a completely square grid geometry when viewed from the side view, so the structural phase transition was detected. Therfore, the wurtzite phase transformed into graphitic phases in 5th compression step. Interestingly, some parts of the structure transformed into cage-like structure at the 8th compression (see Figure 3.80 a). In the case of 5% tensile strain applications at 1 K, the same model preserved its ideal rod structure with hexagonal grid geometry in the first four application of tensile strain steps at 1 K. In the fifth application of tensile strain steps, it has broken into two rods, configured with square geometry (see Figure 3.80 b). As a sample graph the variation of tensile strain energy (ΔE) versus strain (ΔL) for HR1 model at 1 K is presented in the Figure 3.81. The average bond length between atoms in the structure was increased during the application of tensile strain steps whereas firstly it did not change, then it was increased during application of compression steps (see Figure 3.94). Furthermore, in the case of torsion applications, the HR1 model retained its initial torsion modeled structure at first seven torsion applications at 1 K, but the APEPP was increased. Then, when viewed from the cross section, the structure was appeared as a slightly wavy rod like became as at the 7th

torsion step (see Figure 3.82). On the other hand, the same model at 300 K, also preserved its ideal structure when PBC was applied. Then, in the case 5% compression strain applications at 300 K, the same model retained its initial structure at 1st compression step. Then, the structure evolved into a wavy-like rod at the 2nd compressions when viewed from the side (see Figure 3.83 a). When compression rate was increased to 10%, the same model exhibited similarity with 5% compress applications at both 1 and 300 K. Therefore, the velocity of the compression did not play an important role. In the case of 5% tensile strain applications at 300 K, additionally, the structure kept its ideal structure in the first four application of tensile strain steps. Further applications of tensile strain steps, in addition to rod, the atom chain formation (1D), 1L nanoribbon square-net structure was appeared as well (see Figure 3.83 b). In the case of the torsion applications at 300 K, the HR1 model evolved into a wavy rod like structure abruptly at 1st torsion step, as a result of this, we did not continue that work (see Figure 3.84).

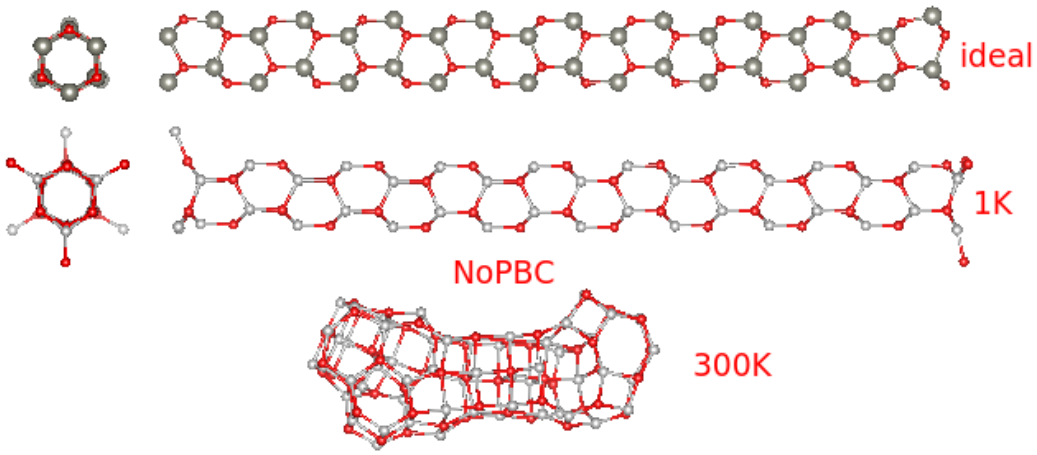

Figure 3.79 The HR1 model with NoPBC at both 1 and 300 K.

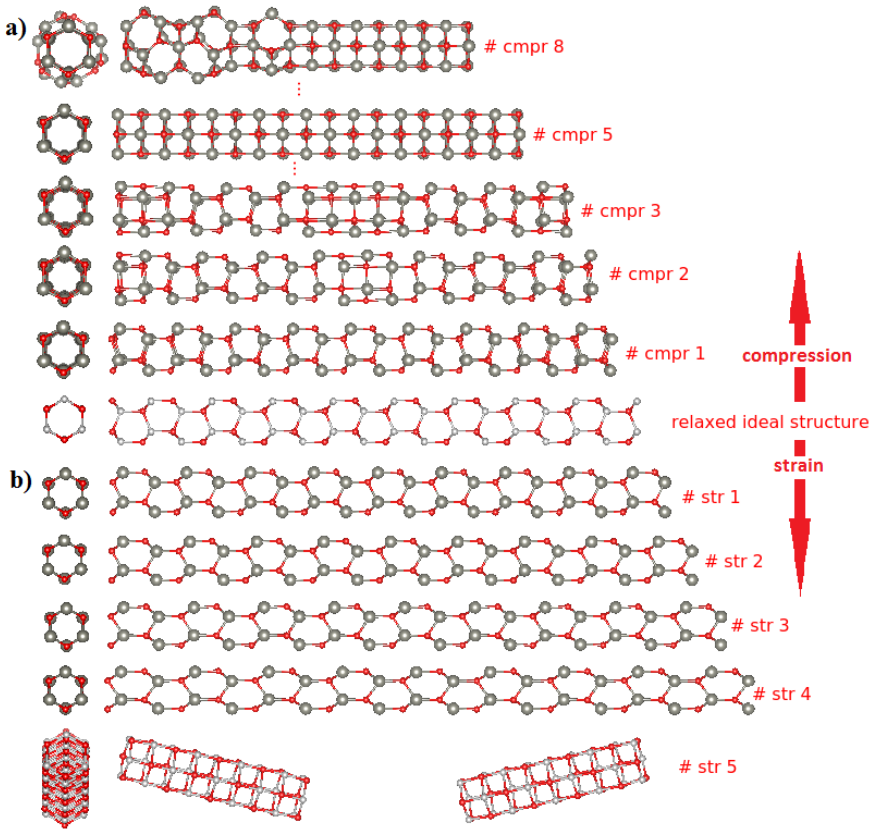

Figure 3.80 The HR1 model at 1 K under strain applications a) compression b) tensile strain.

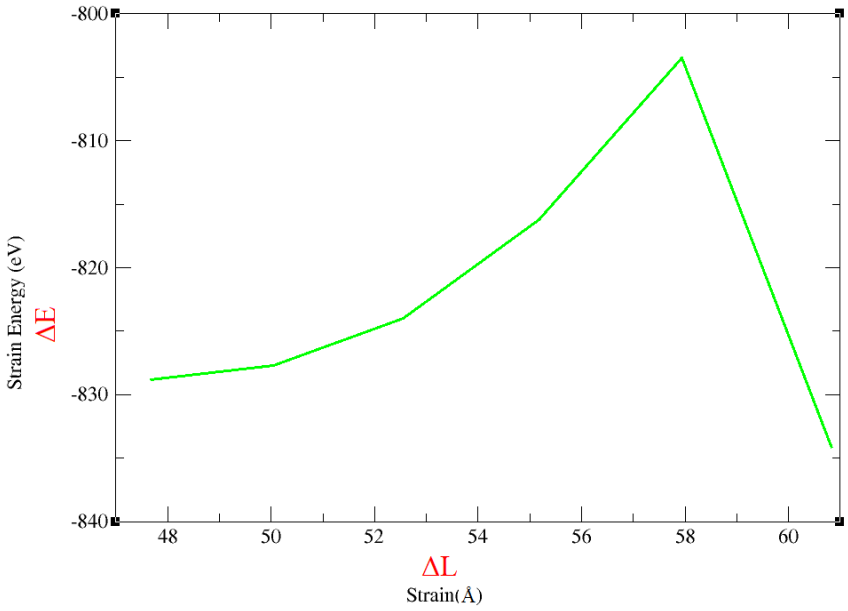

Figure 3.81 Tensile strain energy with respect to elongation for the H1 model at 1 K.

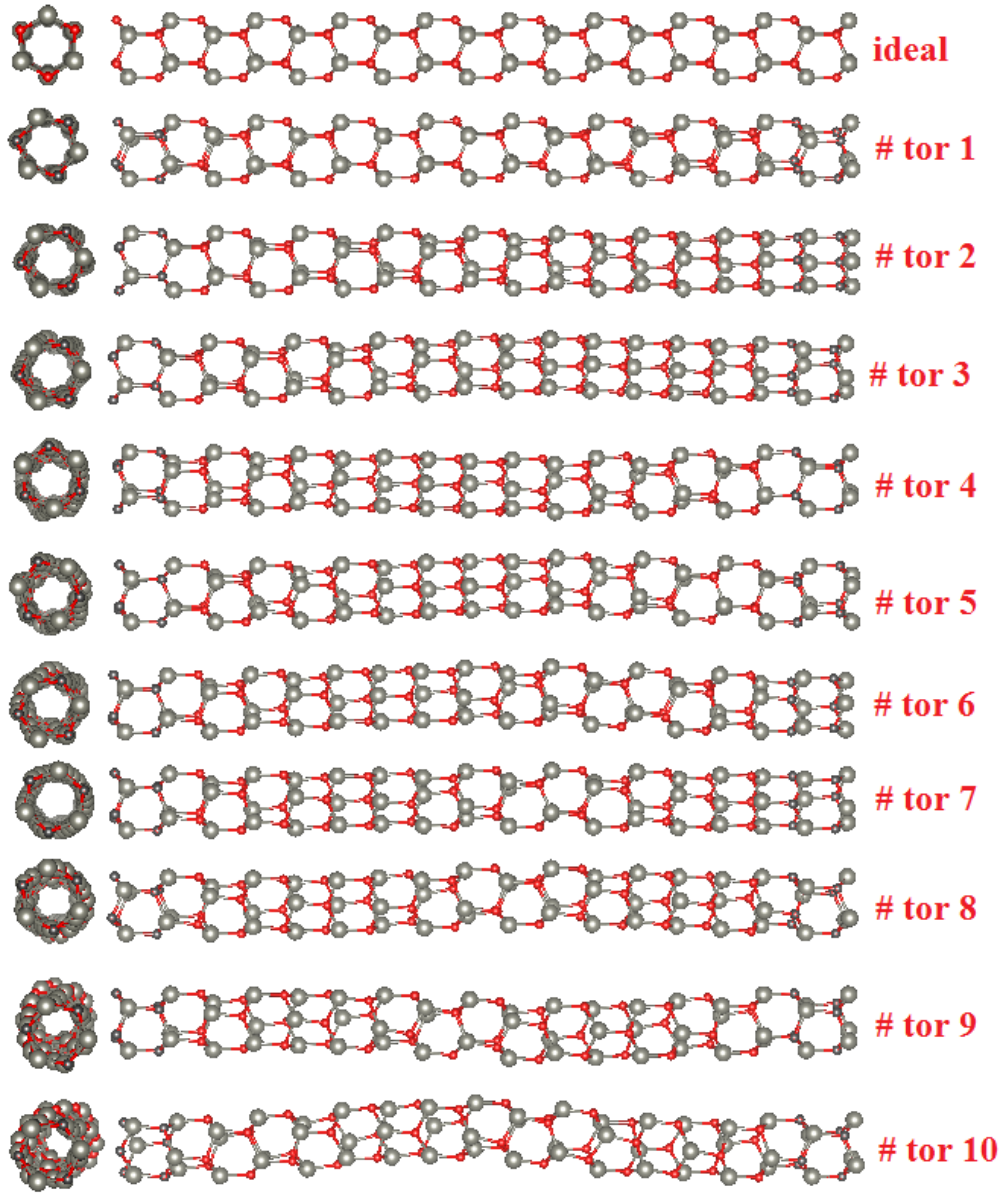

Figure 3.82 The HR1 model at 1 K under torsion applications.

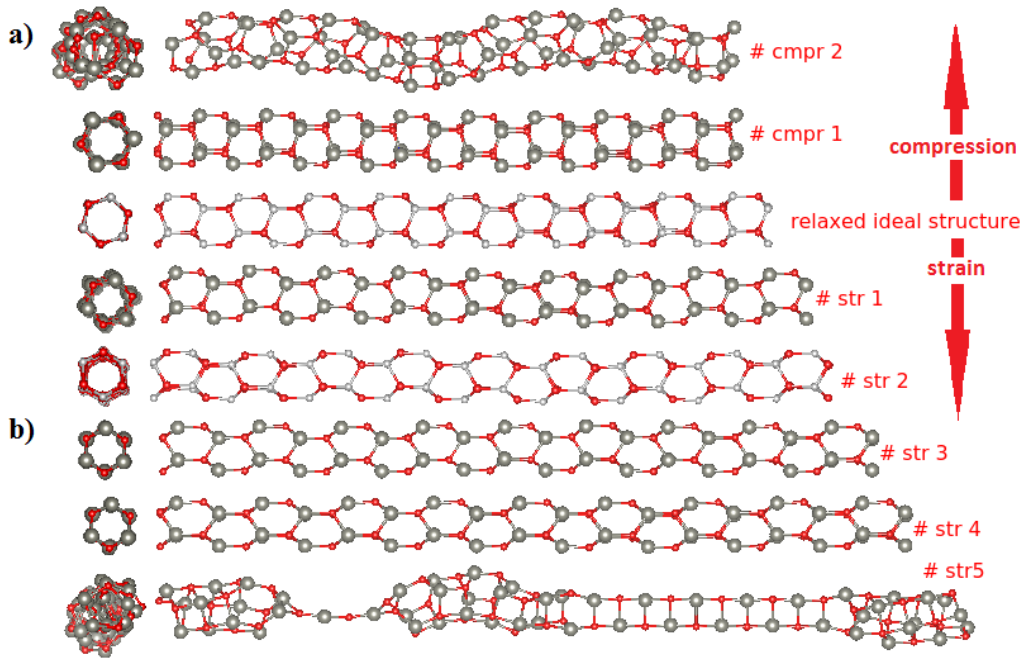

Figure 3.83 The HR1 model at 300 K under 5% strain applications a) compression b) tensile strain.

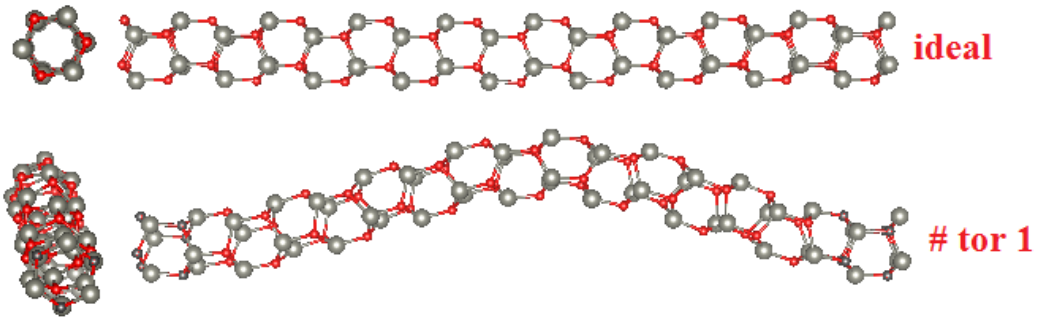

Figure 3.84 The HR1 model at 300 K under torsion applications.

The HR2 model nanorod, after the energetic relaxation, atomic order completely disappeared (looks amorphous-like) at both 1 and 300 K without PBC (see Figure 3.85). The HR2 model, when PBC was applied at 1 K, maintained its ideal rod structure. Then, same model, in the case of 5% compression strain applications, also preserved its ideal structure in the first three compression. In the fourth application of compression steps, the structure configured with a square grid geometry when viewed from the side whereas the hexagonal cross sectional appearance retained when viewed from the top. Thus, the wurtzite phase transformed into graphitic phase at 4^{th} compression step. Then, the structure was clustered at 8^{th} compression (see Figure 3.86 a). Then, in the case of 5% tensile strain at 1 K, the same model retained its perfect rod structure in the first three application of tensile strain steps. The hexagonal cross sectional appearance retained when viewed from the top, whereas consisted of squares and octagons when viewed from the side at 4^{th} tensile strain step. Then, the neck points were observed at 9^{th} tensile strain step (see Figure 3.86 b). Additionally, the average bond length between atoms in the structure was increased (see Figure 3.94) during the both compression and strain applications. Then, in the case of torsion applications at 1 K, the HR2 model maintained its initial torsion modeled structure at the first six torsion applications, such that the hexagonal grid geometry did not change (see Figure 3.87). However, the average potential energy for per particle in the structure also was increased, which as straight line, during the torsion applications (see Figure 3.95). Then, a deformation appeared in the middle of the structure at 7^{th} torsion step. On the other hand, the HR2 model, when PBC was applied at 300 K, also preserved its ideal structure after the energetic relaxation. Then, in the case of 5% compression strain applications, the same model also retained its initial structure in the first three compression steps. Then, the structure configured with square grid geometry at 4^{th} compression when viewed from the side, which means that the graphitic phase was observed. In the seventh application of compression steps, the structure as clustered (see Figure 3.88 a). In the case of 5% tensile strain applications at 300 K, the same model maintained its ideal rod structure at 1^{st} tensile strain step. Then, the structure was abruptly broken into two parts as the perfect rod structure with hexagonal geometry at 2^{nd} tensile strain step (see Figure 3.88 b). In addition, the same model at 300 K, when subject to torsion, exhibited a similar mechanical properties with the same model at 1 K (see Figure 3.89).

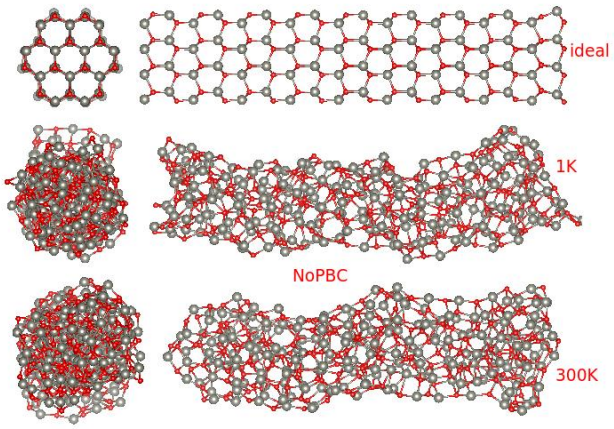

Figure 3.85 The HR2 model with NoPBC at 1 and 300 K.

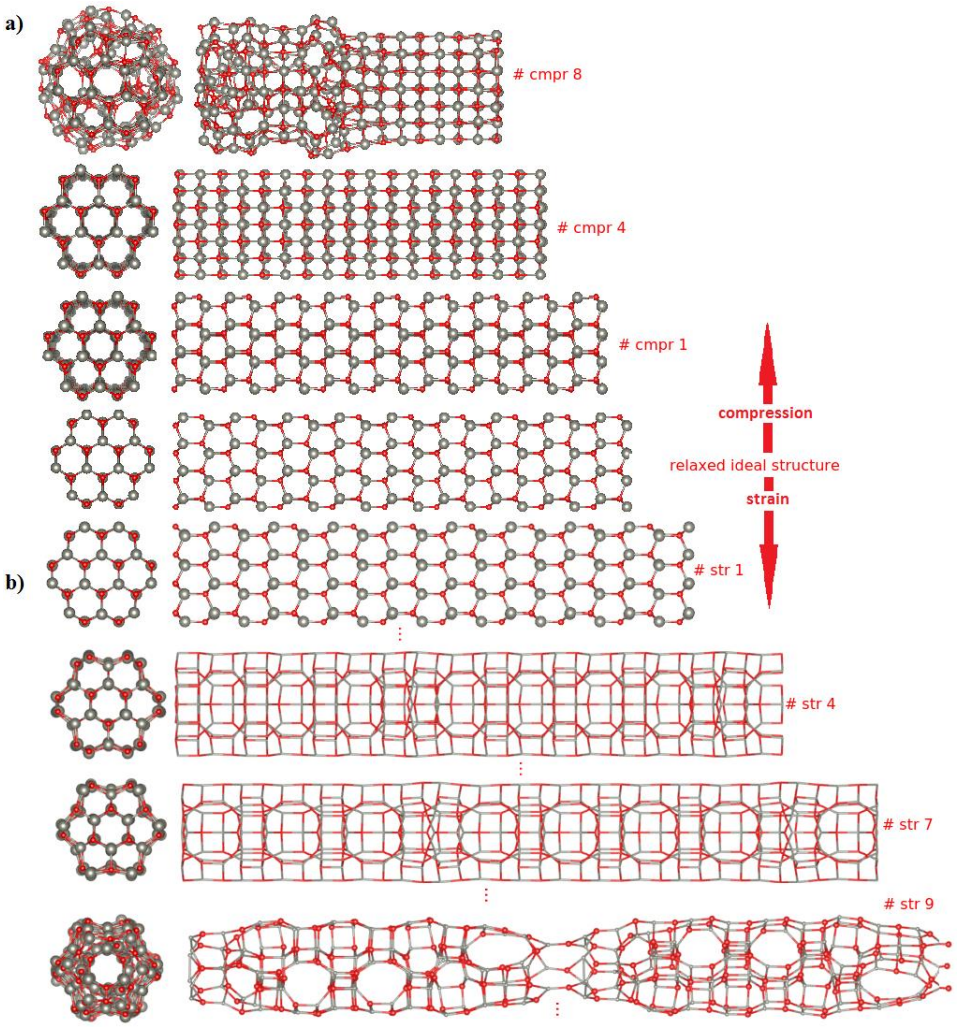

Figure 3.86 The HR2 model at 1 K under 5% strain applications a) compression b) tensile strain.

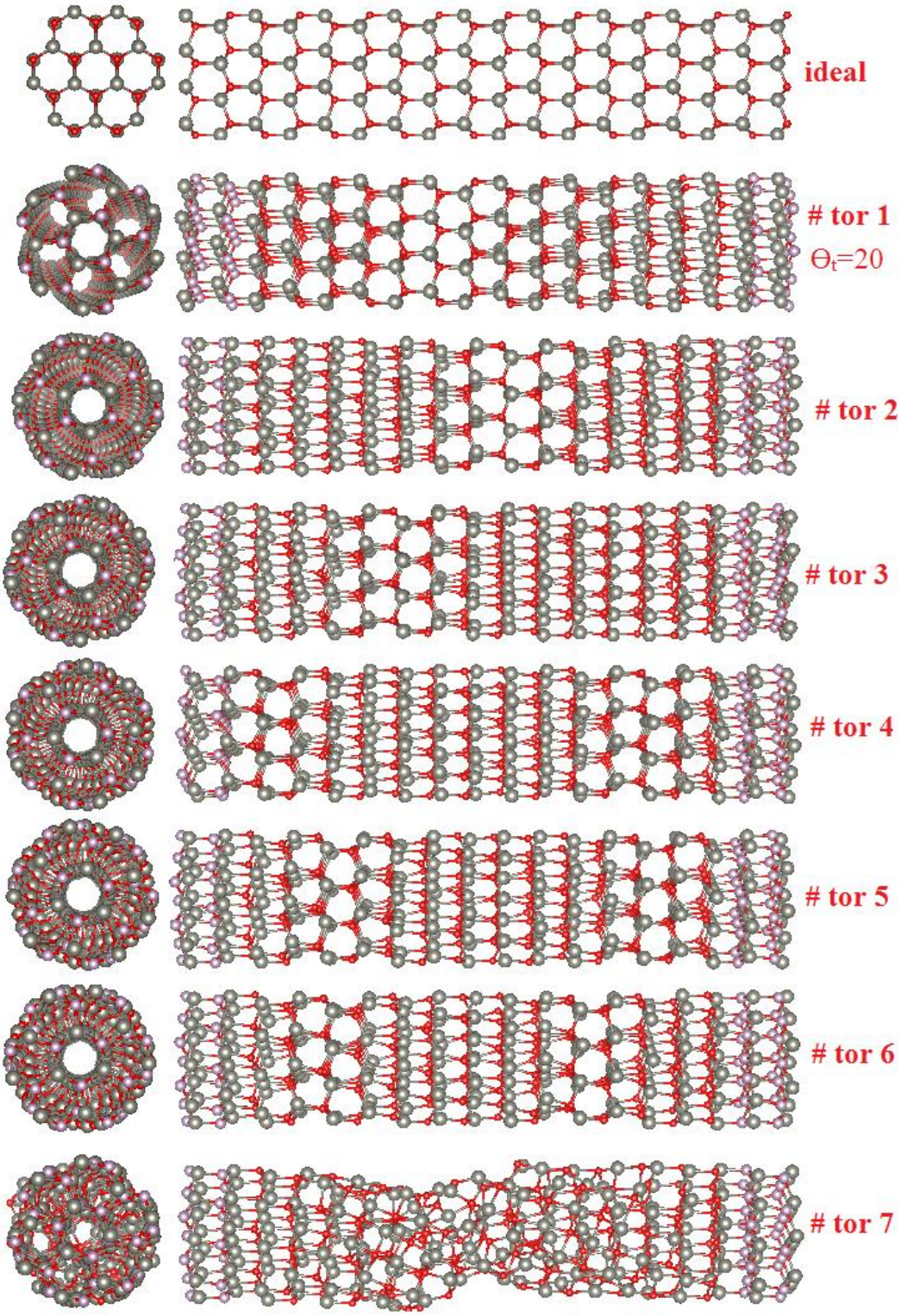

Figure 3.87 The HR2 model at 1 K under torsion applications.

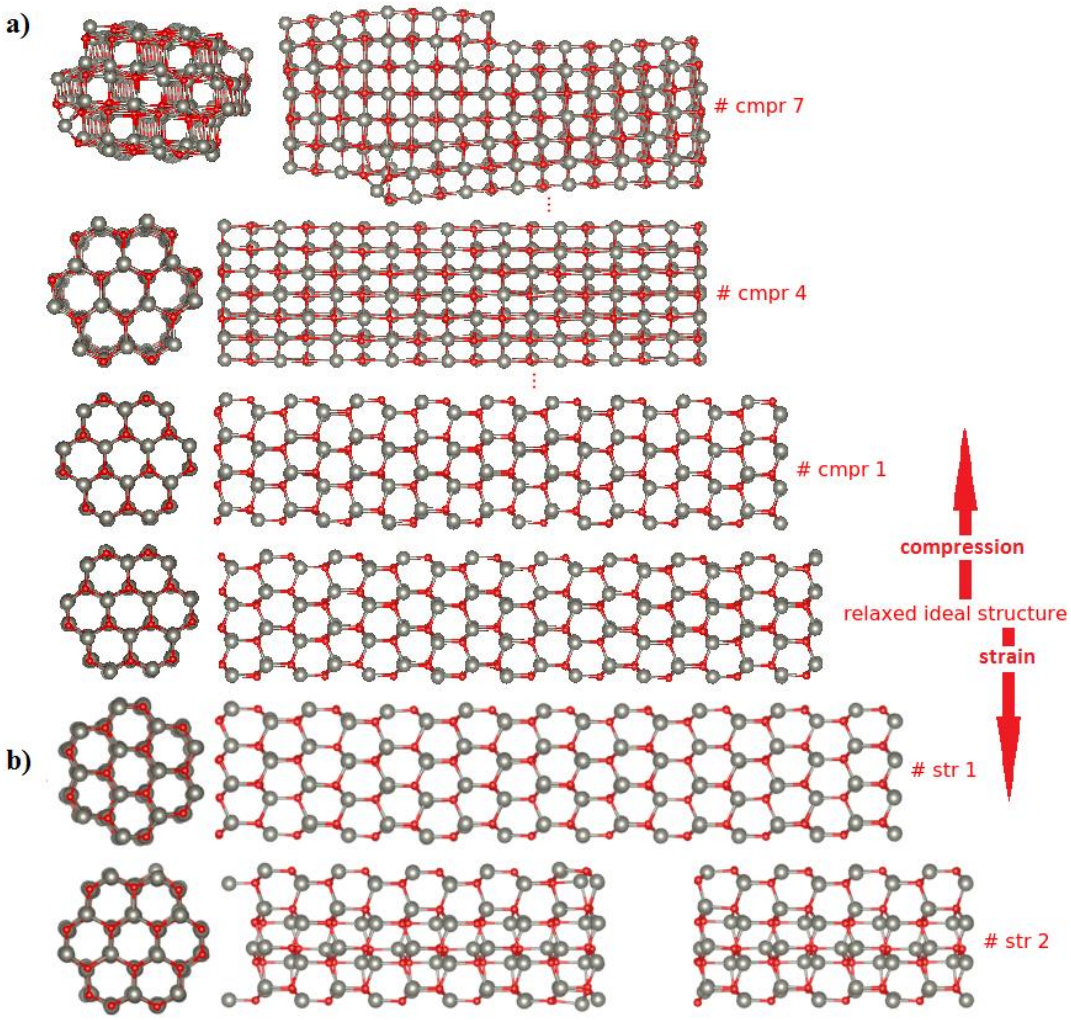

Figure 3.88 The HR2 model at 300 K under 5% strain applications a) compression b) tensile strain.

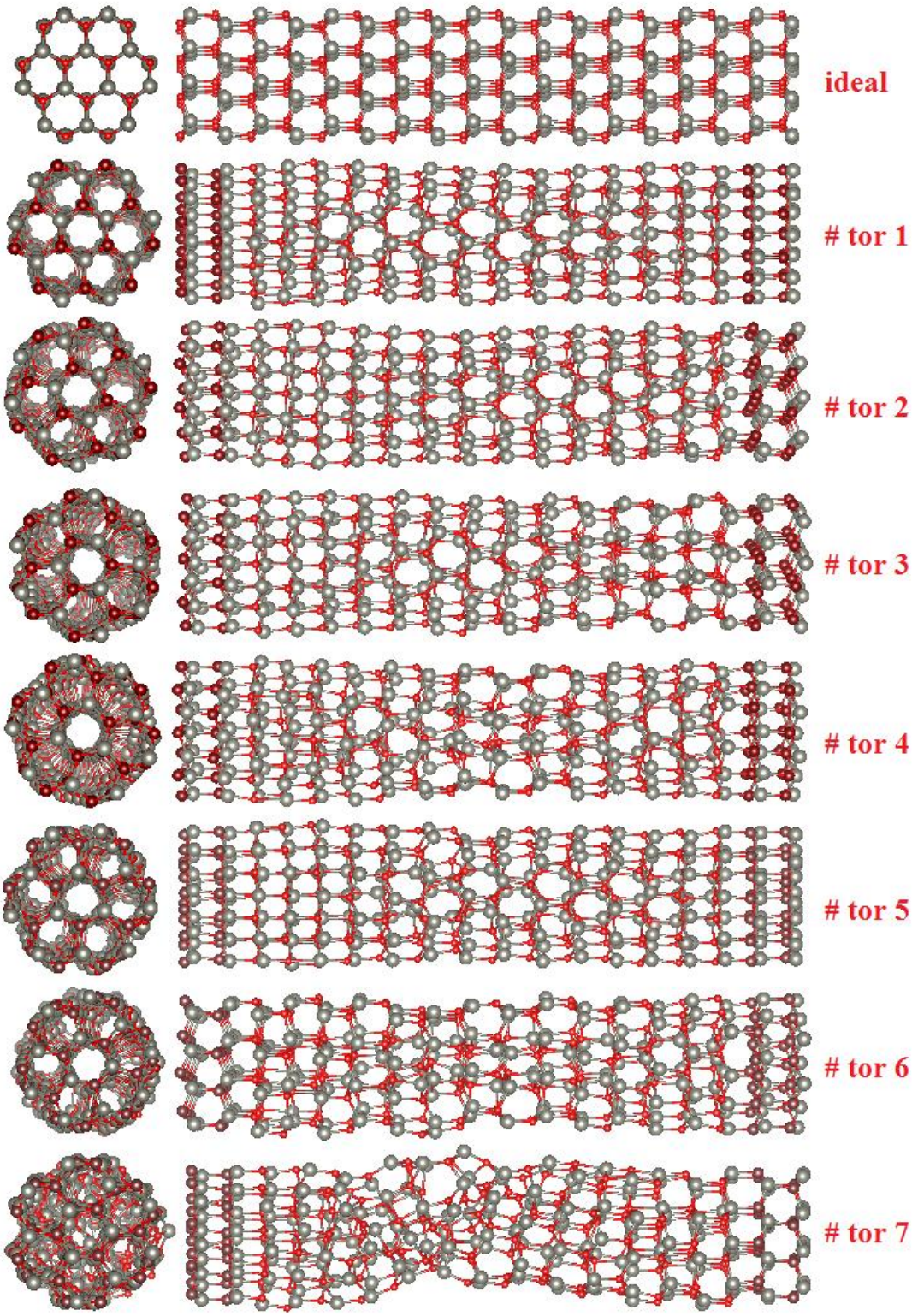

Figure 3.89 The HR2 model under torsion applications at 300 K.

The HR3 model, after the energetic relaxation, was completely clustered at both 1 and 300 K without PBC. When PBC was applied, the HR3 model preserved its ideal structure at 1 K. In the case of 5% compression strain applications, the same model, also maintained its initial structure in the first three compression applications. In the fourth application of compression steps, the hexagonal cross sectional appearance maintained, whereas the hexagonal grid geometry changed into squares when viewed from the side. Then, the structure was fragmented at 8^{th} compression (see Figure 3.90 a). In the case of 5% tensile strain applications at 1 K, the HR3 model at 1 K maintained its initial rod structure in the first three applications of tensile strain step. Then, the structure was abruptly broken into two at 4^{th} tensile strain step (see Figure 3.90 b). Furthermore, the average bond length between atoms in the structure was increased during the compression and strain applications (see Figure 3.94). In addition, when subject to torsion at 1 K, the same model preserved its initial torsion modeled structure such that the hexagonal grid geometry did not change again, but the average potential energy between atoms in the structure was increased at the first five applications of torsion steps. Then, a deformation took place in the middle part of the structure at 6^{th} torsion step (see Figure 3.91). On the other hand, the HR3 model also preserved its initial structure with PBC at 300 K. In the case of 5% compression strain at 300 K, the same model also retained its initial structure in the first three compression steps. Then, the structure configured with square grid geometry at 4^{th} compression when viewed from the side. In the fifth application of compression steps, the structure changed into amorphous like structure at 5^{th} compression (see Figure 3.92 a). When subject to 5% tensile strain at 300 K, the same model maintained its initial structure in the first three tensile strain steps. Then, the neck points in the middle part of structure were detected at 4^{th} tensile strain step. Moreover, the average bond length between atoms in this structure was increased during the both compression and strain applications (see Figure 3.94). Additionally, when subject to torsion applications at 300 K, the same model also retained its initial torsion modeled structure at first six torsion steps, disappeared no deformation was observed in the structure under torsion application (see Figure 3.93). Moreover, the average potential energy between atoms in this structure did not increase as straight line during the torsion applications (see Figure 3.95).

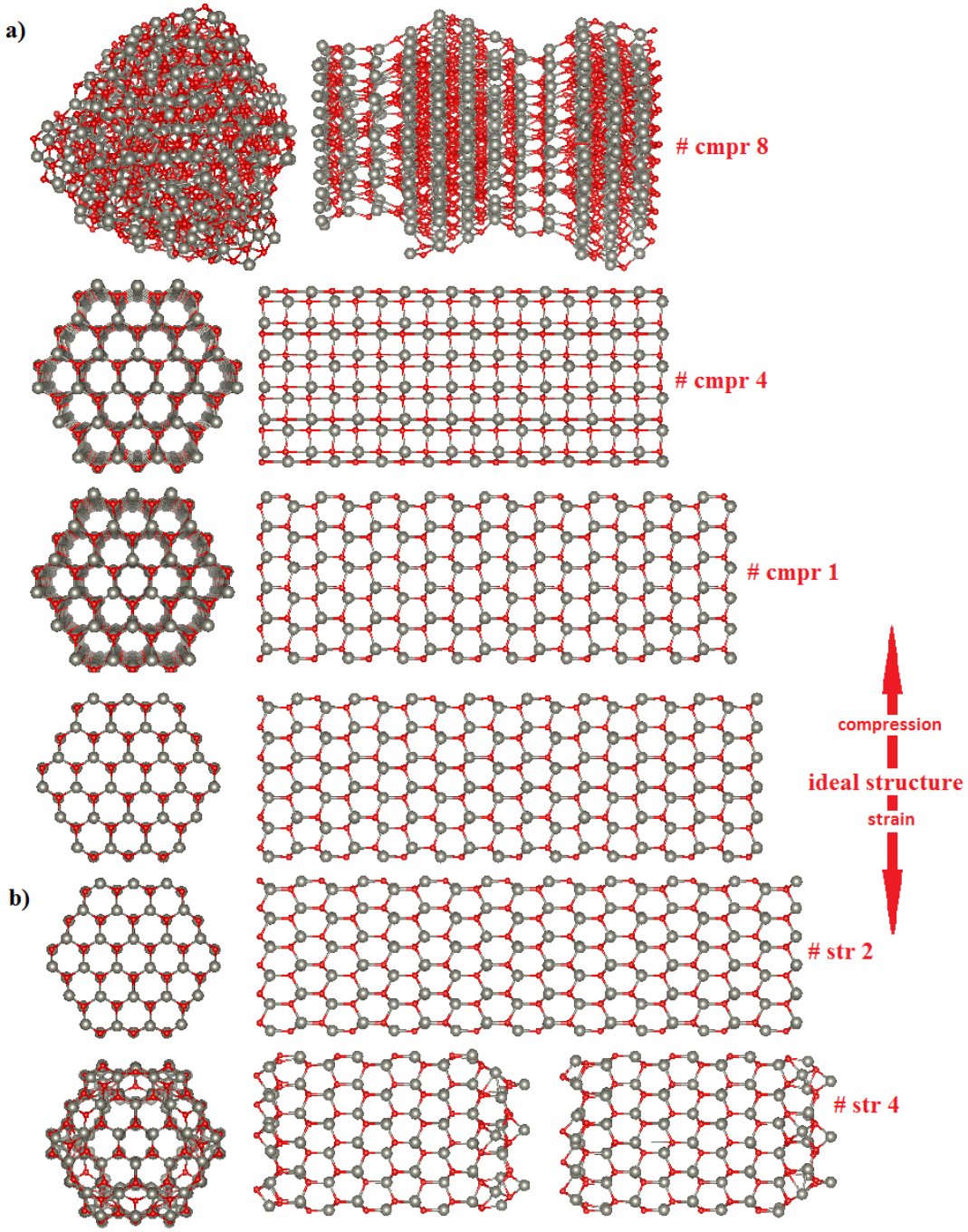

Figure 3.90 The HR3 model at 1 K under 5% strain applications a) compression b) tensile strain.

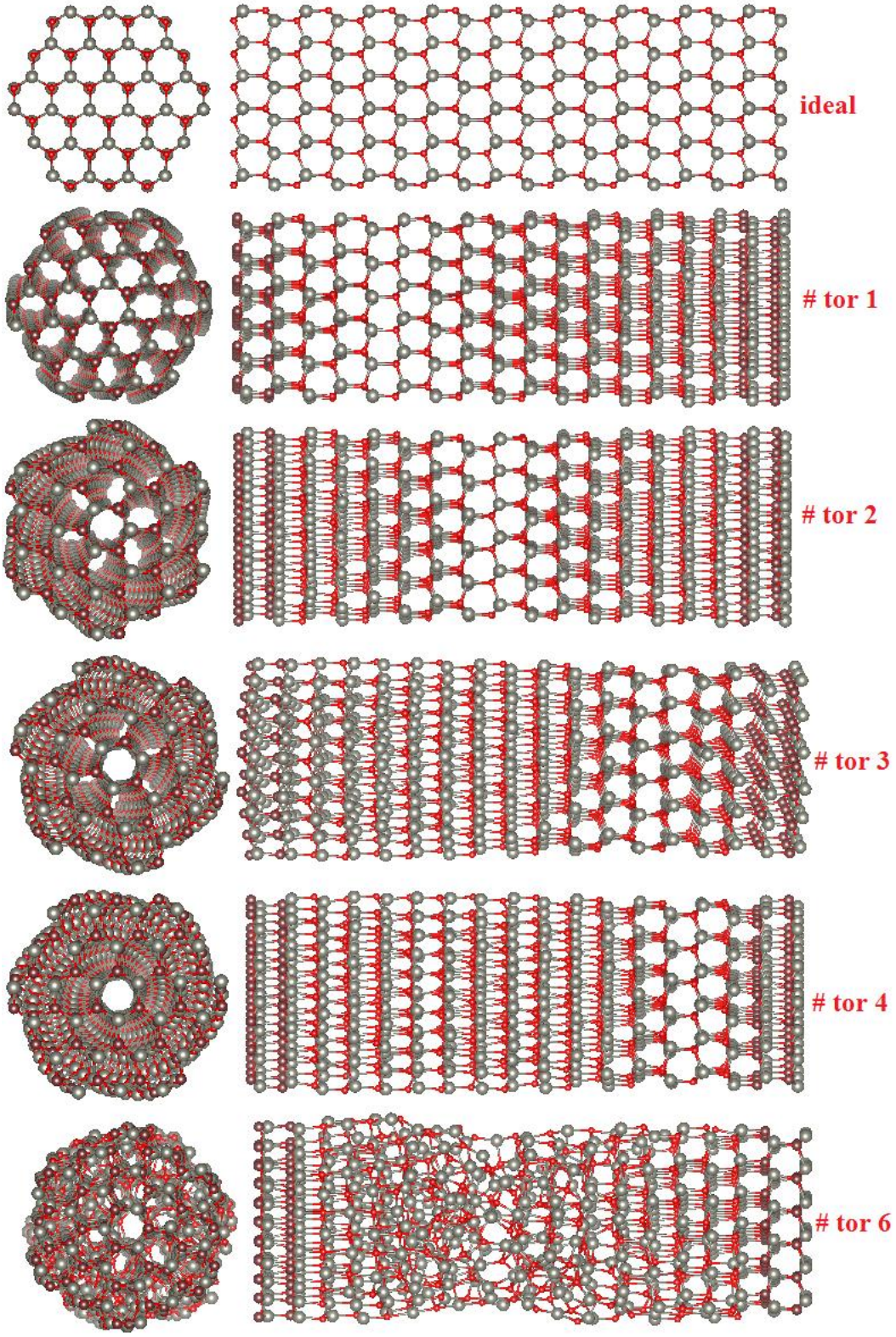

Figure 3.91 The HR3 model at 1 K under torsion applications.

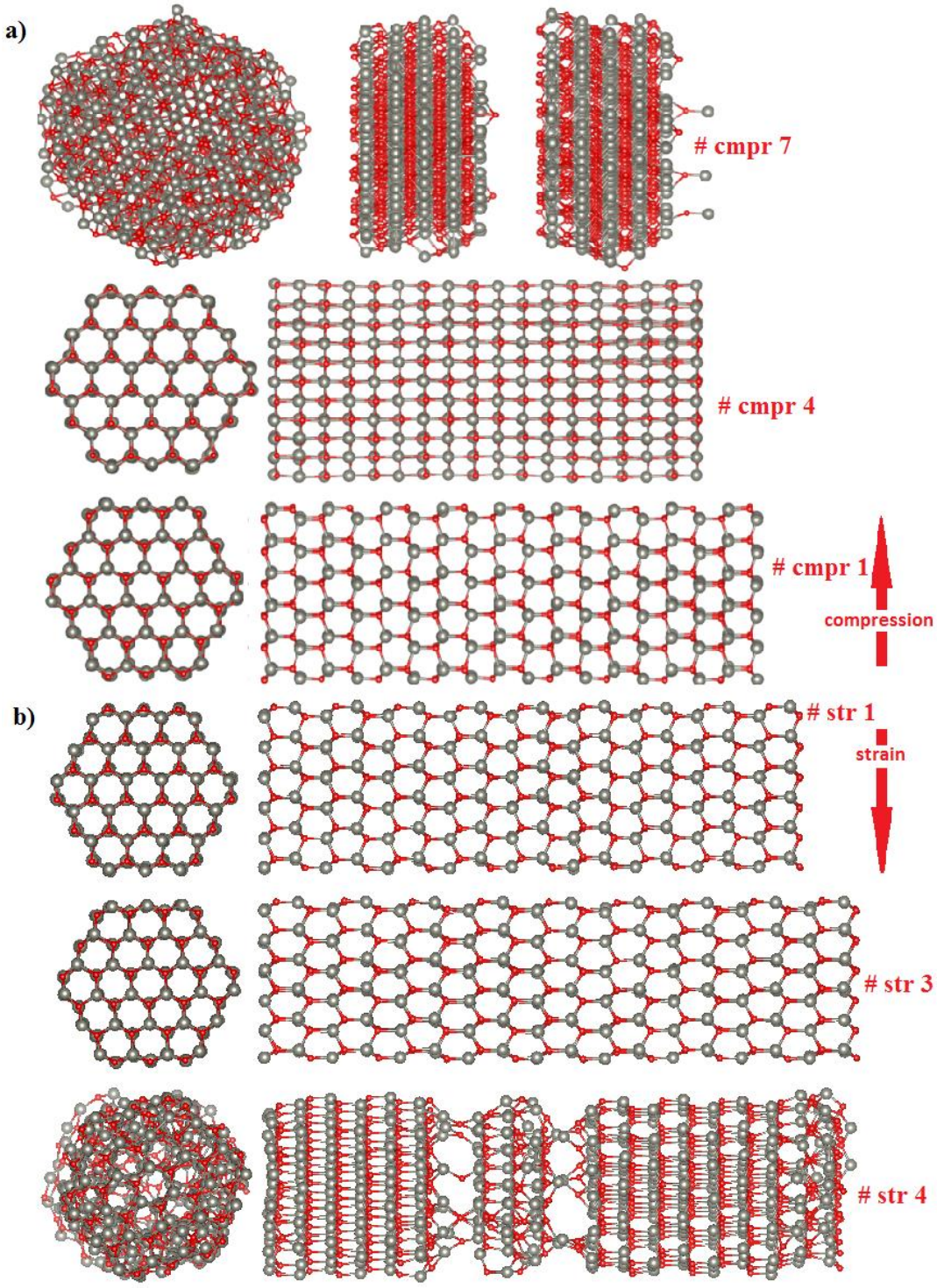

Figure 3.92 The HR3 model at 300 K under 5% strain applications a) compression b) tensile strain.

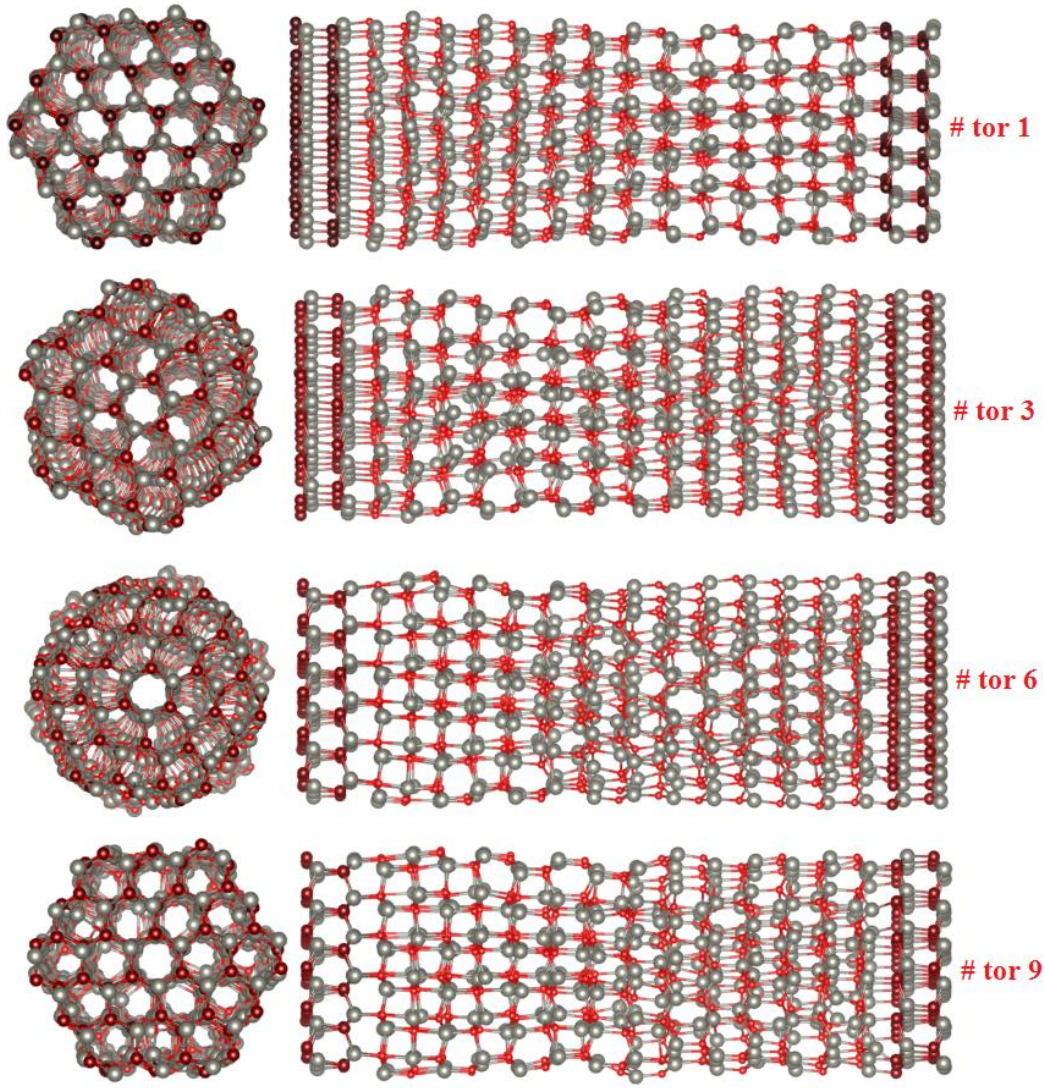

Figure 3.93 The HR3 model at 300 K under torsion applications.

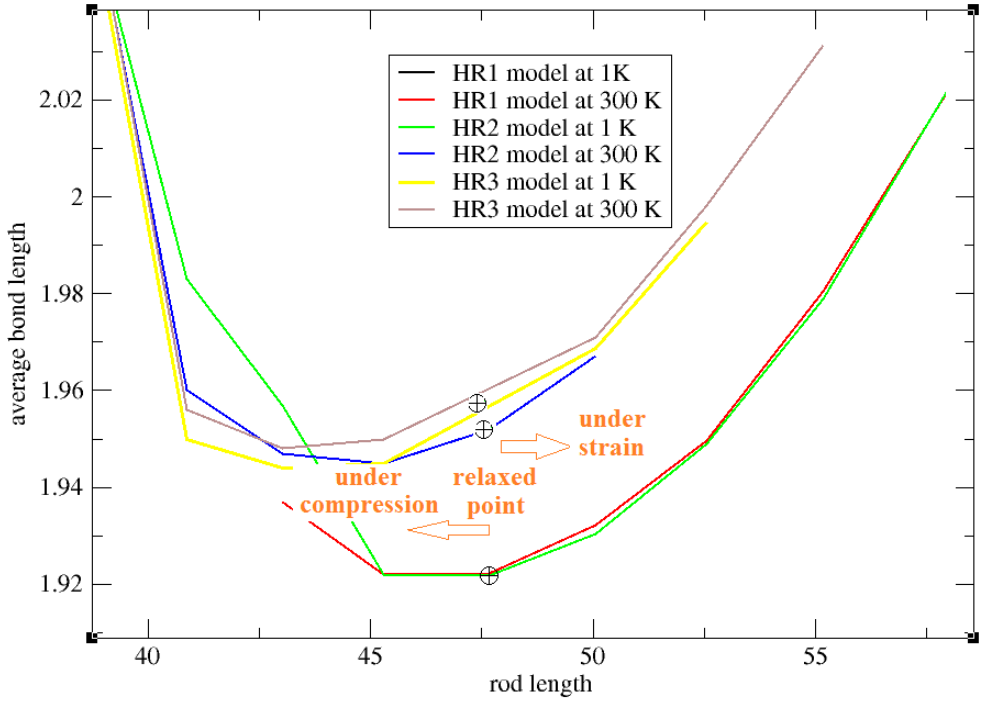

Figure 3.94 The average bond length of HR1, HR2, HR3 models at both 1 and 300 K under compression and tensile strain applications.

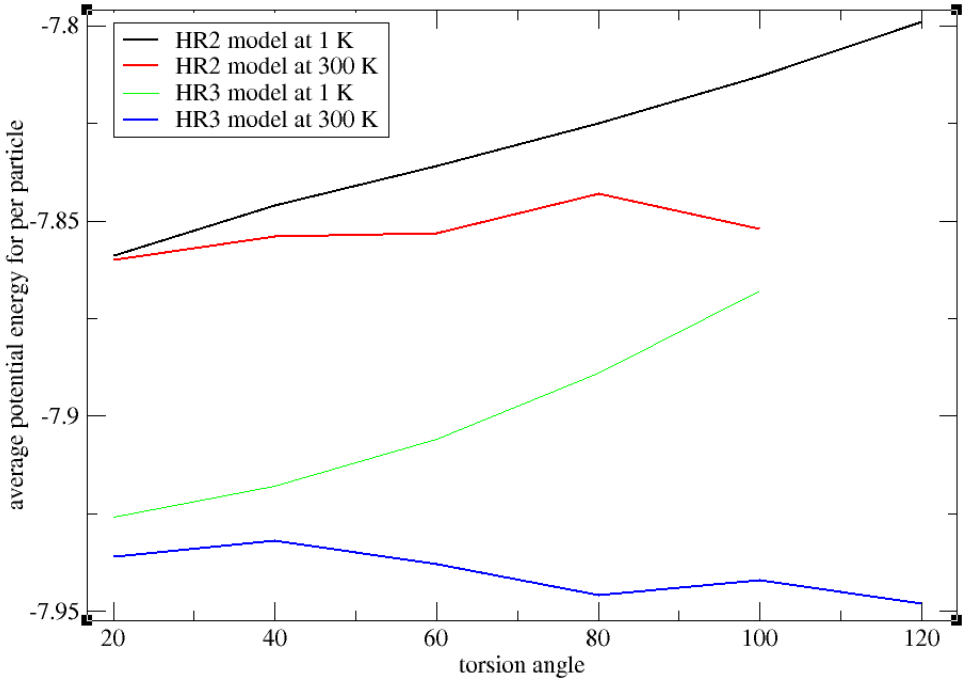

Figure 3.95 The average potential energy for per atom of HR2, HR3 models at both 1 and 300 K under torsion applications.

The TR model, after the energetic relaxation, did not maintain its ideal structure at both 1 and 300 K when PBC was not applied. The ends of structure were clustered since they were free whereas the middle of the structure almost retained rod structure at 1 K, but the structure at 300 K completely appeared as amorphous like with NoPBC (see Figure 3.96). When PBC was applied at 1 K, the TR model preserved its ideal structure after the energetic relaxation. In the case of 5% compression strain applications, the same model also maintained its initial rod structure in the first three applications of compression step. In fourth application of compression step, the structure configured with square grid geometry when viewed from the side. Then, one end of the structure was clustered at 8^{th} compression step (see Figure 3.97 a). In the case of 5% tensile strain applications at 1 K, the same model also maintained its initial rod structure in the first four tensile strain steps. Then, the structure did not preserve hexagonal grid geometry at 5^{th} tensile strain step when viewed from the side, but when viewed from the top, the trigon cross sectional shaped rod appearance maintained. Then, the structure was broken into two rods at 6^{th} tensile strain step (see Figure 3.97 b). On the other hand, the TR model also preserved its ideal structure with PBC at 300 K after the energetic relaxations. When subject to 5% compression strain applications at 300 K, the same model also retained its initial rod structure in the first three compression steps. Then, the structure configured with square grid geometry at 4th compression when viewed from the side. In the fifth application of compression strain steps, the structure was fragmented (see Figure 3.98 a). In the case of 5% tensile strain applications at 300 K, the structure also retained its ideal rod shape in the first four applications of tensile strain steps. Then, the structure was stretched much more at 5^{th} tensile strain step (see Figure 3.98 b).

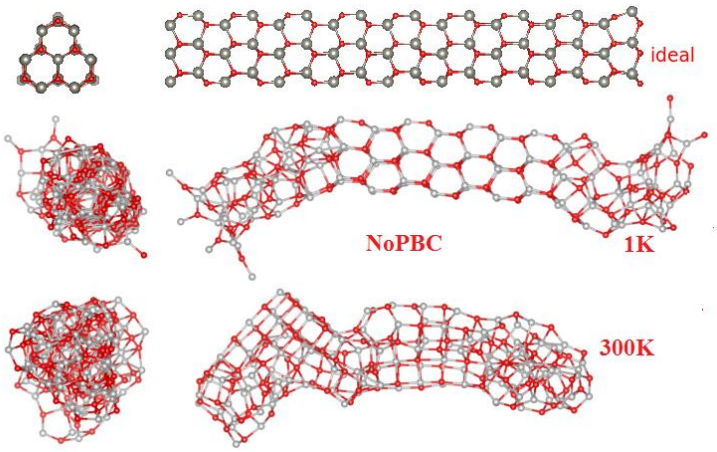

Figure 3.96 The TR model with NoPBC at 1 and 300 K.

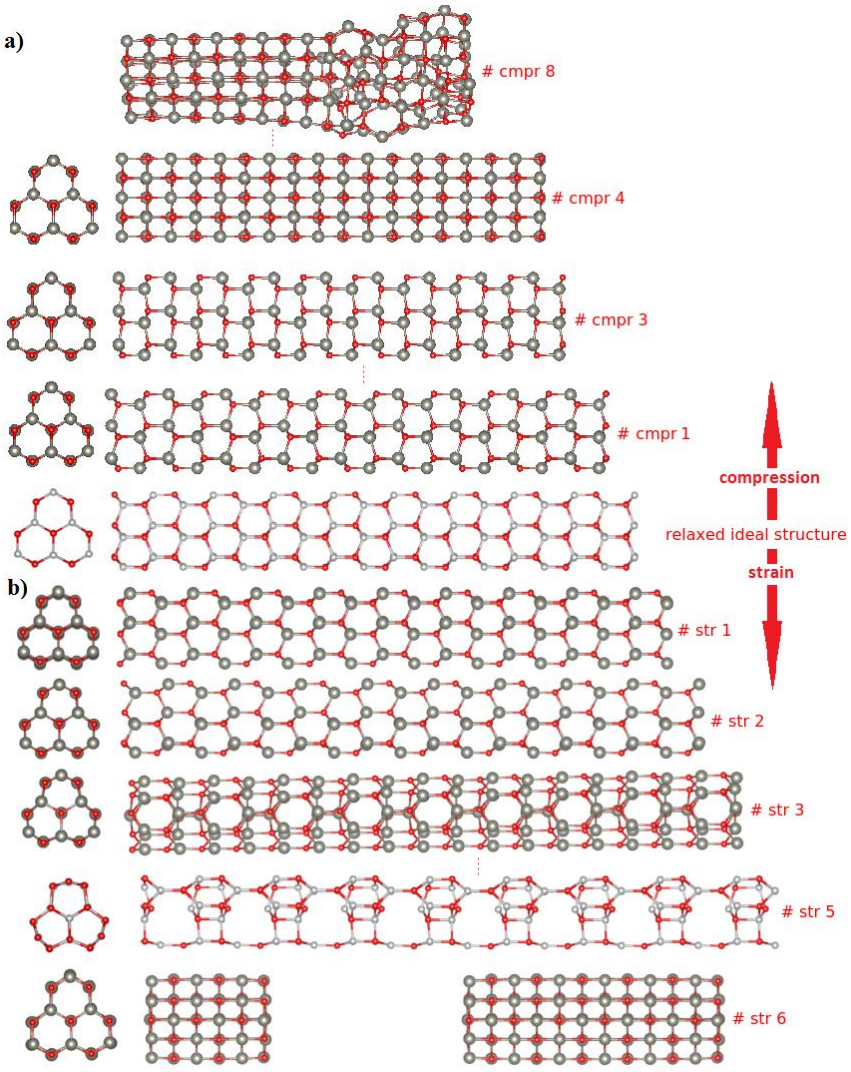

Figure 3.97 The TR model at 1 K under 5% strain applications a) compression b) tensile strain.

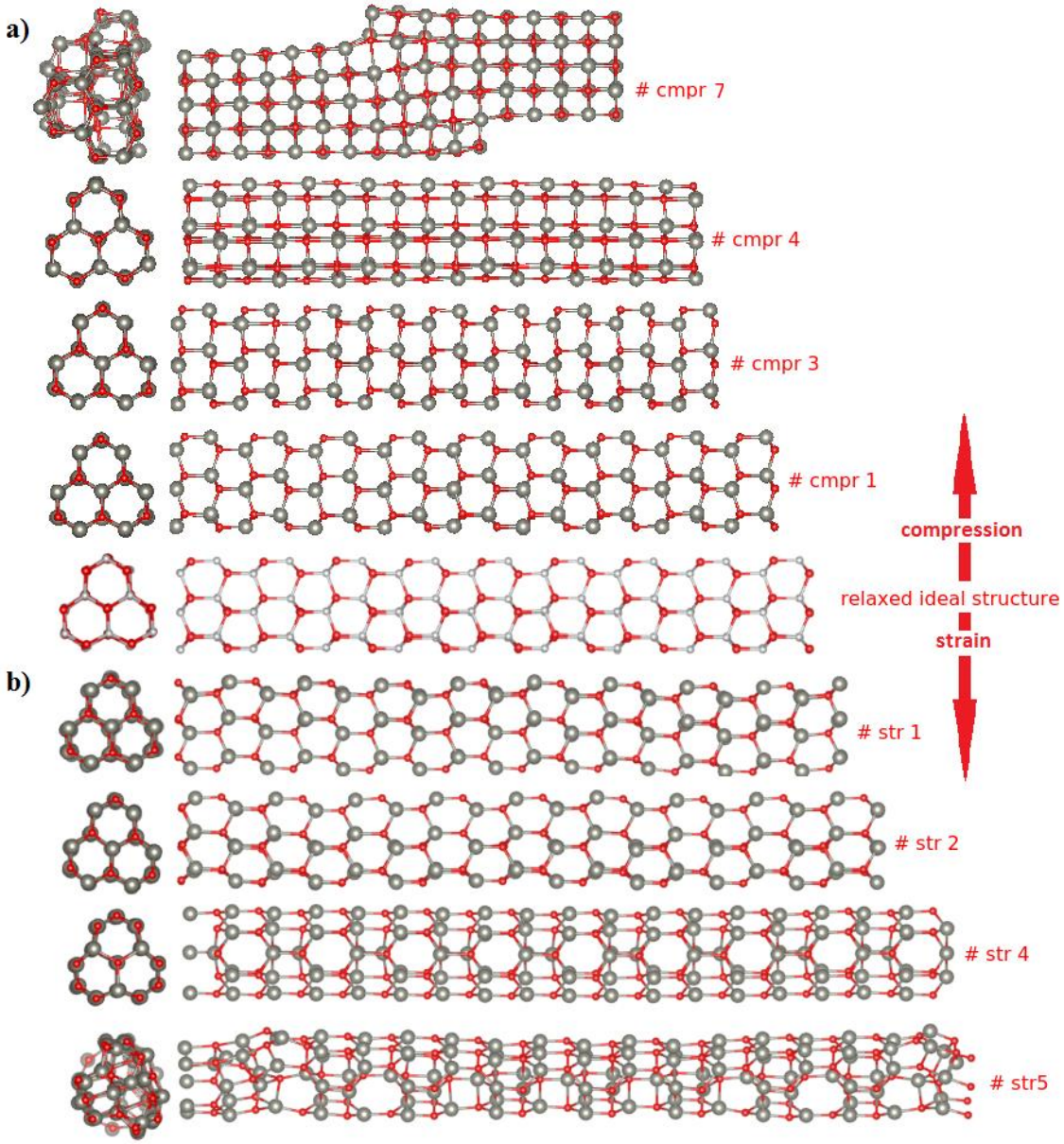

Figure 3.98 The TR model at 300 K under 5% strain applications a) compression b) tensile strain applications.

The atomic order of the RR model was completely disappeared when PBC was not applied at both 1 and 300 K after the energetic relaxation (see Figure 3.99). When PBC was applied at 1 K, the same model was preserved its initial structure after the energetic relaxation. In the case of 5% compression strain applications at 1 K, the same model maintained its initial structure in the first three compression strain steps. Then, the structure configured with square grid geometry when viewed from the side at 4th compression strain step. In the seventh application of compression strain steps, the structure was clustered (see Figure 3.100 a). In the case of 5% tensile strain applications at 1 K, the RR model kept its initial structure in the first three tensile strain steps. Then, the rhombohedra cross sectional appearance of the rod was maintained when viewed from the top whereas configured with another grid geometry when viewed from the side at 4th tensile strain step. In the sixth application of tensile strain steps, the neck points in the structure were detected (see Figure 3.100 b). On the other hand, the RR model, when subject to 5% both strain and compression strain applications at 300 K, exhibited similar structural properties to that of 1 K (see Figure 3.101).

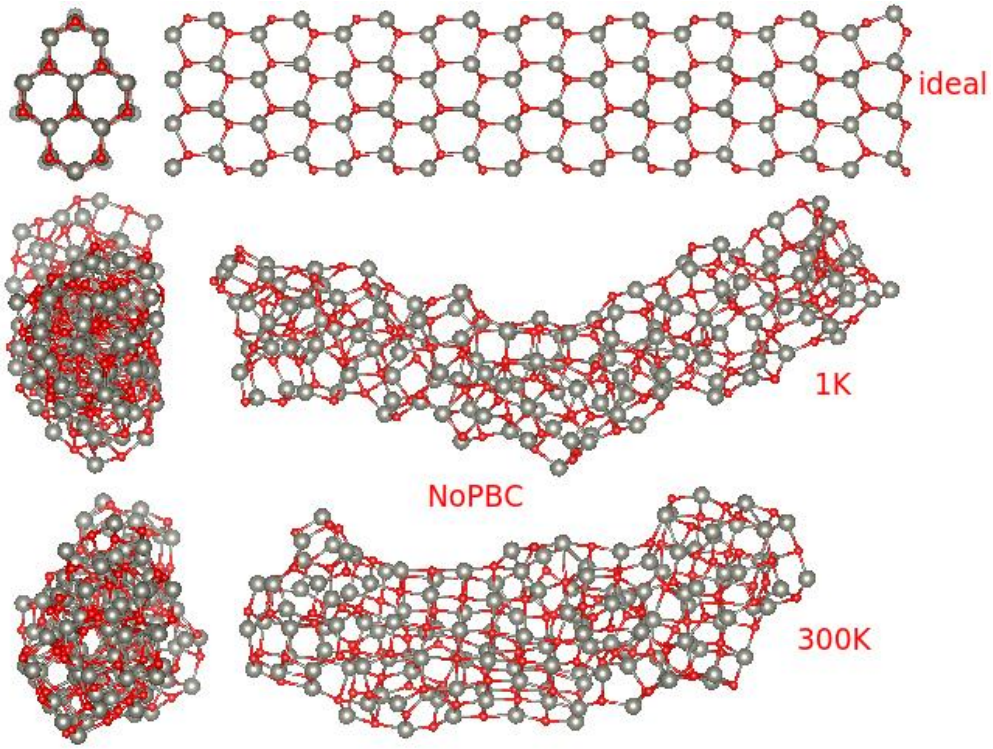

Figure 3.99 The RR model with NoPBC at 1 and 300 K.

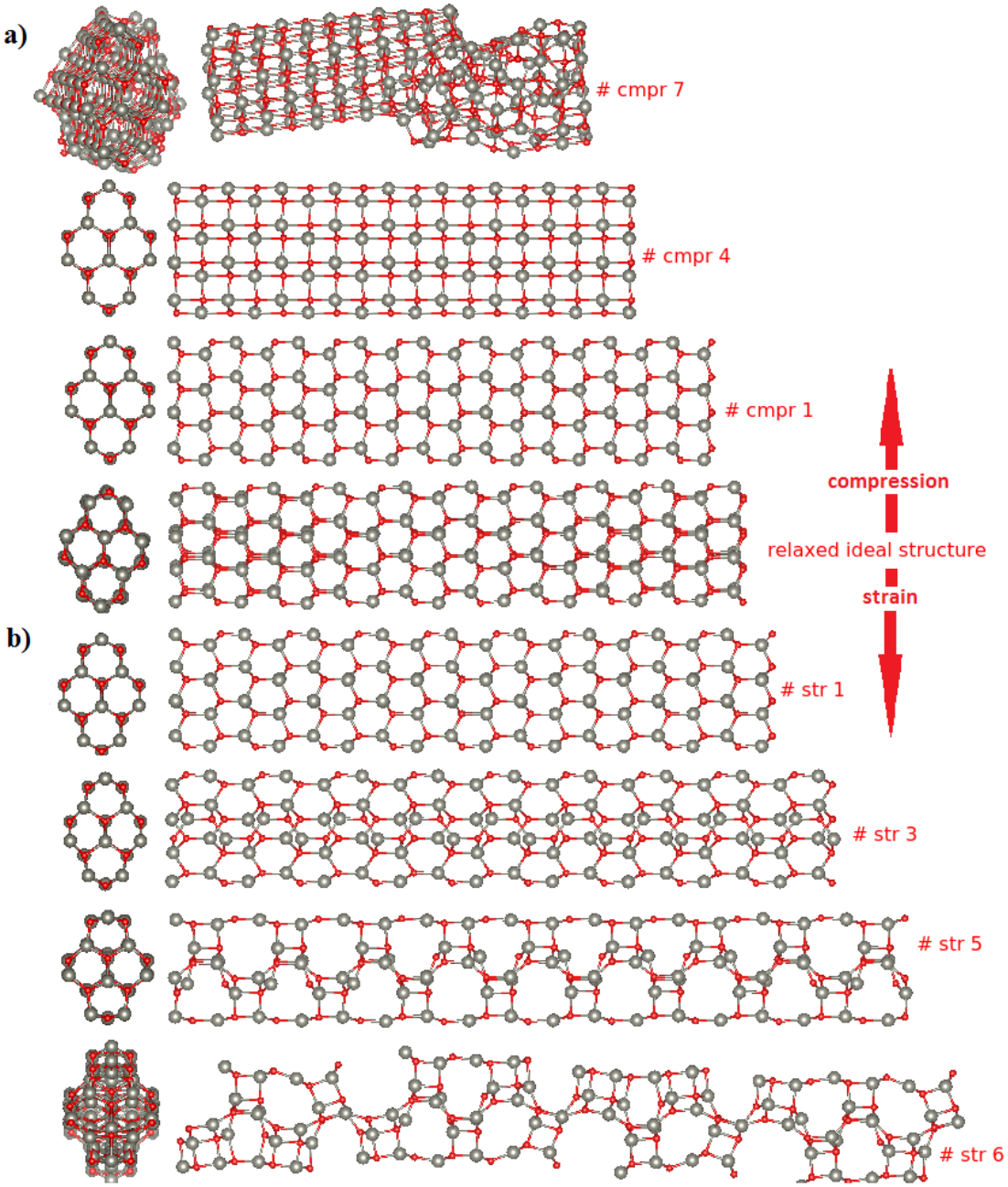

Figure 3.100 The RR model at 1 K under 5% strain applications a) compression b) tensile strain.

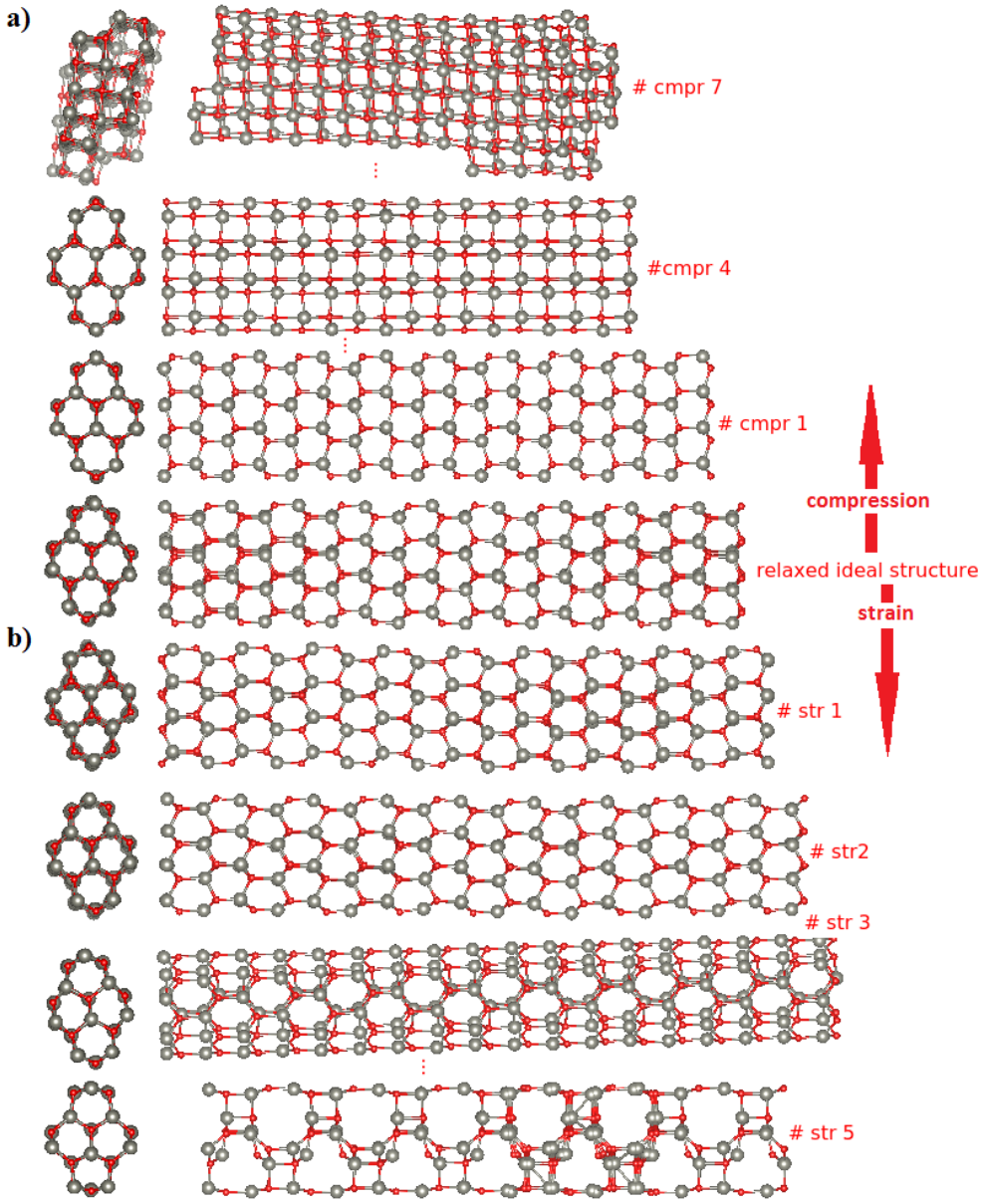

Figure 3.101 The RR model at 300 K under 5% strain applications a) compression b) tensile strain.

Lee and co-workers studied the mechanical properties of ultrathin zinc oxide nanowires by using Buckingham interatomic potential via MD. According to their study, due to the flexibility of Zn-O bond, the phase transformation is observed in addition the atom chains under tensile strain[130]. In other study, Zhou's calculations indicated that a uniaxial strain of ZnO nanowires can lead to a transformation from wurtzite phase to a graphitic phase[131,132]. Similar findings also appear in the present study.

3.2.3 ZnO Nanotubes

We have mentioned in previous section that four different sizes, namely (5,0), (6,0), (7,0) and (8,0) for the zigzag nanotubes (will be referred to as ZT1, ZT2, ZT3 and ZT4, respectively) (see Figure 2.22) and four different sizes, namely (3,3), (4,4), (5,5) and (6,6) for the armchair nanotubes (will be referred to as AT1, AT2, AT3 and AT4, respectively) (see Figure 2.23) have been considered. On the other hand, four different chirality of (5,0) nanotubes model, namely (5,1), (5,2), (5,3) and (5,4), which represented CT1, CT2, CT3 and CT4 respectively (see Figure 2.24), have been considered[9].

After the energetic relaxation process, the ZT1 model transformed into rod structure at both 1 and 300 K when PBC was not applied. The rod structure at 1 K consisted of two hexagonal cross sectional rods whereas the rod structure at 300 K consisted of one hexagon and two squares cross sectional rods when viewed from the top. However, when viewed from the side, the rods at both 1 and 300 K completely configured with square grid geometry (see Figure 3.102). When the PBC was applied at 1 K, the ZT1 model maintained its initial structure at both 1 and 300 K, but both the tube radius and average bond length between atoms increased at both 1 and 300 K. Such that, the average bond length was initially taken of 1.897 Å, after the energetic relaxation process it increased into 1.913 Å for 1 K, 1.916 Å for 300 K. In the case of 5% compression strain applications at 1 K, the ZT1 model also preserved its initial structure, and average bond length between atoms did almost not change, but the tube radius increased from 2.702 Å into 2.968 Å at first three compression strain steps. Then, the hexagonal grid geometry completely changed into squares at 5^{th} compression strain step. In the sixth application of compression strain steps, the tube structure changed into rod structure (see Figure 3.103 a). In the case of 5% tensile strain applications at 1 K, the ZT1 model also retained its initial structure, but the average bond length of the strained structure increased and the tube radius decreased at the first three tensile strain steps. Then, the structure was broken into two as tubes at 4^{th} tensile strain step (see Figure 3.103 b). In the case of 5% compression strain at 300 K, the ZT1 model retained its initial tube structure and the average bond length increased, but the tube radius of the structure was decreased from 2.697 Å into 2.507

Å in the first three compression strain steps. Then, the structure was deformed at 4th compression strain step (see Figure 3.104 a). In the case of 5% tensile strain applications at 300 K, the same relaxed structure at 1 K similarly retained its initial tube structure, and average bond length was increased from 1.916 Å into 2.009 Å but the tube radius was decreased range from 2.697 Å to 2.507 Å at first three tensile strain steps. Then, the structure broken into two parts as bilayers at 4th tensile strain step (see Figure 3.104 b).

After the energetic relaxation, the ZT2 model structure also changed into rod structure in the absence of PBC at both 1 and 300 K. The rod structure at 1 K included two hexagons and one square cross sectional rods whereas the rod structure at 300 K included one hexagon and three squares cross sectional when viewed from the top and when viewed from the side at both 1 and 300 K, the rod structures completely configured with square grid geometry (see Figure 3.105). In the presences of the PBC, the ZT2 model at both 1 and 300 K kept its ideal tube structure after the energetic relaxation. In the case of 5% compression strain at 1 K, the ZT2 model also preserved its initial structure at first four compression strain steps. During these steps, the bond length between atoms did not change, but the tube radius was increased from 3.215 Å into 3.627 Å (see Figure 3.108-Figure 3.109). In the fifth application of compression strain steps, the structure turned into rod structure (see Figure 3.106 a). In the case of 5% tensile strain applications at 1 K, the same model also maintained its initial structure at the first four tensile strain steps. During these steps, the average bond length between the atoms was increased whereas the tube radius was decreased in the structure. In the fifth application of tensile strain steps the structure broken into two tubes (see Figure 3.106 b). In the case of 5% compression strain applications at 300 K, on the other hand, the ZT2 model also maintained its initial structure and the average bond length between atoms did not change, but the tube radius in the structure increased from 3.215 Å into 3.434 Å at first two compression strain steps (see Figure 3.108-Figure 3.109). In the third applications of compression strain steps, the structure turned into rod structure (see Figure 3.107 a). In the case of 5% tensile strain applications at 300 K, the same model retained its initial structure at the first three tensile strain steps. During these steps, the average bond length of between atoms was increased from 1.912 Å into 2.005 Å whereas tube radius was decreased from 3.215

Å into 2.977 Å (see Figure 3.108Figure 3.109). In the fourth application of tensile strain steps the structure fragmented into three parts (see Figure 3.107 b).

Additionally, the ZT3 and ZT4 model structure almost exhibited similar mechanical properties to ZT1 and ZT2 models (see Appendix A).

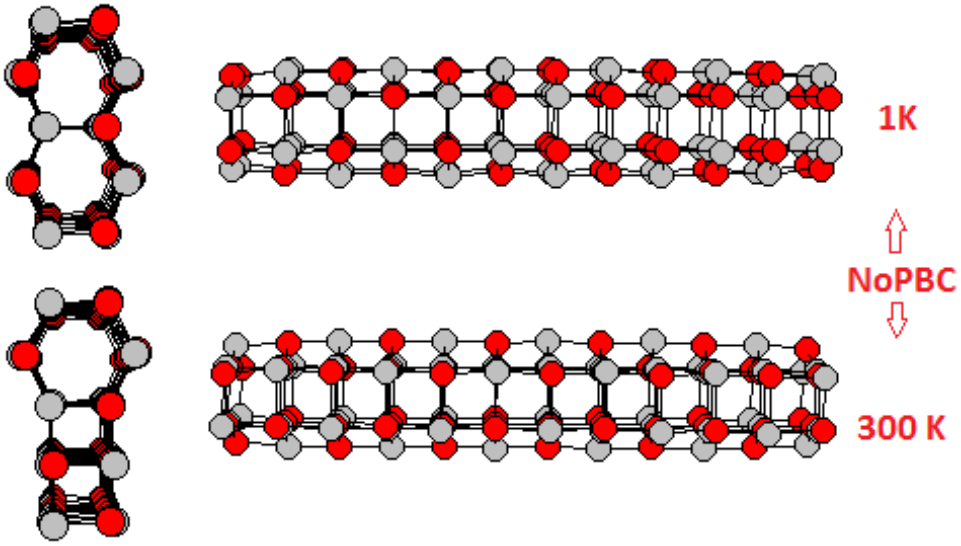

Figure 3.102 The ZT1 model with NoPBC at 1 and 300 K.

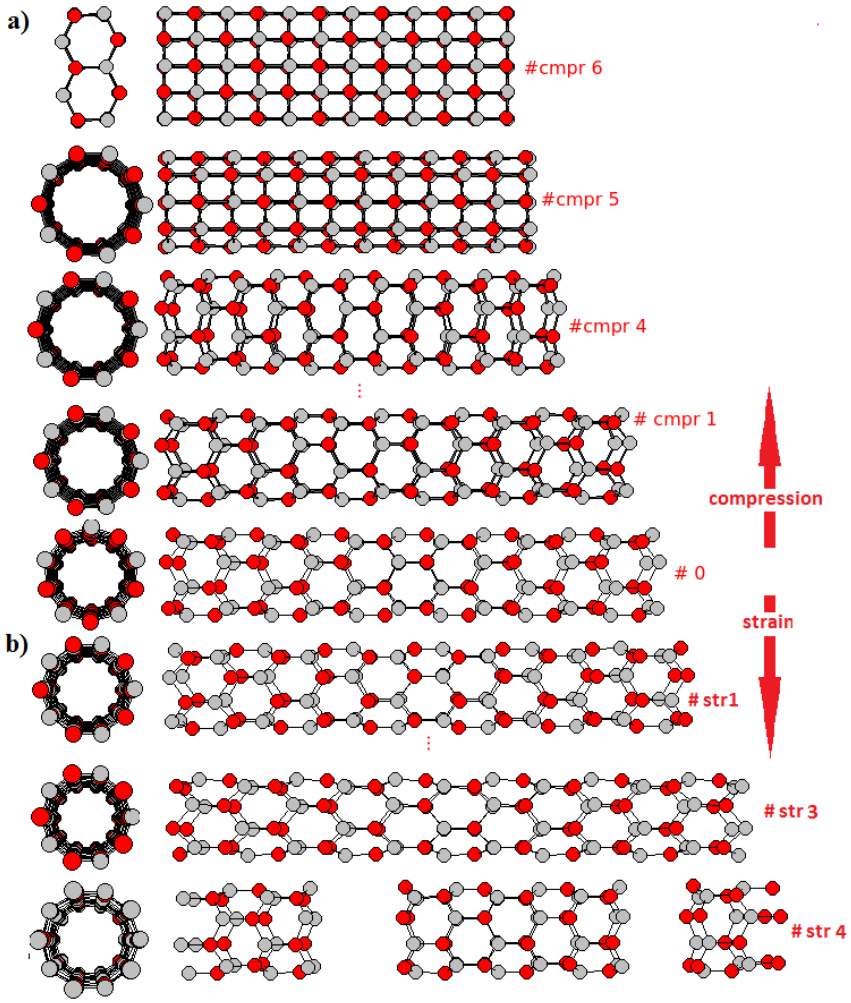

Figure 3.103 The ZT1 model structure at 1 K under strain applications a) 5% compression b) 5% tensile strain.

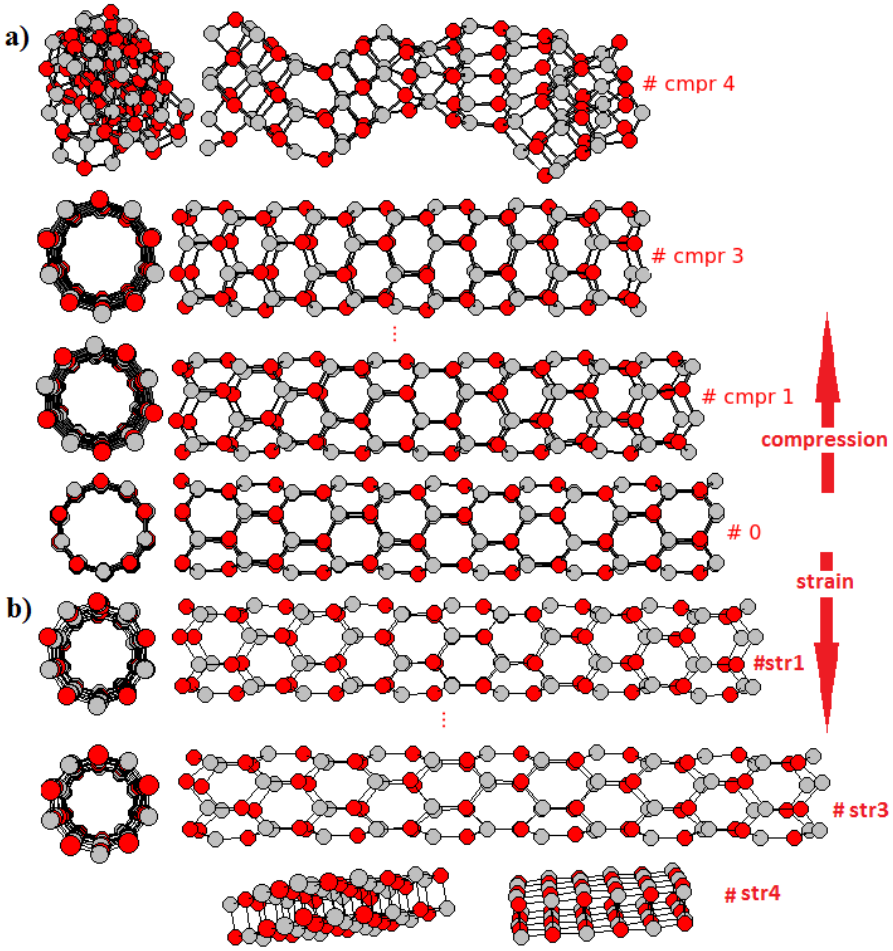

Figure 3.104 The ZT1 model structure at 300 K under strain applications a) 5% compression b) 5% tensile strain.

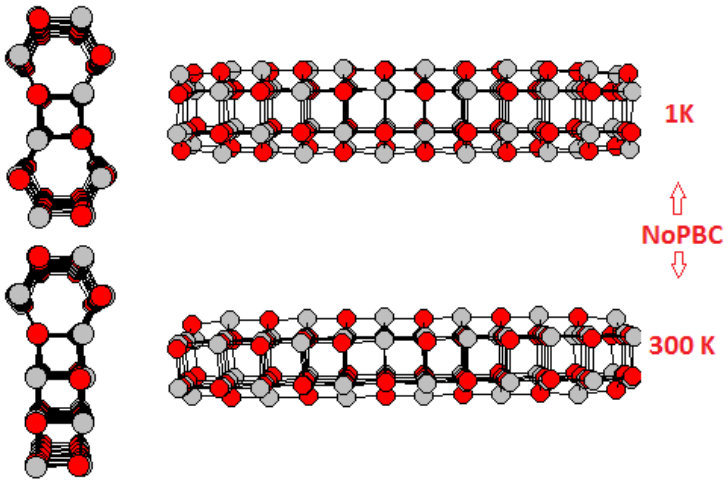

Figure 3.105 The ZT2 model structure with NoPBC at both 1 and 300 K.

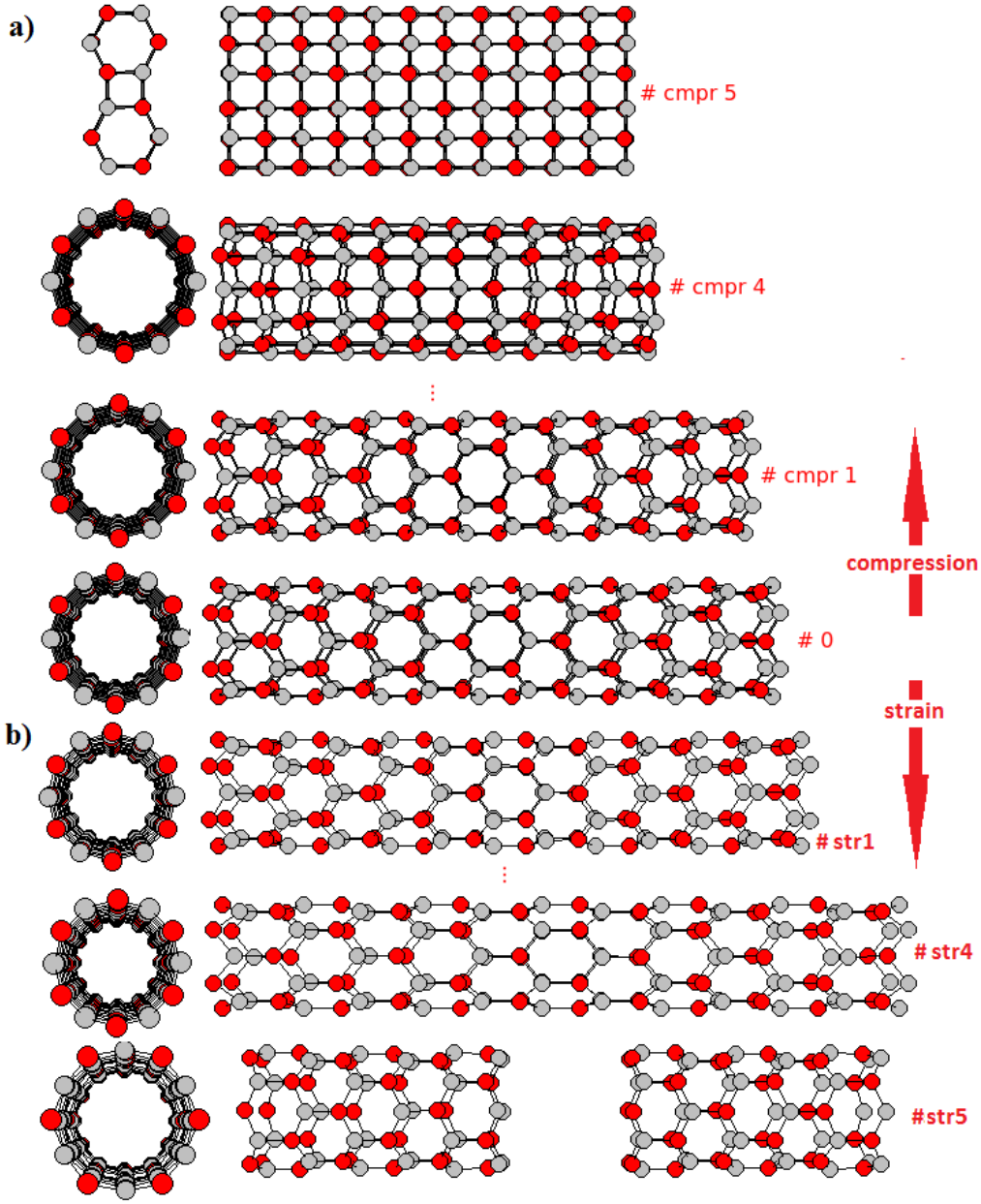

Figure 3.106 The ZT2 model structure at 1 K under strain applications a) 5% compression b) 5% tensile strain.

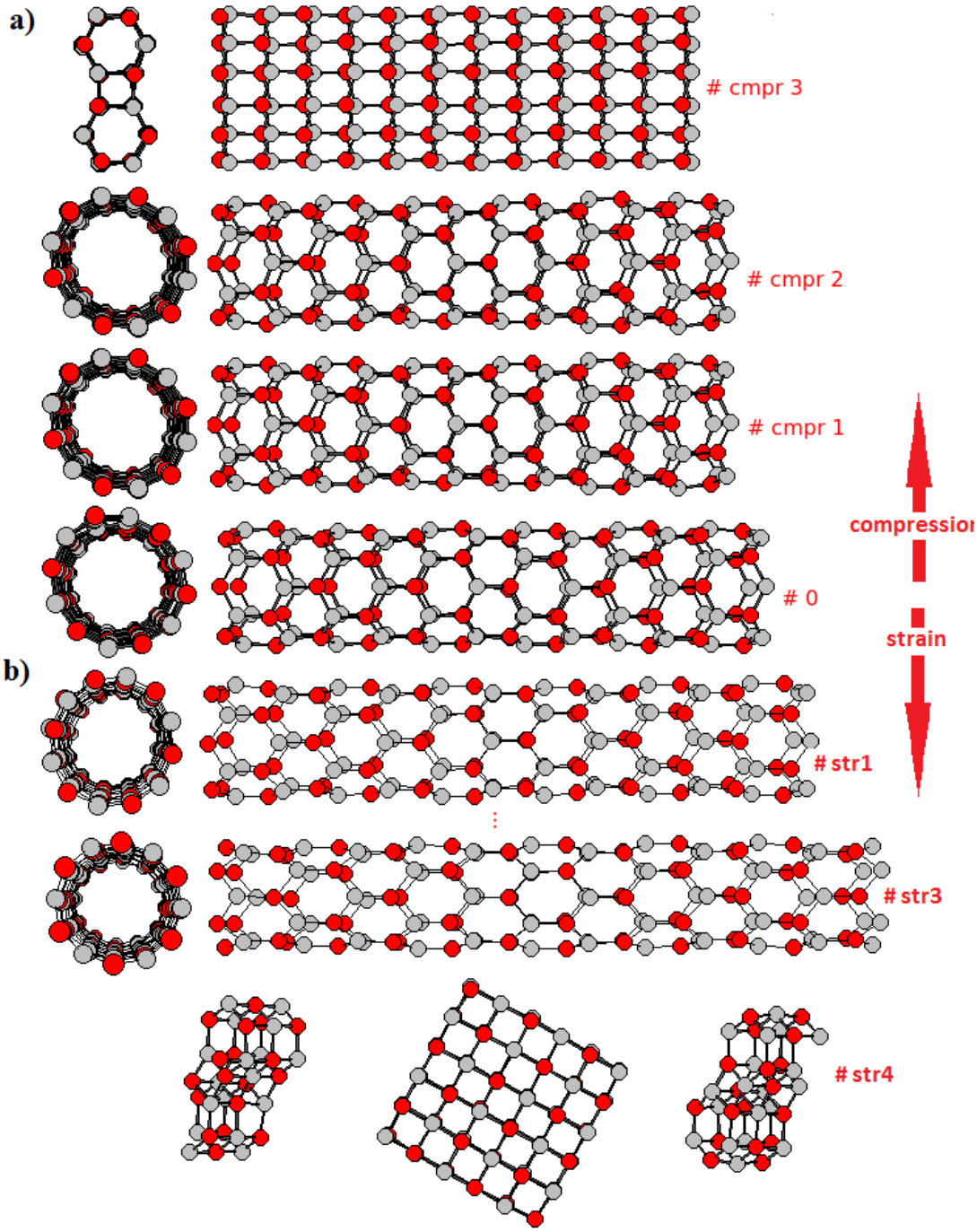

Figure 3.107 The ZT2 model structure at 300 K under strain applications a) 5% compression b) 5% tensile strain.

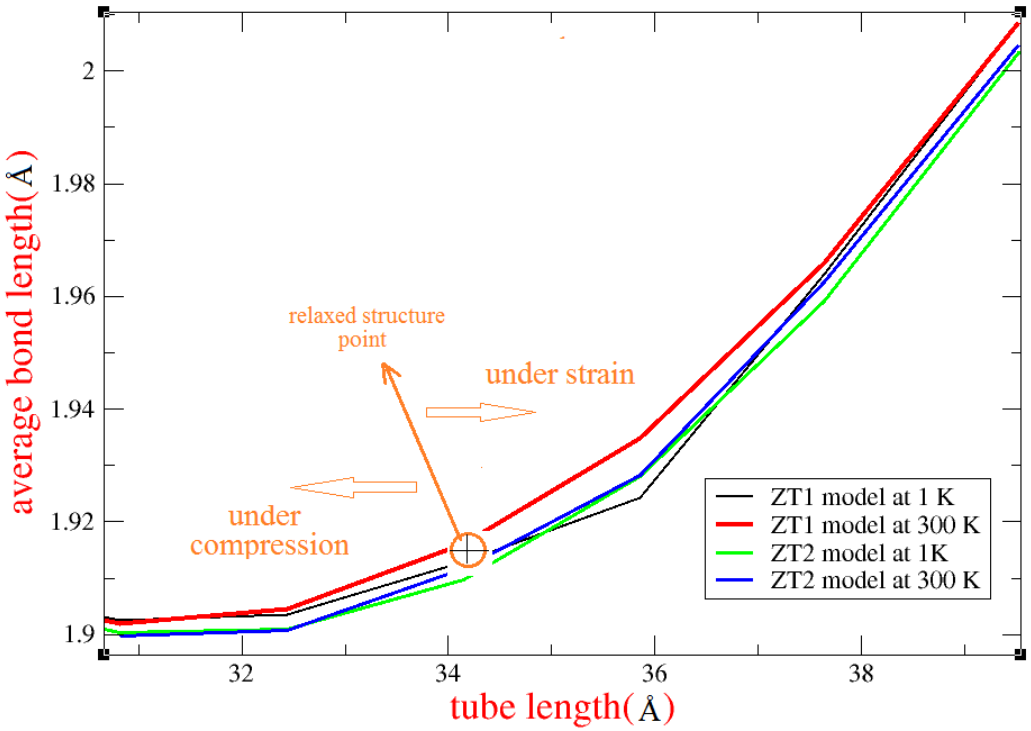

Figure 3.108 The average bond length between atoms versus tube length of the ZT1and ZT2 models at both 1 and 300 K under compression and tensile strain applications.

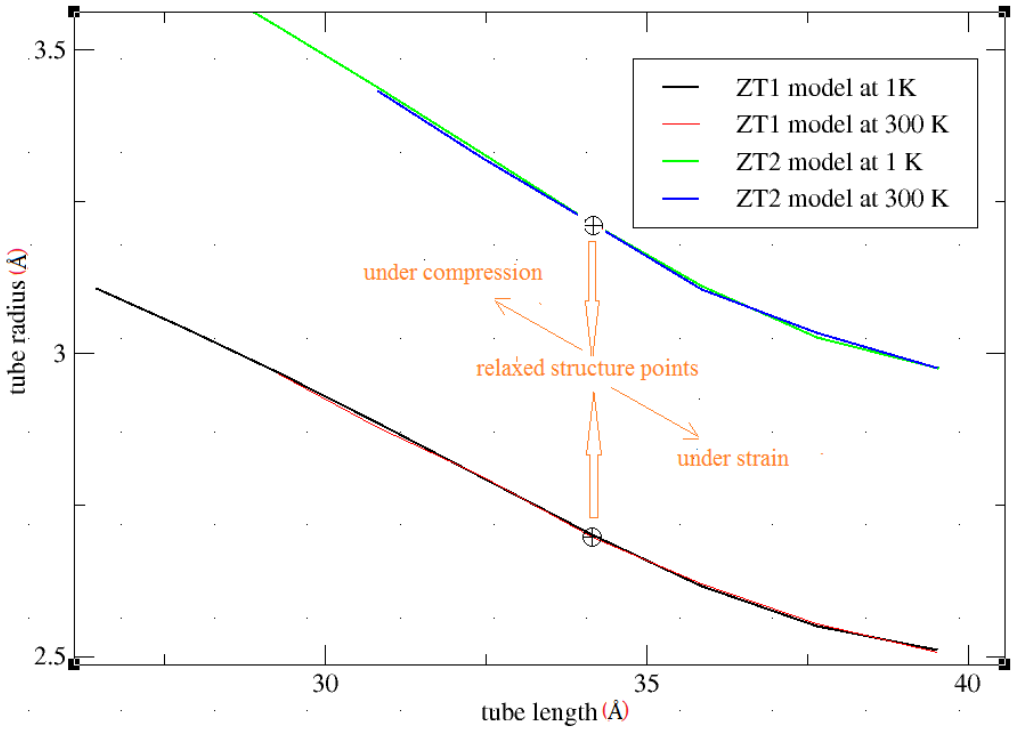

Figure 3.109 The average tube radius versus tube length of the ZT1 and the ZT2 models at both 1 and 300 K under compression and tensile strain.

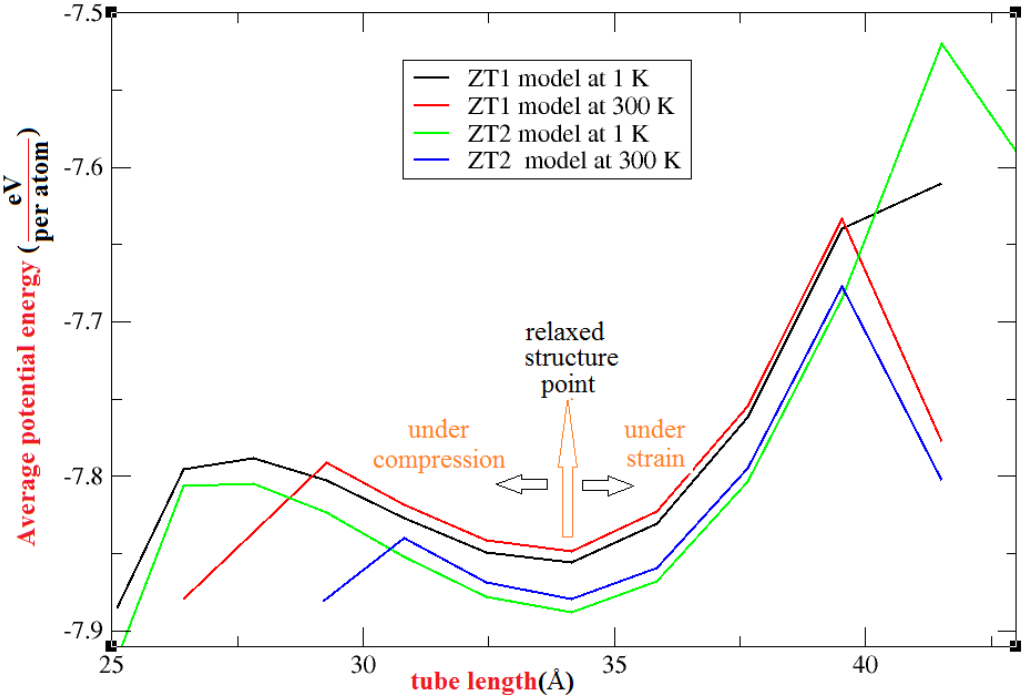

Figure 3.110 The average potential energy for per particle versus tube length for the ZT1 and ZT2 models at both 1 and 300 K under compression and tensile strain.

The AT1 model almost retained tube structure, but the ends of the structure were closed when PBC was not applied at 1 K. So the tube changed into capsule shaped structure at that conditions. The same model at 300 K evolved into a dumbbell shaped structure with NoPBC. When PBC was applied the AT1 model preserved its ideal tube structure both at 1 and 300 K (see Figure 3.111). In the case of 5% compression strain at 1 K, the AT1 model almost maintained its ideal structure, but the average bond length between atoms and the tube radius changed (see Figure 3.117Figure 3.118). In the third application of compression strain steps, the neck points in the structure were detected. In the case of 5% tensile strain applications at 1 K, the same model preserved its tube structure at 1st tensile strain step. In the second application of tensile strain steps, the same parts of the tube structure changed into rod. Then, the structure changed into a dumbbell shaped structure at 3rd tensile strain step. Then, the structure completely changed into rod, which configured with square grid geometry when viewed from the side. After a few applications of tensile strain steps, the square grid geometry in the rod structure changed into hexagonal grid

geometry (see Figure 3.112). In the case of 5% compression strain applications at 300 K, the same model maintained its ideal structure at 1st compression strain. In the second application of compression strain steps, the structure became amorphous. In the case of 5% tensile strain applications at 300 K, the same model abruptly deformed, which appeared as a dumbbell like structure in the first three tensile strain steps. In the fourth application of tensile strain steps the structure changed into rod structure, which configured with square grid geometry when viewed from the side. And then, the rod structure (or actually (3,0) zigzag tube structure) configured with hexagonal grid geometry when viewed from the side at 8th tensile strain step (see Figure 3.113). Moreover, the average bond length between atoms was increased during the tensile strain applications.

After the energetic relaxation, the AT2 model also transformed into a capsule shaped structure at 1 and 300 K without PBC (see 3.114). When the PBC was applied, the same model maintained its ideal structure at both 1 and 300 K after the energetic relaxation. In the case of 5% compression strain applications at 1 K, the same model almost maintained its initial structure at 1st compression strain step. In the second application of compression strain steps, the neck points were detected. In the case of 5% tensile strain applications at 1 K, the AT2 model almost retained its initial structure at 1st tensile strain step. In the second application of tensile strain steps, the structure changed into a perfect dumbbell like structure. Interestingly, in the fourth application of tensile strain steps, the structure also changed into tube structure, but the tube radius was decreased and the tube configured with square grid geometry when viewed from the side. After a few applications of tensile strain steps, the squares in the tube structure changed into hexagons. Then, the (4, 0) zigzag tube structure took place at 9th tensile strain step.

Then, the zigzag tube structure did not change following a few tensile strain steps, but its tube radius was slightly decreased. Then, the structure was broken at 16th tensile strain step (see Figure 3.115). In the case of 5% compression strain at 300 K, the AT2 model abruptly became amorphous at 1st compression strain step. In the case of 5% tensile strain applications at 300 K, the same model slightly preserved its initial tube structure. In the second application of tensile strain steps, the AT2 model changed into a dumbbell like structure (or bamboo like). Then, the structure changed into the rod structure at 4th tensile strain step which looked like one hexagon and one square cross sectional rods. Then, the structure turned into the (4, 0) zigzag tube structure at 10th tensile strain step. The atom chain formation took place in the structure at 14th tensile strain step (see Figure 3.116). The average bond length and the average potential energy versus tube length of the model are shown in Figure 3.117Figure 3.118.

Additionally, the AT3 and AT4 model structure almost exhibited similar mechanical properties with AT1 and AT2 models (see Appendix A).

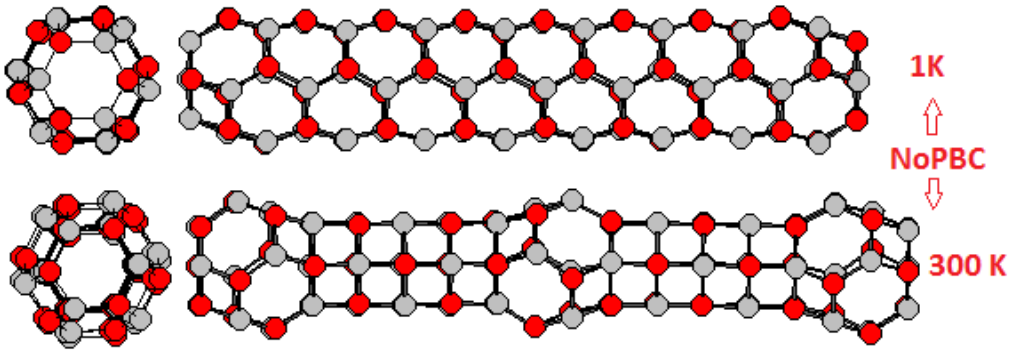

Figure 3.111 The AT1 model structure at both 1 and 300 K with NoPBC. The left picture views from the top, the right picture view from the side in each figures.

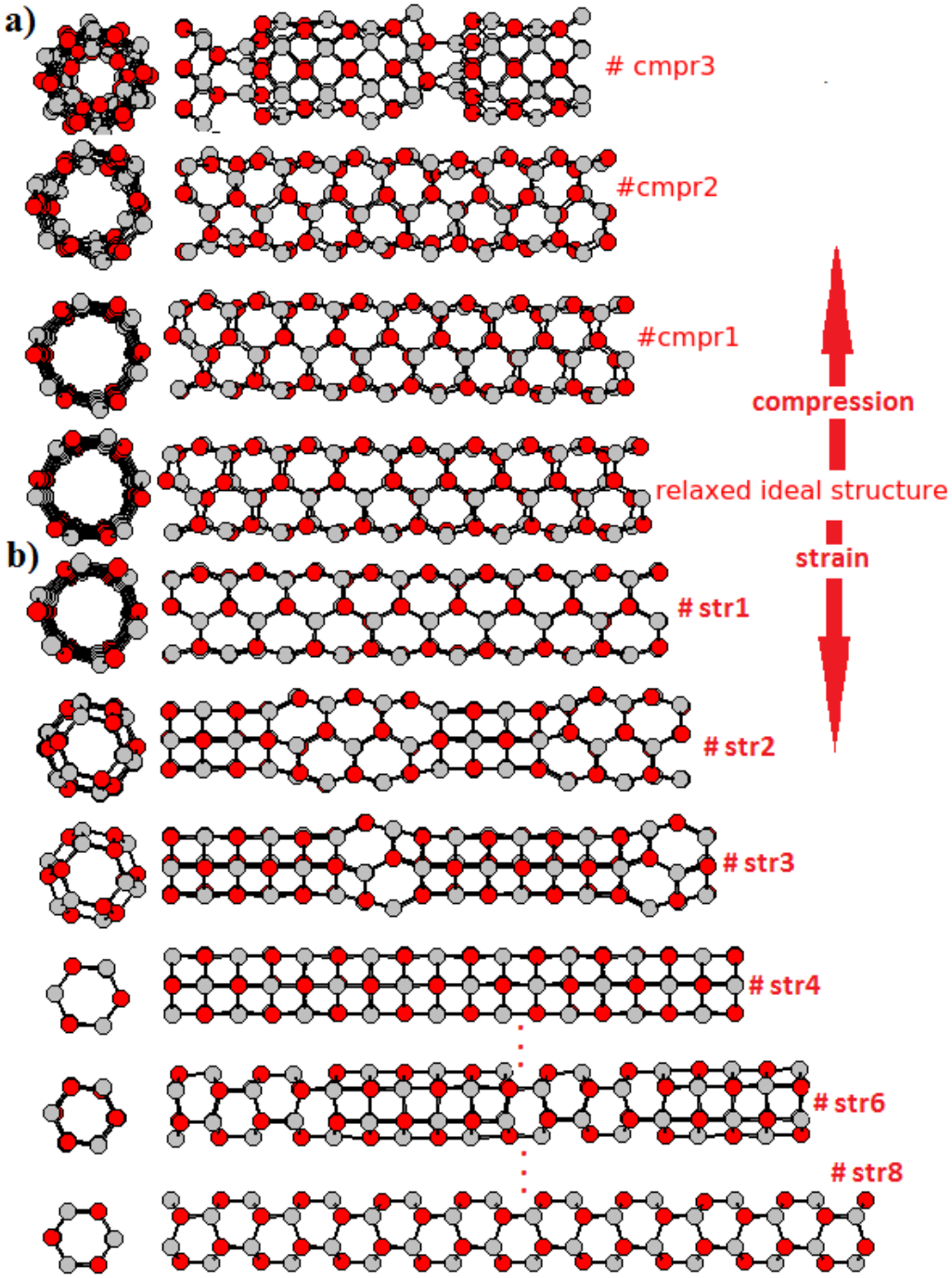

Figure 3.112 The AT1 model structure at 1 K under strain applications a) 5% compression b) 5% tensile strain.

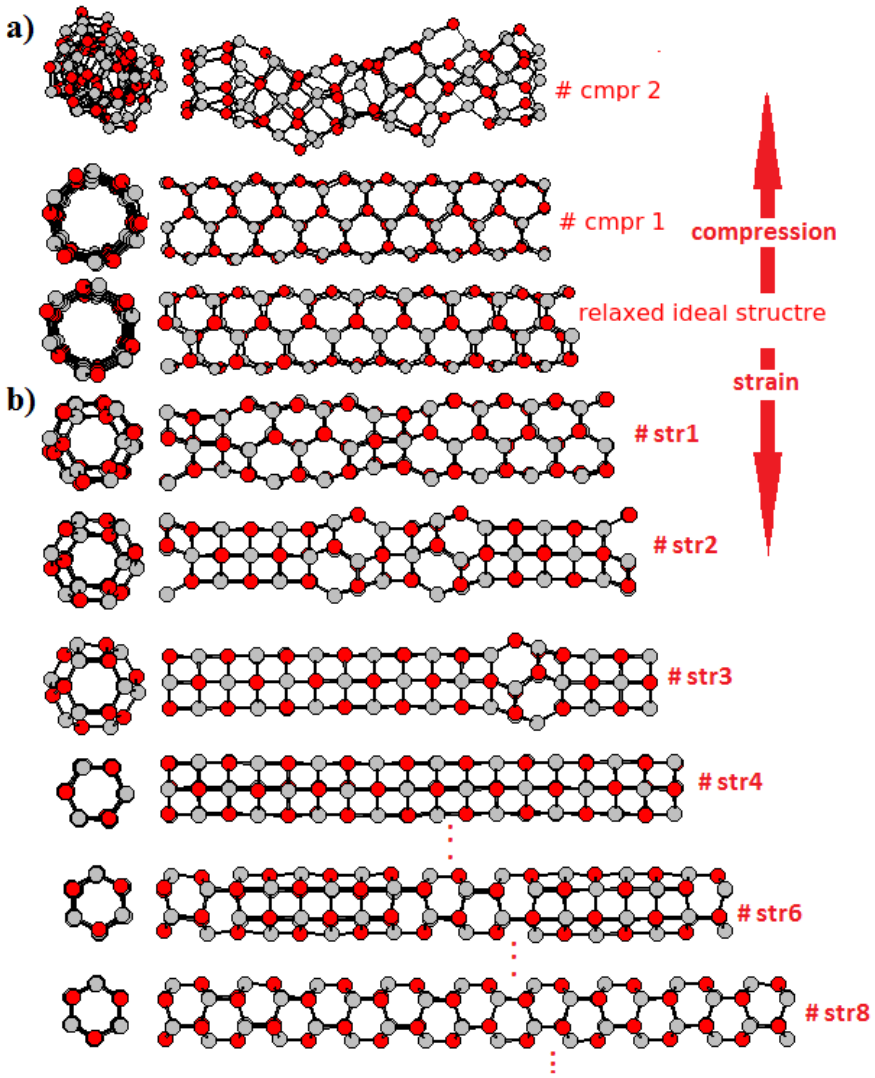

Figure 3.113 The AT1 model at 300 K under strain applications a) 5% compression b) 5% tensile strain.

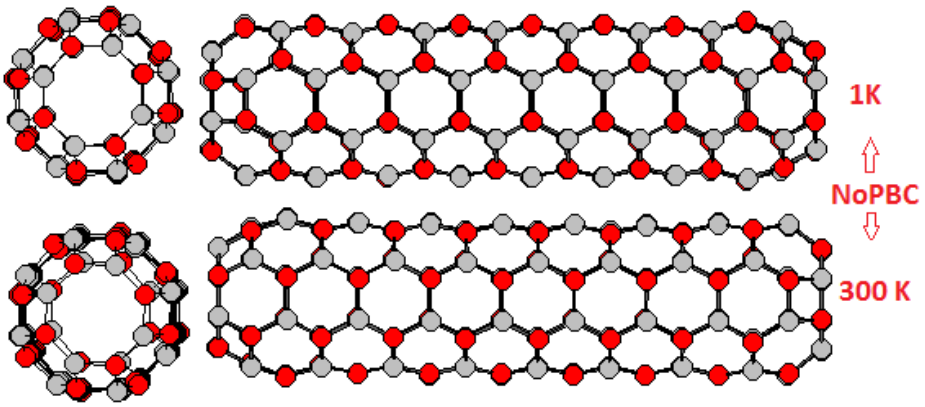

Figure 3.114 The AT2 model structure at both 1 and 300 K with NoPBC.

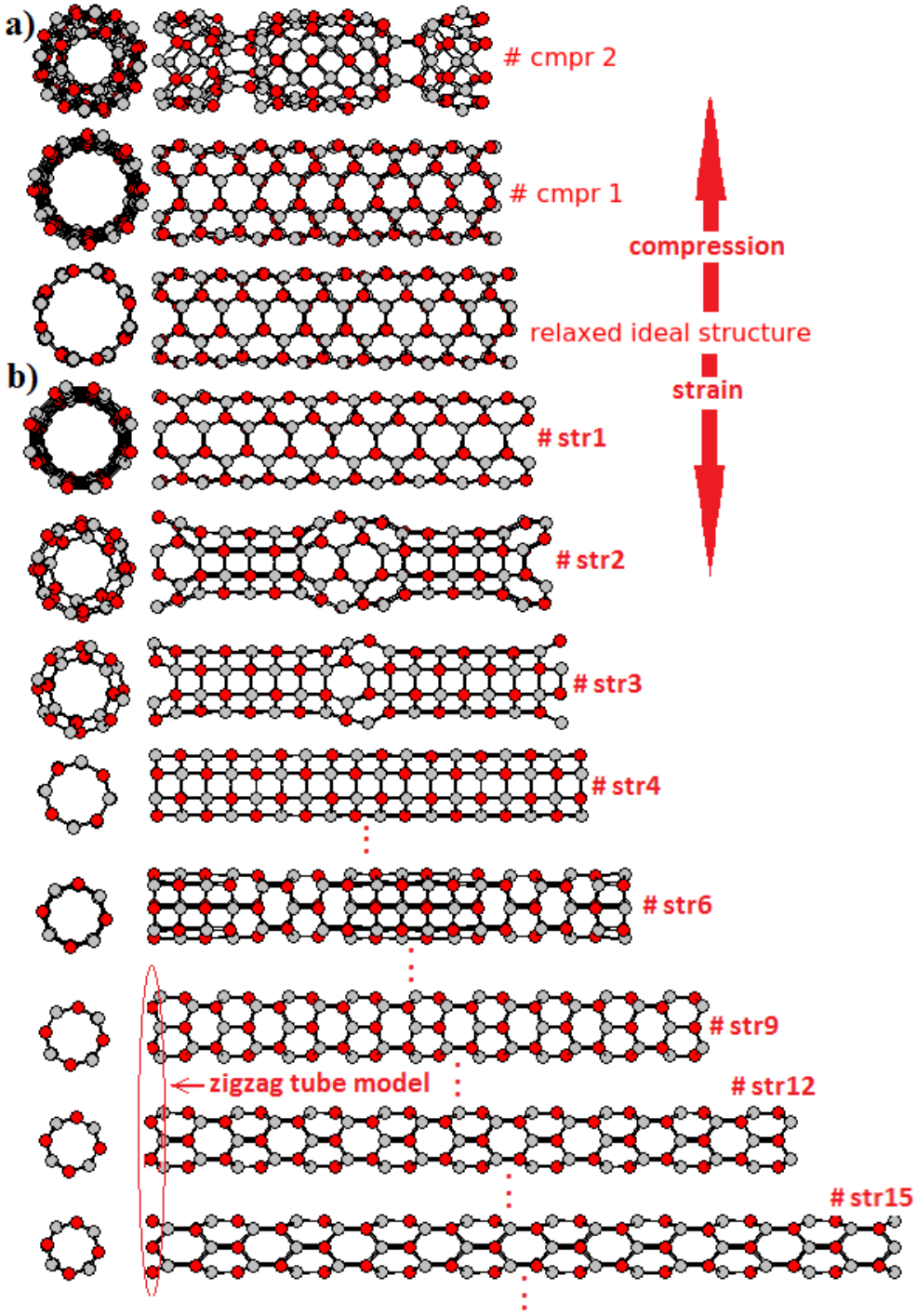

Figure 3.115 The AT2 model at 1 K under 5% strain application a) compression b) tensile strain.

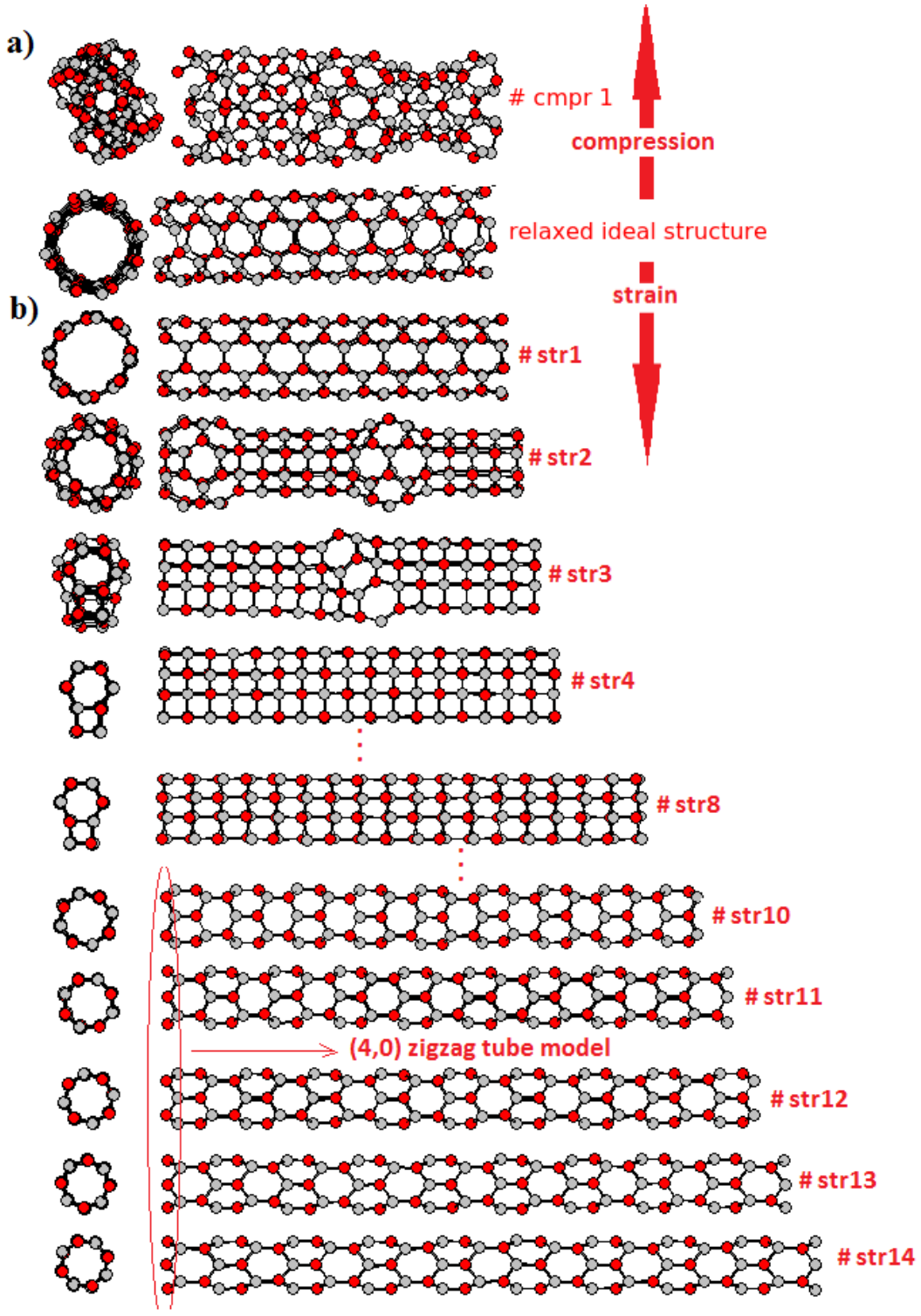

Figure 3.116 The AT2 model at 300 K under 5% strain applications a) compression b) tensile strain.

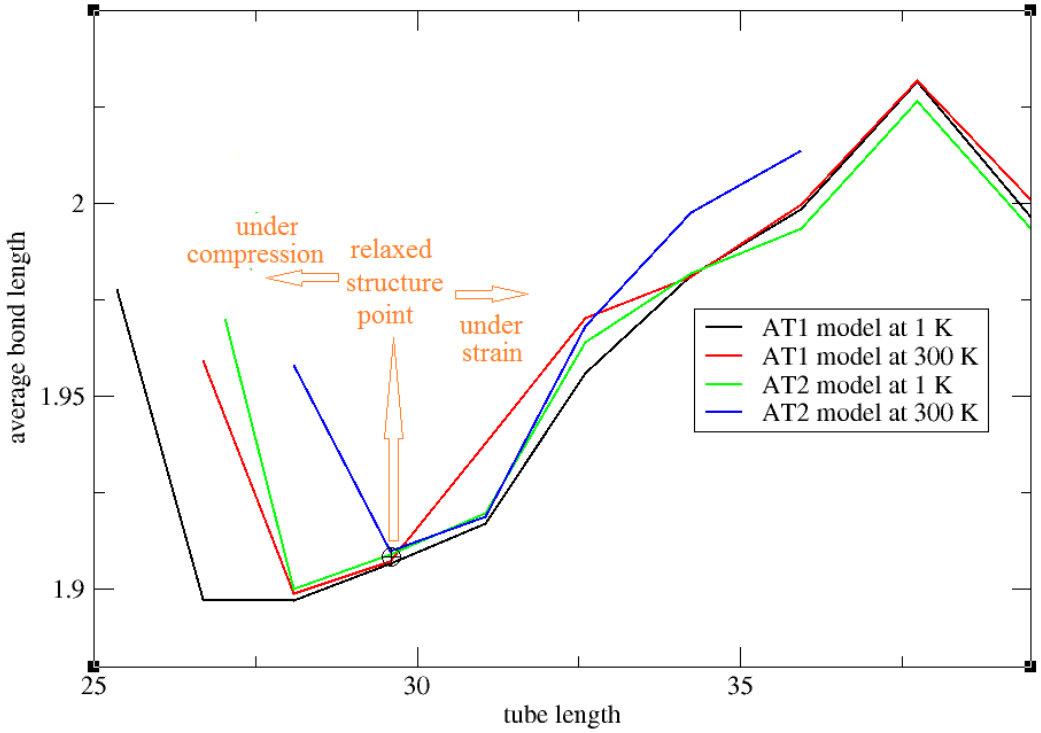

Figure 3.117 The average bond length between atoms versus tube length at both 1 and 300 K under compression and tensile strain applications.

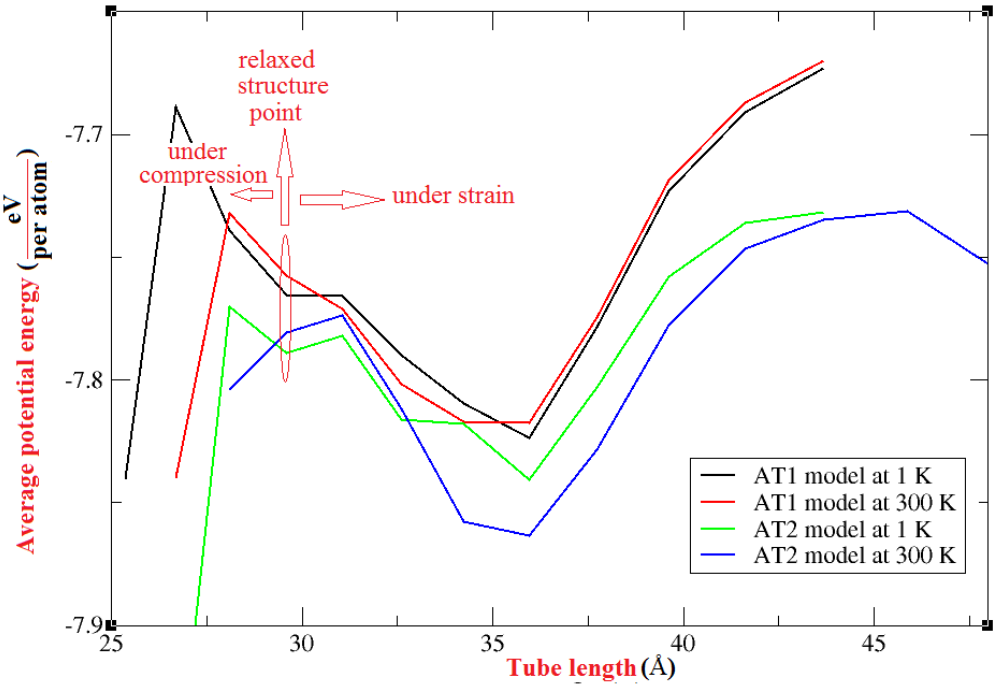

Figure 3.118 The average potential energy for per atom versus tube length of AT1 and AT2 models at both 1 and 300 K under compression and tensile strain applications.

The CT1 model almost did not retain its initial structure at 1 and 300 K when PBC was not applied, which closed one end of the structure after the energetic relaxation (see Figure 3.119 a). However, the same model retained its initial structure at both 1 and 300 K when PBC was applied (see Figure 3.119 b). When subject to 5% tensile strain applications at 1 K, the CT1 model almost preserved its initial structure in the first four applications of tensile strain steps. In the fifth application of tensile strain steps, the tube structure changed into an amorphous like structure, which consisted of the neck points (see Figure 3.120). In the case of 5% tensile strain applications at 300 K, the same model also preserved its initial structure at first three tensile strain steps. In the fourth application of tensile strain steps, the tube appearance also changed into an amorphous like structure (see Figure 3.121).

The two ends of the CT2 model were closed when PBC was not applied at 1 K after the energetic relaxation. Moreover, one end of the structure changed into a rod like without PBC at 300 K (see Figure 3.122 a). However, the same model preserved its initial structure when PBC was applied at both 1 and 300 K (see Figure 3.122 b). In the case of 5% tensile strain applications, the structure retained its initial structure in the first three applications of tensile strain steps. Then, the structure looked like a slightly wavy tube like when viewed from the side at 4^{th} tensile strain step. After, the following the applications of tensile strain steps, the neck points and atom chain formations were detected in the structure, so the tube appearance disappeared (see Figure 3.123). In the case of 5% tensile strain applications at 300 K, the CT2 model maintained its initial relaxed structure in the first two applications of tensile strain steps. In the third applications of tensile strain step, the structure changed into a wavy tube like. In the fifth application of tensile strain steps, the neck points and atom chain formation were detected (see Figure 3.124).

Additionally, the CT3 and CT4 model structure exhibited similar mechanical properties with CT1 and CT2 models (see Appendix A).

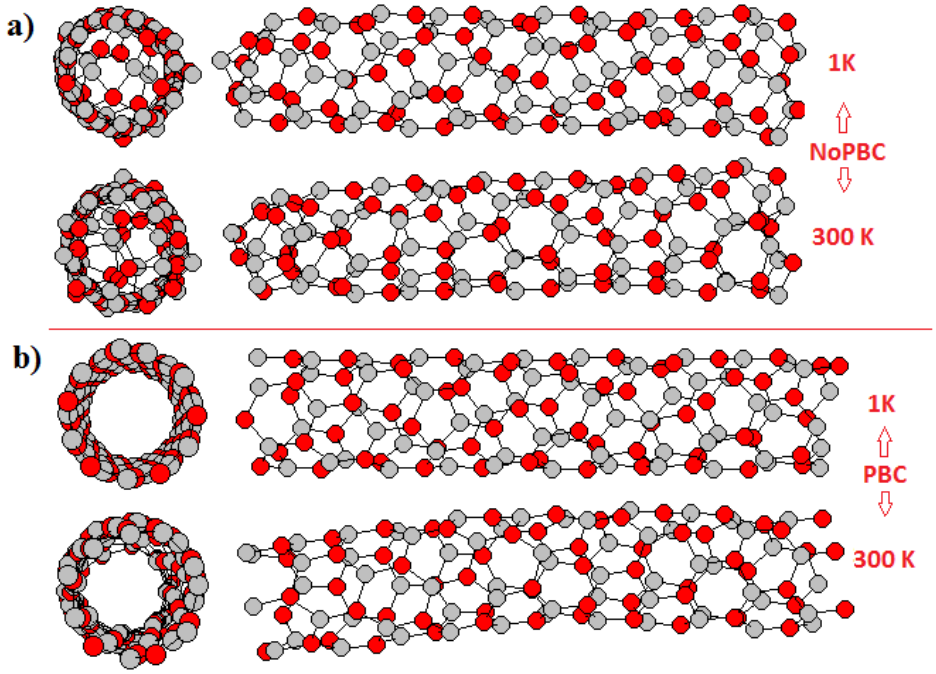

Figure 3.119 The CT1 model at 1 and 300 K a) with NoPBC b) with PBC.

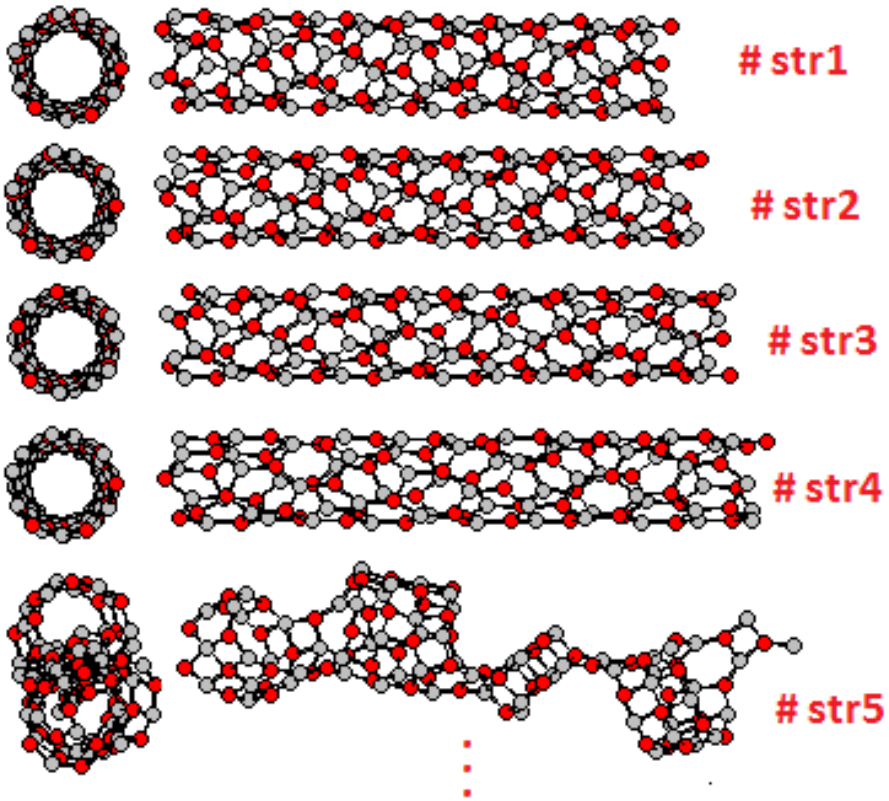

Figure 3.120 The CT1 model at 1 K under 5% tensile strain applications.

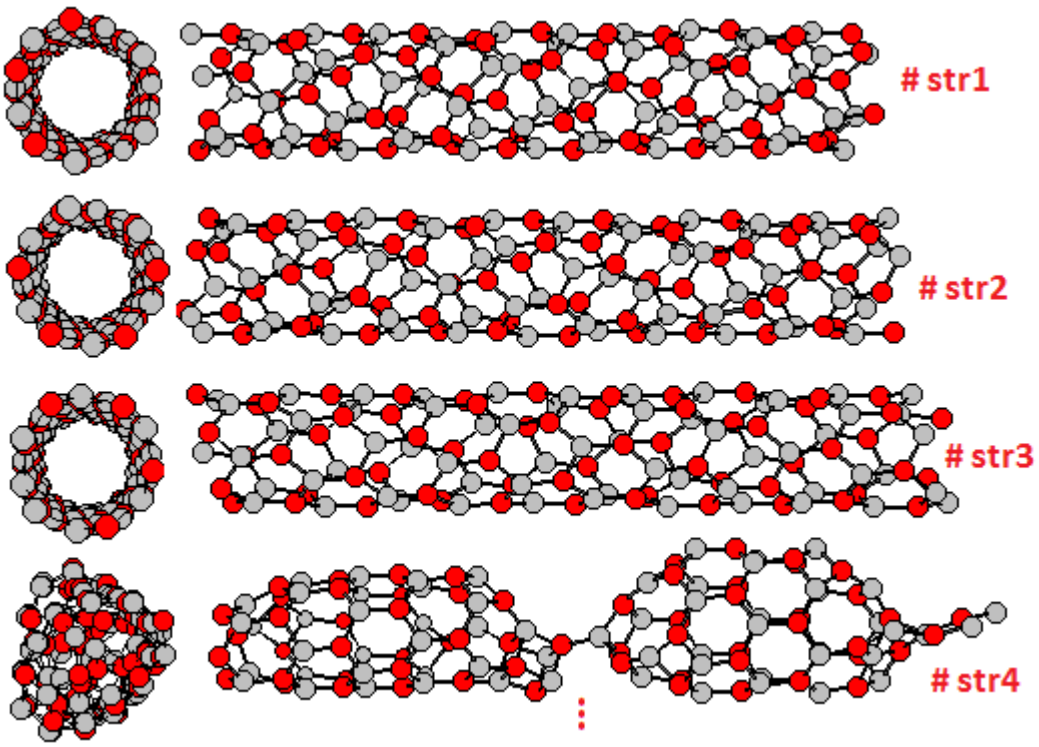

Figure 3.121 The CT1 model at 300 K under 5% tensile strain applications.

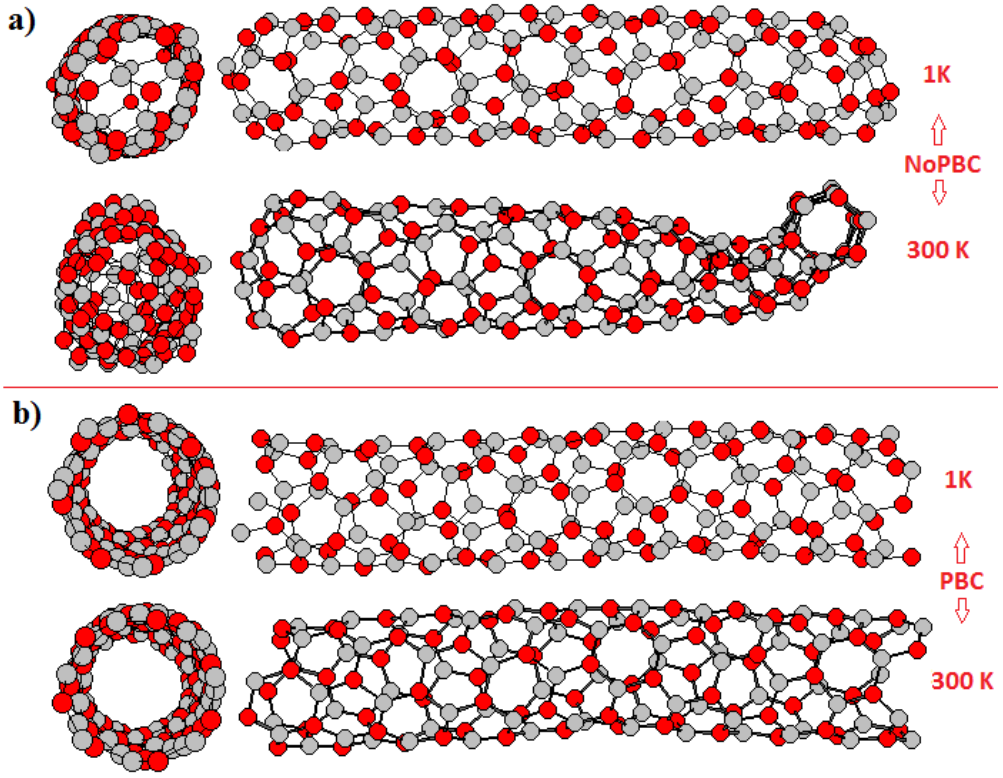

Figure 3.122 The CT2 model at 1 and 300 K a) with NoPBC b) with PBC.

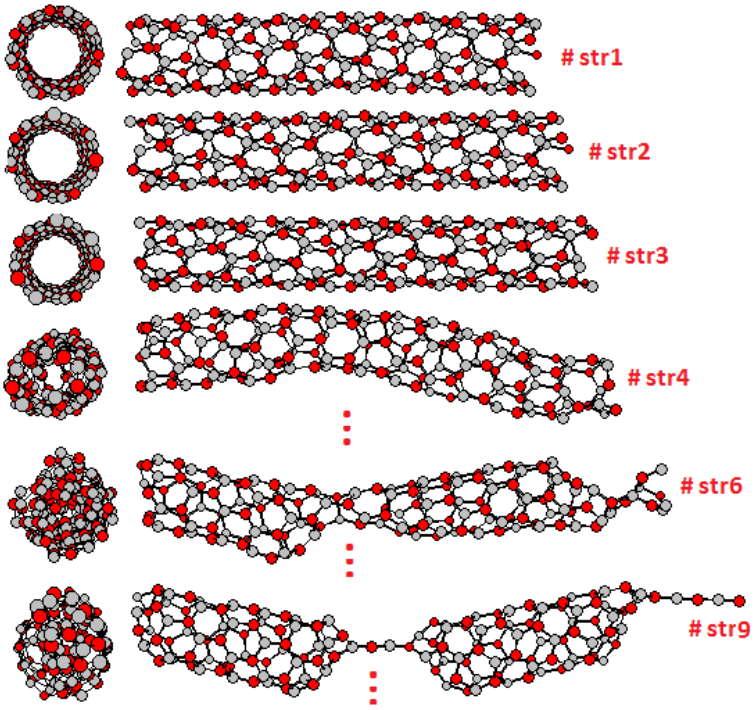

Figure 3.123 The CT2 model at 1 K under 5% tensile strain applications.

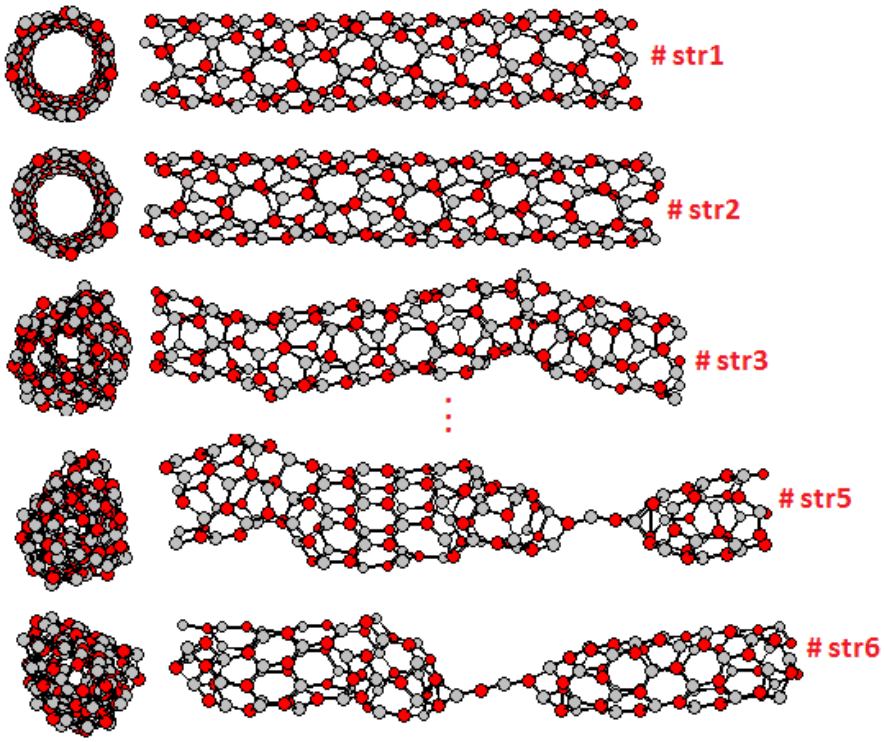

Figure 3.124 The CT2 model at 300 K under 5% tensile strain applications.

3.3 2D ZnO Nanostructures

3.3.1 ZnO Nanosheets

We have mentioned in previous section that we have investigated both pristine defected nanosheets for 2D nanostructures[120].

3.3.1.1 The Pristine Nanosheets

After the energetic relaxation, the hexagonal grid geometry of the PS model changed into square grid geometry at both 1 and 300 K when the PBC was not applied. Additionally, the defects were detected in the edge and corner of the structure at 1 K with NoPBC (see Figure 3.125 a). In the present of PBC, the same model preserved its initial structure at both 1 and 300 K, but looked like a wavy sheet when viewed from the side (see Figure 3.125 b). In the case of 5% tensile strain at 1 K, the PS model retained its initial ideal structure in the first two applications of tensile strain steps. Then, the structure was fragmented at 3rd tensile strain step (see Figure 3.126 a). In the case of 10 % strain at 1 K, the same model exhibited similar structural features to that of twice 5% tensile strain (see Figure 3.126 b). In the case of 15% tensile strain step at 1 K, the structure was abruptly fragmented at 1st tensile strain step (see Figure 3.126 c). Therefore, the rate of strain did not play an important role in that model. Moreover, the same model at 300 K, displayed similar features to that of 1 K run when subject to 5, 10 and 15% tensile strain applications, but the square grid geometry was dominantly appeared following the fragmentation due to the effect of temperature (see Figure 3.127).

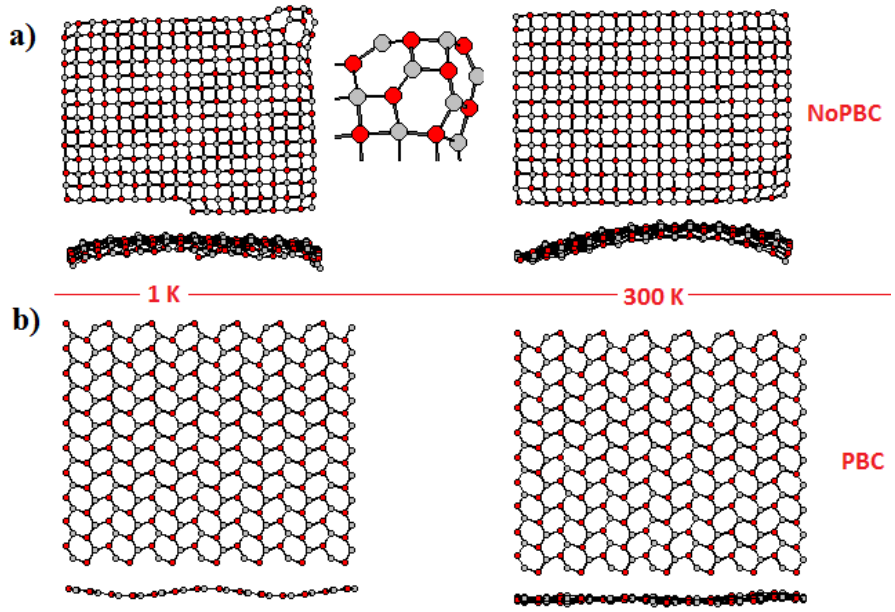

Figure 3.125 The PS model nanosheet structure at 1 and 300 K a) with NoPBC b) with PBC.

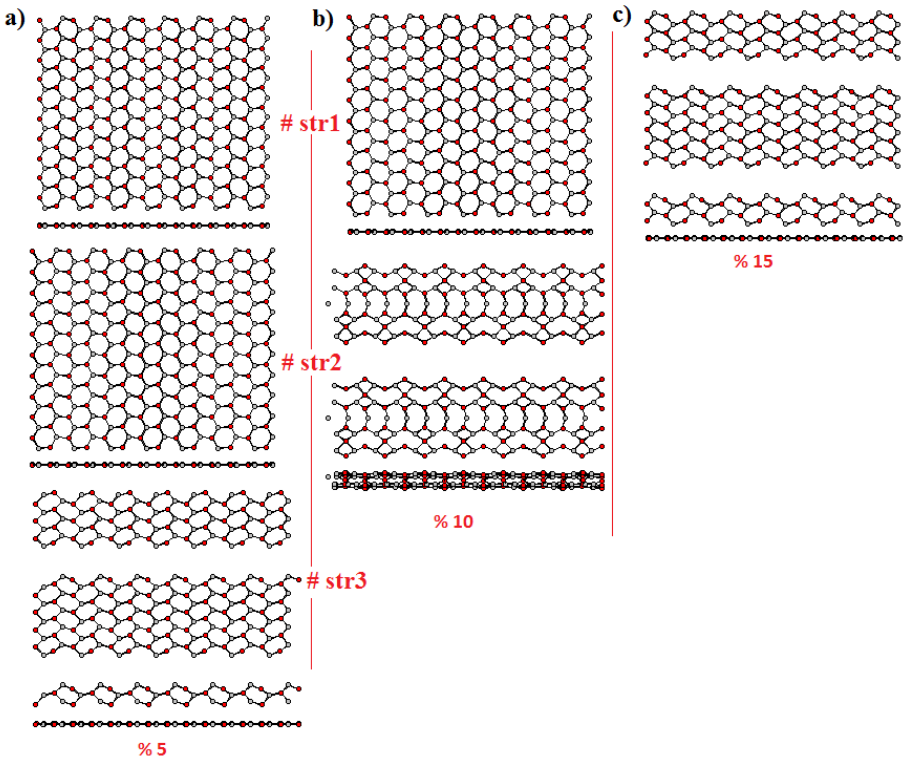

Figure 3.126 The PS model nanosheet under tensile strain applications at 1 K a) 5% strain b) 10% strain c) 15% strain .

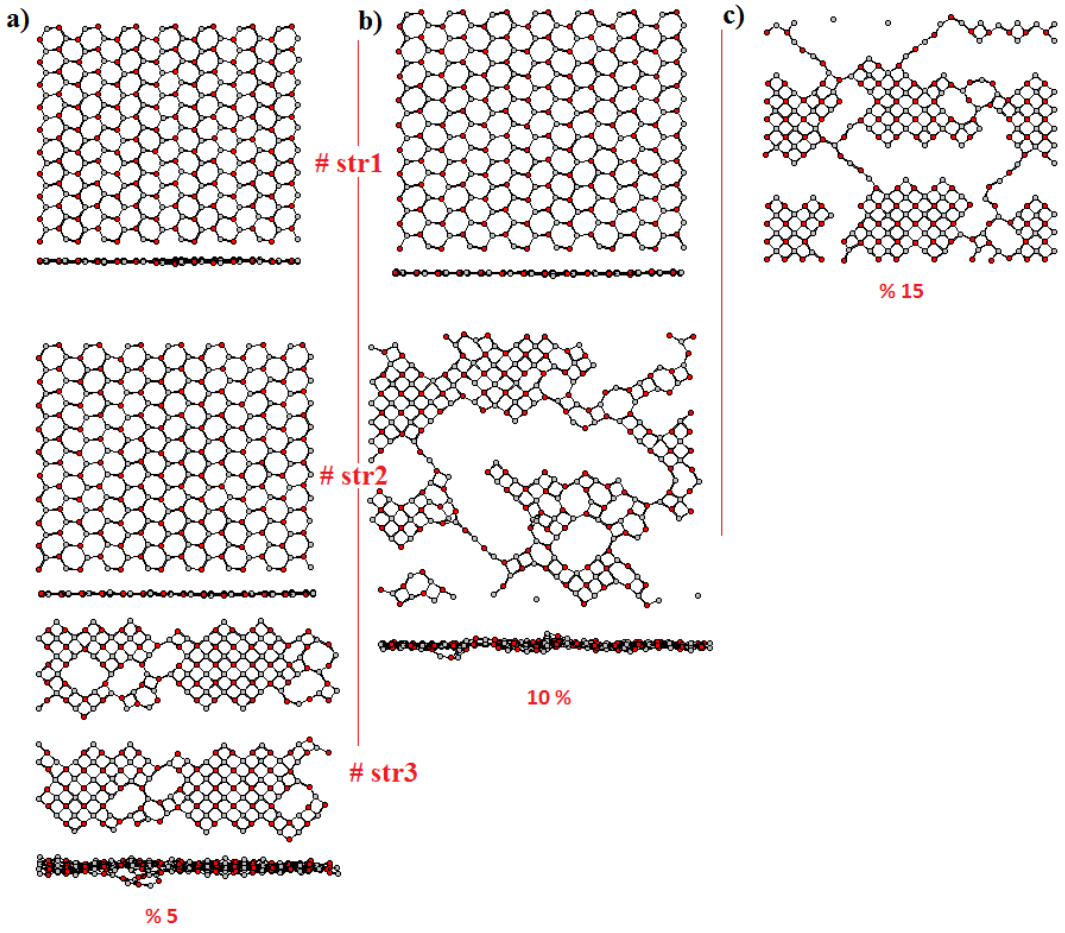

Figure 3.127 The PS model nanosheet at 300 K under tensile strain applications a) 5% strain b) 10% strain c) 15% strain.

3.3.1.2 The Defected Nanosheets

In the first stage of the defect study, we have investigated the vacancy type defects, namely monovacancy and divacancy for the defected nanosheets.

After the energetic relaxation, the SV-Zn model in the absence of PBC completely configured with square grid geometry, and took place a hole at the center of the structure and looked like a slightly out of plane bending structure when viewed from the side at both 1 and 300 K. The structure consisted of defects at the edge of the structure at 1 K as well (see Figure 3.128 b). However, the same model in the presences of PBC mostly maintained its initial vacancy structure, preserved hexagonal grid geometry at both 1 and 300 K, and looked like a slightly wavy structure when viewed from the side. In addition, the defect side moved along the PBC only at 300 K (see

Figure 3.128 c). In the case of 5% tensile strain applications at 1 K, the SV-Zn model was preserved its initial structure at 1st tensile strain step. In addition to the ideal vacancy defect, other defects (squares and irregular decagon geometries) were detected around the vacancy site at 2nd tensile strain step. In the third application of tensile strain steps, the sheet separated into two connected by an atom chain (see Figure 3.129 a). When subject to 10% tensile strain step at 1 K, the structure exhibited similar structural properties to that of twice 5% tensile strain at 1st tensile strain step (see Figure 3.129 b). In the case of 15% tensile strain at 1 K, the structure also exhibited similar structural properties to that of three fold 5% tensile strain, which fragmented at 1st tensile strain step (see Figure 3.129 c). Furthermore, when subject to 5% tensile strain step at 300 K, the SV-Zn model was also preserved its initial defect structure, but the vacancy site moved along the diagonal direction at 1st tensile strain step. In the second applications of tensile strain steps, the structure was fragmented (see Figure 3.130 a). When subject to 10% tensile strain, the SV-Zn model at 300 K was abruptly fragmented at 1st tensile strain step (see Figure 3.130 b).

After the energetic relaxation process, the SV-O model maintained its 2D sheet structure, including both a hole at the center of structure and defects at the edges of structure when PBC was not applied at 1 K. However, the same model changed into rod like structure without PBC at 300 K. Additionally, the structures at both 1 and 300 K dominantly configured with square grid geometry in the absence of PBC (see Figure 3.131 b). However, the same model, when PBC was applied at both 1 and 300 K, almost retained its ideal structure, but another defects (as two squares) were detected around of the vacancy in addition to vacancy defect part. Additionally, the defect site in the structure also moved along the diagonal direction at 300 K with PBC (see Figure 3.131 c). In the case of 5% tensile strain applications at 1 K, the SV-O model retained its ideal structure at 1st tensile strain step. In the second application of tensile strain steps, another defects were detected around of the vacancy site. Then, the structure fragmented at 3rd tensile strain step (see Figure 3.132 a). In the case of 10% tensile strain at 1 K, the same model exhibited similar features to that of twice 5% tensile strain at 1st tensile strain step. Then, the model was fragmented at 2nd tensile strain step (see Figure 3.132 b). In the case of 15% tensile strain at 1 K, the same model was abruptly fragmented at 1st strain, which exhibited similar structural properties to that

of three fold %5 strain (see Figure 3.132 c). Moreover, the SV-O model, when subject to %5 strain at 300 K, maintained its initial structure at 1st tensile strain step, but the vacancy side moved along the diagonal direction. Then, the structure was fragmented at 2nd tensile strain step (see Figure 3.133 a). When subject to %10 strain at 300 K, the same model was abruptly fragmented at 1st tensile strain step, which exhibited similar properties to that of twice 5% tensile strain (see Figure 3.133 b).

After the energetic relaxations, the SV-Zn-O model did not retain its initial structure, which completely configured with square grid geometry and consisted of a rectangular hole at the center of structure when PBC was applied at both 1 and 300 K. Additionally, another defects were detected at the edges of the structure at 1 K without PBC as well (see Figure 3.134 b). However, the same model, when PBC was applied at both 1 and 300 K, preserved its initial structure, but at 300 K the vacancy site moved along the diagonal direction with the effect of the temperature (see Figure 3.134 c). On the other hand, when subject to 5% tensile strain at 1 K, the SV-Zn-O model almost preserved its initial structure, but the vacancy part looked like an elliptical shape hole at 1st and 2nd tensile strain steps, and then separated into two parts 3rd tensile strain step (see Figure 3.135 a). When subject to %10 strain at 1 K, the same model exhibited similar structural properties to that of twice 5% tensile strain (see Figure 3.135 b). When subject to %15 strain at 1 K, the structure was abruptly separated into two sheet parts (see Figure 3.135 c). Moreover, in the case of 5% tensile strain at 300 K, the same model preserved its initial structure, but the defect site moved along the diagonal direction at 1st tensile strain step and then fragmented at 2nd tensile strain step (see Figure 3.136 a). In the case of 10% tensile strain at 300 K, the same model was abruptly fragmented at 1st tensile strain step (see Figure 3.136 b).

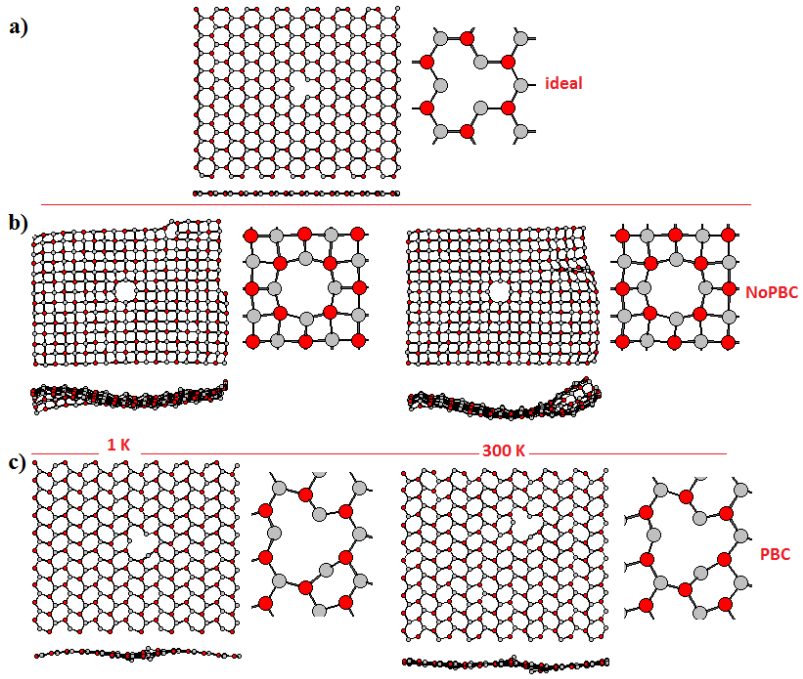

Figure 3.128 The ideal SV-Zn defect model nanosheet at 1 and 300 K b) with NoPBC c) with PBC.

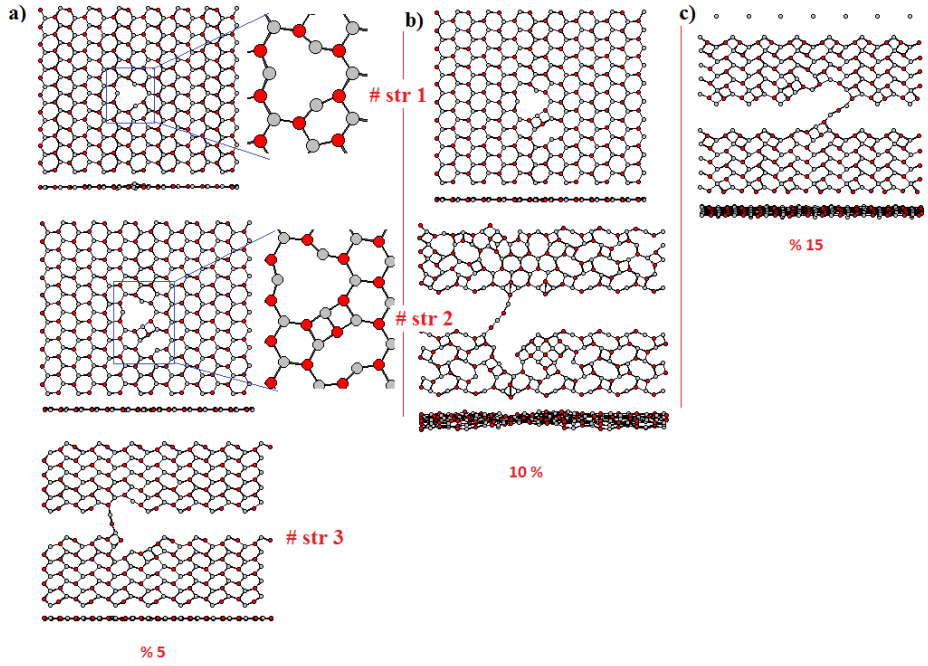

Figure 3.129 The SV-Zn defect model nanosheet at 1 K under tensile strain applications a) 5% strain b) 10% strain c) 15% strain.

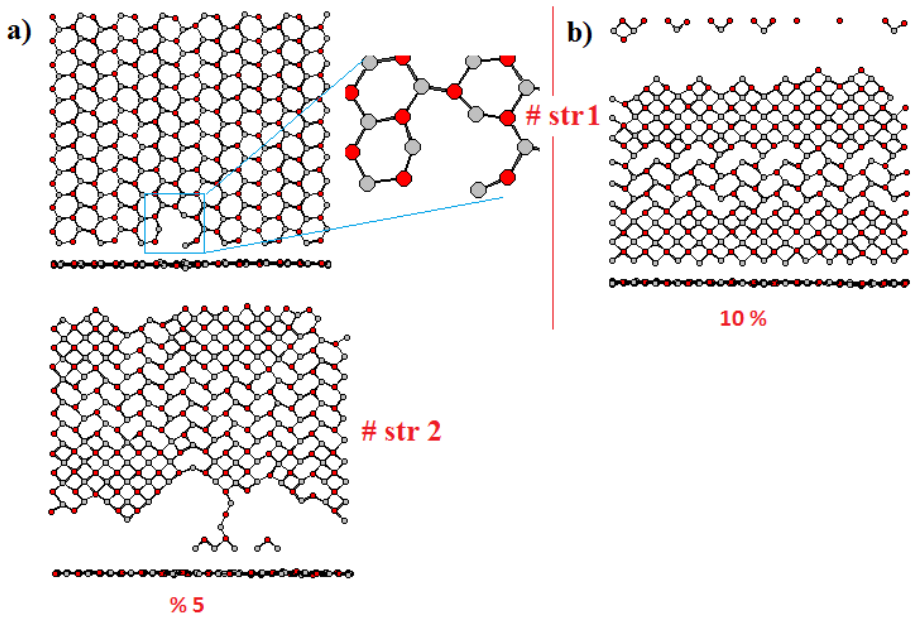

Figure 3.130 The SV-Zn defect model nanosheet at 300 K under tensile strain applications a) 5% strain b) 10% strain.

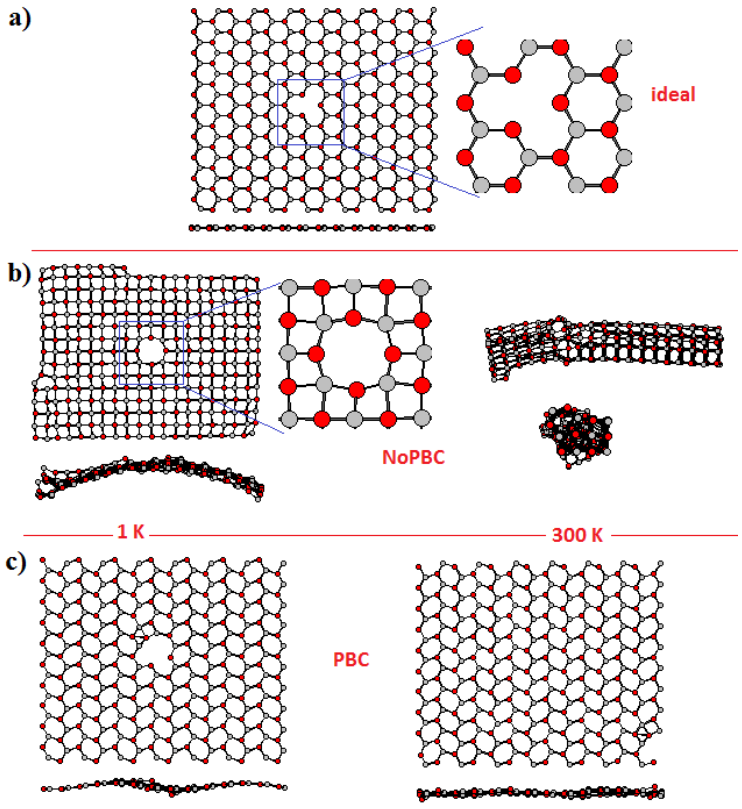

Figure 3.131 The SV-O defect model nanosheets a) ideal b) with NoPBC at 1 and 300 K c) with PBC at 1 and 300 K.

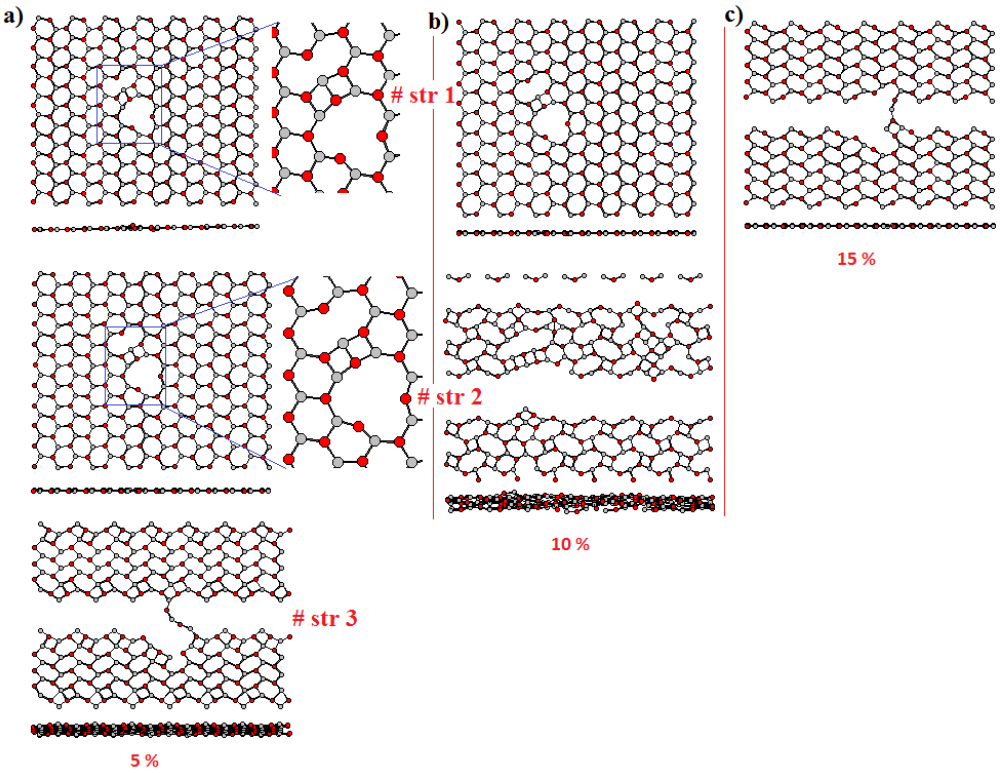

Figure 3.132 The SV-O defect model nanosheet at 1 K under tensile strain applications a) 5% strain b) 10% strain c) 15% strain.

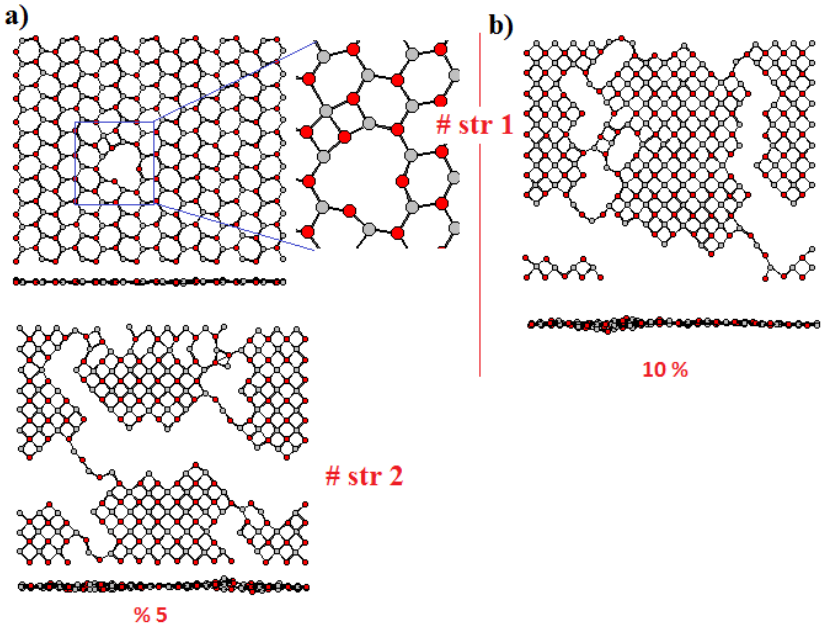

Figure 3.133 The SV-O defect model nanosheets at 300 K under tensile strain applications a) 5% strain b) 10% strain.

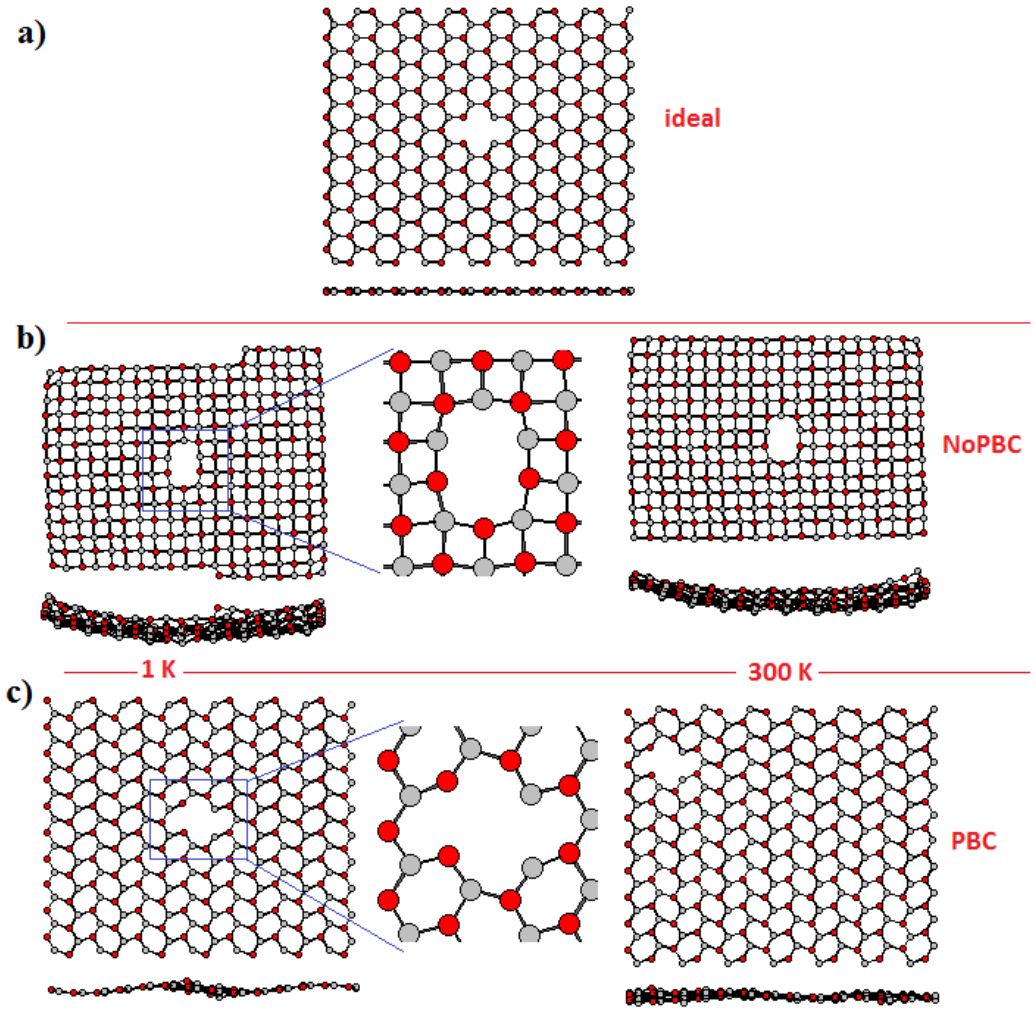

Figure 3.134 The SV-Zn-O defect model nanosheets a) ideal b) with NoPBC at 1 and 300 K c) with PBC at 1 and 300 K.

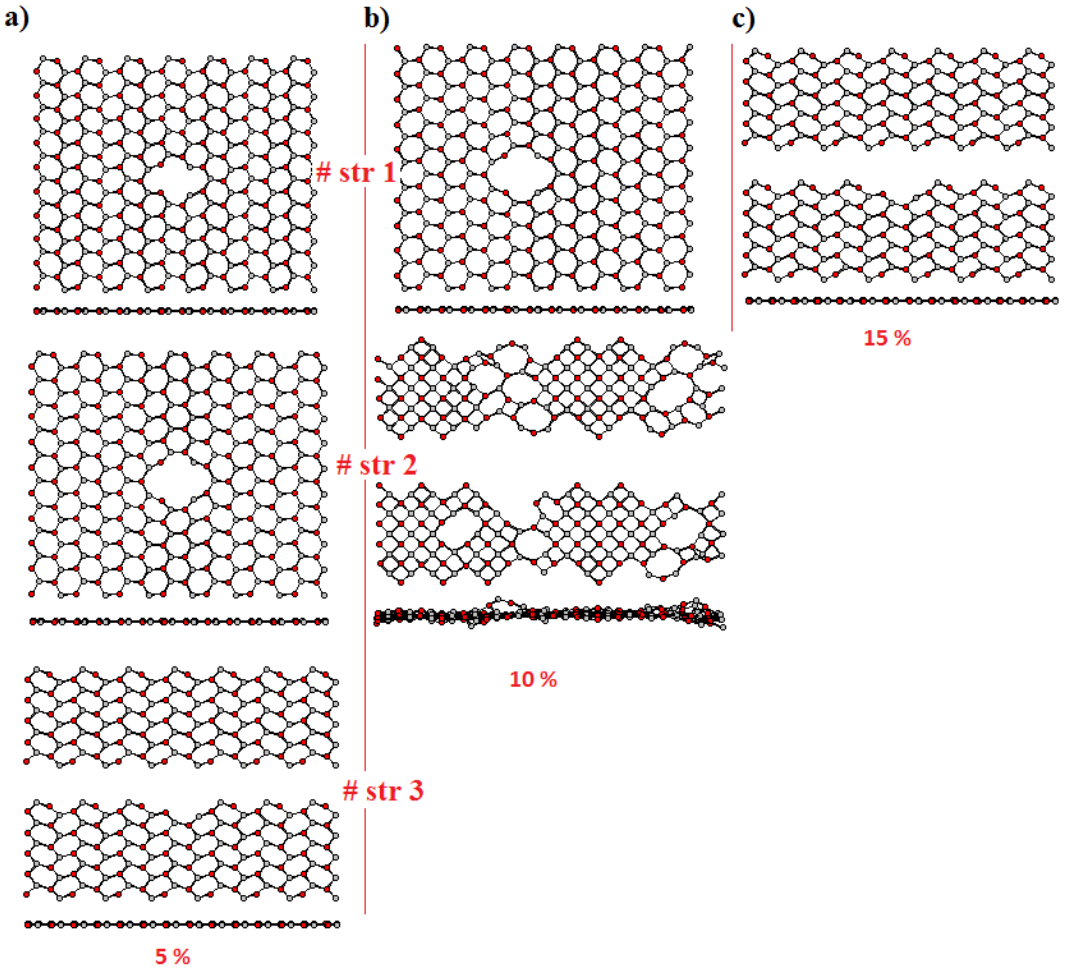

Figure 3.135 The SV-Zn-O defect model nanosheet at 1 K under tensile strain applications a) 5% strain b) 10% strain c) 15% strain.

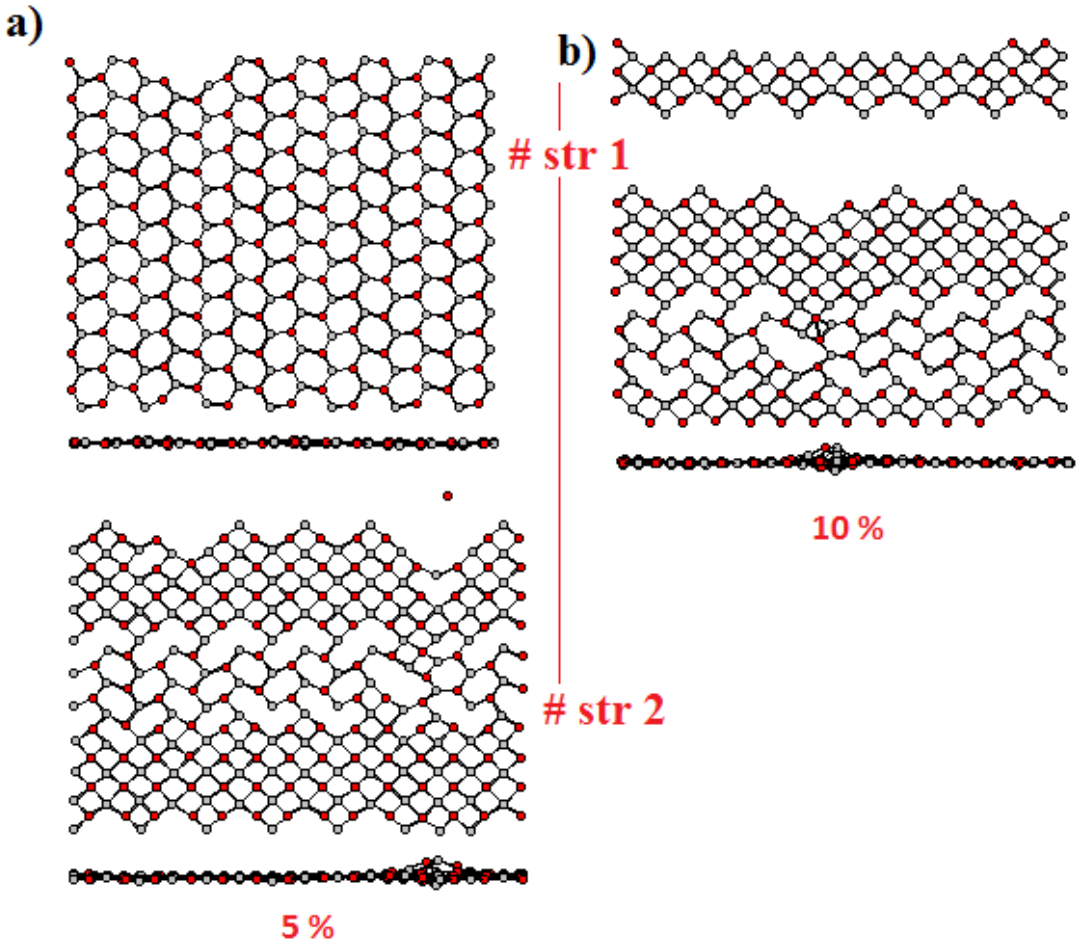

Figure 3.136 The SV-Zn-O defect model nanosheets at 300 K under tensile strain applications a) 5% strain b) 10% strain.

The second part of the defect study is exchange type defects, namely substitute (the SE-SB) and stone-wales like defects (the SE-SW). After the energetic relaxation process, the defect in the central region of both the SE-SB and the SE-SW models disappeared when PBC was not applied at both 1 and 300 K. However, the two models configured with completely square grid geometry at both 1 and 300 K. Additionally, some defects at 1 K appeared at the edges of both two model structures whereas any defect at 300 K disappeared without PBC (see Figure 3.137 b,Figure 3.138 b). When PBC was applied, the same models completely changed into a perfect defect free structure with hexagonal grid geometry at both 1 and 300 K (see Figure 3.137 c,Figure 3.138 c). So re-exchange mechanism was occurred in these conditions. The reason for the re-exchange mechanism could be due to the differences in the strength of the

interatomic interactions. The PEF used in the present study does not consider the Zn-Zn interactions. On the other hand, the O-O interaction is relatively stronger than the Zn-O interaction, but the equilibrium distance of Zn-O is much shorter than that of O-O (see Table 2.2). Moreover, we did not need to continue application of tensile strain steps for both models because of this.

The third part of the defect study is line type defect (the LD model). The LD model structure was generated by changing the hexagonal geometry in a certain array into square and octagon formation. After the energetic relaxation process, the LD model completely configured with square grid geometry at both 1 and 300 K when PBC was not applied. Additionally, the defects at the structure took place at 1 K temperature (see Figure 3.139 b). When PBC was applied at 1 K, the same structure mostly retained its initial structure, but the below part of the defect site moved along the x-axes. Moreover, the LD model consisted of two similar line defects with PBC at 300 K (see Figure 3.139 c). On the other hand, the LD model, when subject to 5% tensile strain applications at 1 K, mostly retained its initial structure at 1st tensile strain step. Then, the atom chain formation took place in the defect site at 2nd tensile strain step. Then, the structure was fragmented at 3rd tensile strain step (see Figure 3.140 a). In the case of 10% tensile strain at 1 K, the atom chains in the defect site of the structure were detected at 1st tensile strain step. Then, atom chains stretched at 2nd tensile strain step (see Figure 3.140 b). However, the structure at 300 K abruptly was fragmented at 1st tensile strain step when subject to 5% tensile strain (see Figure 3.140 c).

The last part of the defect study is the circular hole type defects. Four different type defect models of that study are studied for the nanosheets, namely the CHD1, CHD2, CHD3 and CHD4 models. Ideal models for these models are shown in the Figure 2.29.

The CHD1 model, after the energetic relaxation process, retained its sheet structure when PBC was not applied, but the circular hole changed into a rectangular hole at the central region, and detecting the defects at the edges of the structure as well. The same model at 300 K changed from 2D into rod like structure with NoPBC. The structure at both 1 and 300 K completely configured with square grid geometry (see Figure 3.141 b). However, the same model maintained its initial structure at both

1 and 300 K with PBC. The circular hole defects at both two temperatures preserved its appearance, but looked like a wavy structure when viewed from the side, and the circular hole defect site moved along the PBC direction with the effect of the temperature (at 300 K) (see Figure 3.141 c). On the other hand, the CHD1 model retained its initial structure at 1st tensile strain step when subject to 5 % strain applications at 1 K. Then, the structure still maintained its initial structure, but the circular hole changed into star like hole at 2nd tensile strain step. Then, the structure was fragmented at 3rd tensile strain step (see Figure 3.142 a). When subject to %10 strain, the structure still retained its initial structure at 1st tensile strain step (see Figure 3.142 b). On the other hand, in the case of 5% tensile strain applications at 300 K, the same model maintained its initial structure at 1st tensile strain step, and then the structure was fragmented at 2nd tensile strain step (see Figure 3.143 a). In the case of 10% tensile strain, the structure abruptly fragmented at 1st tensile strain step (see Figure 3.143 b).

After the energetic relaxation process, the CHD2 model did not retain its ideal circular hole shape defect, changed into almost like rectangular hole, when PBC was not applied at K. Additionally, the hexagonal grid geometry turned into squares and appeared as sheet like when viewed from the side. However, the same model transformed into 3D structure without PBC at 300 K (see Figure 3.144 b). When PBC was applied at both 1 and 300 K, the CHD2 model kept its ideal defect structure, but the atoms around the vacancy moved out of plane when viewed from the side and at 300 K the circular hole part moved along the PBC directions (see Figure 3.144 c). ın the case of 5% tensile strain applications at 1 K, the same model almost its initial relaxed structure in the first two applications of tensile strain steps. In the third application of tensile strain step, the structure was fragmented (see Figure 3.145 a). In the case of 5% tensile strain applications at 300 K, the structure also retained its initial relaxed structure at 1st tensile strain step. The separation starts after the 4th tensile strain step (see Figure 3.146 a). In the case of 10% tensile strain applications, the structure abruptly fragmented at 1st tensile strain step (see Figure 3.146 b).

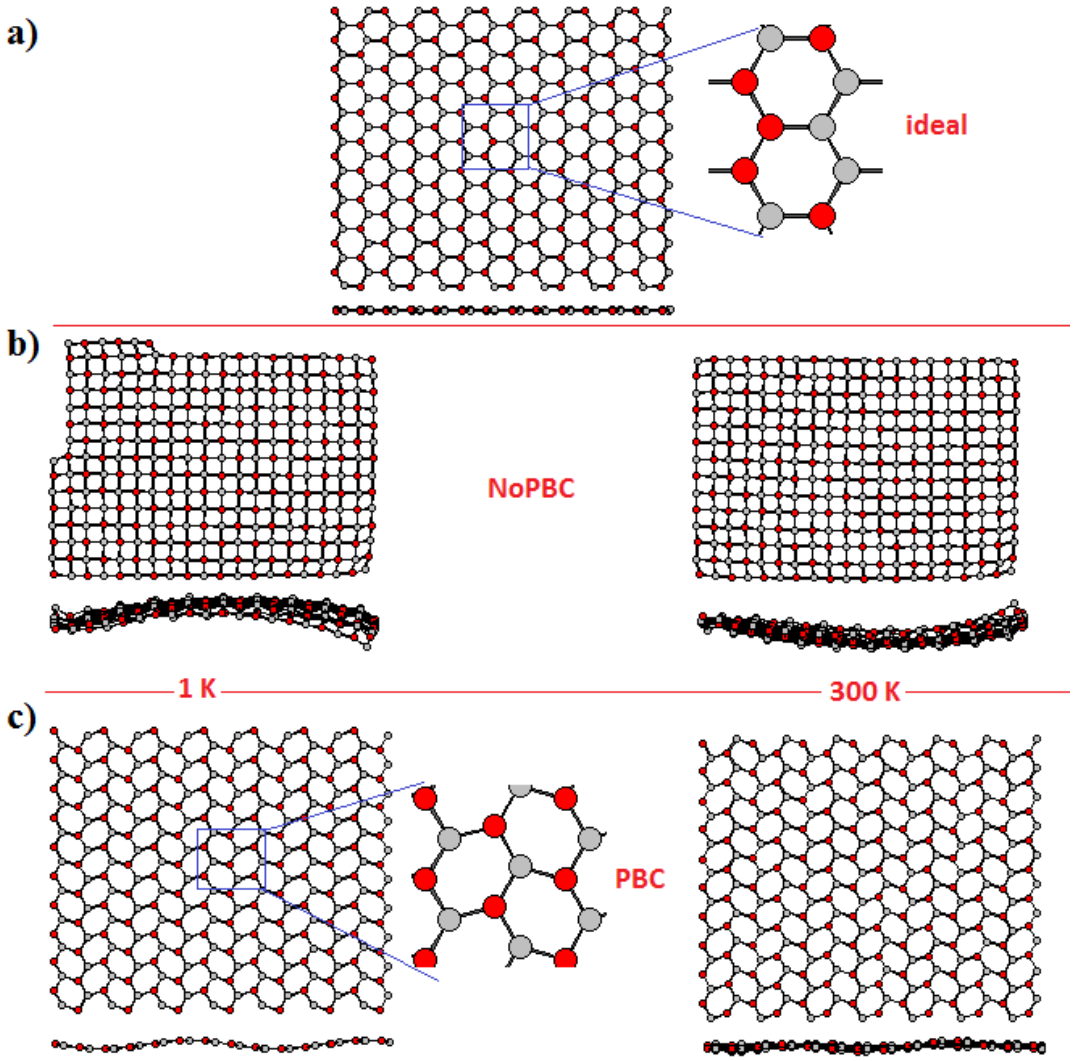

Figure 3.137 The SE-SB defect model nanosheets a) ideal b) with NoPBC at 1 and 300 K c) with PBC at 1 and 300 K.

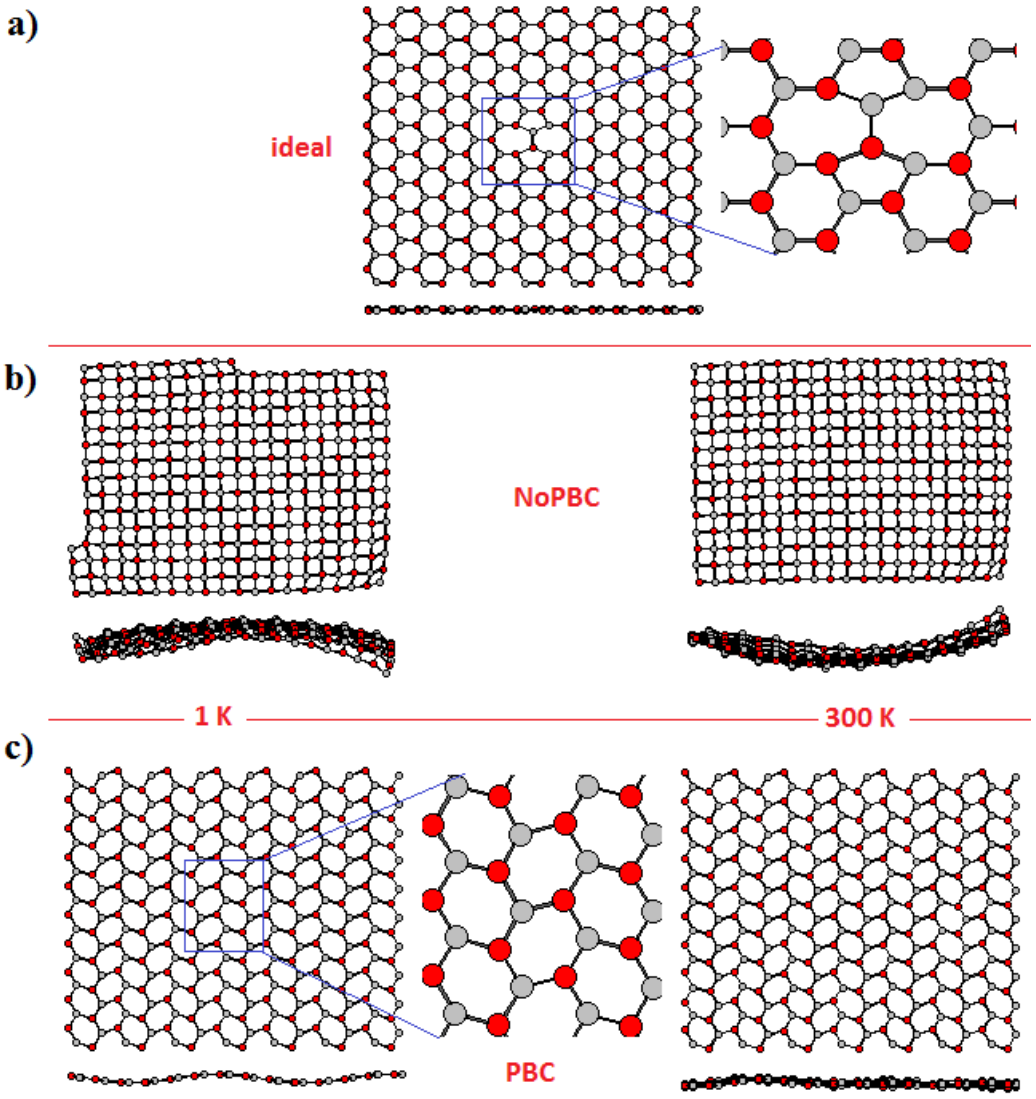

Figure 3.138 The SE-SW defect model nanosheets a) ideal b) with NoPBC at 1 and 300 K c) with PBC at 1 and 300 K.

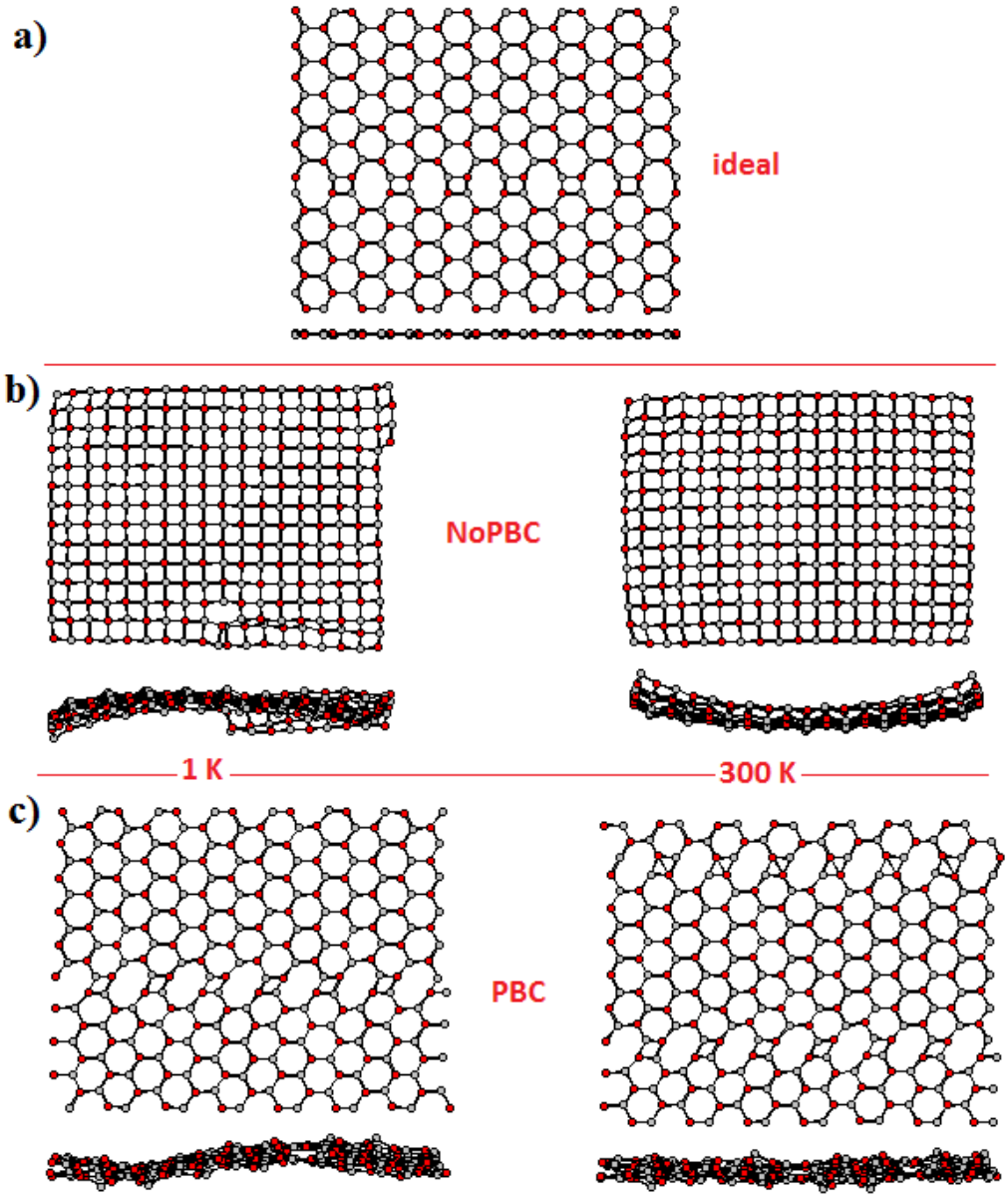

Figure 3.139 The LD defect model nanosheets a) ideal b) with NoPBC at 1 and 300 K c) with PBC at 1 and 300 K.

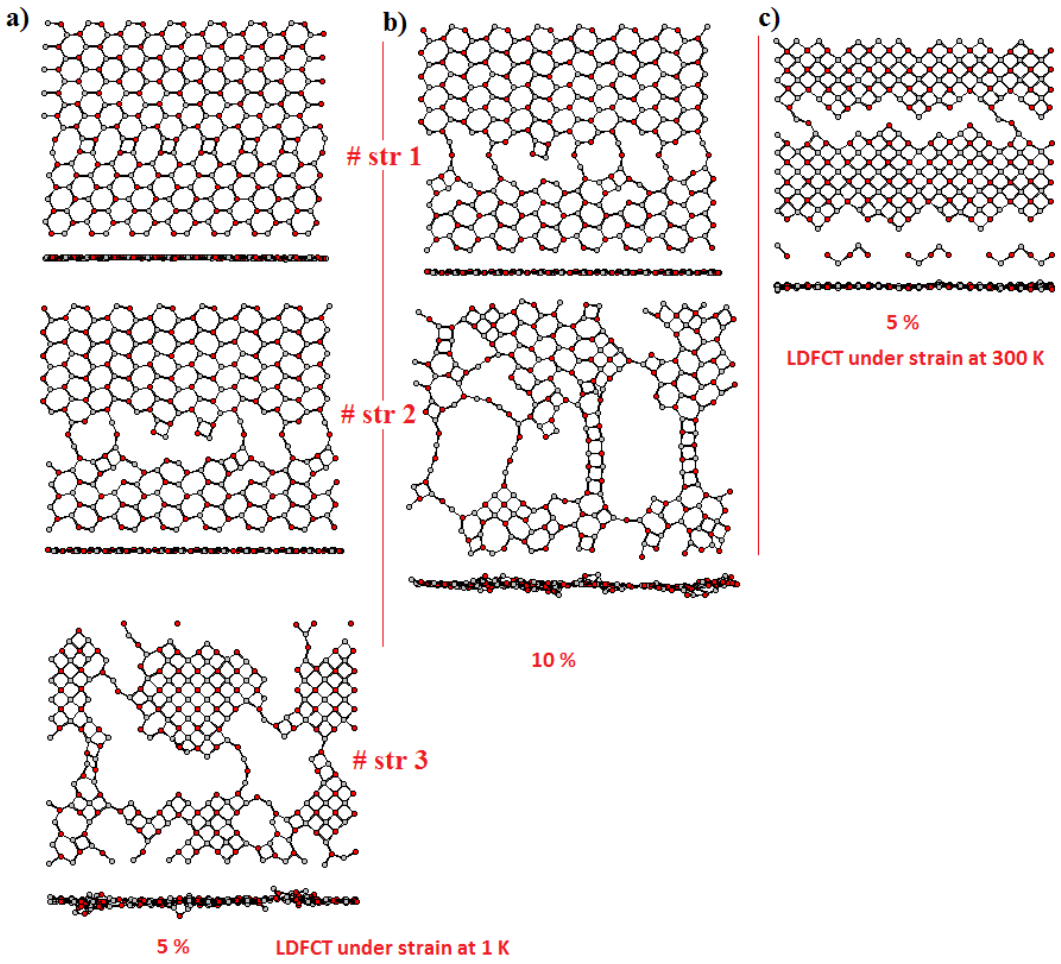

Figure 3.140 The LD defect model nanosheets under tensile strain applications a) 5% strain at 1 K b) 10% strain at 1 K c) 5% at 300 K.

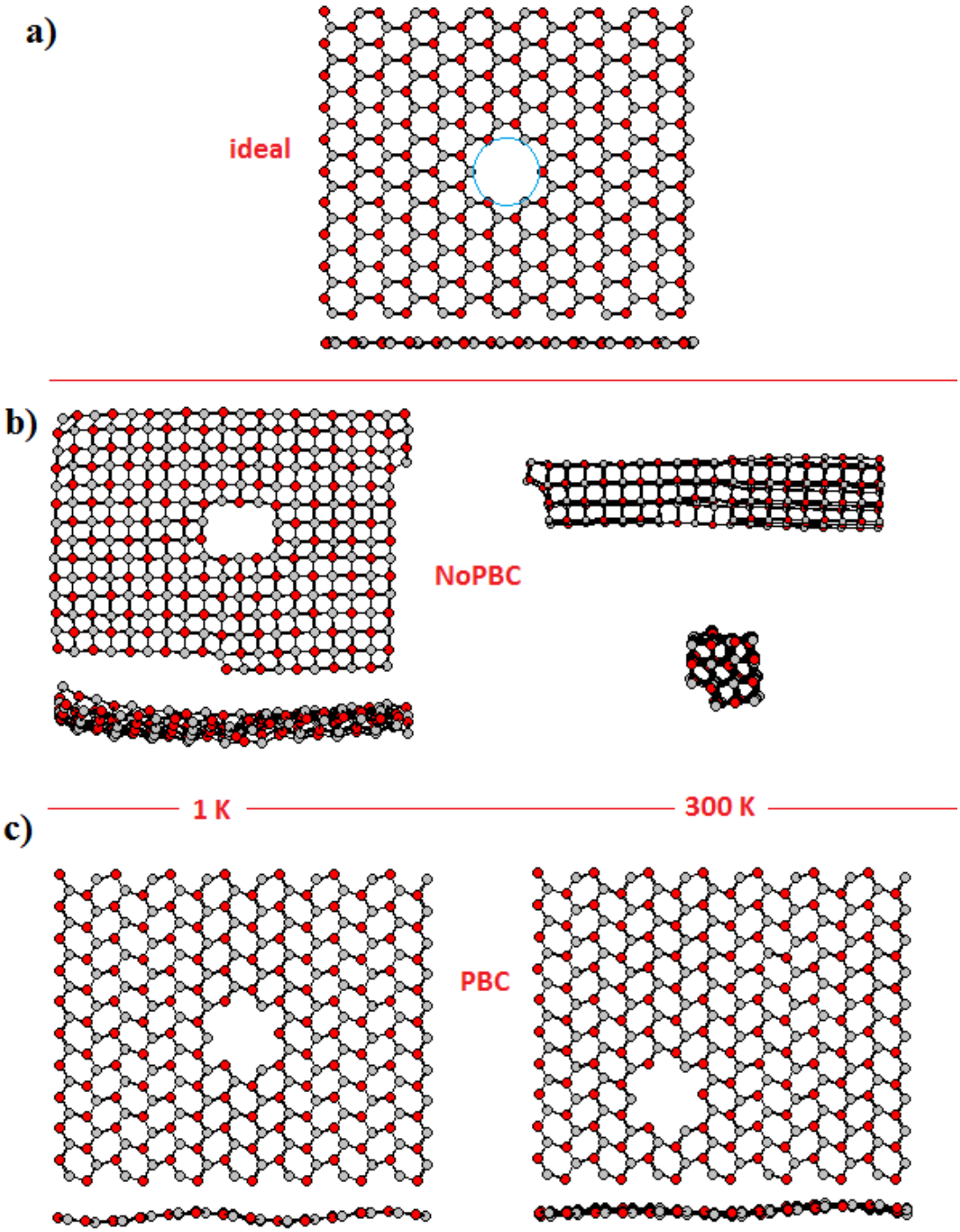

Figure 3.141 The CHD1 defect model nanosheets at 1 and 300 K b) with NoPBC c) with PBC.

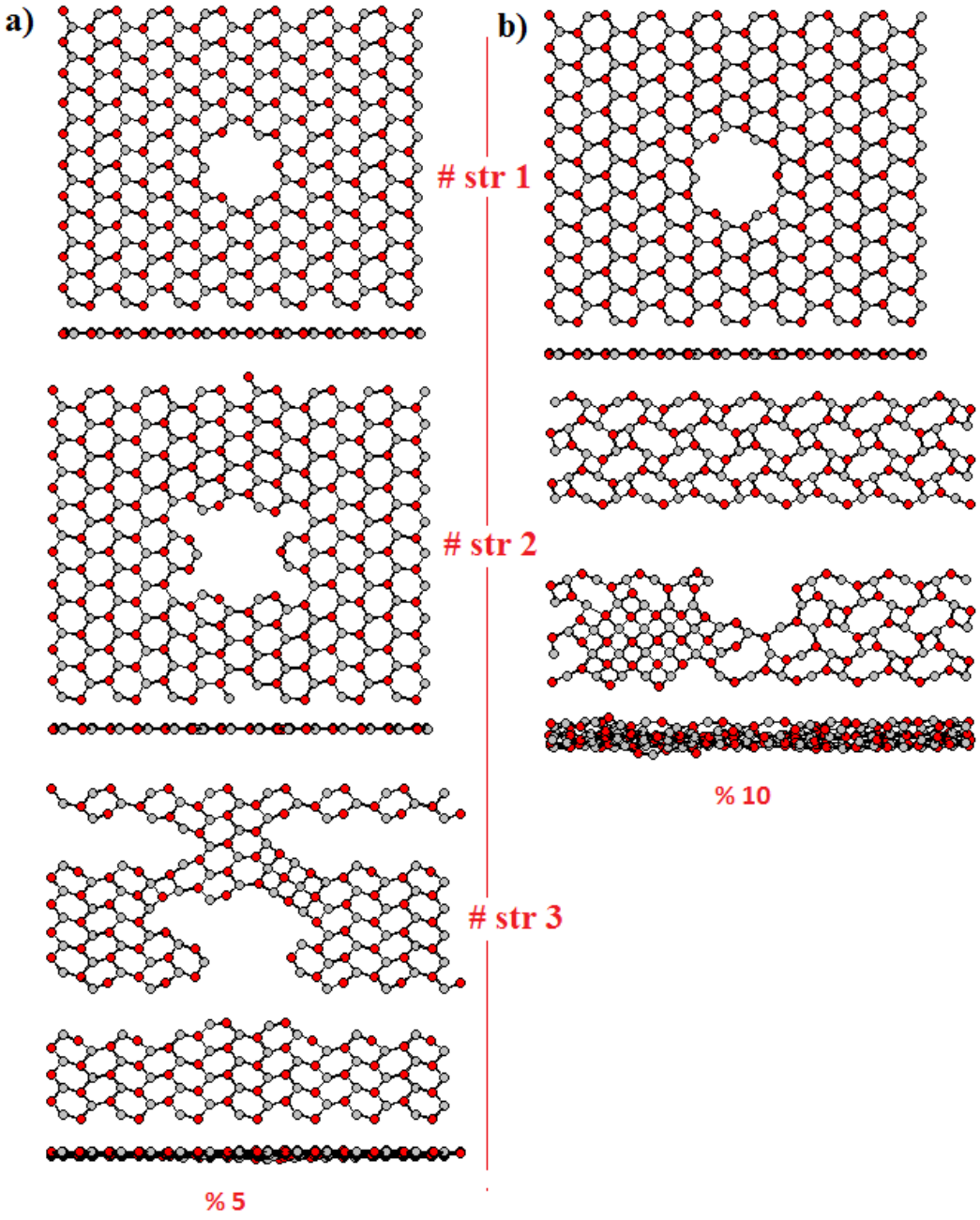

Figure 3.142 The CHD1 defect model nanosheets at 1 K under tensile strain applications a) 5% strain b) 10% strain.

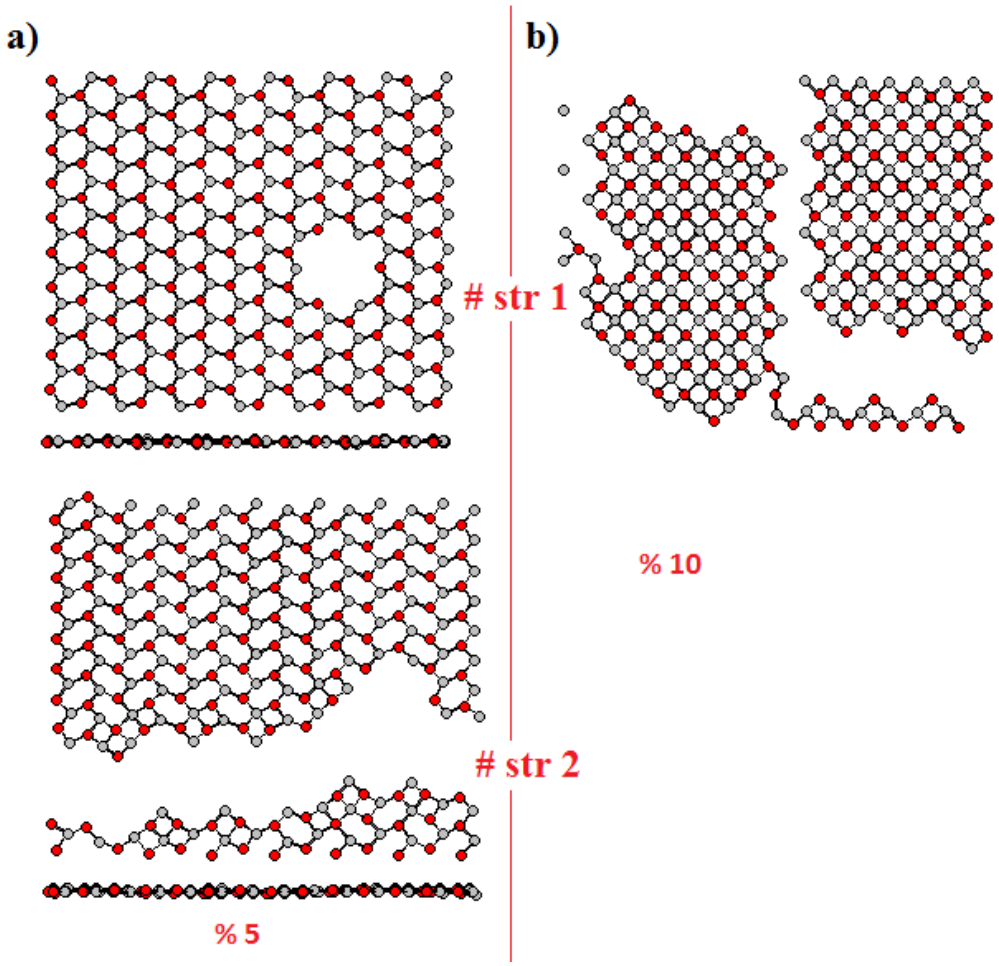

Figure 3.143 The CHD1 defect model nanosheets at 300 K under tensile strain applications a) 5% strain b) under 10% strain.

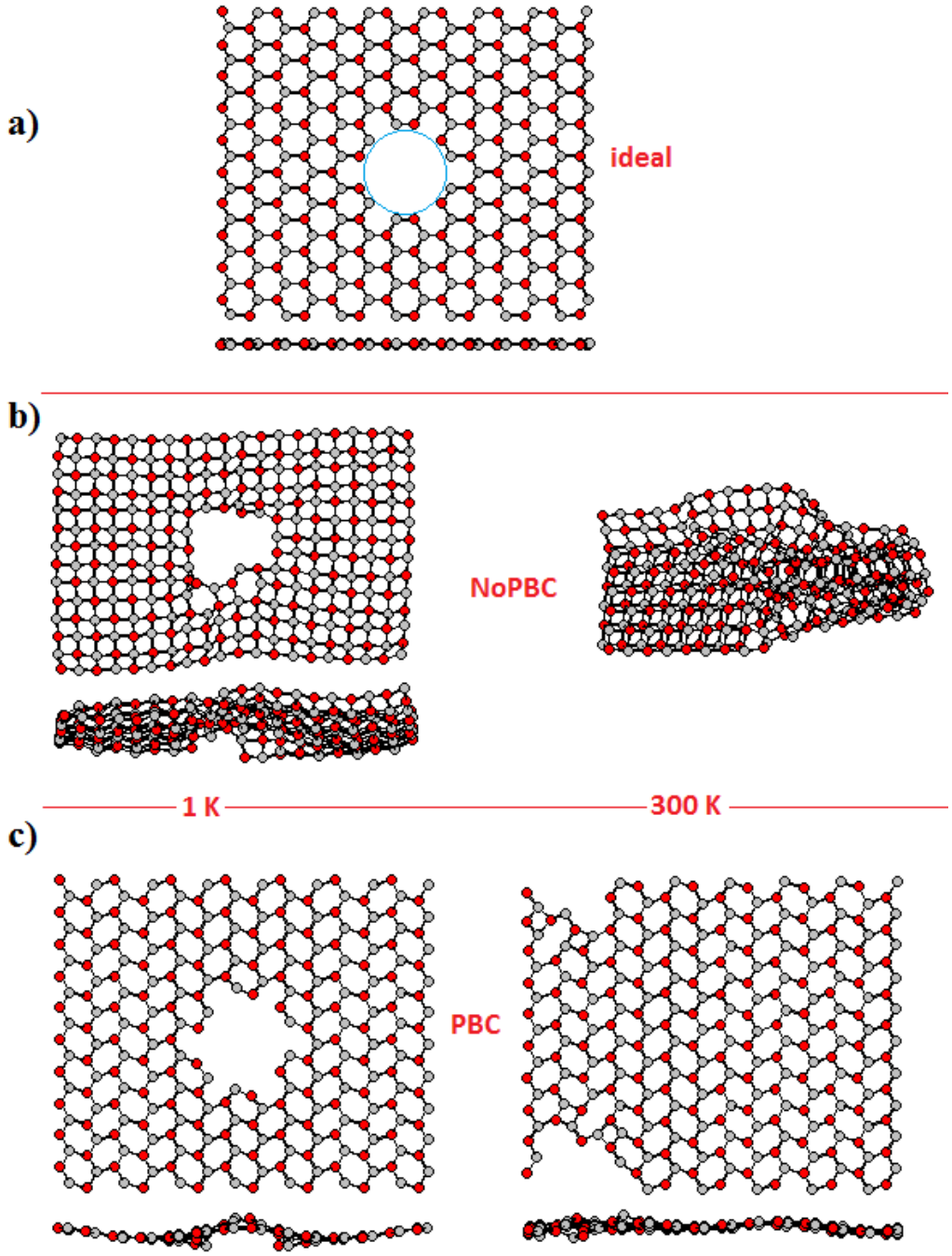

Figure 3.144 The CHD2 defect model nanosheets at 1 and 300 K b) with NoPBC c) with PBC.

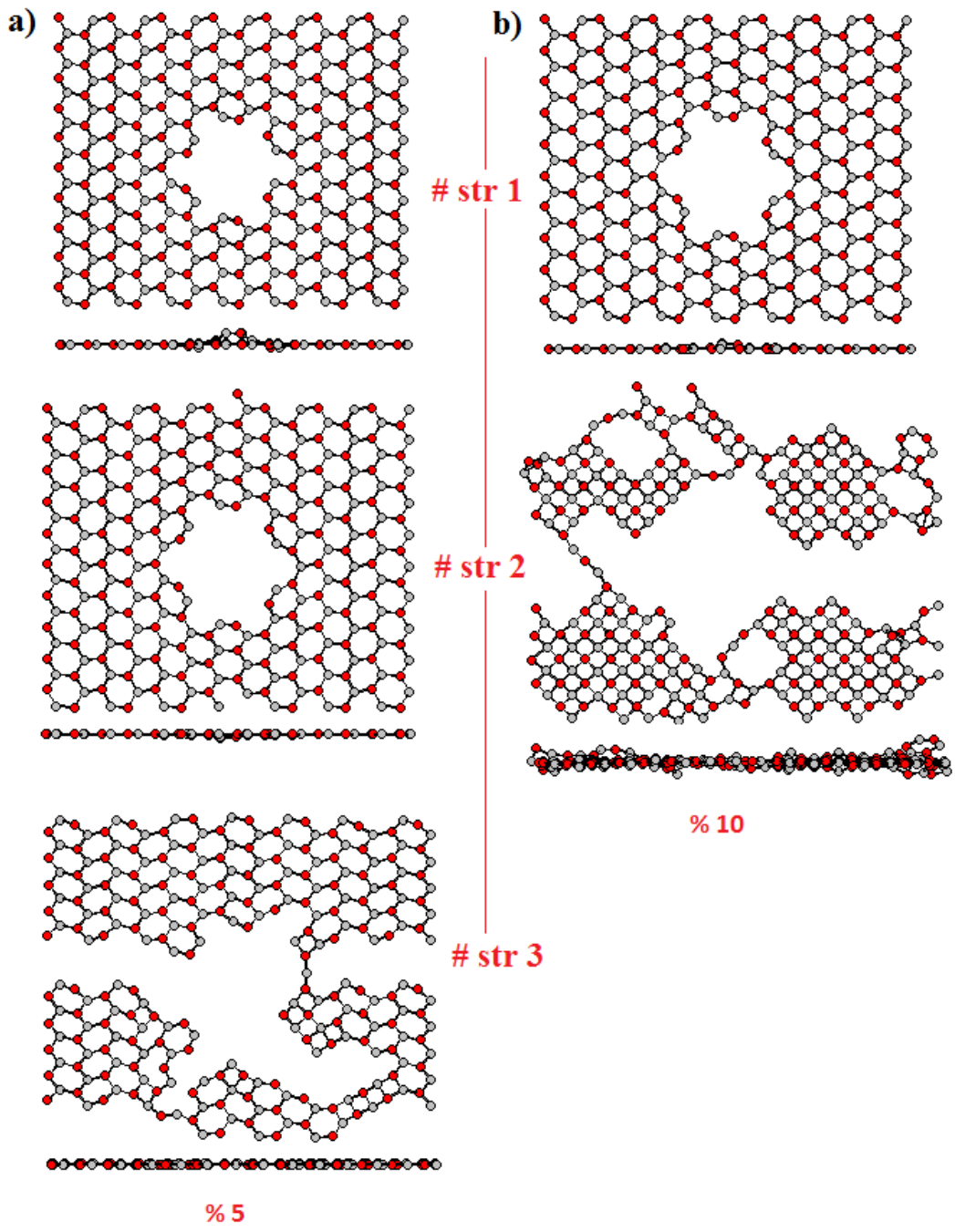

Figure 3.145 The CHD2 defect model nanosheets at 1 K under tensile strain applications a) 5% strain b) 10% strain.

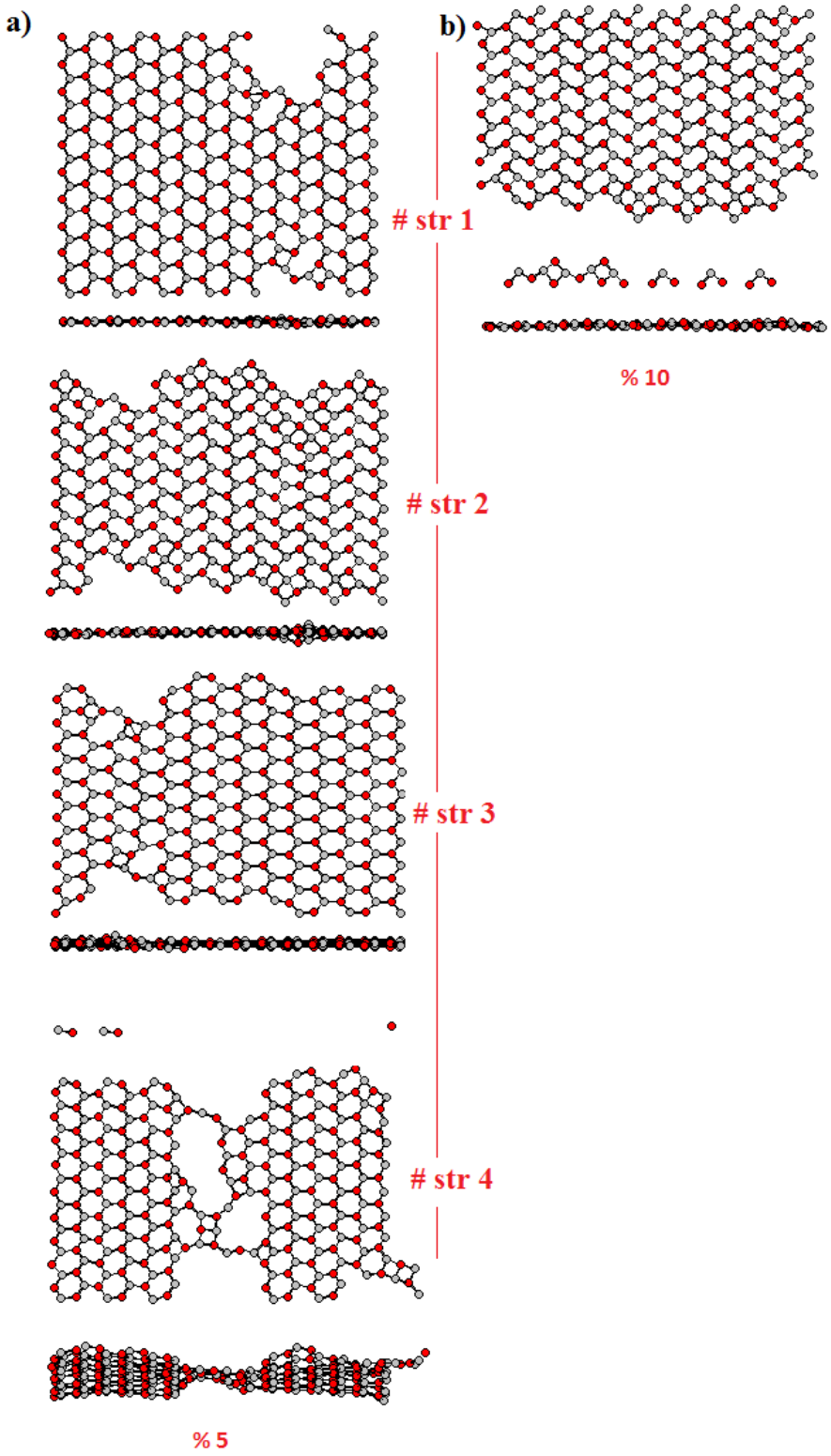

Figure 3.146 The CHD2 defect model nanosheets at 300 K under tensile strain applications a) 5% strain b) 10% strain.

CHAPTER 4

CONCLUSION

During this study, several achievements were made. We have concentrated on the dimensionality of ZnO nanostructures and investigated their mechanical properties by using molecular dynamics simulations at different temperatures. The striking features of the ZnO nanostructures have been investigated. The wurtzite crystal structure is the most stable form of ZnO bulk material. However, when crystal size goes down to nanometers, the wurtzite may not be the most stable phase in particular for 2D ZnO nanofilms and 1D nanowires and nanorods[3,30,35,36,128,131–134]. From the structural and energetic point of view the present calculated results show a good agreement with the literature data. In this theses study may be summarized according to the dimensionality of the systems considered as follows:

For the 0D nanostructures, we have studied nanoparticles (spherical and cubic) during the NEMD process. The spherical nanoparticles almost preserved its spherical shape in the process, and changed into rock salt phase at the high temperatures. On the other hand, the cubic nanoparticles retained its ideal structure during the NEMD process despite the high temperatures. From the stability aspect, the cubic nanoparticles exhibited more stable form to compare with the spherical nanoparticles. Moreover, the stoichiometry in considered nanoparticles (both spherical and cubic) played an important role on their structural and thermodynamic properties. Furthermore, it was realized that the heat capacity of the spherical and cubic nanoparticles almost depended on their sizes and stoichiometry.

For the 1D nanostructures, we have studied nanoribbons, nanorods and nanotubes via EMD simulations. At the first stage, the nanoribbons have been studied as both pristine and defected nanostructure. It is realized that the absence/or presence of PBC and the effect of the temperature played an important role on their structural properties of the nanostructures in addition to the widths (layers) and edges (zigzag and armchair). For example, all the nanoribbons (zigzag and armchair) geometrically changed at both 1 and 300 K with NoPBC. On the other hand, in the presence of PBC the zigzag nanoribbons also changed with square grid geometry whereas the armchair nanoribbons preserved is honeycomb geometry at both temperature runs. When subject to 5% tensile strain applications, the 2L nanoribbons turned into 1L nanoribbons at the high strain steps (4-6), after then atom chains appeared. Furthermore, it was realized that the armchair nanoribbons structurally (from geometry point of view) were more stable than the zigzag nanoribbons. Additionally, the defected nanoribbons exhibited similar structural properties with the pristine nanoribbons, but the defects caused deformation much more on 1D nanoribbons.

Secondly, the structural properties of nanorods (hexagonal, trigonal and rhombohedra cross sectional) have been studied. It was realized that the absence or presence of the PBC played an important structural role on the structural properties of the nanorods. For example, the nanorod models with NoPBC changed into amorphous structures at both 1 and 300 K whereas they preserved its ideal structure with PBC. Moreover, the wurtzite rod structures transformed into graphitic structure when subject to compression strain process. Therefore, the structural phase transitions took place in all the nanorods under the both compression strain and tensile strain applications. The average bond length between atoms was increased during the both compression strain and tensile strain applications. Under the torsion applications, the exchange mechanism in the nanorods has been occurred, result in no change as structural.

Thirdly, the structural properties of the nanotubes (zigzag, armchair and chiral) have been studied via MD. It was realized that all the tube models exhibited very different behaviors both under different environments of freedom (NoPBC and PBC), compression strain and tensile strain process, and the effect of the temperatures (1 and 300 K) in addition to the edges of tube (zigzag, armchair and chiral). For example, the

zigzag tube models changed into rod structures whereas armchair tube models changed into capsule shaped structure and chiral structure changed into different shapes with NoPBC. Interestingly, the both ends of the zigzag tubes were widened whereas the both ends of the armchair and chiral nanotubes was closed with NoPBC. When the PBC was applied at both 1 and 300 K, all the tube models preserved its initial ideal structure. In the case of tensile strain applications, the zigzag tube models mostly preserved their ideal tube structure whereas the armchair tube models did not maintain their initial tube structure, which changed into firstly dumbbell shaped structure, then, changed into rod structure, and then changed into perfect zigzag tube structure during the tensile strain applications. That is, the armchair nanotube models exhibited more phase structural transitions than the zigzag nanotube models under tensile strain applications. Actually, the phase transitions for zigzag nanotubes revealed under compression strain applications whereas the phase transitions for armchair nanotubes revealed under tensile strain applications. Additionally, the average bond length between atoms in all tube models was increased under tensile strain whereas it did almost not change under compression strain. Furthermore, the tube radius of all the models was decreased under tensile strain applications whereas it was increased under compression strain applications.

For the 2D nanostructures we have studied nanosheets as both pristine and defected structures. All the nanosheets changed from honeycomb structure into tiling like structures after the energetic relaxation process. The sheet models also exhibited very different behaviors both under different environments of freedom (NoPBC and PBC) and different temperatures (1 and 300 K) in addition to the types of defect (vacancy, exchange vs.). Firstly, all nanosheet models, when PBC was not applied, did not preserve its ideal structure, which configured with square grid geometry. The type of removed atoms in the monovacancy defect models evolved into the structural features. Additionally, all of the nanosheet models preserved their ideal structure at both 1 and 300 K when PBC was applied. Moreover, the defect site moved along the diagonal direction all sheet models due to the effect of the temperature (300 K). In the case of tensile strain applications, the nanosheet models maintained its 2D structure during the tensile strain step applications at both 1 and 300 K. The rates of strain, namely 5, 10, 15% tensile strain, did not play an important role the sheet models. After

a few tensile strain steps, almost ranging from 1st to 3rd tensile strain steps, the sheet models were fragmented as sheets. Under tensile strain, the models were shown more durable structural properties at 1 K than that of 300 K. Lastly and interestingly, the exchange defect types (substitute and Stone-Wales), having no missing atoms, transformed into perfect defect free sheet structures in the presence of the boundary conditions (PBC). Zn-O pairs were always in perfect order in all of the model structures considered.

REFERENCES

1. Wang ZL, Kang ZC. *Functional and Smart Materials-Structural Evolution and Structural Analysis*. Plenum Pre. New York; 1998.

2. Williams DE. *Semiconducting oxides as gas-sensitive resistors*. 1999;57:1-16.

3. Bunn CW. *The Lattice-Dimensions of Zinc Oxide. Proc Phys Soc London*. 1935;47:835.

4. Mollwo E, Angew Z. *Phys*. 1954;6:257.

5. Damen TC, Porto SPS, Tell B. *Raman Effect in Zinc Oxide. Phys Rev*. 1966;142:570.

6. Tsurkan AE, Fedotova ND, Kicherman L V., Pas'ko PG. *Semicond Semimetals*. 1975;6:1183.

7. Morkoc H, Ozgur U. Zinc Oxide: Fundamentals, materials and device technology. In: *Zinc Oxide: Fundamentals, Materials and Device Technology*. Wiley- VCH. Weinheim; 2009.

8. Sun XW, Chen QF, Wang CW, Li Y, Wang J. . *Phys B*. 2005;355:126.

9. Kilic ME, Erkoc S. Structural properties of ZnO nanotubes under uniaxial strain: Molecular Dynamics Simulations. *J Nanosci Nanotech*. 2013;13:6597-6610.

10. Kilic ME, Erkoc S. Molecular dynamics simulations of ZnO nanostructures under strain: I - nanoribbons. *J Comput Theor Nanosci*. 2013;10:104.

11. Kilic ME, Erkoc S. Structural properties of defected ZnO nanoribbons under uniaxial strain: Molecular dynamics simulations. *Curr Appl Phys*. 2014;14(1):57-67.

12. Kilic ME, Erkoc S. Molecular dynamics simulations of ZnO nanostructures under strain: II - nanorods. *J Comput Theor Nanosci*. 2013;10:112.

13. Kilic ME, Erkoc S. Structural properties of ZnO nanoparticles and nanorings: Molecular dynamics simulations. *J Comput Theor Nanosci*. 2013;10:1490-1496.

14. Tang Q, Li Y, Zhou Z, Chen Y, Chen Z. Tuning electronic and magnetic properties of wurtzite ZnO nanosheets by surface hydrogenation. *ACS Appl Mater Interfaces*. 2010;2(8):2442-2447. doi:10.1021/am100467j.

15. Kou L, Li C, Zhang Z, et al. Magnetic behavior in zinc oxide zigzag nanoribbons. *ACS Nano*. 2008;4(4):2124-2128. doi:10.1021/nl072511q.

16. Botello-Méndez AR, López-Urías F, Terrones M, Terrones H. Magnetic behavior in zinc oxide zigzag nanoribbons. *Nano lett*. 2008;8(6):1562-1565. doi:10.1021/nl072511q.

17. Terrones M. Magnetic Behavior in Zinc Oxide Zigzag. 2008.

18. Garcia M a, Merino JM, Fernández Pinel E, et al. Magnetic properties of ZnO nanoparticles. *Nano Lett*. 2007;7(6):1489-1494. doi:10.1021/nl070198m.

19. Leung YH, Djuris AB. reviews Optical Properties of ZnO Nanostructures ˇic. 2006;(8):944-961. doi:10.1002/smll.200600134.

20. Kitamura K, Yatsui T, Ohtsu M. Optical and Structural Properties of ZnO Nanorods Grown on Polyimide Films. *Appl Phys Express*. 2008;1:081202. doi:10.1143/APEX.1.081202.

21. Willander M, Nur O, Zhao QX, et al. Zinc oxide nanorod based photonic devices: recent progress in growth, light emitting diodes and lasers. *Nanotechnology*. 2009;20(33):332001. doi:10.1088/0957-4484/20/33/332001.

22. Chen S, Liu Y, Shao C, et al. Structural and Optical Properties of Uniform ZnO Nanosheets. *Adv Mater*. 2005;17(5):586-590. doi:10.1002/adma.200401263.

23. Wang L, Chen K, Dong L. Synthesis of Exotic Zigzag ZnO Nanoribbons and Their Optical , Electrical Properties. 2010:17358-17361.

24. Xing YJ, Xi ZH, Xue ZQ, et al. Optical properties of the ZnO nanotubes synthesized via vapor phase growth. *Appl Phys Lett*. 2003;83(9):1689. doi:10.1063/1.1605808.

25. Özgür U, Alivov YI, Liu C, et al. A comprehensive review of ZnO materials and devices. *J Appl Phys*. 2005;98(4):041301. doi:10.1063/1.1992666.

26. Reeber RR. Lattice paremeters of ZnO. *J Appl Phys*. 1970;41:5063.

27. Kisi E, Elcombe MM. . *Acta Crystallogr, Sect C Cryst Struct Commun*. 1989;C 45:1867.

28. Karzel H et al. Lattice dynamics and hyberfine interactions in ZnO and ZnSe at high external pressure. *Phys Rev B.* 1996;53:11425.

29. Gerward L, Olsen JS. The High-Pressure Phase of Zincite. *J Synchrotron Radiat*. 1995;2:233.

30. Catti M, Noel Y, Dovesi R. Full Piezoelectric tensors of wurtzite and zinc blende ZnO and ZnS by first-principles calculations. *J Phys Chem Solids*. 2003;64(11):2183-2190.

31. Recio JM, Pandey R, Luana V. Quantum-mechanical modelling of the high-pressure state equations of ZnO and ZnS. *Phys Rev B.* 1993;47:3401.

32. Recio JM, Blanco MA, Luana V, Pandey R, Gerward L, Olsen JS. Compressibility of the high-pressure rocksalt phases of ZnO. *Phys Rev B.* 1998;58:8949.

33. Fan Z, Lu JG. Zinc Oxide Nanostructures: Synthesis and Properties. *J Nanosci Nanotechnol*. 2005;5:1561-1573.

34. Polian A, Grimsditch M, Grzegory I. Elastic constants of gallium nitride. *J Appl Phys*. 1996;79:3343.

35. Decremps F, Zhang J, Li B, Liebermann RC. Pressure induced softening of shear modes in ZnO. *Phys Rev B.* 2001;63:224105.

36. Decremps F, Pellicer-Porres J, Marco Saitta A, Chervin JC, Polian A. High-pressure Raman spectroscopy study of wurtzite ZnO. *Phys Rev B.* 2002;65:092101.

37. Bai XD, Gao PX, Wang ZL, Wang EG. Dual-mode mechanical resonance of individual ZnO nanobelts. *Appl Phys Lett*. 2003;82:4806.

38. Yum K, Wang Z, Suryavanshi AP, Yu MF. Experimental measurements and model analysis of damping effect in nanoscale mechanical beam resonators in air. *J Appl Phys*. 2004;96:3933.

39. Chen CQ, Shi Y, Zhang YS, Zhu J, Yan YJ. Size Dependence of Young's Modulus in ZnO Nanowires. *Phys Rev Lett*. 2006;96:075505.

40. Feng G, Nix WD, Yoon YK, Lee CJ. A study of mechanical properties of nanowires using nanoindentation. *J Appl Phys*. 2006;99:074304.

41. Tu Z, Hu X. Elasticity and piezoelectricity of zinc oxide crystals, single layers, and possible single-walled nanotubes. *Phys Rev B.* 2006;74(3):035434. doi:10.1103/PhysRevB.74.035434.

42. Corso AD, Posternak M, Resta R, Balderschi A. Ab initio study of piezoelectricity and spontaneous polarization in ZnO. *Phys Rev B*. 1994;50:10715.

43. Wang ZL. Zinc oxide nanostructures: growth, properties and applications. *J Phys Con Mat*. 2004;16(25):R829-R858. doi:10.1088/0953-8984/16/25/R01.

44. Dietl T, Ohno H, Matsukura F, Cibert J, Ferrand D. Zener model description of ferromagnetism in zinc-blende magnetic semiconductors. *Science (80-)*. 2000;287(5455):1019-1022.

45. Pearton SJ, Norton DP, Ip K, Heo YW, Steiner T. Recent advancesin processing of ZnO. *J Vac Sci Technol B*. 2004;22:932.

46. Xu HY, Liu YC, Xu CS, Liu YX, Shao CL, Mu R. *Appl Phys Lett*. 2006;88:242502.

47. Kitttilstved KR, Gamelin DR. *J Am Chem Soc*. 2005;127:5292.

48. Pan H, Yi JB, Shen L, et al. Room Temperature Ferromagnetism in Carbon-Doped ZnO. *Phys Rev Lett*. 2007;99:127201.

49. Xing YJ, Xi ZH, Xue ZQ, Zhang XD, Song JH. Optical properties of the ZnO nanotubes synthesized via vapor phase growth Optical properties of the ZnO nanotubes synthesized via vapor phase growth. 2012;1689(May). doi:10.1063/1.1605808.

50. Kong X, Sun X, Li X, Li Y. Catalytic growth of ZnO nanotubes. *Mater Chem Phys*. 2003;82(3):997-1001. doi:10.1016/j.matchemphys.2003.09.004.

51. Kong XY, Ding Y, Wang ZL. Metal−Semiconductor Zn−ZnO Core−Shell Nanobelts and Nanotubes. *J Phys Chem B*. 2004;108(2):570-574. doi:10.1021/jp036993f.

52. Yan BH, Johnson J, Law M, et al. ZnO Nanoribbon Microcavity Lasers. *Adv Mater*. 2003;15(22):1907-1911. doi:10.1002/adma.200305490.

53. Xing YJ, Xi ZH, Zhang XD, et al. Nanotubular structures of zinc oxide. *Solid State Commun*. 2004;129(10):671-675. doi:10.1016/j.ssc.2003.11.049.

54. Wang RC, Liu CP, Huang JL, Chen SJ. Growth and Field Emission Properties of Single-Crystalline Conic ZnO Nanotubes. *Nanotechnology*. 2006;17:753-757.

55. Hughes WL, Wang ZL. Formation of piezoelectric single-crystal nanorings and nanobows. *J Am Chem Soc*. 2004;126(21):6703-6709. doi:10.1021/ja049266m.

56. Hu JQ, Bando Y, Zhan JH, Li YB, Sekiguchi T. Two-dimensional micrometer-sized single-crystalline ZnO thin nanosheets. *Appl Phys Lett*. 2003;83(21):4414. doi:10.1063/1.1629788.

57. Guo L, Ji YL, Xu H, Simon P, Wu Z. Regularly Shaped , Single-Crystalline ZnO Nanorods with Wurtzite Structure. *J Am Chem Soc*. 2002;124:14864-14865.

58. Ding Y, Kong X, Wang Z. Doping and planar defects in the formation of single-crystal ZnO nanorings. *Phys Rev B*. 2004;70(23):235408. doi:10.1103/PhysRevB.70.235408.

59. Tuomisto F, Ranki V, Saarinen K, Look DC. Evidence of Zn Vacancy Acting as the Dominant Acceptor in n-Type ZnO, *Phys Rev Lett*. 2003;91:205502.

60. Zubiaga A, Tuomisto F, Plazaola F, et al. Zinc vacancies in the heteroepitaxy of ZnO on sapphire: Influence of the substrate orientation and layer thickness, *Appl Phys Lett*. 2005;86:042103.

61. Wang ZL. Zinc oxide nanostructures: growth, properties and applications. *J Phys Condens Matter*. 2004;16(25):R829-R858. doi:10.1088/0953-8984/16/25/R01.

62. Wang ZL, Song J. Piezoelectric Nanogenerators Based on Zinc Oxide Nanowire Arrays. *Science*. 2006;312:242-246.

63. Voss T, Svacha GT, Mazur E, Ronning C, The influence of local heating by nonlinear pulsed laser excitation on the transmission characteristics of a ZnO nanowire waveguide. *Nanotechnology*. 2009;20:095702.

64. Ohashi N, Kataoka K, Ohgaki T, Miyagi T HH and MK. . *Appl Phys Lett*. 2003;83:4857.

65. Grundmann M, Frenzel H, Lajn A, Lorenz M, Schein F, Wenckstern H V. pss solidi. *Phys Status Solidi A*. 2010;207(6):1437-1449. doi:10.1002/pssa.200983771.

66. Ohashi N, Kataoka K, Ohgaki T, Miyagi T, Haneda H, Morinaga K. Synthesis of zinc oxide varistors with a breakdown voltage of three volts using an intergranular glass phase in the bismuth-boron-oxide system. *Appl Phys Lett*. 2003;83:4857.

67. Duan XF, Huang Y, Cui Y, Wang JF, Lieber CM. Indium phosphide nanowires as building blocks for nanoscale electronic and optoelectronic devices. *Nature*. 2001;409:66.

68. Lin X, He XB, Lu JL, et al. *Surf Interface Anal*. 2006;38:1096.

69. Wang XD, Summers CJ, Wang ZL. . *Nano Lett*. 2004;4:423.

70. Seiyama T, Kato A, Fulishi K, Nagatani M. . *Anal Chem*. 1962;34:1502.

71. Topsakal M, Cahangirov S, Bekaroglu E, Ciraci S. A First-Principles Study of Zinc Oxide Honeycomb Structures. *Phys Rev B*. 2009;80:235119.

72. Djurisic AB, Leung YH. . *Wiley-VCH*. 2006;2:944-961.

73. Pearton SJ, Norton DP, Ip K, Heo YW, Steiner T. . *Prog Mater Sci*. 2005;50:293.

74. Chang PC, Fan ZY, Wang DW, Tseng WY, Chiou WA. ZnO nanowires synthesized by vapor trapping CVD method. *Chem Mater*. 2004;16(24):5133-5137.

75. Lee JS, Park K, Kang MI, et al. . *J Cryst Growth*. 2003;254:423.

76. Weintraub B, Zhou Z, Li Y, Deng Y. Solution synthesis of one-dimensional ZnO nanomaterials and their applications. *Nanoscale*. 2010;2(9):1573-1587. doi:10.1039/c0nr00047g.

77. Duan J, Huang X, Wang E. PEG-assisted synthesis of ZnO nanotubes. 2006;60:1918-1921. doi:10.1016/j.matlet.2005.12.052.

78. Le HQ, Chua SJ, Chen Z. Growth of single crystal ZnO nanorods on GaN using an aqueous. *Appl Phys Lett*. 2005;87:101908. doi:10.1063/1.2041833.

79. Fan BX, Zhang M, Shafiq I, Zhang W, Lee C, Lee S. ZnS / ZnO Heterojunction Nanoribbons. *Adv Mater*. 2009;21:2393-2396. doi:10.1002/adma.200802049.

80. Li DP, Wang GZ, Han XH. Raman property of In doped ZnO superlattice nanoribbons. *J Phys D Appl Phys*. 2009;42:175308. doi:10.1088/0022-3727/42/17/175308.

81. Maffeis TGG, Penny MW, Garbutt JDW, Wilks SP, Zinc I. STM-STS investigation of vacuum annealed ZnO nanoribbons. *Phys Status Solidi A*. 2010;207(2):282-285. doi:10.1002/pssa.200982485.

82. Pan ZW, Dai ZR, Wang ZL. . *Science (80-)*. 2001;291:1947.

83. Gao P, Ding Y, Wang ZL. . *Nano lett*. 2003;3:1315.

84. Wang ZL. ZnO nanowire and nanobelt platform for nanotechnology. *Mater Sci Eng R Reports*. 2009;64(3-4):33-71. doi:10.1016/j.mser.2009.02.001.

85. Zhao MH, Wang ZL, Mao SX. . *Nano Lett*. 2004;4:587.

86. Yi G-C, Wang C, Park W Il. ZnO nanorods: synthesis, characterization and applications. *Semicond Sci Technol*. 2005;20(4):S22-S34. doi:10.1088/0268-1242/20/4/003.

87. Vayssieres L. Growth of Arrayed Nanorods and Nanowires of ZnO from Aqueous Solutions **. *Adv Mater*. 2003;15(5):464-466.

88. Li Q, Kumar V, Li Y, Zhang H, Marks TJ, Chang RPH. Fabrication of ZnO Nanorods and Nanotubes in Aqueous Solutions. *Chem Mater*. 2005;17(5):1001-1006.

89. Park WI, Kim DH, Jung S, Yi G. Metalorganic vapor-phase epitaxial growth of vertically well-aligned ZnO nanorods. *Appl Phys Lett*. 2002;80(22):4232-4234. doi:10.1063/1.1482800.

90. Dikovska AO, Nedyalkov NN, Atanasov PA. Fabrication of ZnO nanorods using metal nanoparticles as growth nuclei. *Mater Sci Eng B*. 2011:4-7. doi:10.1016/j.mseb.2011.02.030.

91. Xu S, Wang ZL. One-dimensional ZnO nanostructures: Solution growth and functional properties. *Nano Res*. 2011;4(11):1013-1098. doi:10.1007/s12274-011-0160-7.

92. Saunders RB, Sc B, Sc M. Theoretical and Experimental Studies of ZnO Nanowires Grown by Vapour Phase Transport by. 2012:18.

93. Yan H, He R, Johnson J, Law M, Saykally RJ, Yang P. . *J Am Chem Soc*. 2003;125:4728.

94. Kong XY, Ding Y, Yang R, Wang ZL. . *Science (80-)*. 2004;303:1348.

95. Ding Y, Kong XY, Wang ZL. Doping and planar defects in the formation of single-crystal ZnO nanorings. *Phys Rev B*. 2004;70:235408.

96. Lu HB, Li H, Liao L, et al. Low-temperature synthesis and photocatalytic properties of ZnO nanotubes by thermal oxidation of Zn nanowires. *Nanotech*. 2008;19(4):045605. doi:10.1088/0957-4484/19/04/045605.

97. Wang RM, Xing YJ, Xu J, Yu DP. Fabrication and microstructure analysis on zinc oxide nanotubes. *New J Phys*. 2003;5:115-115. doi:10.1088/1367-2630/5/1/115.

98. Wei A, Sun XW, Xu CX, Dong ZL, Yu MB, Huang W. Stable field emission from hydrothermally grown ZnO nanotubes. *Appl Phys Lett*. 2006;88(21):213102. doi:10.1063/1.2206249.

99. Hua JQ, Bando Y. Growth and optical properties of single-crystal tubular ZnO whiskers. *Appl Phys Lett*. 2003;82:1401.

100. Wu JJ, Liu SC, Wu CT, Chen KH, Chen LC. Heterostructures of ZnO-Zn coaxial nanocables and ZnO nanotubes. *Appl Phys Lett*. 2002;81:1312-1314.

101. Ahsanulhaq Q, Kim SH, Kim JH, Hahn YB. Structural properties and growth mechanism of flower-like ZnO structures obtained by simple solution method. *Mater Res Bull*. 2008;43(12):3483-3489. doi:10.1016/j.materresbull.2008.01.021.

102. Tokumoto MS, Briois V, Santilli C V, Pulcinelli SH. Preparation of ZnO Nanoparticles : Structural Study. *J Sol-Gel Sci Technol*. 2003;26:547-551.

103. Anas S, Mahesh K V, Ambily KJ, et al. New insights on physico-chemical transformations of ZnO : From clustered multipods to single crystalline nanoplates. *Mater Chem Phys*. 2012;134(1):435-442. doi:10.1016/j.matchemphys.2012.03.014.

104. Zhu Y-C, Bando Y. Large scale preparation of zinc nanosheets by thermochemical reduction of ZnS powders. *Chem Phys Lett*. 2003;372(5-6):640-644. doi:10.1016/S0009-2614(03)00472-X.

105. Umar A, Hahn YB. ZnO nanosheet networks and hexagonal nanodiscs grown on silicon substrate: growth mechanism and structural and optical properties. *Nanotechnology*. 2006;17(9):2174-2180. doi:10.1088/0957-4484/17/9/016.

106. Deng G, Ding A, Cheng W, Zheng X, Qiu P. Two-dimensional zinc oxide nanostructure. *Solid State Commun*. 2005;134(4):283-286. doi:10.1016/j.ssc.2005.01.022.

107. Spanhel L, Anderson MA. Semiconductor Clusters in the Sol-Gel Process: Quantized Aggregation, Gelation, and Crystal Growth in Concentrated ZnO Colloids. *J Am Chem Soc*. 1991;113:2826-2833.

108. Zhang H, Yang D, Ji Y, Ma X, Xu J, Que D. Low Temperature Synthesis of Flowerlike ZnO nanostructures by Cetyltrimethylammonium Bromide-Assisted Hydrothermal Process. *J Phys Chem B*. 2004;108:3955.

109. Sun TJ, Qiu JS, Liang CH. . *J Chem Phys C*. 2008;112:715-721.

110. Yan H, Johnson J, Law M, et al. ZnO nanoribbon Microcavity Lasers. *Adv Mater*. 2003;15:1907.

111. Wei DP, Ma Y, Pan HY, Chen Q. . *J Phys Chem C*. 2008;112:8594-8599.

112. Tusche C, Meyerheim HL, Kirschner J. Observation of Depolarized ZnO (0001) Monolayers: Formation of Unreconstructed Planar Sheets. *Phys Rev Lett*. 2007;99:026102.

113. Wang R, Wang S, Wu X, Li S, Liu L. Nonlinear elasticity of monolayer zinc oxide honeycomb structures: A first-principles study. *Phys E Low-dimensional Syst Nanostructures*. 2011;43(4):914-918. doi:10.1016/j.physe.2010.11.013.

114. Alder BJ, Wainwright TE. Phase transition for hard sphere system. *J Chem Phys*. 1957;27:1208-1209.

115. Gibson JB, Goland AN, Milgram M, Vineyard GH. Dynamics of radiation damage. *Phys Rev*. 1960;120:1229-1253.

116. Rahman A. Correlations in the motion of atoms in liquid argon. *Phys Rev*. 1964;136:A405-A411.

117. Zhigilei L. *Introduction to Atomic Simulation*.; :4270-7270.

118. Michael P. Allen. Introduction to Molecular Dynamics Simulation. *Comput Soft Matter*. 2004;23:1-28.

119. Pedone A, Malavasi G, Menziani MC, Cormack AN, Segre U. A new self-consistent empirical interatomic potential model for oxides, silicates, and silica-based glasses. *J Phys Chem B*. 2006;110(24):11780-11795. http://www.ncbi.nlm.nih.gov/pubmed/16800478.

120. Kilic ME, Erkoc S. Structural properties of defected ZnO nanosheets under biaxial strain: Molecular Dynamics Simulations. *J Nanosci Nanotech*. 2015;15:xx.

121. Kilic ME, Erkoc S. Structural properties of hexagonal shaped ZnO nanorods under torsion and compression: Molecular Dynamics Simulations. *Int J Mod Phys C*. xx:xx.

122. Pathria RK, Beale PD. *Statistical Mechanics*.; 2009:Third Edidition.

123. Erkoç S. *Lecture Notes on Simulations of Many-Particle Systems*. METU; 2004.

124. Verlet L. Computer "Experiments" on Classical Fluids. I. Thermodynamical Properties of Lennard-Jones Molecules. *Phys Rev*. 1967;159(1):98-103. doi:10.1103/PhysRev.159.98.

125. Verlet L. Computer "Experiments" on Classical Fluids. II. Equilibrium Correlation Functions. *Phys Rev*. 1968;165(1):201-214. doi:10.1103/PhysRev.165.201.

126. Kerson H. *Statistical Mechanics*. New York: Wiley; 1987.

127. Richard C, Catlow A, Bromley ST, et al. Modelling nano-clusters and nucleation. *Phys Chem Chem Phys*. 2010;12:786-811.

128. Li L, Zhou Z, Wang X, Huang W, He Y, Yang M. First-princeples study of static polarizability, first and second hyperpolarizabilities of small-sized ZnO clusters. *Phys Chem Chem Phys*. 2008;20:6829-6835.

129. Sun XW, Liu ZJ, Chen QF, Lu HW, Song T, Wang CW. Heat capacity of ZnO with cubic structure at high temperatures. *Solid State Commun*. 2006;140(5):219-224.

130. Lee WJ, Chang JG, Ju SP, Weng MH, Lee CH. Structure-dependent mechanical properties of ultrathin zinc oxide nanowires. *Nanoscale Res Lett*. 2011;6:352.

131. Kulkarni AJ, Zhou M, Ke FJ. Orientation and size dependence of the elastic properties of zinc oxide nanobelts. *Nanotechnology*. 2005;16:2749.

132. Kulkarni AJ, Zhou M, Sarasamak K, Limpijumnong S. Novel Phase Transformation in ZnO nanowires under Tensile Loading. *Phys Rev Lett*. 2006;97:105502.

133. Wen B, Melnik R. Relative stability of nanosized wurtzite and graphitic ZnO from density functional theory. *Chem Phys Lett*. 2008;466:84-87.

134. Wang B, Zhao J, Jia J, Shi D, Wan J, Wang G. Structural, mechanical and electronic properties of ultrathin znO nanowires. *Appl Phys Lett*. 2008;93:021918.

APPENDIX A

NANOSTRUCTURE FIGURES

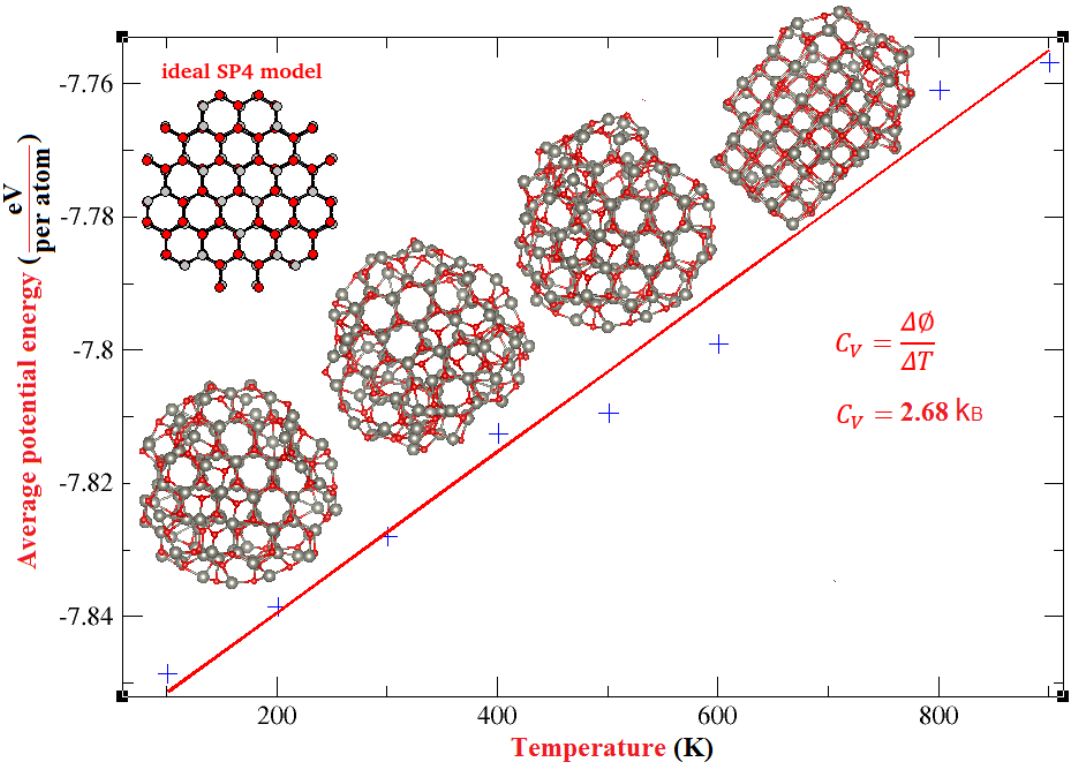

Figure A.1 The structural properties of the SP4 model under the increasing temperatures during the NEMD process.

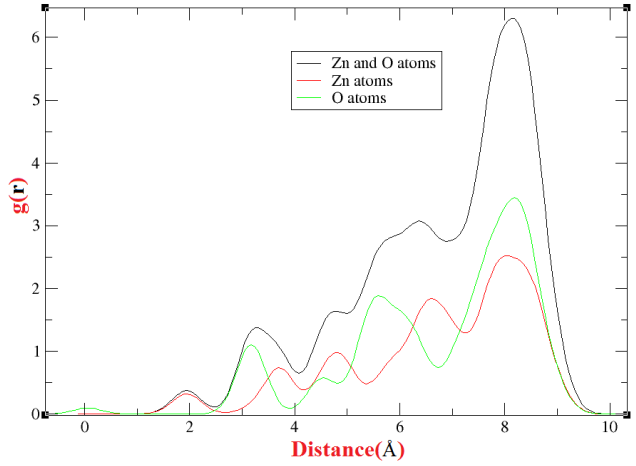

Figure A.2 Radial atomic distribution of the SP4 model at 1 K.

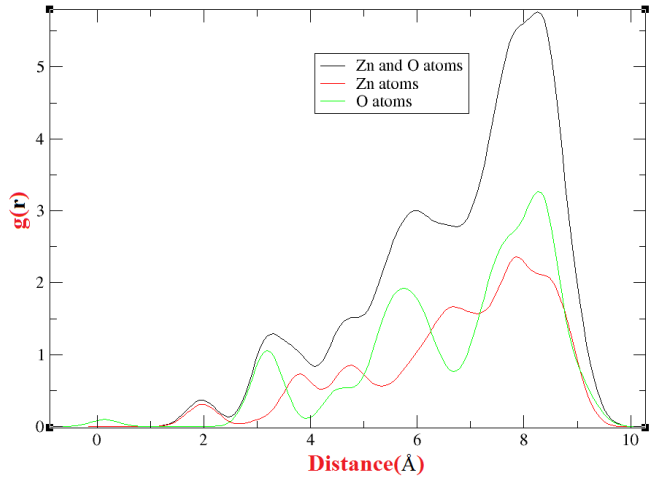

Figure A.3 The same as Figure A.2, but at 300 K.

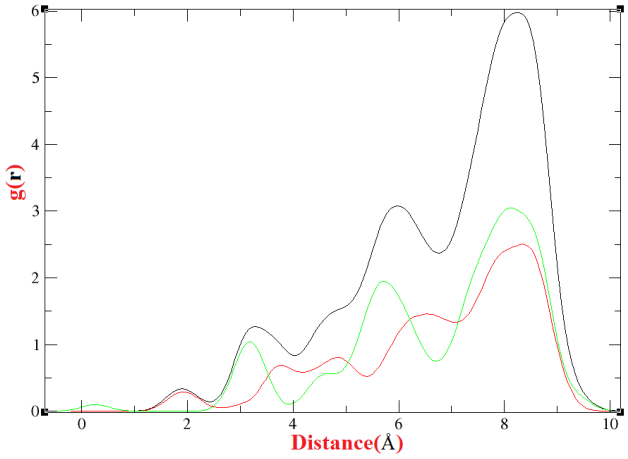

Figure A.4 The same as Figure A.2, but at 600 K.

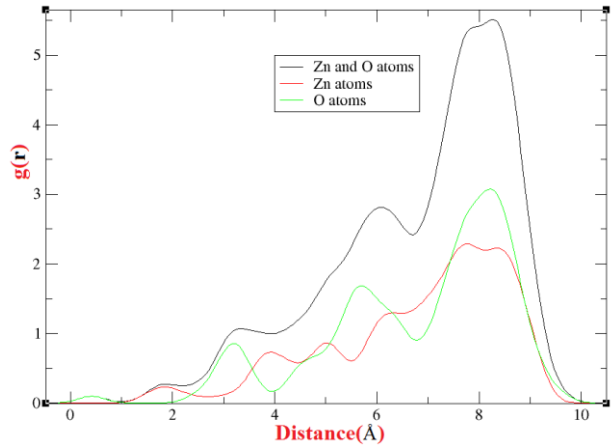

Figure A.5 The same as Figure A.2, but at 800 K.

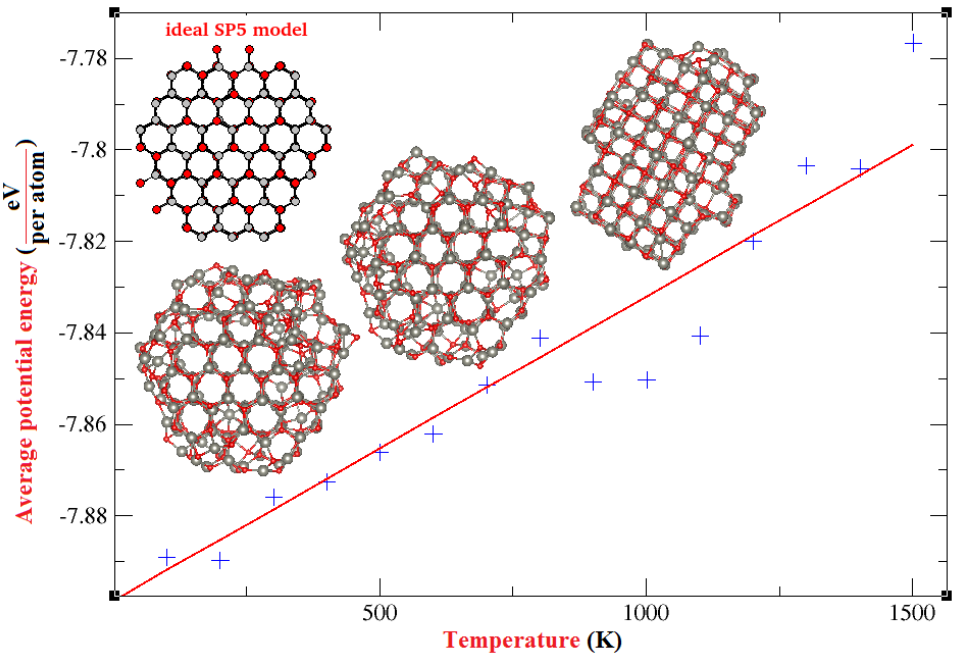

Figure A.6 The structural properties of the SP5 model under the increasing temperatures during the NEMD process.

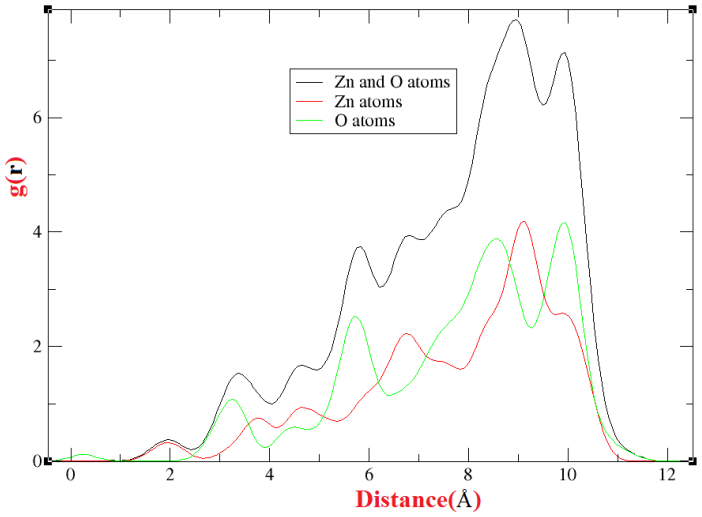

Figure A.7 Radial atomic distribution of the SP5 model at 1 K.

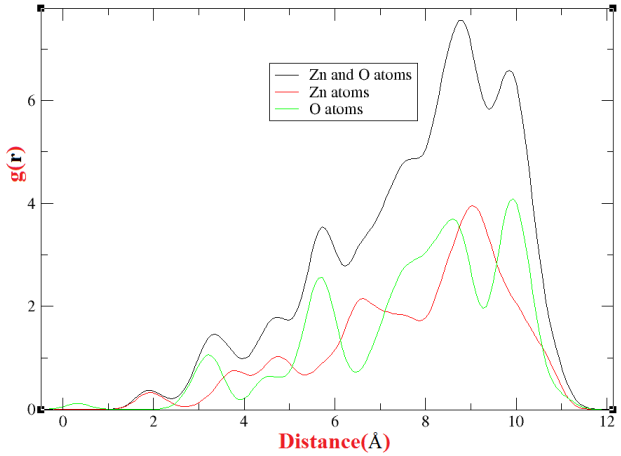

Figure A.8 The same as Figure A.2, but at 300 K.

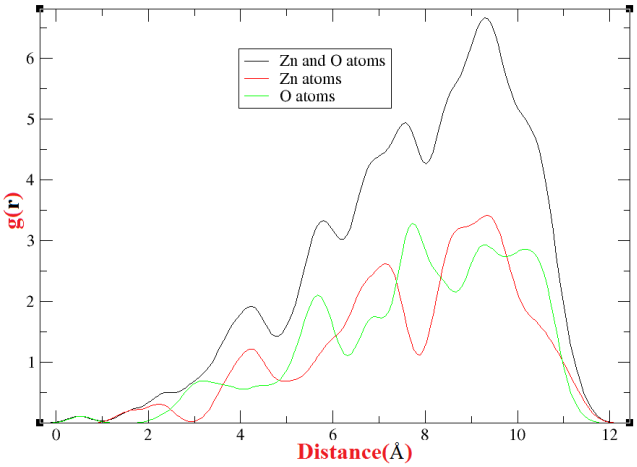

Figure A.9 The same as Figure A.2, but at 600 K.

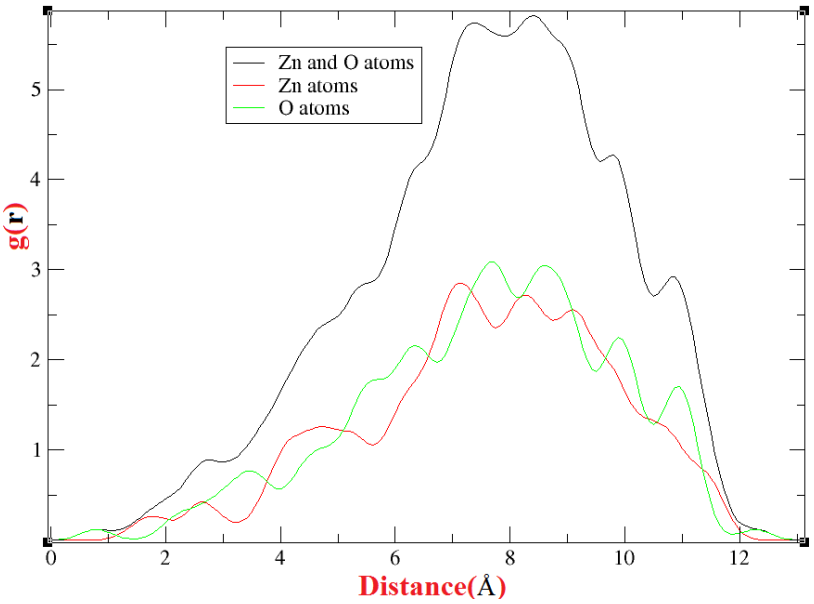

Figure A.10 The same as Figure A.2, but at 1100 K.

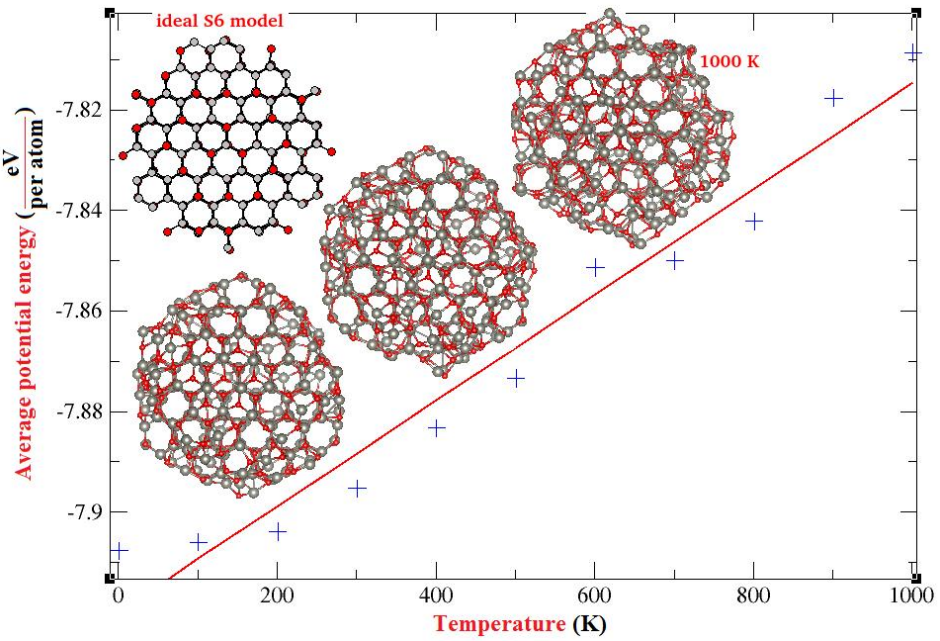

Figure A.11 The structural properties of the SP6 model under the increasing temperatures during the NEMD process.

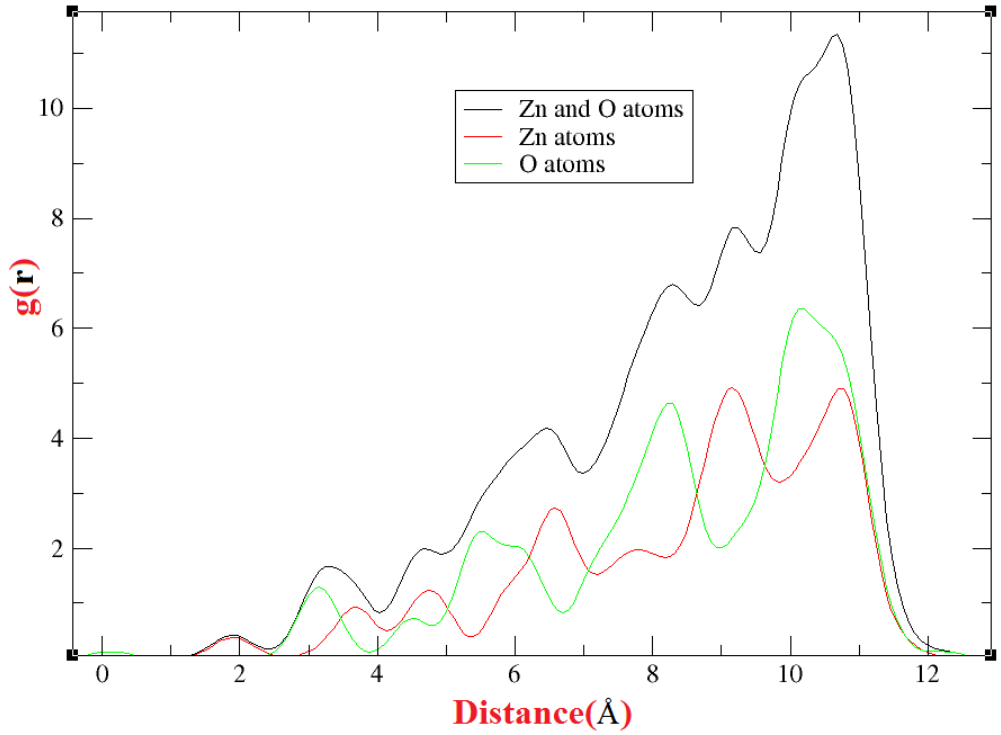

Figure A.12 Radial atomic distribution of the SP6 model at 1 K.

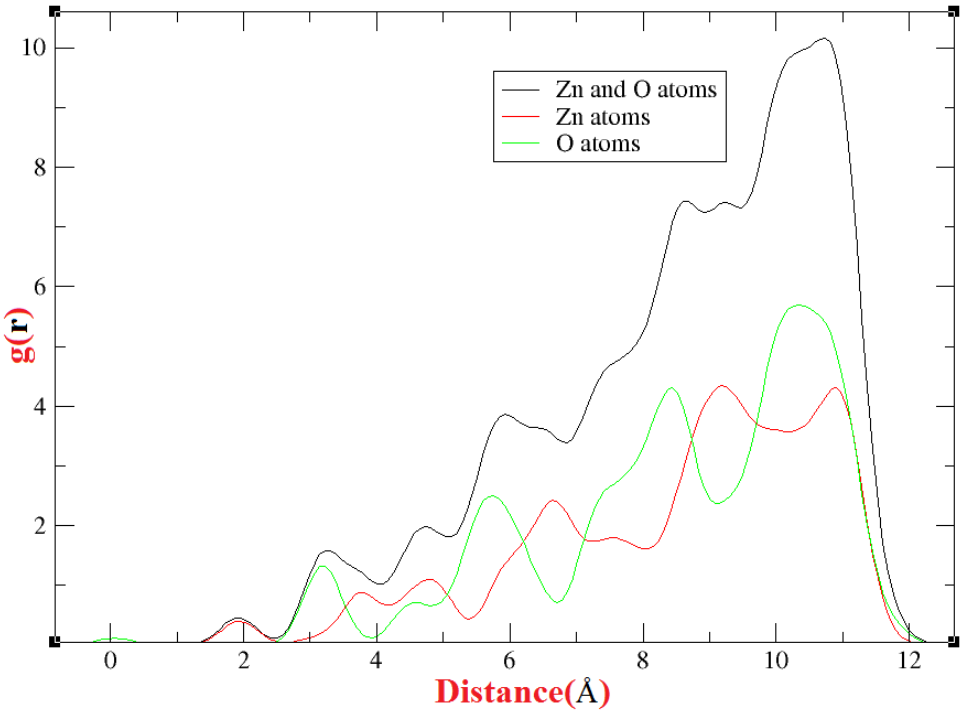

Figure A.13 The same as Figure A.12, but at 300 K.

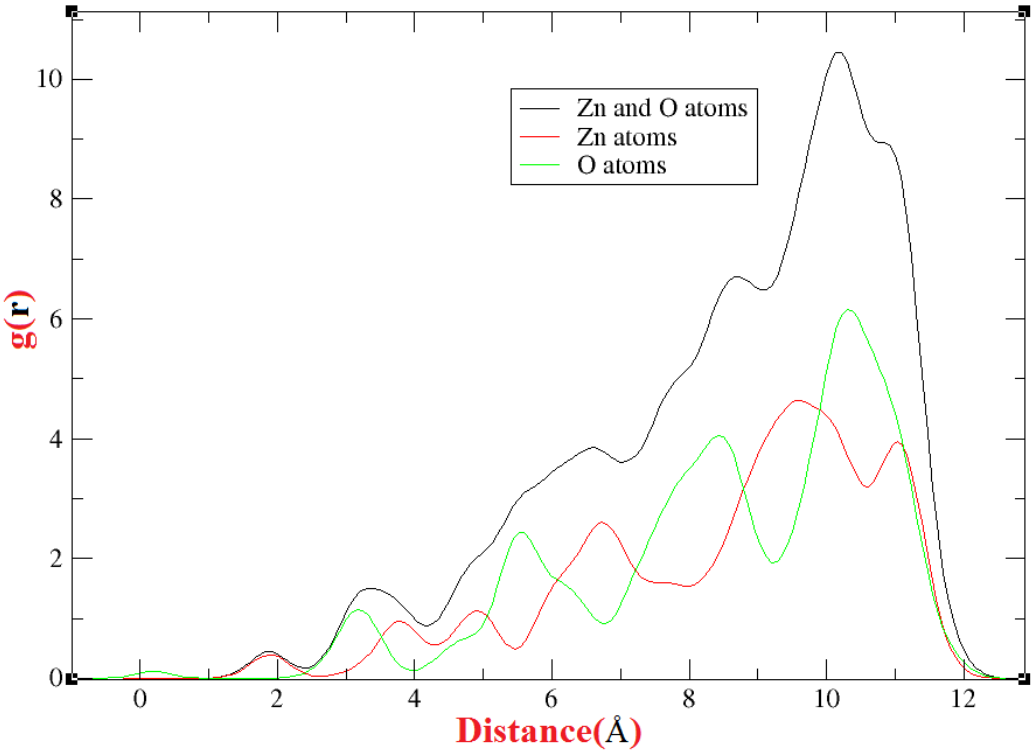

Figure A.14 The same as Figure A.12, but at 600 K.

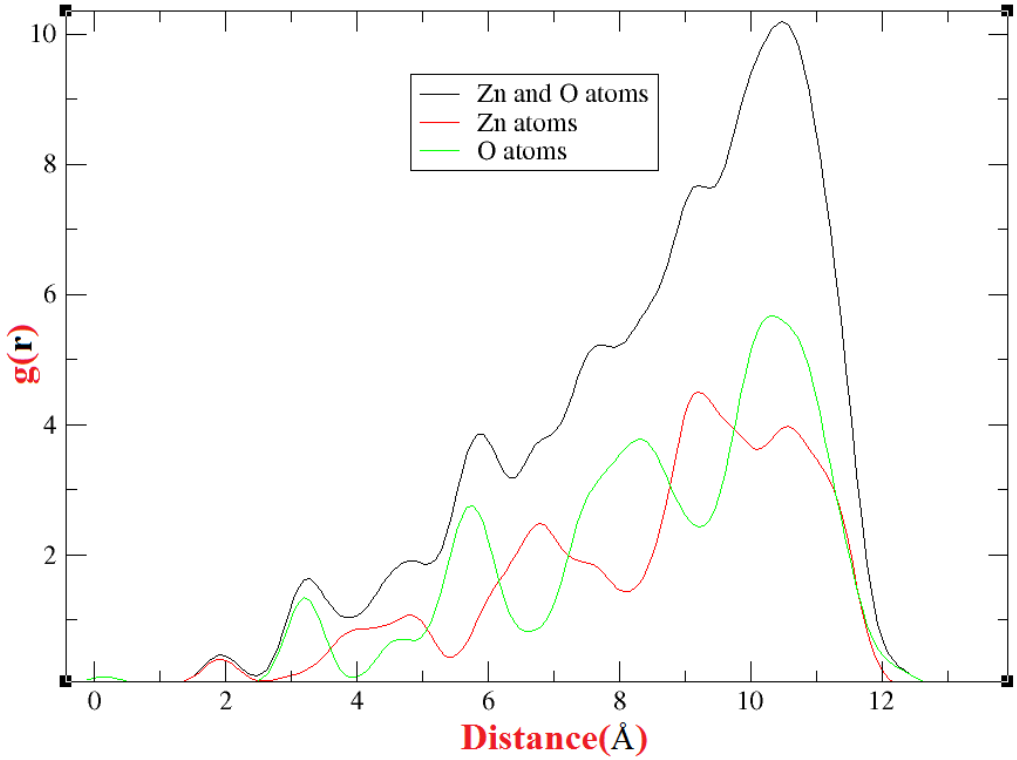

Figure A.15 The same as Figure A.12, but at 1000 K.

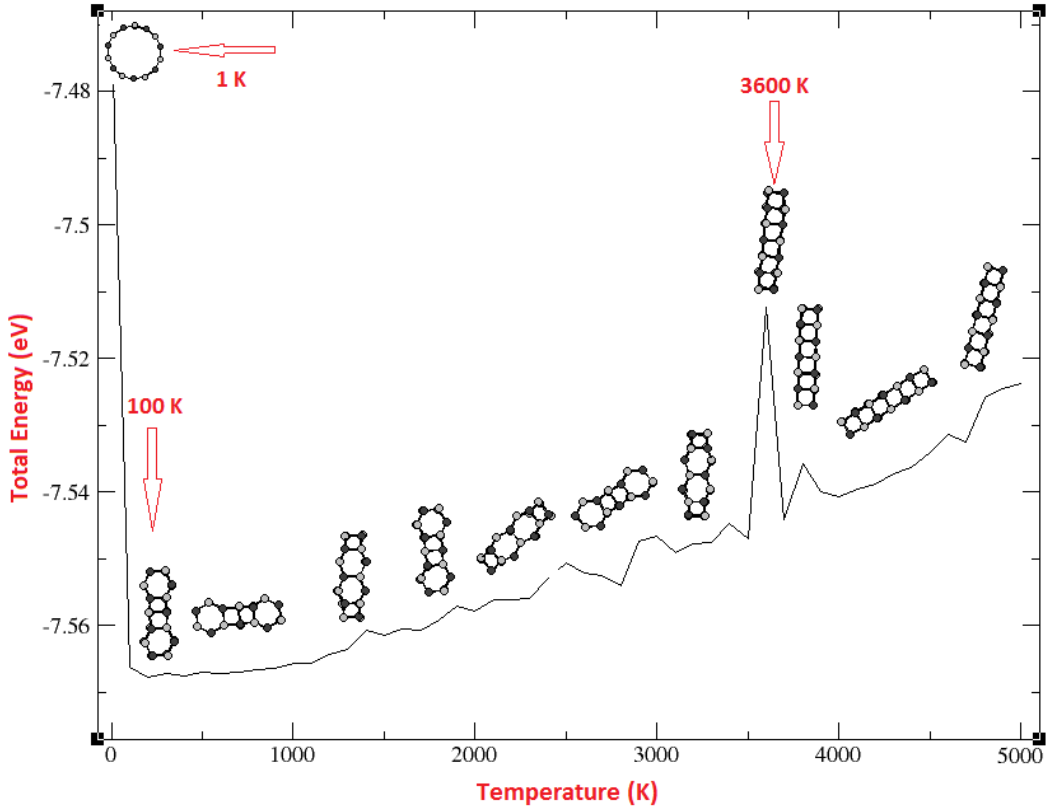

Figure A.16 The R3 model nanoring at the increasing temperatures in the case of NEMD.

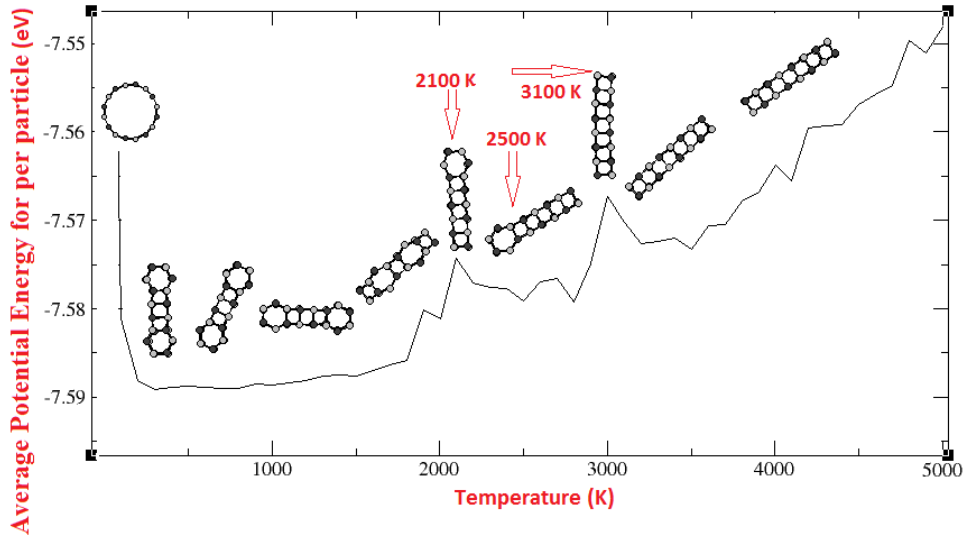

Figure A.17 The R4 model nanoring at the increasing temperatures in the case of NEMD.

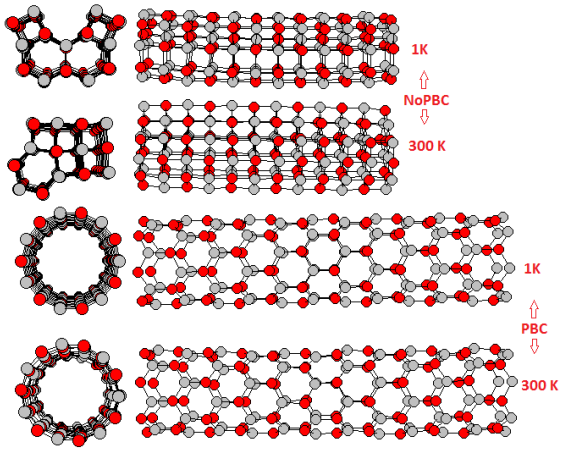

Figure A.18 The ZT3 model with NoPBC and PBC at both 1 and 300 K.

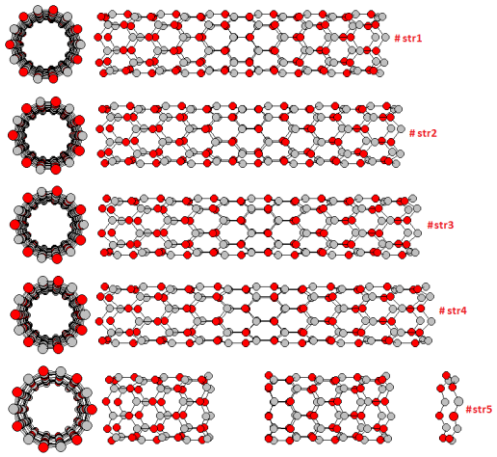

Figure A.19 The ZT3 model structure under tensile strain applications at 1 K.

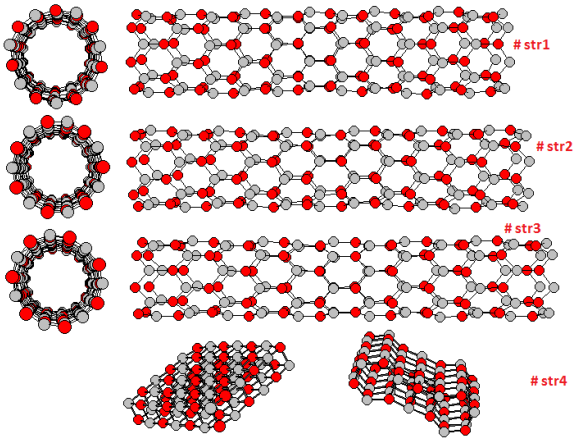

Figure A.20 The ZT3 model structure under tensile strain applications at 300 K.

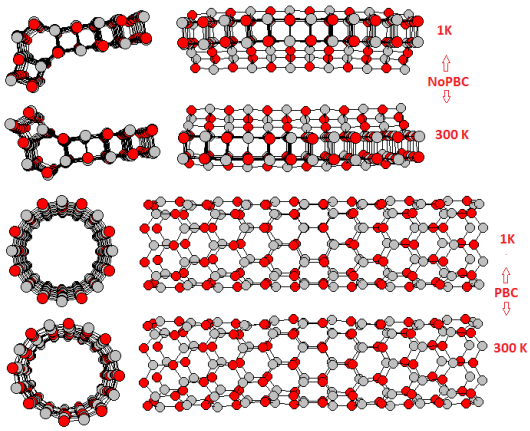

Figure A.21 The ZT4 model with NoPBC and PBC at both 1 and 300 K.

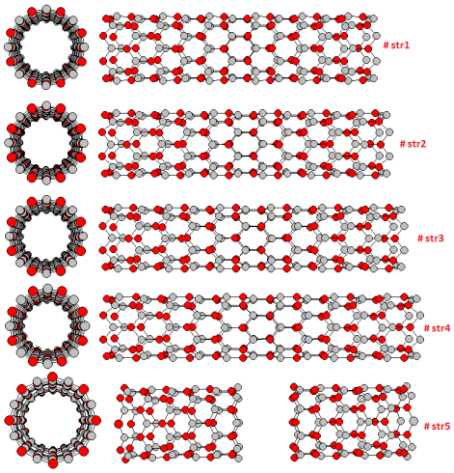

Figure A.22 The ZT4 model structure under tensile strain applications at 1 K.

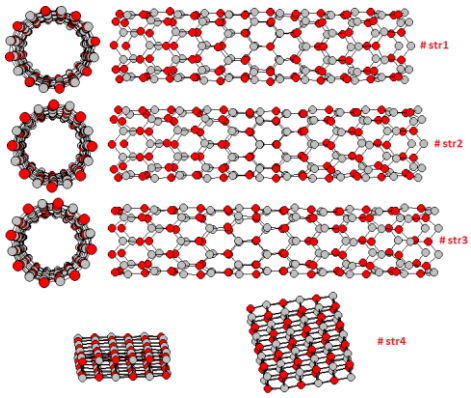

Figure A.23 The ZT4 model structure under tensile strain applications at 300 K.

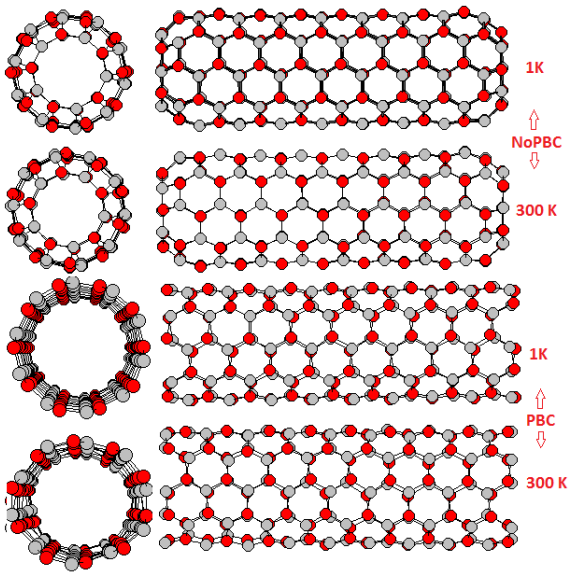

Figure A.24 The AT3 model with NoPBC and PBC at both 1 and 300 K.

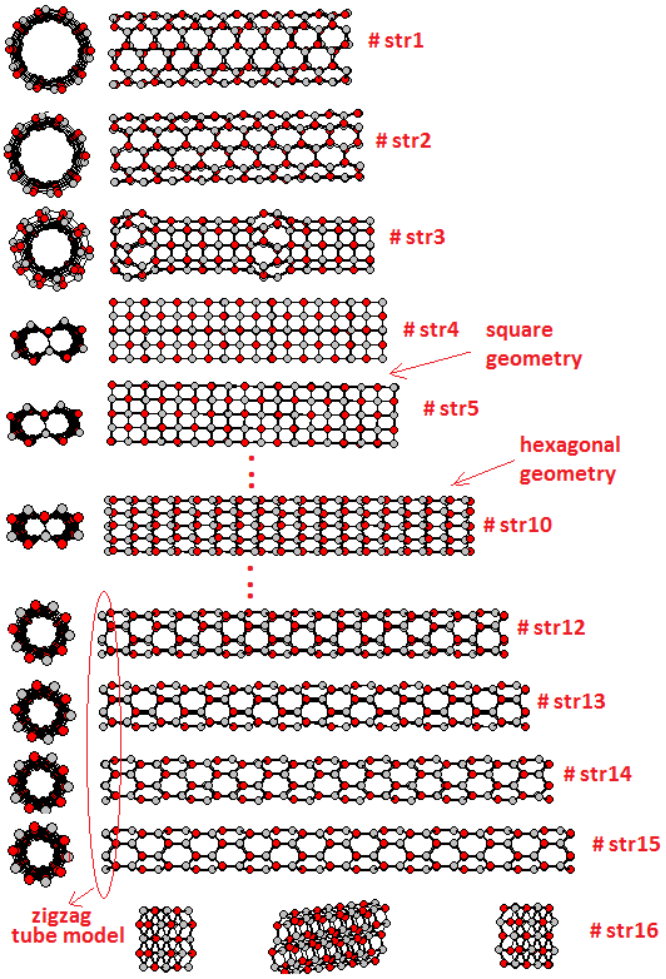

Figure A.25 The AT3 model structure under tensile strain applications at 1 K.

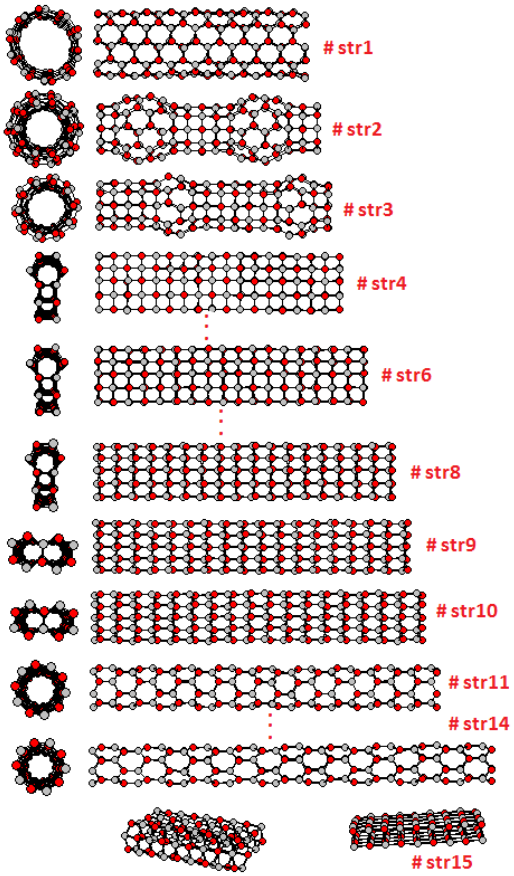

Figure A.26 The AT3 model structure under tensile strain applications at 300 K.

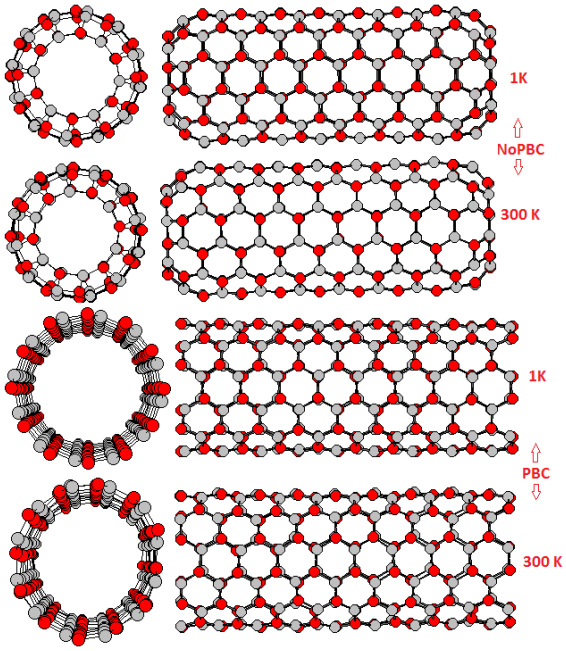

Figure A.27 The AT4 model with NoPBC and PBC at both 1 and 300 K.

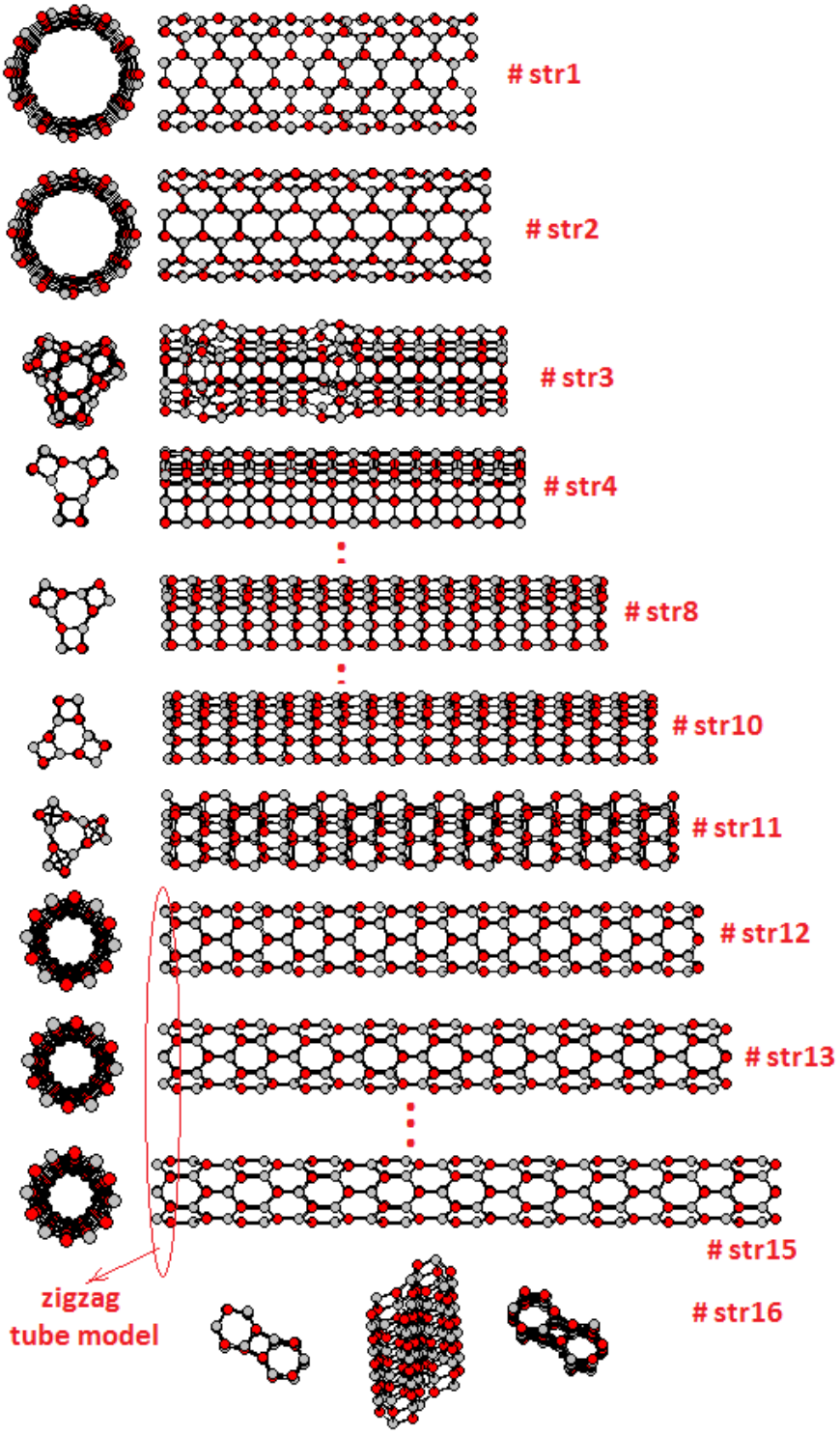

Figure A.28 The AT4 model structure under tensile strain applications at 1 K.

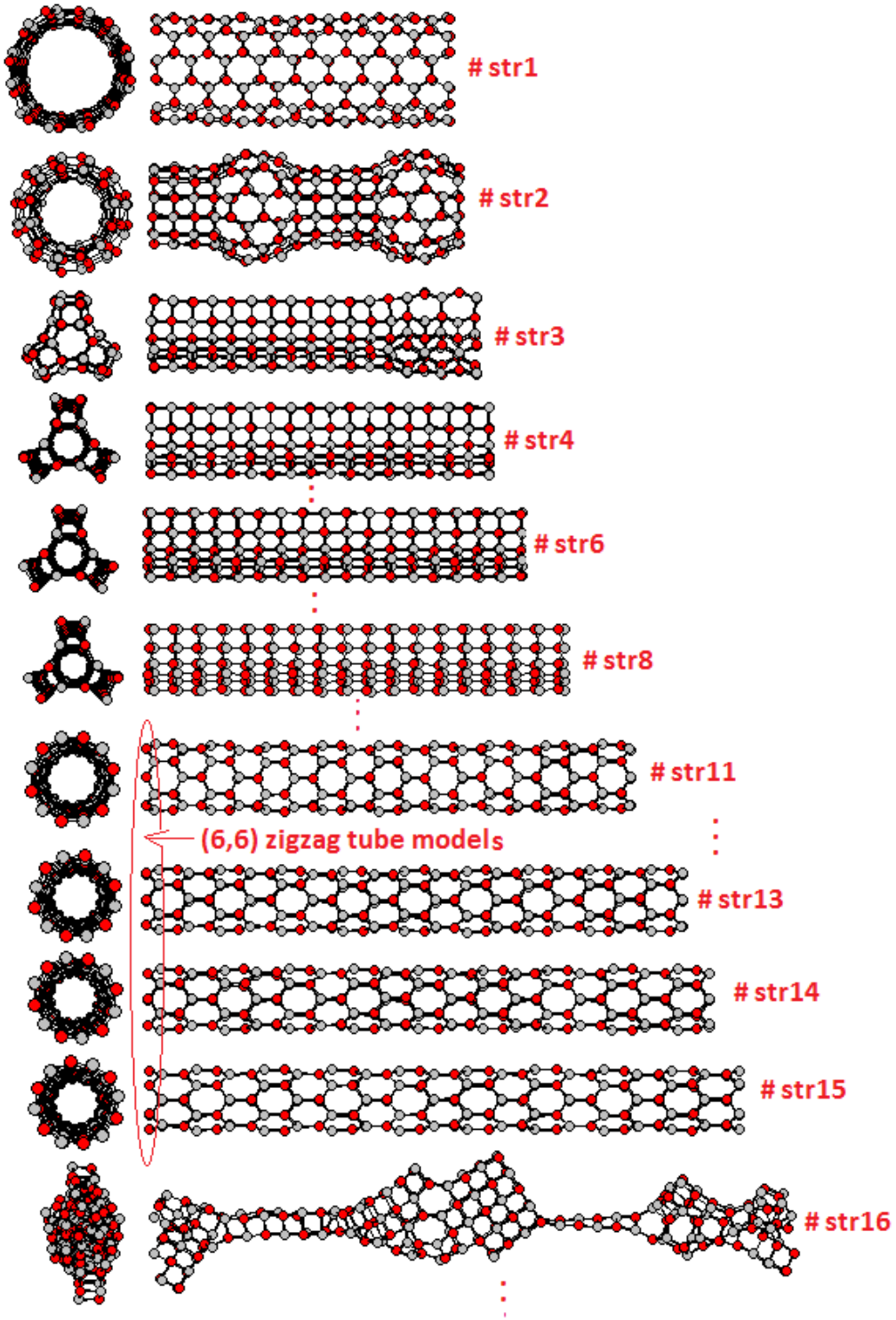

Figure A.29 The AT4 model structure under tensile strain applications at 300 K.

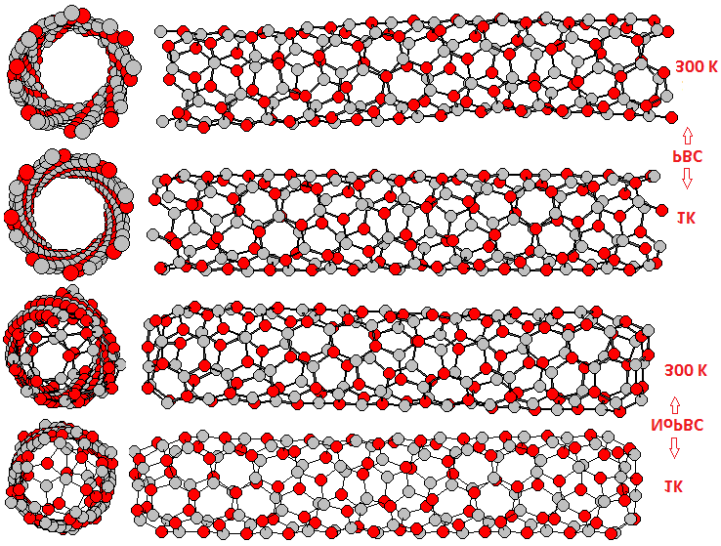

Figure A.30 The CT3 model with NoPBC and PBC at both 1 and 300 K.

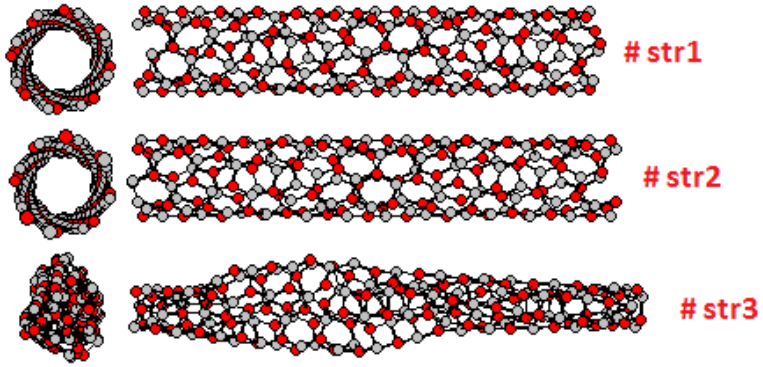

Figure A.31 The CT3 model structure under tensile strain applications at 1 K.

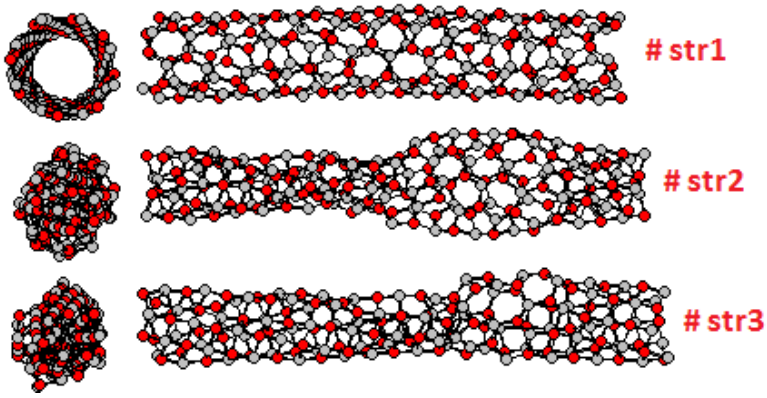

Figure A.32 The CT3 model structure under tensile strain applications at 300 K.

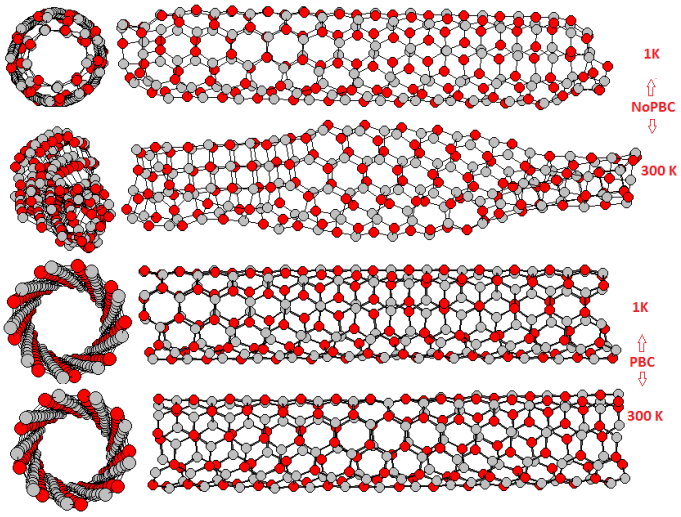

Figure A.33 The CT4 model with NoPBC and PBC at both 1 and 300 K.

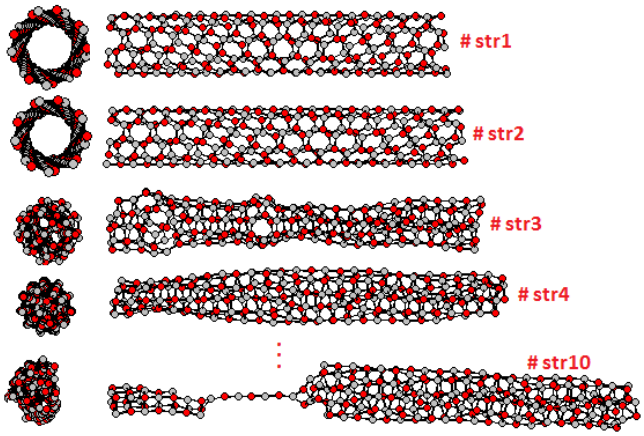

Figure A.34 The CT4 model structure under tensile strain applications at 1 K.

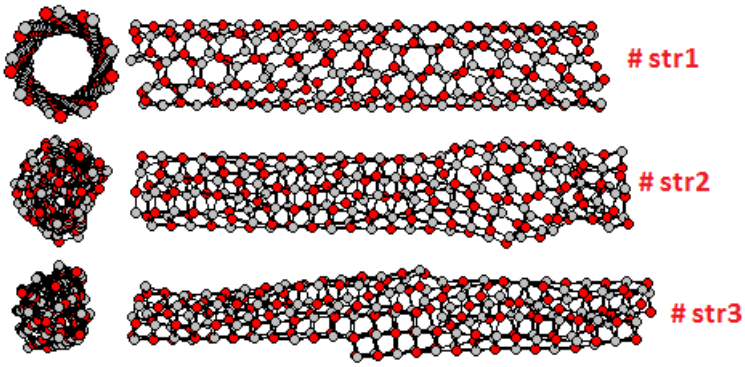

Figure A.35 The CT4 model structure under tensile strain applications at 300 K.

APPENDIX B

SAMPLE INPUT AND OUTPUT FILES

```
**************************************************************************
 MOLECULAR-DYNAMICS SIMULATION FOR ZnO Nanoribbons
**************************************************************************
 MDSL=100000 IAVL= 100 IPPL= 500 ISCAL= 2
 IPD= 0 TE=   1.00 IPBC= 1 IC=2 NA= 60
 PP (I):    56.85000     0.00000     0.00000
**************************************************************************
    INPUT DATA FOR TYPE= 1
   AMASS=    65.39000    (IN ATOM GRAM.)    LAYER= 3
 ..........................................................................
   1    2.84250    0.00000    0.00000    5.68500    3.28224    1.00000 10   1   1
   2    2.84250    3.28224    0.00000    5.68500    3.28224    1.00000 10   1   1
   3    0.00000    1.64112    0.00000    5.68500    3.28224    1.00000 10   1   1
    NUMBER OF ATOMS FOR THIS TYPE=   30
**************************************************************************
    INPUT DATA FOR TYPE= 2
   AMASS=    15.99940    (IN ATOM GRAM.)    LAYER= 3
 ..........................................................................
   1    0.94750    0.00000    0.00000    5.68500    3.28224    1.00000 10   1   1
   2    3.79000    1.64112    0.00000    5.68500    3.28224    1.00000 10   1   1
   3    0.94750    3.28224    0.00000    5.68500    3.28224    1.00000 10   1   1
    NUMBER OF ATOMS FOR THIS TYPE=   30
**************************************************************************
 NUMBER OF MOVING ATOMS: NA= 60
 NUMBER OF TOTAL ATOMS: NN= 60
```

INITIAL COORDINATES OF ALL ATOMS: (X, Y, Z)

1 1 51.16500 1.64112 0.00000
2 1 45.48000 1.64112 0.00000
3 1 39.79500 1.64112 0.00000
4 1 34.11000 1.64112 0.00000
5 1 28.42500 1.64112 0.00000
6 1 22.74000 1.64112 0.00000
7 1 17.05500 1.64112 0.00000
8 1 11.37000 1.64112 0.00000
9 1 5.68500 1.64112 0.00000
10 1 0.00000 1.64112 0.00000

****

1 1 51.16500 1.64112 0.00000
2 1 45.48000 1.64112 0.00000
3 1 39.79500 1.64112 0.00000
4 1 34.11000 1.64112 0.00000
5 1 28.42500 1.64112 0.00000
6 1 22.74000 1.64112 0.00000
7 1 17.05500 1.64112 0.00000
8 1 11.37000 1.64112 0.00000
9 1 5.68500 1.64112 0.00000
10 1 0.00000 1.64112 0.00000

And others

PRINT IN CONVER: P= 56.8500000 0.0000000 0.0000000 I, J, K = 1 1 1

1 0.00000 56.85000 56.85000

INITIAL COORDINATES, FORCES AND ENERGIES:

I	X	Y	Z	FX	FY	FZ	EE
1	51.16500	1.64112	0.00000	0.349E+00	0.208E-04	0.000E+00	-0.808E+01
2	45.48000	1.64112	0.00000	0.400E+00	0.208E-04	0.000E+00	-0.808E+01
3	39.79500	1.64112	0.00000	0.400E+00	0.208E-04	0.000E+00	-0.808E+01
4	34.11000	1.64112	0.00000	0.349E+00	0.208E-04	0.000E+00	-0.808E+01
5	28.42500	1.64112	0.00000	0.400E+00	0.208E-04	0.000E+00	-0.808E+01
6	22.74000	1.64112	0.00000	0.400E+00	0.208E-04	0.000E+00	-0.808E+01
7	17.05500	1.64112	0.00000	0.349E+00	0.208E-04	0.000E+00	-0.808E+01
8	11.37000	1.64112	0.00000	0.349E+00	0.208E-04	0.000E+00	-0.808E+01
9	5.68500	1.64112	0.00000	0.400E+00	0.208E-04	0.000E+00	-0.808E+01
10	0.00000	1.64112	0.00000	0.349E+00	0.208E-04	0.000E+00	-0.808E+01

And others

PERIODIC PRINTING OF COORDINATES, FORCES AND ENERGIES: AT MDS= 500

I	X	Y	Z	FX	FY	FZ	EE
1	51.19041	1.64048	-0.00304	-0.760E-03	0.781E-03	0.185E-01	-0.801E+01
2	45.50683	1.63962	0.00175	-0.464E-01	0.178E-02	-0.529E-02	-0.802E+01
3	39.82270	1.63915	0.00145	-0.646E-01	0.552E-02	-0.760E-02	-0.801E+01
4	34.13485	1.64061	-0.00015	-0.486E-01	-0.263E-03	0.424E-02	-0.802E+01
5	28.45345	1.63971	0.00134	-0.181E-01	0.126E-01	-0.698E-02	-0.802E+01
6	22.76543	1.64158	-0.00033	-0.458E-01	-0.523E-02	0.268E-03	-0.801E+01
7	17.08181	1.64159	0.00043	-0.793E-02	-0.196E-02	0.502E-02	-0.802E+01
8	11.39707	1.63871	0.00432	-0.560E-02	0.770E-02	-0.126E-01	-0.801E+01
9	5.70937	1.64014	0.00490	0.110E-01	0.113E-01	-0.150E-01	-0.802E+01
10	0.02853	1.63677	-0.00032	-0.537E-01	0.151E-01	0.655E-02	-0.802E+01

And others

EPOT=-0.43434E+03 EKIN= 0.15511E-01 TCALC= 1.00 SCFAC= 0.977791652E+00

FINAL COORDINATES, FORCES AND ENERGIES:

I	X	Y	Z	FX	FY	FZ	EE
1	51.16903	1.63253	0.14508	0.281E-01	-0.112E-01	-0.778E-03	-0.803E+01
2	45.46435	1.62819	0.50208	0.571E-01	0.552E-01	0.271E-02	-0.801E+01
3	39.84221	1.65427	-0.33039	-0.227E-01	-0.317E-01	-0.672E-02	-0.802E+01
4	34.17151	1.63838	0.07462	-0.208E-02	0.974E-03	0.963E-02	-0.804E+01
5	28.46659	1.64066	-0.28755	0.261E-01	-0.175E-01	0.785E-02	-0.804E+01
6	22.74505	1.63730	-0.14283	-0.123E+00	-0.236E-01	-0.117E-01	-0.804E+01
7	17.03941	1.64372	0.38051	-0.333E-01	-0.341E-01	-0.110E-01	-0.801E+01
8	11.41527	1.63609	-0.47894	0.652E-01	0.510E-01	0.180E-01	-0.802E+01
9	5.74427	1.64380	-0.08563	-0.952E-02	-0.486E-01	0.246E-02	-0.804E+01
10	0.04199	1.64164	0.25832	-0.263E-01	-0.426E-01	0.245E-02	-0.804E+01

And others

EPOT=-0.43434E+03 EKINA= 0.14827E-01 ETOT=-0.43432E+03 TCALC= 0.10000E+01

********** END OF THE CALCULATION **********

CURRICULUM VITAE

PERSONAL INFORMATION

Surname, Name: Kilic, Mehmet Emin

Nationality: Turkey

Date and Place of Birth: 1982, Istanbul

Email: klcmemin@gmail.com

EDUCATION

B.S: Department of Physics, Y.Y. University, 2004

M.Sc: Department of Physics, Y.Y. University, 2007

Phd: Department of Physics, Middle East Technical University, 2015

WORK EXPERIENCE

2008-2015 Department of Physics, Middle East Technical University, Research Assistant.

PUBLICATIONS

1) M.E. Kilic, S. Erkoc, "*Molecular dynamics simulations of ZnO nanostructures under strain: I - nanoribbons*", Journal of Computational and Theoretical Nanoscience **10**, 104 (**2013**).

2) M. E. Kilic, S. Erkoc, "*Molecular dynamics simulations of ZnO nanostructures under strain: II - nanorods*", Journal of Computational and Theoretical Nanoscience **10**, 112 (**2013**).

3) M. E. Kilic, S. Erkoc, "*Structural properties of ZnO nanoparticles and nanorings: Molecular dynamics simulations*", Journal of Computational and Theoretical Nanoscience **10**, 1490-1496 (**2013**).

4) M. E. Kilic, S. Erkoc, "*Structural properties of ZnO nanotubes under uniaxial strain: Molecular dynamics simulations*", Journal of Nanoscience and Nanotechnology **13**, 6597-6610 (**2013**).

5) M. E. Kilic, S. Erkoc, "*Structural properties of defected ZnO nanoribbons under uniaxial strain: Molecular dynamics simulations*", Current Applied Physics **14**, 57-67 (**2014**).

6) M. E. Kilic, S. Erkoc, "*Structural properties of defected ZnO nanosheets under biaxial strain: Molecular dynamics simulations*", Journal of Nanoscience and Nanotechnology, **15**, xx (**2015**)

7) M. E. Kilic, S. Erkoc, "Structural properties of hexagonal shaped ZnO nanorods under torsion and compression: Molecular Dynamics Simulations", International Journal of Modern Physics C (submitted for publication).

INTERNATIONAL SCHOOLS / WORKSHOPS ATTENDED

1. M. E. Kilic, International School on Fundamental Crystallography: Introduction to International Tables for Crystallography, 30 September-5 October, Sofia-Gyulechitza, Bulgaria (**2013**).

2. M. E. Kilic, IYCr 2014 Powder Diffraction course for MS&PhD students, 12-14 May, 2014, Hacettepe Univ. (**2014**).

PROCEEDINGS PRESENTED MEETINGS

1. M. E. Kilic, S. Erkoc,"Structural properties of ZnO nanoribbons under strain: Molecular dynamics simulations", NanoTR7, 27 June-1 July 2011, Sabanci University, Istanbul. Abstract Book, P2.B.9 (**2011**).
2. M. E. Kilic, S. Erkoc, "Structural properties of ZnO nanorods under strain: Molecular dynamics simulations", Turkish Physical Society 28th International Physics Congress (TFD-28), 6-9 September 2011, Bodrum-Turkey, Abstract Book, PP-502 (**2011**) .
3. M. E. Kilic, S. Erkoc, "Structural properties of ZnO nanoparticels and nanorings: Molecular Dynamics Simulations", NanoTR8, 25-29 June 2012, Hacettepe University, Ankara, Abstract: 0124, PP-008 (**2012**).
4. M. E. Kilic, S. Erkoc, "Structural properties of ZnO nanotubes under uniaxial strain: Molecular Dynamics Simulations", Turkish Physical Society 29th International Physics Congress (TFD-29), 5-8 September 2012, Bodrum-Turkey, Abstract Book, PP-408 (**2012**).
5. M. E. Kilic, S. Erkoc, "Structural properties of defected ZnO nanotubes: Molecular Dynamics Simulations", NanoTR9, 24 - 28 June 2013, Atatürk University, Erzurum, Abstract Book, PP-227 (**2013**).
6. M. E. Kilic, S. Erkoc, "Structural properties of pristine and defected ZnO nanosheets under biaxial strain: Molecular Dynamics Simulations", NanoTR9, 24 - 28 June 2013, Atatürk University, Erzurum, Abstract Book, PP-104 (**2013**).
7. M. E. Kilic, S. Erkoc, "Structural properties of defected ZnO nanoribbons under uniaxial strain: Molecular Dynamics Simulations", NanoTR9, 24 - 28 June 2013, Atatürk University, Erzurum, Abstract Book, PP-197 (**2013**).
8. M. E. Kilic, S. Erkoc, " Thermal properties of ZnO spherical nanoparticles: Molecular Dynamics Simulations", Turkish Physical Society 30th International Physics Congress (TFD-30), 2-5 September 2013, İstanbul-Turkey, Abstract Book, PP-361 (**2013**).
9. M. E. Kilic, S. Erkoc, " Thermal properties of ZnO nanotubes: Molecular Dynamics Simulations", Turkish Physical Society 30th International

Physics Congress (TFD-30), 2-5 September 2013, Istanbul-Turkey, Abstract Book, PP-362 (**2013**).

10. M. E. Kilic, S. Erkoc, " Structural and thermal properties of ZnO cubane structures: Molecular Dynamics Simulations", Turkish Physical Society 30th International Physics Congress (TFD-30), 2-5 September 2013, Istanbul-Turkey, Abstract Book, PP-363 (**2013**).

11. M. E. Kilic, S. Erkoc, "Structural properties of defected bilayer ZnO nanosheets: Molecular dynamics simulations", NanoTR10, 17-21 June 2014, Yeditepe Univ., Istanbul, Abstract Book, PP-221(**2014**).

12. M. E. Kilic, S. Erkoc, "Structural properties of hexagonal shaped ZnO nanorods under torsion: Molecular dynamics simulations", NanoTR10, 17-21 June 2014, Yeditepe Univ., Istanbul, Abstract Book, PP. 341(**2014**).

13. M.E. Kilic, S. Erkoc, "Structural properties of hexagonal shaped ZnO nanorods under compress: Molecular dynamics simulations", NanoTR10, 17-21 June 2014, Yeditepe Univ., Istanbul, Abstract Book, PP-342 (**2014**).

14. M.E. Kilic, S.Erkoc, "Structural properties of ZnO nanotubes under uniaxial compression: Molecular dynamics simulations", YMF20, 26 December 2014, Hacettepe University, PP-70 (**2014**).